This is to certify that the

dissertation entitled

OPTIMIZED FABRICATION OF HIGHLY TEXTURED BSCCO/AG
SUPERCONDUCTING TAPE THROUGH MECHANICAL DEFORMATION
AND CONTROLLED MELT PROCESSING

presented by

Jaimoo Yoo

has been accepted towards fulfillment
of the requirements for

Ph.D. degree in Materials Science

Kali Mukherjee
Major professor

Date April 4, 1994

OPTIMIZED FABRICATION OF HIGHLY TEXTURED BSCCO/AG SUPERCONDUCTING TAPE THROUGH MECHANICAL DEFORMATION AND CONTROLLED MELT PROCESSING

By

Jaimoo Yoo

A DISSERTATION

Submitted to
Michigan State University
in partial fulfillment of the requirements
for the degree of

DOCTOR OF PHILOSOPHY

Department of Materials Science and Mechanics

1994

This is to certify that the

dissertation entitled

OPTIMIZED FABRICATION OF HIGHLY TEXTURED BSCCO/AG SUPERCONDUCTING TAPE THROUGH MECHANICAL DEFORMATION AND CONTROLLED MELT PROCESSING

presented by

Jaimoo Yoo

has been accepted towards fulfillment
of the requirements for

Ph.D. degree in Materials Science

Kali Mukherjee
Major professor

Date April 4, 1994

ABSTRACT

OPTIMIZED FABRICATION OF HIGHLY TEXTURED BSCCO/AG SUPERCONDUCTING TAPE THROUGH MECHANICAL DEFORMATION AND CONTROLLED MELT PROCESSING

BY

JAIMOO YOO

Engineering applications of high temperature superconducting oxides, in either bulk or thin film form, demand synthesis and processing that lead to chemically, mechanically, and electronically optimized microstructures. The achievement of such ideal microstructures depends upon fulfilling: i) a high degree of densification, ii) a sharp crystallographic texture characterized by a high degree of alignment of superconducting crystal planes lying parallel to the conducting direction, and iii) a minimal volume % of second phase particles. The need for a strong microstructural control is due to the intrinsic anisotropic properties, weak-link effect, and flux creep phenomena associated with these materials.

Three techniques have been developed to mitigate the problems in Bi-Sr-Ca-Cu-O (BSCCO) superconductors. These are: production of high density, production of superconductor/silver composites, and production of highly textured superconducting tapes. The problems associated with densification in sintering of high-T_c 2223 BSCCO system has been studied. A HIP process technique, for 2223 BSCCO system, has been established which optimizes the stability of high-T_c 2223 phase and densification. Experimental results reveal that the crystal structure of 2223 BSCCO superconducting compound is quite stable with respect to oxygen stoichiometry, under increasing temperature up to 850°C and high pressure, unlike the $YBa_2Cu_3O_7$ superconductor.

For the melt processed 2212 BSCCO/Ag tapes, minimization of the second phase particles, which severely interrupt the local 2212 alignment and reduce J_c, requires

an understanding of the relationship between processing conditions and resulting microstructures. In order to analyze these relationships, various processing conditions have been employed to determine what effect these conditions have on the second phase particles, the resulting texture, and the superconducting properties.

In the present study, the texture evolution in a high-T_c 2223 BSCCO system under thermomechanical deformation has been systematically investigated. Experimental measurements of the microstructural evolution, including crystallographic texture and grain morphology, are presented as a function of the degree of deformation. The orientations of the conducting planes (c planes) have been studied by using X-ray pole figures and analyses of these orientations are reported. Finally, flux pinning phenomena in BSCCO superconductors have been investigated through magnetization measurements (*M-H* curves). The comparison of magnetization measurements for 2212 and 2223 BSCCO/Ag tape reveals that the critical current, J_c, is controlled by flux pinning at high temperatures (> 30K), while the weak links limit the J_c at low temperatures (~5K).

ACKNOWLEDGEMENTS

I would like to express my most sincere gratitude to Professor Kalinath Mukherjee, for his valuable guidance and continual support throughout my Ph. D program and research project. I would also like to thank my committee members, Professor Tom Bieler, Professor Jerry Cowen, and Professor K. N. Subramanian, for their helpful suggestions. Special thanks are extended to the colleagues in Laser laboratory for their helpful support during the years.

Finally, I wish to express my sincere gratitude to my parents and my wife Jungsook for their continual encouragement and support.

TABLE OF CONTENTS

LIST OF TABLES

LIST OF FIGURES

1. INTRODUCTION

Since the discovery of high temperature BSCCO superconducting compounds in 1988 [1-3], a great deal of effort has been dedicated to producing bulk wires and tapes for practical engineering applications (e.g., motors, energy storage, magnetic resonance imaging, and transmisssion lines). Of the three major families of high temperature superconductors [1-7], Y-Ba-Cu-O, Bi-Sr-Ca-Cu-O (BSCCO), and Tl-Ba-Ca-Cu-O, the best wires or tapes, to date, have been made with the BSCCO system. At present all YBaCuO wires are weak linked and have only small J_c in magnetic fields. In the Tl-based system, the superconducting properties are potentially very interesting, but the toxicity of Tl together with the complex processing requirements have limited practical development [6,7]. Three superconducting phases exist in the Bi-Sr-Ca-Cu-O system [2,8,9]. They are known by their ideal Bi:Sr:Ca:Cu stoichiometries as 2201 (T_c ~7-20 K), 2212 (T_c ~75-90 K), and 2223 (T_c ~110 K). Throughout this thesis, 2201, 2212, and 2223 refer to the respective superconducting phases, not the actual composition of the phases.

While significant progress and understanding have been obtained in the processing and properties of these material, over the past five years, there are two major problems which must be overcome for widespread use of the BSCCO superconductor. The first is the ***weak link*** effect [10-13] which results in very low transport critical current, typically found in sintered BSCCO superconductor. For the BSCCO system, the weak-link problem can be greatly reduced by the minimization of high angle grain boundaries in the paths of the transport current. This can be achieved by producing sharp crystallographic texture, characterized by a high degree of alignment of superconducting crystal planes lying parallel to the conduction direction.

The second is related to thermally activated ***flux creep*** [14-20], which will severely limit the maximum operating temperature. Unless the flux creep is reduced by enhanced flux pinning, the operating temperature and magnetic field will have to be reduced to less than 30K, and few tesla respectively for the BSCCO system. Besides these two fundamental difficulties, a unique retrograde densification characteristic [21], coupled with a narrow sintering range overlapping the melting temperature, cause this compound a difficult one to sinter. Specimens sintered conventionally in air had merely 46.5 % to 62 % of theoretical density [21-24].

Three techniques have been developed to date, to mitigate the above mentioned problems in oxide superconductors: (1) high degree of densification, (2) production of superconductor/silver composites, and (3) production of highly textured superconducting tapes. For the sintering problem in bulk BSCCO superconductor, a new hot isostatic pressing (HIP) technique was developed with an objective to enhance densification of the high T_c phase of a Pb-doped BSCCO superconductor. With HIP densification process, $Bi_{1.6}Pb_{0.4}Sr_2Ca_2Cu_3O_Z$ superconductor was densified to 94 % of the theoretical density at a HIP temperature of 850°C, maintaining the high T_c phase [24], and without requiring any post fabrication heat treatment.

It has been shown that melt processing is more suitable for manufacturing 2212 BSCCO/Ag tape system [25,26]. On the other hand, thermomechanical processing has been proven to be the most effective technique for processing 2223 BSCCO/Ag tape system [7,27] because of a decomposition of the high T_c phase and the difficult growth of 2223 BSCCO phase from the melt [7,17,28]. Both 2212 and 2223 tapes are being studied, with the major emphasis on 2223 because of its higher T_c.

For the melt processed 2212 BSCCO/Ag tapes, the second phase particles and pores interrupt the local 2212 alignment, perhaps because they interfere with 2212 growth along the plane of the tape. In some micrographs, the 2212 grains appear to have grown around the second phase particles, whereas in other cases the 2212 alignment is totally disrupted in the vicinity of the second phase [29,30]. In this regard, attempts have been made to reduce the amount of secondary phase material present in the superconducting layer, and to find the optimum processing that will yield the highest degree of texture by using a "controlled melt process". This goal was accomplished by processing the superconductor tape under various processing conditions to determine what effect these conditions have on the resulting grain texture.

For applications involving wires or tapes [31-34], the brittle nature of oxide ceramic superconductors imposes major difficulties in production and handling. These problems can be ameliorated by forming a layered composite of the superconductor and a ductile metal. This configuration also allows a nearly conventional thermomechanical treatment suitable for mass production. Such thermomechanical processing methods have distinct advantages over simple melt processing and tape casting methods, which yield highly textured materials, but do not readily lead to sufficient densification of the powder. Also such production of a long length (> 100m) is difficult. Recent HRTEM (High Resolution Transmission Electron Microscopy) study [35,36] revealed high density of dislocation in 2223 BSCCO/Ag tapes after conventional thermomechanical processing, suggesting the possibility of reducing the flux creep problem.

There are, however, some particular challenges which must be overcome before we can produce long lengths of conductors via thermomechanical processing. First, it is necessary to develop an understanding of the mechanical behavior of the BSCCO superconductor, and of the microstructural development during mechanical processing. Since superconductivity occurs on $\{00l\}$ planes of the orthorhombic unit cell [37], it is necessary that the processing produces a texture characterized by $\{00l\}$ type planes lying parallel to the plane of the tape or parallel to the axis of a wire, and thus along the direction of current flow. For example, in BSCCO/Ag based tapes, a number of experimental results show that a strong crystallographic texture is essential to minimize weak links, and to achieve a high critical current density. Enomoto et al. [38] found that the critical current density increased sharply as the degree of c-axis texture of the tapes increased. A similar result has been reported, for 2223 (BSCCO) tapes, by Jin et al. [39].

Therefore, preferred orientation, *i.e.* "texture" appears to be a key parameter in enhancing critical current density (J_c).

The exact mechanism for texture formation in the silver-clad BSCCO tape, during the rolling process, is not clearly described in the literature. Consequently, a systematic study has been undertaken to investigate the effect of mechanical deformation on the c-axis texture of $Bi_{1.6}Pb_{0.4}Sr_2Ca_2Cu_3O_Z$ /Ag composite, initially compacted by a HIP-cladding technique. An understanding of these effects would be useful in controlling the microstructure that is essential to achieve high critical current density (J_c). The objective of this research is to develop a basic understanding of the mechanical behavior, and to utilize this understanding to develop synthesis and processing methods to allow predictions of the microstructures that would result from particular processing methods.

Some pinning mechanisms, such as Y_2BaCuO_5 precipitate pinning and twin plane pinning [15], have been demonstrated in 123 YBaCuO superconductors. The pinning mechanism in BSCCO/Ag superconducting wires, however, has not been well studied. In this regard, the pinning phenomena in BSCCO/Ag superconducting tapes were discussed according to the magnetization measurements, since one can gain valuable insights into the pinning phenomena in high-T_c superconductors from the magnetization-field (*M-H*) curves. The enhancement in the magnetization hysteresis (ΔM) for the thermomechanically processed 2223 BSCCO/Ag tape shows a good candidate for the high temperature and high magnetic field applications.

The overall objective of this research is to mitigate two fundamental problems, weak-link and flux creep, and to investigate the feasibility of obtaining a dense superconductor which is mechanically reliable and has a highly textured microstructure. This practical goal is coupled with the primary objective of understanding the relationship between processing conditions, microstructure, and superconducting properties.

2. LITERATURE SURVEY

2.1 Fundamental Problems in High T_c Superconductors

2.1.1 Weak-link and Flux Creep

Two electromagnetic phenomena have hindered the widespread commercialization of high critical temperature oxide superconductors in bulk form. The first is known as the weak-link effect, which gives rise to a relatively weak critical transport current, J_c, across most high-angle grain boundaries linking neighboring oxide grains when exposed to a modest applied magnetic field. For example, the critical current density for a randomly oriented polycrystalline $YBa_2Cu_3O_y$, at 77 K in an applied magnetic field of a few hundred gauss, is typically less than 100 A/cm^2.

High-angle grain boundaries are the immediate obstacle to further development of materials for applications that require high J_c values in high magnetic fields. The problem arises because most high-angle grain boundaries act like a Josephson junction [11, 13]. The characteristic properties of such junctions are a reduced zero-field J_c value and, more importantly, a strongly magnetic-field-dependent J_c that can decrease by more than an order of magnitude in fields of a few hundred gauss.

For the BSCCO system, the weak link problem can be greatly reduced by minimizing high angle grain boundaries in the paths of transport current. This can be achieved by producing a sharp crystallographic texture characterized by a high degree of alignment of superconducting crystal planes lying parallel to the conducting direction. Thus, an important processing challenge has been to develop long, continuous lengths of highly textured superconducting oxide.

The second phenomenon is known as flux creep (or giant flux creep) [14-17]. Significant magnetic field penetration can occur in the interior of cuprate superconductors above a critical magnetic field. If the magnetic flux lines within the superconductor are not rigidly pinned in place, then Lorentz forces can cause the flux lines to migrate, resulting in resistive energy dissipation[14,15]. Cuprate superconductors have been found to exhibit significant flux creep in modest magnetic fields, at temperatures well below the critical temperature. For example, in a magnetic field of ~10,000 gauss (1tesla=10,000 gauss), oriented parallel to the c axis of a 2212 BSCCO or 2223 BSCCO superconductor, a significant drop in intragranular critical current density is observed as the temperature is raised above ~30 K [17]. Thus, a second key challenge has been to develop processes to introduce effective flux-pinning sites into superconducting oxides. The following issues describe the origin of flux creep and the current status of problem.

2.1.2 A Model for Flux Creep in High T_c Superconductors

A magnetic flux penetrates into High T_c superconductors as lines of Abrikosov vortices having one magnetic flux quantum [40]. These vortices (Figure 1) and their interaction with inhomogeneities and defects of the material (pinning) determine both the magnetic properties of superconductors and the ability of superconductors to carry the superconducting current. The limiting value, the critical current density, is given by the balance of two opposing forces acting on the magnetic flux lines: The pinning force due to spatial variations of the condensation energy and the Lorentz force exerted by the transport current [14]. Energy is dissipated whenever flux lines move. Traditionally, one distinguishes two regimes of dissipation: "flux creep" when the pinning force dominates and "flux flow" when the Lorentz force dominates [14].

Extensive studies in the flux creep revealed the dissipation behavior in the mixed state of single-crystal $Bi_{2.2}Sr_2Ca_{0.8}Cu_2O_8$. Palstra et al. [14,15] found a current-independent resistance which is thermally activated and can be described by an

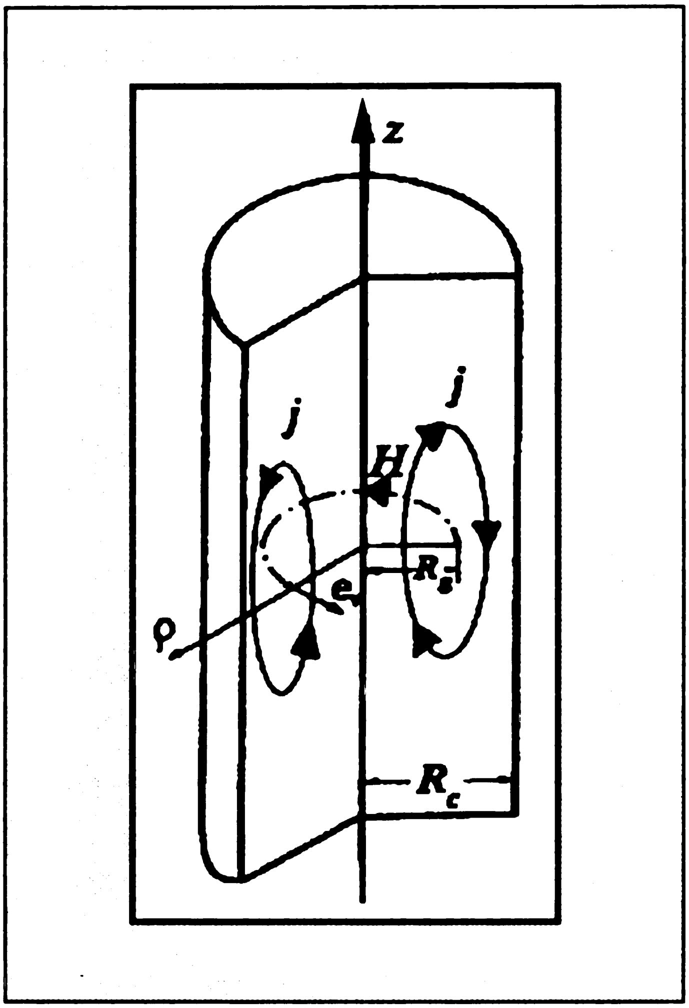

Figure 1. Toroidal Abrikosov vortex inside a superconducting cylinder of radius R_c. VL (circumference of radius R_s) is shown by a dash-dotted line (Ref. 40)

Arrhenius law, $\rho=\rho_0\exp(-U_0/T)$, where ρ, ρ_0, U_0, T stand for resistivity, preexponential term, activation energy, temperature. The U_0 depends weakly on magnetic field and orientation, and is relatively small. The preexponential factor in the Arrhenius law, ρ_0, is magnetic field and orientation independent. It is three orders of magnitude larger than that for the normal-state resistance. This behavior is distinctly different from previous observations in traditional superconductors.

Flux creep was first predicted as a possibility by Anderson [41] and investigated by Beasley, Labusch and Webb [42]. It can be, and generally is, ignored for strong-pinning, high current density superconductors, such as those used in commercial devices when operating at 4.2 K. However, at much higher temperatures it is likely to have a significant effect upon the overall flux-pinning situation and critical current density in even strongly pinning materials.

2.1.2.1 General Formalism of Stress-assisted Thermal Activation

It is assumed that some entity, whether it be a diffusing atom, a crystal dislocation or, as in this case, a quantized flux vortex, sits at the bottom of a potential well of depth U [16]. U is the difference in the Gibbs Function of the system between when the entity is in the well and when it is moved away from it. In the absence of any imposed stress the entity can, by thermal activation, hop out of the well at the following rate (for both forward and backward directions)

$$R = \Omega_o \exp(-U / kT) \qquad (1)$$

where Ω_o is the frequency with which the entity tries to escape from the well [16] and k_B is Boltzmann constant.

2.1.2.2 Application to Flux Creep

The basic concept of flux creep is that a flux line or flux bundle can be thermally activated over the pinning energy barrier, even if the Lorentz force exerted on the flux bundle by the current is smaller than the pinning force (Figure 2) [15]. The rate with which this process occurs is given by the attempt frequency, the value of the unperturbed pinning potential U_o, and the Lorentz force energy U_L. The rate of forward hopping (in the direction of the Lorentz force) is then given by [14,15]

$$\nu_o \exp[(-(U_o - U_L) / k_B T] \qquad (2)$$

and the rate of reverse hopping (opposite the direction of the Lorentz force) is given by

$$\nu_o \exp[(-(U_o + U_L) / k_B T]. \qquad (3)$$

This results in a net hopping rate:

$$\nu_{eff} = \nu_o \exp(-(U_o / k_B T) \sinh(U_L / k_B T). \qquad (4)$$

The Lorentz force energy U_L is given by the Lorentz force density $F_L = J \times B$, the volume of the flux bundle V_c, that moves independently of the other flux bundles, and the range of the pinning potential r_p:

$$U_L = (J \times B) V_c r_p \qquad (5)$$

In addition to thermal activation, this model predicts a linear *I-V* curve for small current densities, which can be checked experimentally [15]. For current density J for which

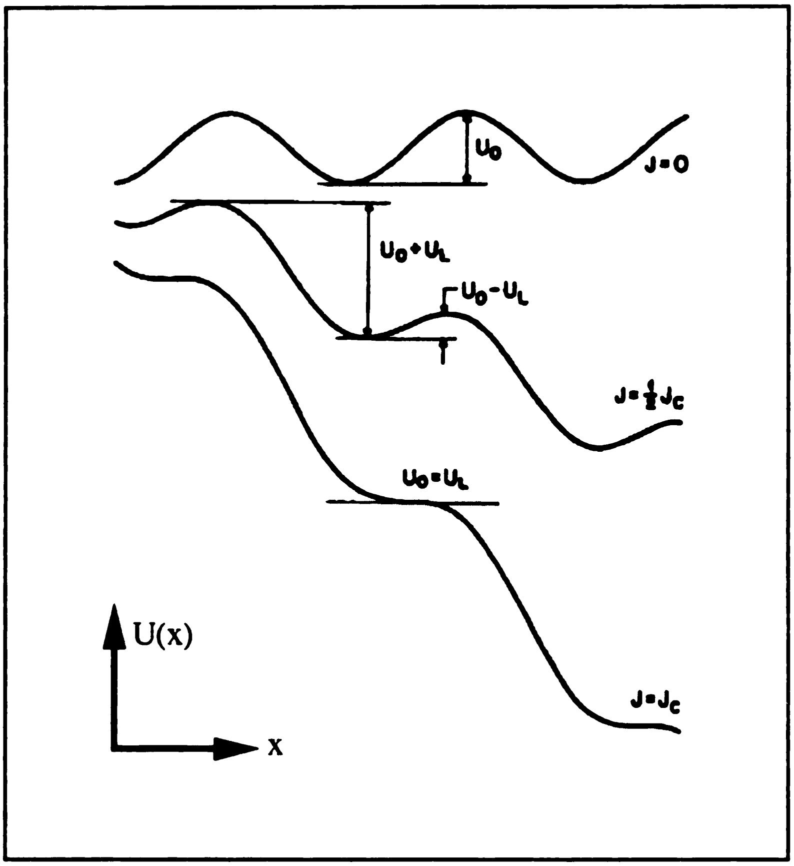

Figure 2. Schematic representation of the condensation energy along the coordinate of the Lorentz force. The upper curves shows the unperturbed potential U_o and the lower curve shows depinning (U_o=U_L) (Ref. 15)

$U_L \leq k_B T$, $Sinh(x) \cong x$ and the average flux velocity $v_\phi = v_{eff} L$, with L the hopping distance, is proportional to the current density:

$$v_\phi = 2 v_o L \frac{JBV_c r_p}{k_B T} \exp(-(U_o / k_B T). \qquad (6)$$

The range over which ohmic dissipation is observed $(E \propto J)$ sets an upper limit on the flux bundle volume V_c.

E is proportional to J only if $JBV_c r_p \leq k_B T$. Assuming that the pinning in this material is governed by point defects, or that $r_p \approx \xi_{GL}$, the Ginzburg-Landau coherence length [15], one can find that at least for high fields the flux bundle volume V_c, cannot be much larger than $a_o^2 d$, which is the volume of one flux line (a_o is the flux line separation and 'd' the sample thickness). It is possible that the bundle volume is even smaller than this value, if the length of the bundle (the correlation length L_c) is shorter than the sample thickness 'd'. This means that at least for large magnetic fields and the temperature range probed the flux line lattice is in the "amorphous limit", $V_c \approx a_o^2 L_c$. Supposing that the hopping distance is of order of a_o, one can rewrite Eq. (6) as

$$\rho = \frac{v_\phi B}{J} = \frac{2 v_o \phi_o^2 L_c}{k_B T} \exp(-(U_o / k_B T) \qquad (7)$$

2.1.2.3 Thermally Activated Dissipation in BSCCO Superconductors

Figure 3 shows the resistive transition of $Bi_2Sr_2CaCu_2O_8$ in magnetic fields of 0, 2, 5, and 12 T both perpendicular and parallel to the basal planes [14]. The inset shows the zero-field transition up to 300 K. The transition in zero field is very sharp, but broadens considerably upon applying a field. In order to show the low-resistance data more clearly, the resistivity data is replotted in Figure 4(a) on a logarithmic scale, versus

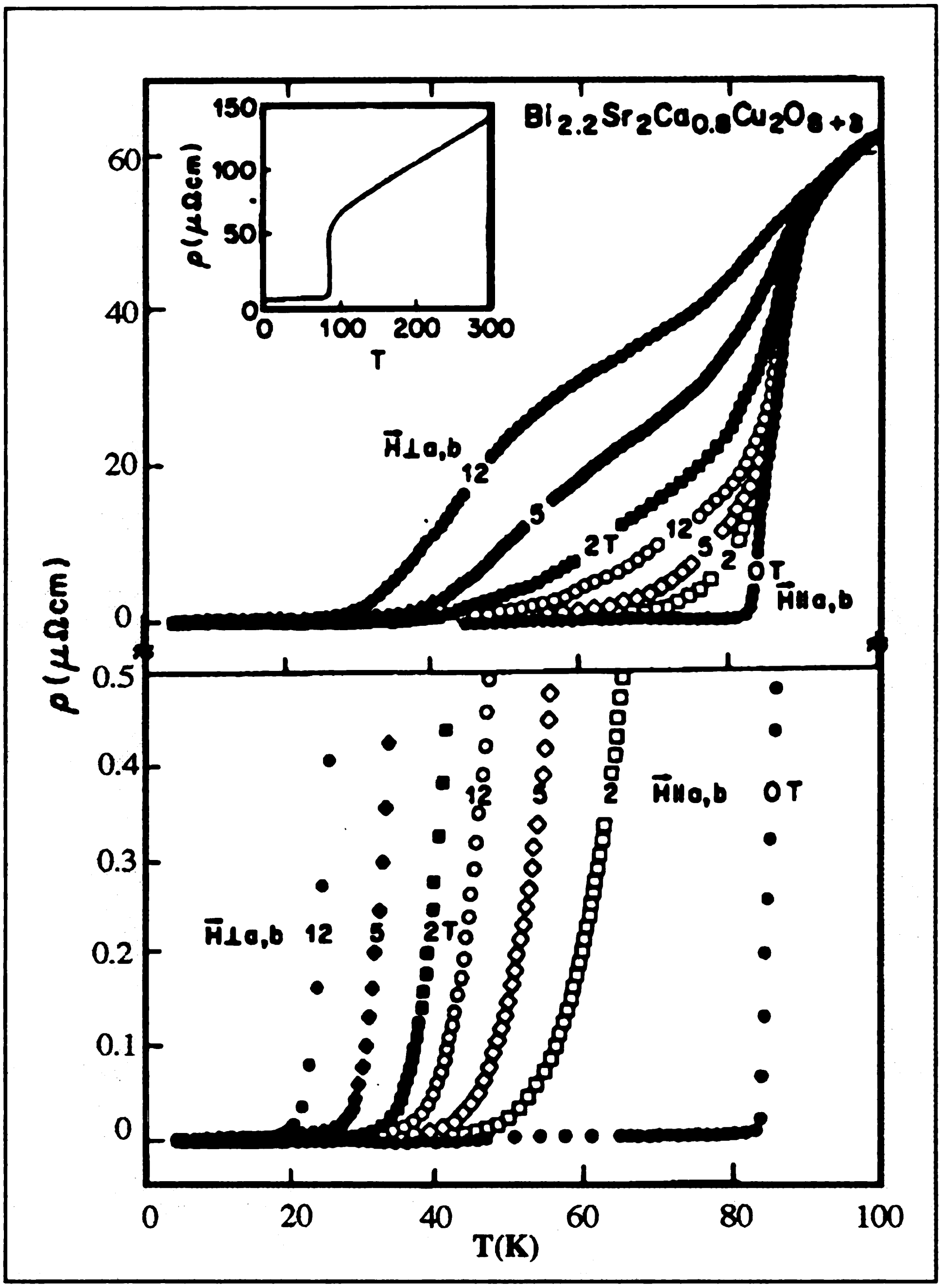

Figure 3. Temperature dependence of the electrical resistivity $Bi_2Sr_2CaCu_2O_8$ in four selected magnetic fields, 0, 2, 5, and 12T, oriented parallel (open symbols) and perpendicular to the basal planes. The lower part of the figure is a magnification by about a factor 100 to emphasize the exponential behavior. The inset shows the zero field resistivity up to room temperature (Ref. 14)

inverse temperature for four magnetic fields 0, 0.1, 1, and 10 T perpendicular to the basal plane [15]. While the anomaly at T_c, is very small in this data, this Arrhenius plot shows that the resistivity is thermally activated over four orders of magnitude from 10^{-4} to 1 μΩ cm below about 1 μΩ cm or 1% of the normal-state resistivity, from 17 to 75 K, and from 0.1 to 12 T. The slope of the curves below this 1% criterion is related to the activation energy U_o, and the resistivity can therefore be described as [14]

$$\rho(T,H,\phi) = \rho_o \exp(-U_o / k_B T) \qquad (8)$$

The temperature scale for the activation energy can be normalized as U_o/T. This is shown in Figure 4(b) for three magnetic fields 0.1, 1, and 10 T perpendicular to the basal plane [14]. All curves coalesce on one line which means that the preexponential factor ρ_o is field independent. The value of ρ_o is about 10^5 μΩ cm, about three orders of magnitude larger than the normal-state resistivity.

Comparing this experimental result (Eq. (8)) with previous theoretical result of Eq. (7) [15], one can relate the preexponential factor ρ_o to the attempt frequency v_o. Assuming that $L_c \approx 0.1d$, one can find that $v_o \approx 10^{12}$ Hz. For large current densities but still in the flux creep regime $J \geq k_B T / BV_c r_p$ this linear $E(J)$ behavior will turn into an exponential behavior. This is regime in which flux creep has been studied in traditional superconductors. In these materials the current densities to obtain linear E-J characteristics are much smaller than in the high-T_c, materials, because (1) thermal energies are much smaller, (2) V_c, is larger, and (3) r_p is larger because the coherence lengths are larger for low temperature superconductors [15].

Unpinning occurs when $U_o = U_L$ which means that the effective barrier height $U_o - U_L$ has been reduced to zero (see Figure 2). For these currents one gets in the regime of flux flow, where the flux line velocity is no longer determined by the probability of

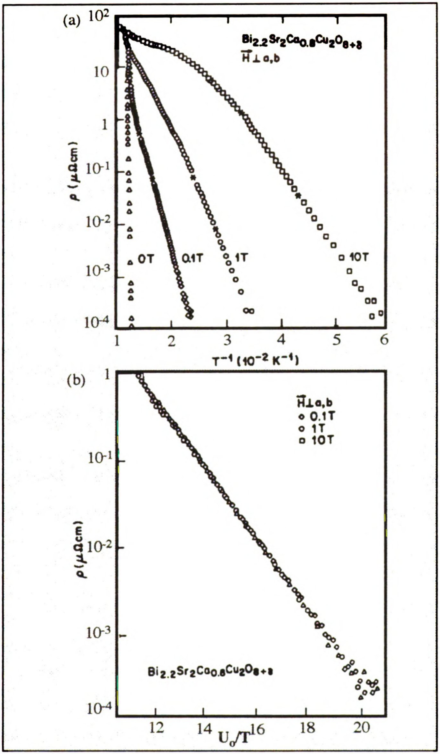

Figure 4. (a) Arehenius plot of the resistivity of $Bi_2Sr_2CaCu_2O_8$ four selected magnetic fields, 0, 0.1, 1.0, and 10T, perpendicular to the basal planes (Ref. 15) (b) Universal behavior of the thermally activated electrical resistivity for the data of (a)by use of a normalized temperature scale U_o/T (Ref. 14)

hopping over an energy barrier, but by the viscosity (or the mutual interactions) within the vortex system [14].

2.1.2.4 Pinning Behavior in High T_c Superconductors

It has been argued that the large activation energies, in the $YBa_2Cu_3O_7$ compound, stem from the presence of twin planes which form extended defects [15]. In contrast, the dominant pinning points in $Bi_2Sr_2CaCu_2O_8$ are speculated to be point defects. Palstra et al. [14,15] argue that this difference in defect structure is not the origin of the difference in pinning energies. They think that the different pinning energies stem from the difference in anisotropy. Namely, it has been shown that the anisotropy in electronic properties is much larger in $Bi_2Sr_2CaCu_2O_8$ than in $YBa_2Cu_3O_7$ [43,44]. A large electronic anisotropy directly results in a reduction of the tilt modulus of the flux lines, which means that the correlation length along the flux lines L_c, is reduced. In the extreme limit of completely decoupled layers, there is no correlation between the vortices in adjacent planes, and L_c, is reduced to the interlayer spacing. A short correlation length along the vortices L_c, results in small activation energies, because of the small flux bundle volume [15]:

$$U_o = \mathbf{J}_c \times \mathbf{B} V_c r_p = \mathbf{J}_c \times \mathbf{B} R_c^2 L_c r_p \qquad (9)$$

with R_c, the correlation length of the vortices in the planes, and L_c the correlation length along the vortex. Assuming we are in the amorphous limit of the vortex system ($R_c = a_o$), and that the main defects are point defects ($r_p \approx \xi_{GL}$), this relation reduces to

$$U_o = \mathbf{J}_c \times \phi_o L_c \xi_{GL} \qquad (10)$$

Large flux creep is thus favored by: (1) small values of L_c, which is intrinsic to large anisotropy compounds and thin films [43,44] and (2) a short coherence length which holds for extreme type-II superconductors including the high-T_c superconductors. Palstra et al. [15] interpretation is corroborated by two experimental findings: (1) The layered compound $NbSe_2$ (with a low transition temperature T_c=7.2 K) and various other thin film superconductors have as large a flux creep effect [45] as in the high-temperature superconductor $Bi_2Sr_2CaCu_2O_8$; (2) a comparison of $YBa_2Cu_3O_7$ (T_c ~90 K) with $YBa_2Cu_3O_{6.7}$ (T_c, 60 K), which is shown in Figure 5(b).

Figure 5 shows a comparison of the flux creep behavior of various compounds, including $Tl_2Ba_2CaCu_2O_8$ and $Pb_2Sr_2RCaCu_3O_8$ for a magnetic field of 5 T perpendicular to the basal planes. The results are normalized with respect to the transition temperature T_c and the normal state resistivity ρ_n. Palstra et al. [15] associate the broadening of resistive transition with the electronic anisotropy, as equivalently with the tilt modulus of the flux lines for the various materials. Apparently, the Tl compound is even more anisotropic than the Bi compound. From this point it is clear that the 90-K-phase $YBa_2Cu_3O_7$ is by far the least anisotropic and therefore this material has the largest activation energy for flux motion. Furthermore, it can be expected that the anisotropy of compounds in homologous series, i.e., with equivalent building blocks between the $[CuO_2]_\infty$ layers, is similar. This means that the activation energy for flux motion for the various Bi and Tl compounds are of the same magnitude, but much smaller than that for the $YBa_2Cu_3O_7$.

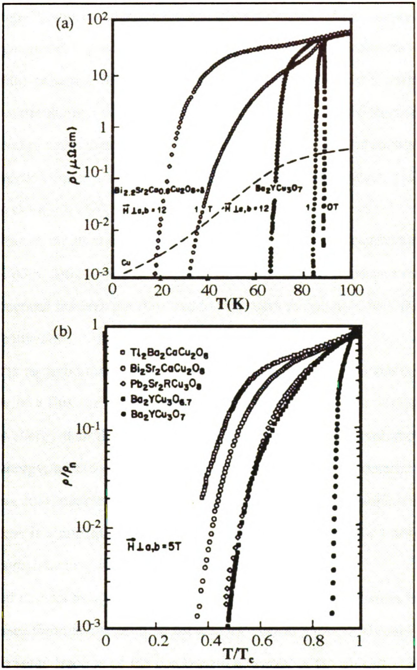

Figure 5. Temperature dependence of electrical resistivity of (a) $Bi_2Sr_2CaCu_2O_8$ and $YBa_2Cu_3O_7$ on a semilogarithmic scale, and (b) several high temperature superconductors. The data are nomalized for the transition temperature and the normal state resistivity (Ref. 15)

2.2 Flux Pinning and Intragranular J_c

The high-T_c superconductors are classified as Type II superconductors, which means that magnetic fields greater than some small value (H_{c1}, typically less than a few tens of millitesla) penetrate the superconductor as quantized units of magnetic flux, surrounded by a circulating vortex of electrons. In the presence of an electrical current, the flux lines tend to move under the influence of the Lorentz force, as shown in Eq. (5). Motion of these flux lines is a dissipative process manifested as electrical resistance [14,15], as seen in Eq. (7) and (8).

Because of the short coherence lengths (ξ) in oxide superconductors, stacking faults and even point defects may be effective flux pinners. It is important to determine which microstructural features pin flux, and to find ways to optimize both their number density and effectiveness.

Size is an important characteristic of a pinning center. At the center of the vortex structure of a flux line is a normal core of diameter $\sim 2\xi$. The superconducting state has lower energy than the normal state by an amount per unit volume called the condensation energy, as shown in Figure 2. The pinning energy is determined by the volume of vortex core occupied by the pin and the decrease in condensation energy at the pin. This decrease is a maximum equal to the condensation energy, for a normal region (e.g., a non superconducting second-phase precipitate).

Crystal defects may cause smaller decreases in the condensation energy. If a vortex core passes through one of these defects, the system gains an amount of pinning energy equal to some fraction of the condensation energy in the pinned volume of the core [46]. An ideal pin has a dimension $\sim\xi$ in the direction of the Lorentz force and, to increase the volume of core pinned. Therefore, properly oriented linear defects, such as those produced by heavy-ion irradiation are especially effective, as will be discussed in subsequent section. Planar structures are also expected to be effective.

At temperatures substantially below their critical temperature, all of the high T_c materials exhibit reversible magnetization and resistive behavior due to flux creep, indicating very weak flux pinning. For each compound, there exists Δ M defined by $M_+ - M_-$, where M is the magnetization and $M_{+,-}$ corresponds to increasing or decreasing field, respectively in the magnetization (M vs. H) curve. Hysteresis (Δ M) is proportional to intragranular J_c at certain temperature and magnetic field. The irreversibility line (IL), the disappearance of pinning at certain temperature and a certain field, can be determined from the magnetization curves by determining the disappearance of hysteresis (Δ M=0) in the magnetization curves at fixed temperatures. Thus, it is clear that the temperature range for applications of all known high temperature superconductor is severely limited by this phenomenon. In fields ~10,000 gauss, directed parallel to the c axis, the collapse of intragranular J_c determined from magnetization curve, occurs at 25-35 K in the highly anisotropic 2212 BSCCO compounds [17].

Recent theoretical and experimental work [15,48,49] suggests that the important structural parameter is the distance between the Cu-O plane. Those compounds that have a single nonconducting oxide layer between Cu-O planes exhibit the least anisotropic behavior and the highest irreversibility lines. In the bismuth and thallium 2223 and 2212 structures, double layers of Bi-O or Tl-O effectively divide the structures into isolated superconducting layers. For magnetic fields parallel to the c axis, which is reportedly to be worst case [17], these insulating layers are thought to cause flux lines to break up into short segments or "pancakes" that may decouple and move independently under the influence of the Lorentz force and thermal activation.

As discussed before, for flux pinning, two consequences of this decoupling are a reduction of the effective pinning volume by limiting the length of flux line pinned, and an increase in the required pin density, since each pancake along the length of a flux line must be pinned separately. Reduction of the pinning volume reduces the pinning energy, which reduces the thermal activation barrier (U_o), and thus increases the rate of thermally activated flux motion, as shown in Eq.(10). It is clear that the presence and, to a large extent, the position of the irreversibility line are intrinsic properties of the material, determined by its structure. Nevertheless, recent studies of flux pinning by radiation damage [46,50,51] indicate that the position of the irreversibility line depends to a significant degree on the specific characteristics of the pinning centers, and that it can be moved to a higher field and temperature by increasing the density of pinning centers.

2.2.1 Techniques for Flux Pinning Enhancement

While the weak link problem in bulk materials can be avoided through c-axis texture, the high-field J_c still seems limited to less than 10^4 A/cm^2 at 77 K due to thermally activated flux creep, as noted before. Unless the flux creep is reduced by enhanced flux pinning, the operating temperature and field will have to be reduced to less than 30K for the 2212 BSCCO system or to $H < 50{,}000$ gauss for the YBaCuO system. Effective flux-pinning requires the presence of extremely fine defects with the size scale comparable to the superconducting coherence length. Several processing techniques can induce fine defects and improve the flux pinning.

2.2.1.1 Proton /Heavy Ion/Neutron Irradiation

Deliberately introducing defects, by particle irradiation, is an effective way to increase the flux pinning in high critical temperature superconductors. Proton irradiation generates a random distribution of point defects, which largely enhances the critical current in YBaCuO single crystals; but it is not effective in shifting the irreversibility line to higher magnetic fields.

For irradiation that produces randomly distributed defects, the most important factor determining the resulting pinning is the size distribution of the induced defects [46]. When a material is irradiated with 3 MeV protons, defects are formed through energy transferred to the atoms of the solid by direct impact. Energy transfer to the electronic system plays a negligible role. The size of the damaged region increases with the primary recoil energy (i.e., with the energy transferred to the target nucleus in the primary collision). Figure 6(a), (b) shows magnetization loops of YBaCuO single crystal for several fluences of 3 Mev proton irradiation. The innermost loops in both Figure 6(a) and (b) correspond to the unirradiated state, and the progressively larger loops correspond to increasing irradiation fluences. The large and systematic enlargement of magnetic hysteresis with irradiation, which is a consequence of the extra pinning generated by the radiation-induced defects, is apparent in both sets of data.

Apparent in the 77 K data (Figure 6(b)) is the change from irreversible to reversible magnetization behavior observed at high fields. The boundary between these regimes represents the irreversibility field at that temperature [H_{irr} (T)]. It can be seen that, although the hysteresis at low fields is increased by orders of magnitude, H_{irr} is nearly independent of dose. This implies that proton irradiation is not effective in enlarging the irreversible regime of $YBa_2Cu_3O_7$ in the field versus temperature diagram. Figure 6(c) shows the results of these measurements in two crystals before irradiation and after irradiation at several fluences. It is clear that proton irradiation produces only minor shifts in the irreversibility line, in spite of the large enhancements in J_c. Others reached the same conclusion [52].

To overcome the limitations of random distributions of point defects, the pinning capabilities of a different microstructure have been explored [53]. Obviously, defects that confine a longer section of a vortex core should provide a better pinning. The optimum pinning sites should consist of columns of nonsuperconducting material that completely traverse the sample in the direction of the applied field. To provide the

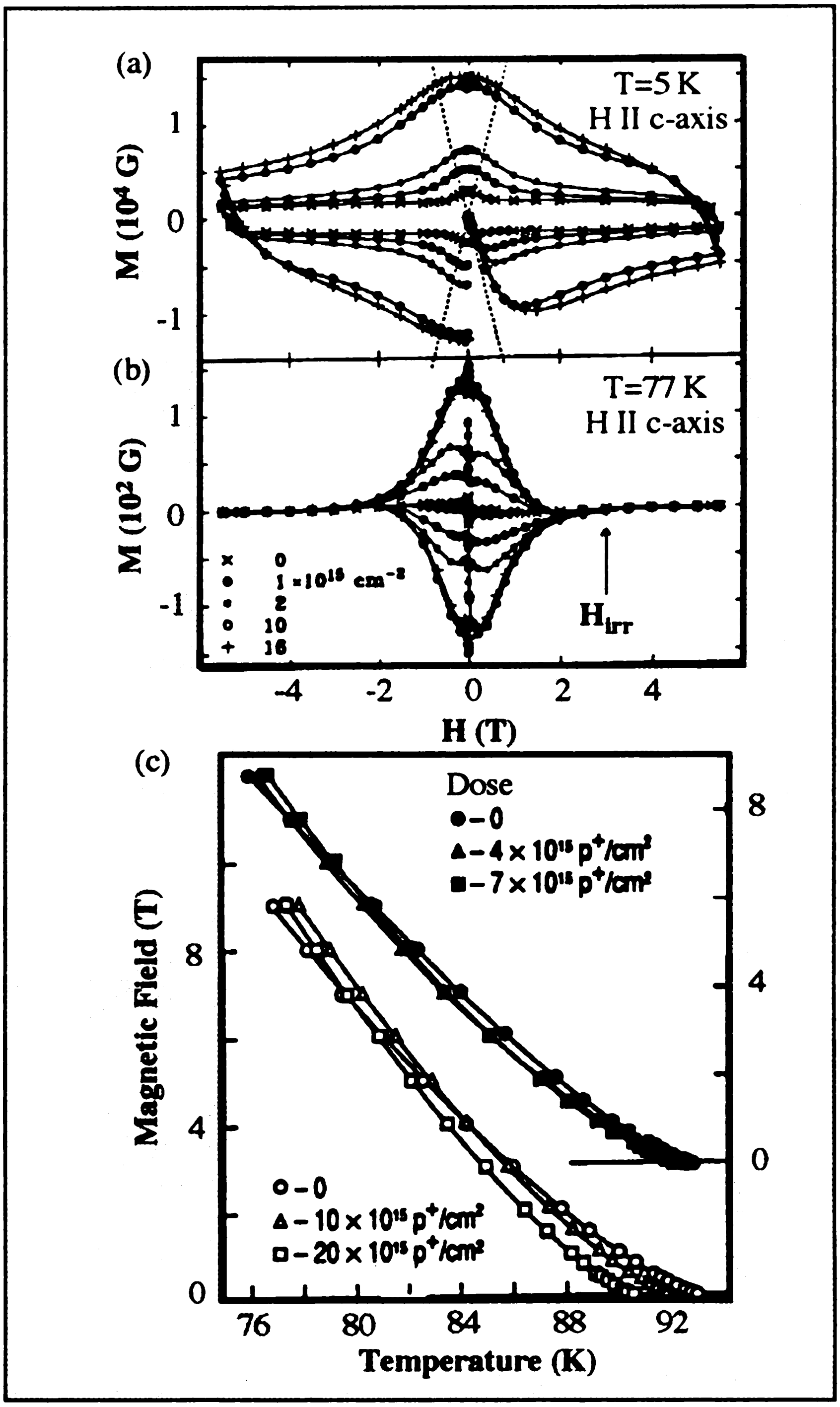

Figure 6. Magnetization as a function of applied magnetic field [M(H)] for $YBa_2Cu_3O_7$ crystal at various doses of proton irradiation at (a) 5 K and (b) 77K (c) The irreversibility line [H_{irr}(T)] for two crystals as a function of proton dose (Ref. 46)

maximum pinning force, the diameter of these columns should be of the order of the core diameter (ξ). Such defects have been produced by irradiation with high-energy heavy ions.

The aligned columnar defects created by high-energy heavy-ion irradiation generate even stronger vortex pinning, resulting in higher critical currents at high temperatures and fields and a large displacement of the irreversibility line to higher fields [46]. Recent research [54] shows that the damage produced by high-energy heavy ions in some metals is due to energy transfer to the electronic system. This results in an unbalanced positive charge along the path of the ion, generating a Coulomb explosion that produces a track of heavily damaged, probably amorphous material.

It also has been demonstrated by several researchers that irradiation with fast neutrons enhances the flux pinning in high T_c superconductors [50,51]. The most striking effect has been reported by van Dover et al. [51] in a $YBa_2Cu_3O_7$ single crystal. A hundred-fold-improved critical current density (magnetization J_c) to 0.6×10^6 A/cm^2 has been obtained at 77K in $H = 0.9$ T, which is the highest in bulk high-T_c superconductors and approaches those in epitaxial thin films.

The exact nature of the induced flux pinning defects is not understood. Because of the small cross section in neutron collision, a relatively homogeneous distribution of extremely fine defects is anticipated. The neutron bombardment technique may not be as practical a route as is desired for industrial applications, such as high T_c superconductor wires, not only from the convenience point of view but also because of the radioactivity generated by fast neutron irradiation (especially if silver cladding is present).

2.2.1.2 Other Methods

The need for a more practical method for flux pinning enhancement led to the development of the phase decomposition technique [55]. This technique is based on the decomposition of $YBa_2Cu_4O_8$ (1-2-4 phase) precursor into $YBa_2Cu_3O_7$ (1-2-3 phase) containing a high density of phase-transformation-induced defects. Since copper atoms have to come out of every unit cell, extremely fine-scale defects are anticipated [55]. Transmission electron microscopys [56] reveals the presence of extremely fine scale stacking faults on the order of 1-3 nm thick, and other associated microstructural features, such as fine twin structure (10-50 nm spacing) and coarse CuO particles (~250 nm in average diameter which is too large for efficient flux-pinning).

The dispersion of nonsuperconducting second phase inclusions is useful for pinning enhancement. Reported examples include the Y_2BaCuO_5 (2-1-1 phase) particles in the melt-processed $YBa_2Cu_3O_7$ superconductor [57], and the Ca_2CuO_3, $CaSrPbO_4$, and $Sr_2Ca_2Cu_3O_x$, precipitates in the Bi-Sr-Ca-Cu-O superconductors [58]. These particles are typically on the order of submicrometer to micrometer size.

Recent high resolution transmission electron microscopy work of Dou et al. [36] found aligned and high density of dislocation (area density of $\sim 10^{12}$lines/cm^2) in 2223 BSCCO/Ag tapes after conventional thermomechanical (rolling and annealing) processing. The pinning mechanism in Ag-clad BSCCO superconducting tapes, however, has not been well studied.

2.2.2 Extended Bean Model

Because of their technological and scientific importance, much effort has been put into the study of the critical current density (J_c) of the high-temperature superconductors (HTS). An accurare determination of intrinsic J_c is essential to the understanding of the flux pinning phenomena and, therefore, to the ultimate goal of improving the J_c of HTSs with a view to practical applications. Although estimations of J_c's have been obtained from various pulse experiments [59,60], a poor resolution in conjunction with the lack of systematic study calls for further investigation into the pulsed-current method. In addition, it is believed that one can gain valuable insights into the pinning phenomena in high temperature superconductors from the magnetization-field (*M-H*) curves.

Many researchers [37,61] use the Bean model [62], to deduce the critical current density J_c from magnetization measurements, since the shape of the hysteresis loop being a consequence of the critical current density in the sample and its dependence on the local field. The Bean model has following equation, $J_c=30\times \Delta M/w$ [17,28], where ΔM is the magnetization difference (in emu/cm^3) for increasing and decreasing field and w is the average diameter (in cm) of the circulating current loop (which will be grain size if the grain boundaries were the weak links).

If one uses the measured avearage grain size of ~10^{-3} cm as 'w', then calculated J_c will be overestimated by at least 5~10 times higher than that of using sample thickness size, typically 50~100^{-3} cm for BSCCO/Ag tapes. Also they do not explicitly include the anisotropy of the critical current in their calculations. For some geometries, neglect of this anisotropy can lead to substantial errors in the deduced values of J_c. The effect of an anisotropic critical current density on the observed magnetic behavior in an applied field $H_a > H_{c1}$ has, as yet, not been considered in detail.

Gyorgy et al. [63] developed what they called "extended Bean model", considering the sample geometries and the anisotropic critical current density. Followings are the description of their model. First they consider a rectangular parallelepiped sample with the applied field perpendicular to one surface of dimensions l by t (Figure 7). They define the current density along the t -direction to be J_{c2} and along the l -direction J_{c1}. The critical state equation is identical to the equation determining the height of a sand pile on the surface under consideration [63].

As a consequence of Amperes law ($\nabla\times\overline{H_i} = \overline{J_c}$), the slope of the sand perpendicular to an edge is corresponding to the critical current density parallel to that edge. That height of the sand anywhere is corresponding to the magnetic field H,

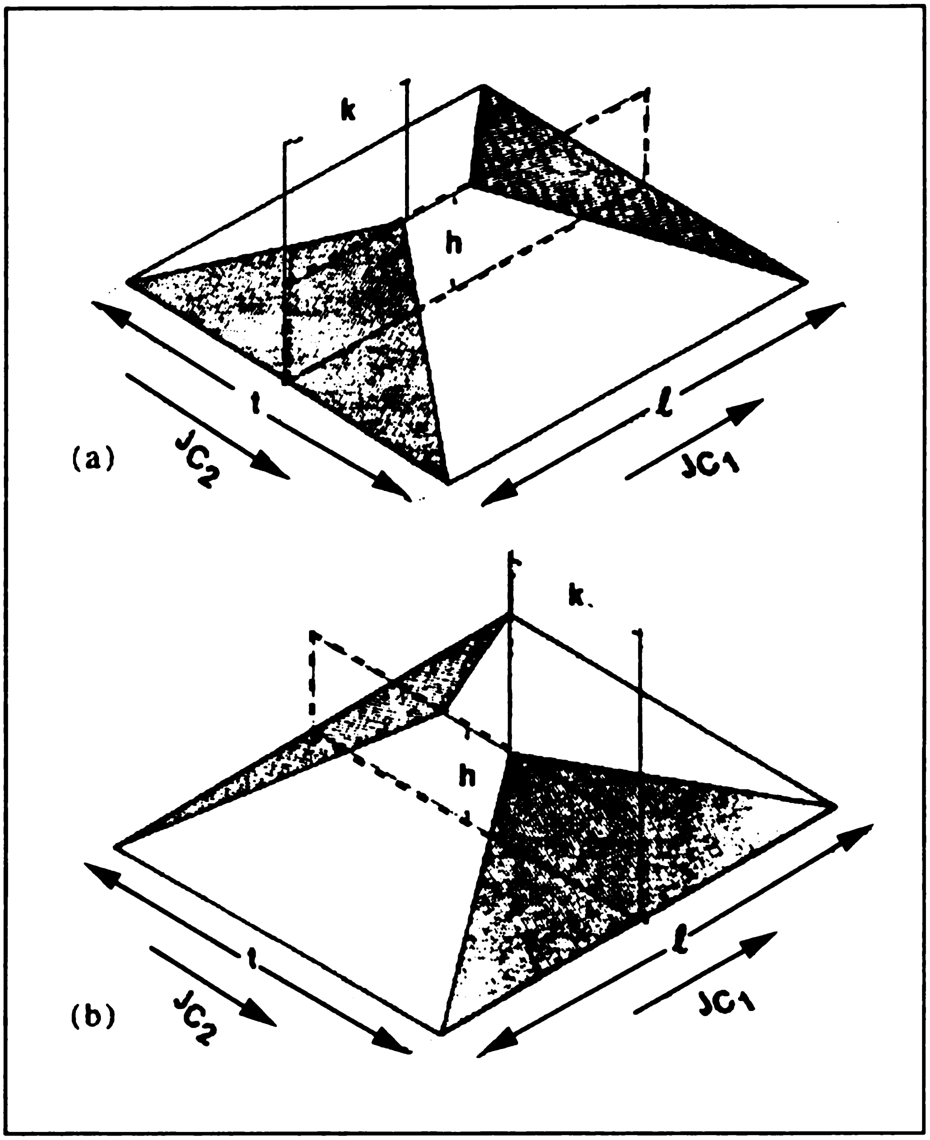

Figure 7. Construct to determine the current flow with an applied field normal to the surface. The vertical height gives the field induced by the circulating currents. The volume is proportional to the magnetization. (a) $J_{c1}/J_{c2}<l/t$, (b) $J_{c1}/J_{c2}>l/t$ (Ref. 63)

resulting from the induced current flow. The total volume of the sand divided by area of the base is corresponding to the magnetization M resulting from the circulating currents. This construction leads to a roof-like shape for which the vertical height to the ridge line is h and the horizontal distance from the appropriate edge to the ridge line is k, as in Figure 7. In Figure 7(a), the slopes give $2h/t = J_{c1}$ and $h/k = J_{c2}$. This is the appropriate structure for $k < l/2$ *or* $J_{c1}/J_{c2} < l/t$.. They calculate the volume shown in Figure 7(a) and it gives

$$\Delta M = \frac{J_{c1}t}{20}\left(1 - \frac{t}{3l}\frac{J_{c1}}{J_{c2}}\right) \qquad (11)$$

where ΔM is the width of the hysteresis loop for increasing and decreasing magnetic field, the current densities are in A/cm^2 and the dimensions in cm. For $l \gg (J_{c1}\,t)/3J_{c2}$,

$$\Delta M = \frac{J_{c1}t}{20} \qquad (12)$$

the solution for a long slab of thickness t, which is the same geometry of BSCCO/Ag tape. Therefore, one can use Eq. (12) to calculate the critical current density, J_c, from magnetization measurements for BSCCO/Ag tape.

For $l = t$ and $J_{c1} = J_{c2} = J_c$,

$$\Delta M = \frac{J_{c1}t}{30} \qquad (13)$$

the usual solution for a cylinder (current loop) of diameter t, which is just the Bean model [62]. For the crossover case $J_{c1}/J_{c2} = l/t$, ΔM also equals $J_{c1}t/30$.

For $J_{c1}/J_{c2} > l/t$, the construct of Figure 7(a) is no longer appropriate, and instead one must consider the configuration of Figure 7(b), where now $h/k = J_{c1}$ and $2h/l = J_{c2}$. In this case

$$\Delta M = \frac{J_{c2} l}{20}\left(1 - \frac{l}{3t}\frac{J_{c2}}{J_{c1}}\right) \tag{14}$$

Therefore, the importance of sample geometry is proved by Eq. (11)-(14).

2.3 Nature of Bi-Sr-Ca-Cu-O Compounds

Three superconducting phases exist in the Bi-Sr-Ca-Cu-O (BSCCO) system. They are known by their ideal Bi:Sr:Ca:Cu stoichiometries as 2201 (T_c ~ 7-20 K), 2212 (T_c ~75-90 K), and 2223 (T_c ~110 K). All three are two-dimensional pseudotetragonal mica-like materials that cleave easily along the (001) planes due to weak bonding between the two adjacent Bi-O planes [7,35]. The supercurrent is carried preferentially in the (001) CuO_2 planes.

Both the 2212 and 2223 phases exist over a range of stoichiometries, and neither has been prepared absolutely phase pure. 2212 exists over a wider range of stoichiometries than 2223, and it forms more readily than 2223. 2223 is difficult to synthesize, however substitution of Pb for part of the Bi makes it easier to synthesize 2223 [64-66]. 2223 is stable in a narrow temperature range between about 805 and 840°C in 0.075 atm O_2 [7]. At higher temperatures it melts, and at lower temperatures it decomposes.

2.3.1 Recent Discoveries of High T_c Superconductors and Crystal Structures of BSCCO Superconductors

It is known empirically that critical temperature is influenced by the crystal structure and long range order, while critical current density depends predominantly on the microstructural features such as grain boundaries, microcracks, grain alignment (texture), and defect (flux pinning site) density. Since the discovery of YBaCuO superconductor in 1987, higher values of T_c have been observed in new cuprate compounds exhibiting the well known sequence of atomic layers $BM_rB(CuO_2/Ca)_{n-1}CuO_2$, usually referred to as the $[r^2\ (n-1)n]$ compound [67] of the cuprate family M, where usually B is Sr or Ba and M is Bi, Tl, or Hg. For n = 1, 2, and 3, T_c is clearly an increasing function of n. However, until now conventional techniques did not allow the making of pure $[r^2(n - 1)n]$ phases with $n > 3$, which are suspected to be unstable at least at high deposition temperatures [67].

In 1988, the (2223) compound of the Tl family [68] was found, and reached a critical temperature of 125 K, the record that held for 5 years until 1993 when the [1223] compound of the Hg family was shown to exhibit a superconductive transition at 135 K under atmospheric pressure [69], and 157 K under high pressure [70]. Chu et al. [70] demonstrated that their $HgBa_2Ca_2Cu_3O_8$ samples, if squeezed to 235,000 atmospheres (the maximum pressure possible with their sintered diamond anvil vise), begin the transformation to a superconductor at 157 K and just about finish at 150 K. Neither group can say why the high pressure boosts the transition temperature, because the samples can not be salvaged for study when the pressure is released. They assume, however, that the pressure reduces the distance between adjacent layers of the crystal, a change that often increases the transition temperature of a ceramic superconductor. By substituting "chemical pressure" for "mechanical pressure", the researchers hope to create a compound that would have the same properties under normal conditions. Replacing the compound's relatively large barium ions with smaller ones such as strontium, should pull the layers together, mimicking the effect of squeezing.

The unit cell of the $Bi_2Sr_2Ca_{n-1}Cu_nO_{4+2n}$ superconductor is made up of two bismuth-oxygen and two strontium-oxygen planes with copper-oxygen planes in between them. For the n=2 and n=3 phases the copper-oxygen planes are separated by calcium planes, as shown in Figure 8. For the n=3 phase, i.e. assuming that there are five nonequivalent oxygen sites in this material, designated as Bi-O(1), Sr-O(2), Cu(1)-O(3), O(4) and Cu(1)-O(5), respectively. The central Cu-O plane is flat with 4 equal Cu-O(5) distances. but the oxygen atoms in the outer Cu-O planes (O(3), O(4)) are slightly displaced towards the calcium planes. The n=2 and n=3 phases are known to exhibit an incommensurate distortion such that the Bi-O distance is modulated [9]. As noted above, the superconducting transition temperature increases with increasing n, the n = 1 phase

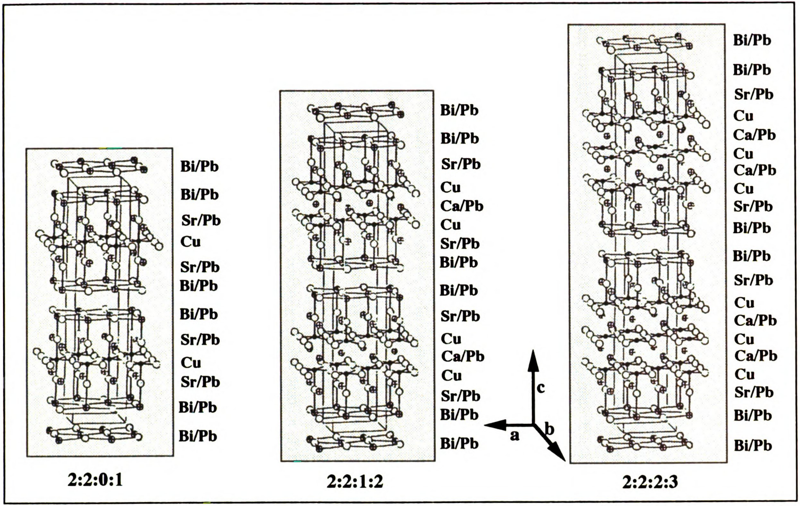

Figure 8. The structure of the $Bi_2Sr_2Ca_{n-1}Cu_nO_{4+2n}$ phases (Ref. 9)

being either nonsuperconducting or having a low $T_c \sim$ 6-10 K depending on the sample treatment and doping, while for the n = 2 and n = 3 phases T_c is ~80 K and ~110 K, respectively.

2.3.2 Sintering Problem in BSCCO Compound

The Bi(Pb)-Sr-Ca-Cu-O powders, as shown in Figure 9 (a), are in the form of thin plate-like crystals which cleave easily along the (001) plane due to weak bonding between two adjacent Bi-O planes from structural point of view [7,35]. This material is difficult to sinter into dense ceramic in that it had a very narrow sintering range between temperatures of no densification and those where excessive amounts of liquid phase is formed [21].

Beyond the difficulty of the narrow sintering range, it has a unique retrograde densification characteristic which is demonstrated in the temperature range from 850°C to 890°C where by the material first becomes less dense as the sintering temperature is raised. The reason for this retrograde densification is due to the growth of thin plate-like crystallites (Figure 9 (b)) which grow in randomly oriented fashion [21]. Therefore, this retrograde densification, coupled with a narrow sintering range overlapping the melting temperature, cause this compound a difficult one to sinter. Specimens sintered conventionally in air has densities of 3 to 4 g/cm^3, merely 46.5 % to 62 % of theoretical density [21-24].

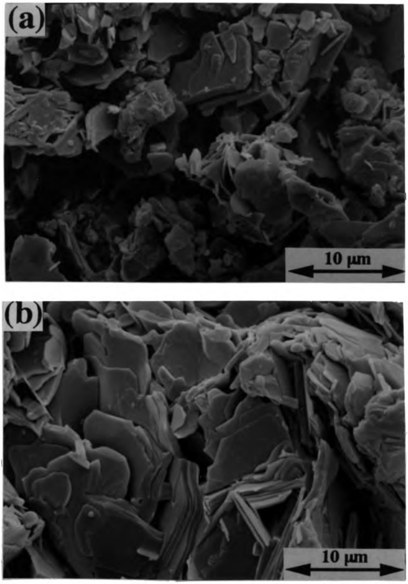

Figure 9. SEM secondary electron micrographs from (a) powder sample of 2223 BSCCO superconductor and (b) fracture surface of conventionally sintered 2223 BSCCO superconductor, at 850°C for 12 hr.

2.4 BSCCO Superconductor Processing Techniques

2.4.1 Conventional Sintering and Hot Isostatic Pressing (HIP) Process in High-T_c Superconductors

The term "sintering" refers to the pore shape change, pore shrinkage, and grain growth which particles in contact undergo during heating [71]. In conventional sintering powders, densification occurs by capillary-driven, long range diffusional processes. The driving force for sintering is a reduction in the system free energy via the decreased surface curvatures and an elimination of surface area. A typical feature of sintering is that the rate is strongly depend on temperature. As a result, full densification has a chance to occur only at temperatures approaching the melting temperature where diffusion becomes rapid.

For many materials, including the high-T_c superconductors, there are other considerations that limit the sintering temperature. For example, for refractory metals and ceramics, the melting points are so high that the achievement of high homologous sintering temperatures becomes technically difficult. For superalloys, the sintering temperature is limited by phase stability considerations. Similarly, the sintering of high-T_c superconductors is limited by phase stability and incipient melting considerations. This prevents ordinary sintering from being an effective process for achieving full density.

HIP, on the other hand, densifies through hot deformation process whereby the powder particles deform under high stress at contact points, and thus achieve densification. Under a hydrostatic pressure at elevated temperatures, densification occurs by massive movement of material as well as by diffusion of individual atoms as in any solid state sintering process. Consequently, relatively rapid densification can occur at shorter times than are necessary for conventional sintering.

As discussed before, it is difficult to densify $Bi_{1.6}Pb_{0.4}Sr_2Ca_2Cu_3O_Z$ (2223 BSCCO) superconductor to its full theoretical density while maintaining the high T_c phase by conventional sintering process. Hot Isostatic Pressing is considered to be an effective technique to densify various types of superconductors. HIP has been widely used to densify $YBa_2Cu_3O_X$ class of superconductors [72-74]. However, HIP densified $YBa_2Cu_3O_X$ requires extensive post processing heat treatment to recover superconducting phase, because $YBa_2Cu_3O_X$ decomposes to other oxide compounds, such as Y_2BaCuO_5, CuO, $BaCuO_2$ etc., at high pressures and high temperatures experienced during HIP densification [75,76].

Contrary to that, 2223 BSCCO superconductors lose very little oxygen on heating in vacuum up to the melting temperature [77]. Although, the crystal structure of $Bi_{1.6}Pb_{0.4}Sr_2Ca_2Cu_3O_Z$ superconducting compound is quite stable with respect to oxygen stoichiometry, hot isostatic pressing data for high-T_c (110K) 2223 phase in $Bi_{1.6}Pb_{0.4}Sr_2Ca_2Cu_3O_Z$ superconductors has not yet been reported. So far, the reported T_c value of as hot isostatically pressed Bi based superconductor is in the range of 80K - 90K [78-80].

There are three different types of HIP techniques: (1) post-HIP, (2) sinter-HIP [81] and (3) encapsulation HIP [81,82]. Among three different HIP techniques, the encapsulation HIP requires the material to be contained within evacuated container while still in the green state and then HIPed. The container should be deformable at the processing temperature so that the pressure can be transmitted to the specimen to enhance the sintering process. The container must also remain intact in order to protect the material from the gas.

The main attraction of encapsulation HIP is that the material does not need pre-sintering to give a completely closed pore system and therefore high levels of sintering aids are not required. Another benefit is that a higher degree of densification is obtained. By encapsulation HIP processing from the green state, the increased densification rate at lower sintering temperatures, due to the application of the pressure, enables higher densification. Therefore, it can minimize the phase stability problem by using lower sintering temperatures in BSCCO superconductors. There are many methods of encapsulation using glass materials [82]: glass capsule method, glass bath method, glass powder coating method and glass powder pressing method. Also high melting point metals such as tantalum can be used to form deformable cans which are packed under vacuum and sealed by welding.

2.4.2 HIP Mechanisms as Applied to BSCCO Superconductor Consolidation

During hot isostatic pressing (HIP), plastic flow, power law creep [83], Nabarro-Herring creep, Coble creep [84], grain boundary sliding in the particles, and grain boundary and bulk diffusion at the particle contacts can all contribute to densification. Which of these mechanisms dominates shrinkage and neck growth rate depends on a number of parameters related to the powder (size, grain size, bulk properties, and interface properties) and to processing condition (pressure, temperature, time) [85]. When pressure is applied to packed powders, it is transmitted through the powder bed as a set of forces acting across the particle contacts. If an external pressure P is applied to the compact with a density D and coordination number Z, the average contact force, F can be calculated according to the following equation [83].

$$F = 4\pi PR^2 / ZD \tag{15}$$

where R is the average powder particle radius. The contact force produces a contact pressure, P_{con}, on each particle contact area of A:

$$P_{con} = F / A = 4\pi PR^2 / AZD \tag{16}$$

The deformation at these contacts is, at first elastic but as the pressure rises, the contact forces increase, causing plastic yielding and expanding the points of contact into contact areas [83]. Yielding occurs when the contact pressure exceeds yield strength of the material, and hot deformation occurs almost instantaneously. When yielding stops, time-dependent deformation processes determine the rate of further densification. These time dependent processes are power-law creep in the contact zones and diffusion from a grain boundary source to the void surface. Power law creep [83], a slower process, is governed by the usual equation;

$$\dot{\varepsilon}_P = B\sigma^n \exp\left(\frac{-Q_{creep}}{RT}\right) \qquad (17)$$

where, $\dot{\varepsilon}_P$ is the creep rate, B and n are material constants, Q_{creep} is the creep activation energy, R is gas constant and T is temperature.

Nabarro-Herring creep and Coble creep [84] occur by grain boundary diffusion and sliding and is therefore grain size dependent. Both are classified as diffusional creep. Nabarro-Herring creep results from vacancy redistribution from a higher vacancy concentration in the region of a material experiencing a tensile stress to the lower vacancy concentration regions subject to compressive stresses. This results in a vacancy flux from the former to the latter areas, and a mass flux in the opposite direction. Therefore, the grain elongates in one direction and contracts in the other, that is, creep deformation occurs. Nabarro-Herring creep is expressed by following equation:

$$\dot{\varepsilon}_{NH} = B_{NH}\left(\frac{D_L}{d^2}\right)\left(\frac{\sigma\Omega}{k_B T}\right) \qquad (18)$$

where, B_{NH} represent geometric factors, D_L is self-diffusion coefficient, ' d' is grain size, σ is applied stress, Ω is the atomic volume, k_B is Boltzmann constant and T is temperature. Nabarro-Herring creep is accomplished entirely by diffusional mass transport and dominates creep processes at much lower stress levels and higher temperatures than those at which creep is controlled by dislocation glide.

Coble creep [84] is closely related to Nabarro-Herring creep and is driven by the same vacancy concentration gradient that causes Nabarro-Herring creep. However, in Coble creep mass transport occurs by diffusion along grain boundaries in a polycrystal or along the surface of a single crystal. Coble creep mechanism is expressed by the following equation:

$$\dot{\varepsilon}_C = B_C\left(\frac{D_{GB}\,\delta'}{d^3}\right)\left(\frac{\sigma\Omega}{k_B T}\right) \tag{19}$$

where, B_C represent geometric factors, D_{GB} is grain boundary-diffusion coefficient, δ' is an appropriate grain boundary thickness, d is grain size, σ is applied stress, Ω is the atomic volume.

Comparing the above equations ((18) and (19)), it can be seen that Coble creep is more sensitive to grain size than is Nabarro-Herring creep. Even though both forms of creep are favored by high temperatures and low stresses, it is expected that Coble creep will dominate the creep rate in very fine grained materials. Also both deformation modes are effective only when the powder is polycrystalline and the grain size is small compared to the powder particle size.

Additional mass-transfer processes must occur at the grain boundaries to prevent the formation of internal voids or cracks during these diffusional creep of a polycrystal. These result in grain-boundary sliding and the diffusional creep rate must be balanced exactly by the grain-boundary sliding creep rate if internal voids are not to be formed. The mass transfer is driven by vacancy concentration gradients in the same manner that diffusional creep is driven. Diffusional flow and grain-boundary sliding, therefore, can be considered sequential processes in which mass is first transported by Nabarro-Herring and/or Coble creep and a grain shape change and separation is effected.

The overall behavior is complicated because each densifying mechanism has a different dependence on particle size, on the external variables P and T, and on powder properties and current geometry [85]. One way of analyzing it is to construct hot isostatic pressing (HIP) maps which identify the dominant mechanism and predict densification rates and times, as a function of pressure and temperature [83].

2.4.3 Overview of BSCCO/Ag Tape Processing

For practical engineering applications, the superconducting compounds should have sufficient current carrying capability and should be fabricated into desired shapes such as wires, tapes, etc. Of the three major groups of high temperature superconductors, YBaCuO, Bi-Sr-Ca-Cu-O (BSCCO), and Tl-Ba-CaCu-O, the best wires to date have been made in the BSCCO system. At this time, all YBaCuO, wires are weak linked and have only small J_c in magnetic fields, as shown in Figure 10 [30]. In the Tl-based system, the superconducting properties are potentially very interesting, but the toxicity of Tl and the system's complex processing have limited conductor development [6,7].

For the Bi-based system, the basic processing steps are becoming known, the grains are well connected, and the weak link problem can be greatly reduced by the minimization of high angle grain boundaries in the paths of the super current. This can be achieved by producing sharp crystallographic textures characterized by a high degree of alignment of superconducting crystal planes lying parallel to the conducting direction. This permits applications in the temperature range 4-77 K, depending on the field and current density requirements of the particular use.

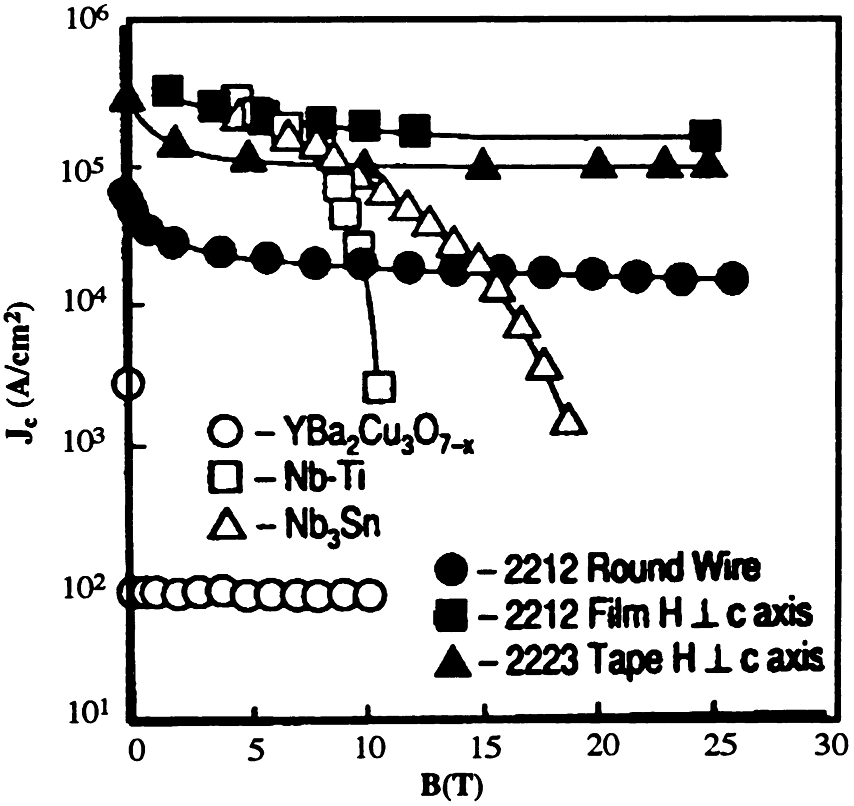

Figure 10. The J_c at 4.2 K as a function of magnetic field for 2212 BSCCO wire, 123 YBaCuO tape, 2212 BSCCO film, 2223 BSCCO tape, Nb-Ti, and Nb_3Sn (Ref. 30)

Several processing techniques are available to form this materials into final superconducting wires or tapes, such as the powder-in-tube (PIT) method [31,38,86], surface coating method [17,28] as well as Doctor-blade and melt-processed tapes [25,26,87], as shown in Figure 11. One of the critical problems frequently encountered in the "powder in tube method" is non uniform and discontinuous core distribution. In addition melt process that is a necessary step for densification in "Doctor-blade tape" decomposes high T_c (2223) phase into low T_c (2212 or 2201) and non superconducting phase in BSCCO system.

Melt processing is more suitable for manufacturing 2212 BSCCO/Ag tape system [25,26]. On the other hand, thermomechanical process has been proven to be the most effective technique for processing 2223 BSCCO/Ag tape system [7,27] because of a decomposition of the high T_c phase and the difficult growth of 2223 BSCCO phase from the melt [7,17,28].

2.4.3.1 Thermomechanical Process

In the PIT process [31,38,86], prereacted precursor powders are initially prepared with nominal composition optimized for the high-T_c 2223 phase. For some of the best results, high purity (>99.9%) oxides or carbonates of Bi, Pb, Sr, Ca, and Cu with the cation ratio 1.6:0.4:2.0:2.0:3.0 are carefully mixed, heat treated, and reground. As shown in the schematic diagram of Figure 11(a), the powders are packed into silver tubes, lightly swaged and drawn through a series of dies, then rolled to final size (0.1-0.2 mm thick). Reduction ratios are kept below 30% per pass to achieve optimum properties. Two to three intermediate heat treatments are provided to initiate reaction in the core to form the 2223 phase and also to prevent failure due to work hardening. The intermediate and final anneals of the composite tapes are typically performed between 830°C and 870°C for 24-150 h. Lower partial pressures of oxygen (5-10%) have also been used with

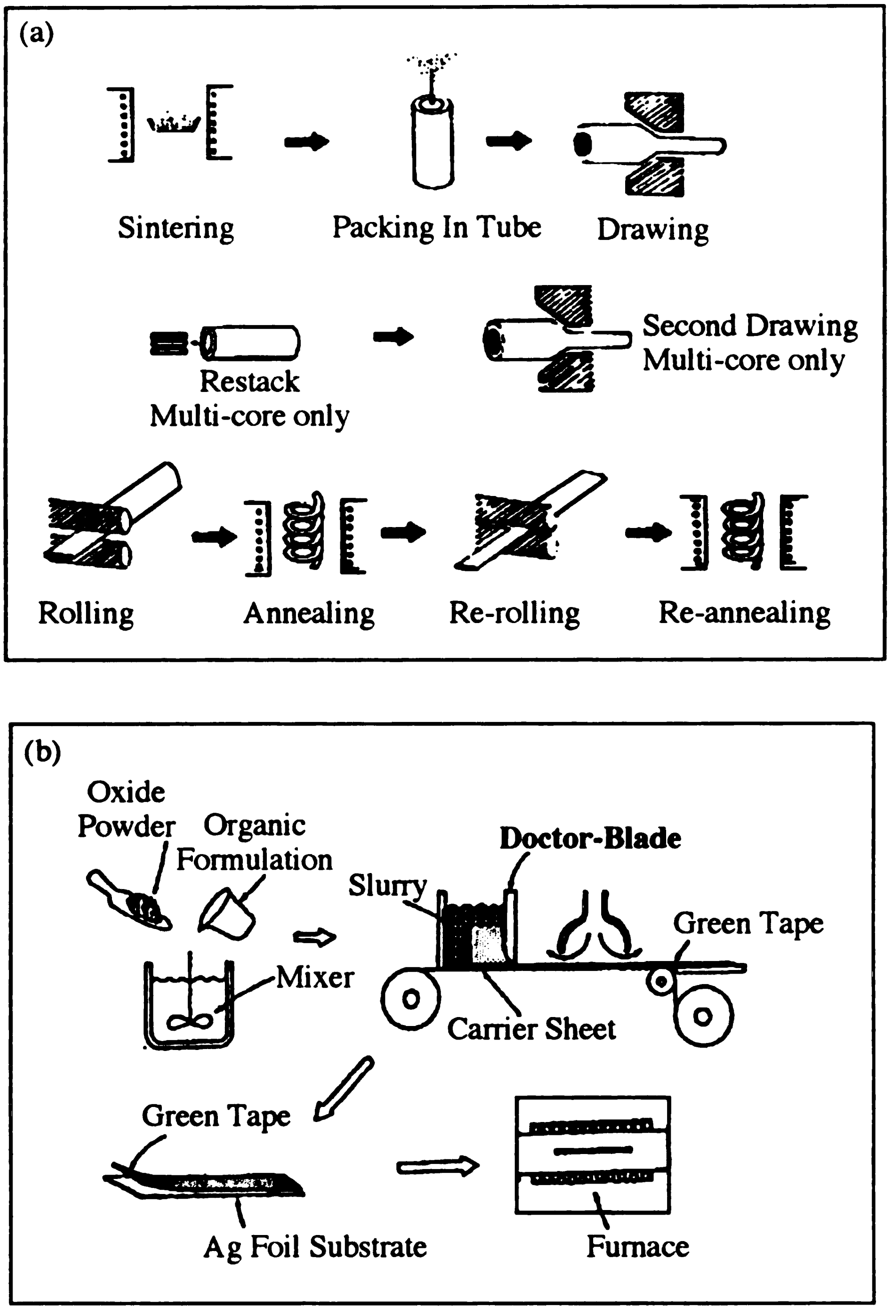

Figure 11. A schematic flow sheet of (a) the powder-in-tube (PIT) process used to fabricate single and multifilament BSCCO/Ag wires and tapes, and (b) doctor-blade casting method for 2212 BSCCO/Ag tape (Ref. 90)

slightly lower temperatures (800-840°C) resulting in similar properties in the final tape [88].

For fabricating multifilament wires, additional steps are added as shown in Figure 11(a). Multiple lengths are usually cut from a drawn rod and restacked into a second tube for another series of drawing operations. Final thermomechanical operations are similar to that used for single-core tapes. The fabrication of long tapes can thus be accomplished, and up to 100 m lengths with practical levels of J_c have already been reported [88].

A large number of parameters during powder preparation and thermomechanical processing are known to affect the final properties of the composite wires or tapes. These parameters must be carefully monitored and controlled to reproducibly achieve a high degree of Bi-2223 phase development, texture, density, and uniformity in the superconducting core.

2.4.3.2 Melt Process

Silver clad round wire and tape (Figure 11) are made using the oxide-powder-in-tube (OPIT) method, which was reviewed by Sandhage et al [89]. To make an OPIT conductor, fully or partially reacted powder is packed into a silver tube, which is sealed and then drawn to a round wire; the wire can be rolled flat to make tape. Typical dimensions for a tape are a total thickness of 100~200 μm and a width of 2~3 mm, with the oxide core ranging from 40 μm to 80 μm thick and 1.0 mm to 1.5 mm wide. The OPIT wire or tape is then thermally processed. An important, but little understood issue for OPIT processing is the relation between the properties of the powder that is packed into the tube and how the tube and oxide core deform during drawing and rolling. The ideal tape microstructure has uniform powder distribution and uniform cross section with no undulations (called sausaging) in the core thickness.

Thick films (>10 μm) for conductors are made by painting a slurry of powder in organics or by placing a piece of doctor-blade tape [25,26,87] (a semirigid mixture of 2212 powder in organics) onto a substrate, typically silver foil, followed by thermal processing, as shown in Figure 11(b). Long films (ribbons) are made by passing a long piece of silver foil through a bath of 2212 powder mixed with organics [90].

For doctor-blade casting and films, the heating step must be modified slightly to burn off the organics. In tapes, it was found that the 2212 phase was partially melted above ~870°C in air; after heating to 920°C, 2212 began to crystallize at ~875°C [91]. The higher crystallization temperature may be due to a nonequilibrium phase assemblage (second phases) in the melt on cooling [91]. The Ag-O eutectic limits the maximum processing temperature to about 930°C in air. The optimum processing temperature to attain high J_c has been claimed to be 880~890°C [26]. The cooling rate from the maximum temperature is critical as it affects the degree of alignment of the 2212; the alignment increases with decreasing cooling rate. During the extended, low-temperature anneal (810~860°C, 1~100 h) the remaining liquid transforms to 2212 and the 2212 alignment increases for faster cooled sample [29].

The final step in melt-processing is cooling to room temperature. This is a critical step, since if it is done improperly, it can seriously degrade J_c. If the sample is quenched, the thermal shock can create microcracks in the oxide core that lower J_c. However, slow cooling can be deleterious, as the sample can pick up oxygen on cooling, which decreases T_c and presumably J_c. In addition, 2212 is thermodynamically stable only at elevated temperatures (stable at 800°C, but not at 750°C in air), and it was found to decompose to $Bi_2Sr_2CuO_y$ (the 2201 phase) + Ca_2CuO_3+ CuO below 800°C in air and in pure O_2 [92]. Thus if the cooling is too slow, 2212 can decompose.

2.4.3.3 Kinetics of Forming 2212 BSCCO from the Melt

Since 2212 melts incongruently, liquid and crystalline phases coexist in equilibrium in the melt. The 2:2:1:2 composition is in the CaO primary phase field, and at 920°C in air, liquid coexists with CaO in the tapes. The phase relations in melts within the tapes have been studied as a function of temperature [30], and it was found that the 2212 melting reaction is

$$2212 \rightarrow \mathit{Liquid} + (Sr,Ca)CuO_2 + \mathit{Cu\ free\ phase} \quad \text{, Reaction 1.}$$

Using electron-probe microanalysis (EPMA), the copper-free phase has been identified as $Bi_2(Sr,Ca)_4O_7$. Between 870°C and 920°C, the melt goes through several different solid-plus-liquid phase assemblages, complicating the phase chemistry during melt processing.

On cooling, 2212 should form from the melt by the reverse of Reaction 1. However, 2212 appears to nucleate and grow directly from the liquid. From a thermodynamic point of view, the crystalline phases and liquid must react to form 2212 via Reaction 1, but the cooling rates used are probably too fast to allow this formation. Consequently, the crystalline phases (second phases) in the melt are not consumed on forming 2212, but instead are present in the fully processed tape. These are metastable phases that do not coexist with 2212 in the solid state [93]. The metastable phases shift the liquid composition away from 2:2:1:2, and since they are not consumed on cooling, the liquid cannot transform completely to 2212 on cooling.

The high-temperature phase relations in melt processed 2212 tapes can be studied on quenched samples in which the high-temperature equilibria have been frozen. A fast quench, such as into ice water [94], or oil [91], is crucial to preserve the high temperature microstructure. With slower quenches, such as into air, 2201 crystallizes from the liquid during the quench and the high-temperature phase assemblage is lost

[91]. Hellstrom et al. [30] show that 2201 is not present in the melt above temperatures where 2212 first begins to crystallize during fast quench. On the other hand, Kase et al. [87] have proposed that 2201 forms first from the liquid, then 2212 forms from the 2201. It is now apparent that this proposed reaction path is incorrect, as it was based on results from air quenched films in which 2201 formed from the liquid during the slow quench, whereas oil-quenched tapes showed 2212 first on cooling.

The second phases that persist from the melt are too large to pin flux effectively, and they degrade J_c. In the most deleterious phase, $(Sr,Ca)CuO_2$, large grains are formed that approach the thickness of the oxide core. The nonsuperconducting phases in fully processed tapes lower J_c by physically blocking portions of the oxide core from carrying supercurrent, disrupting the 2212 alignment in their immediate vicinity and shifting the composition of the solidifying liquid to be bismuth-rich, which allows phases such as 2201 to crystallize along with 2212.

At the high temperatures used for melt processing, vaporization of the components can be a problem. Sata et al. [95] calculated the apparent vapor pressure of copper and bismuth over 2212 by the transpiration method. In silver-clad wires and tapes, vaporization is a relatively minor problem, as the major loss occurs through the open ends of the wire or tape. Vaporization from the surface of thin films, on the other hand, can be a serious problem. To reduce loss from films, the total time at elevated temperature must be minimized, which requires carefully optimizing the temperatures, times, and cooling rates to attain high J_c.

In the BSCCO system, the three superconducting phases (2201, 2212, and 2223) are very difficult to prepare in high purity on the microscopic level. Specifically, TEM studies of 2212 show intergrowths of 2201 and occasionally 2223 within the grains. These intergrowths, which are one half cell or more thick, do not show up as separate phases in an x-ray diffraction pattern, but they may affect the electromagnetic properties of the sample. In 2223 tapes, Umezawa et al. [96] showed that J_c increased when the number of 2212 intergrowths at twist boundaries decreased. In 2223 tapes, these intergrowths of the lower temperature superconducting phase (2212) are thought to act as weak-link sites that allow magnetic flux to penetrate the sample. The same sort of deleterious relation between 2201 intergrowths at twist boundaries and the electromagnetic properties of 2212 may exist.

Silver is slightly soluble in the liquid phase and dissolves into it during melting. On cooling, the silver precipitates from the liquid, as it is not soluble to any appreciable extent (<0.1 at.%) in any of the crystalline oxide phases that form in the tape [30]. In fast-quenched samples, regions in which silver is found (by EPMA or energy-dispersive spectroscopy [EDS]) are assumed to be liquid at the quench temperature. In fully processed tapes, EPMA studies clearly show that the oxide core contains silver, but exact location is not apparent. Scanning TEM-EDS studies shows no conclusive evidence of silver at the (001) twist boundaries. Some TEM studies have shown silver metal at high-angle grain junctions in fully processed tapes. Silver grains are difficult to find in TEM samples, because the 2212 grains are so large that TEM samples contain few grain junctions where silver could be present. In addition, the silver thins much faster than the oxide during the ion milling used to make the TEM samples, so the silver is lost before the oxide becomes electron transparent.

2.4.3.4 Forming High Degree of Texture from the Melt

In melt processed tapes, initial rolling mechanically aligns the two dimensional 2212 grains. However, this mechanical alignment (rolling texture) is totally lost when the 2212 grains melt during melt processing. New 2212 grains grow and align during the cooling and annealing stages of processing. Ray et al. [97] studied c-axis texture as a function of cooling rate (10~240°C/h) and found that the degree of texture in the melt-processed tape increased with decreasing cooling rate. Controlling the cooling rate is important in the temperature range over which 2212 forms and grows (~880°C down to ~840°C for tapes).

The important issues regarding texture formation during melt processing are how it occurs and its limitations, and how the 2212 grains align as they form from the liquid. Kase et al. [87] proposed texture model based on studies of the microstructure of air-quenched films. This model assumes that 2212 begins to form at the silver/liquid interface and aligns with the c-axis parallel to this interface. With continued cooling, additional 2212 forms on the aligned 2212, resulting in a strong c-axis texture of 2212 growing into the oxide core from the silver/oxide interface. This model accounts for the highly aligned 2212 layer that is often found along the silver interface in fully processed tapes. Recent high resolution TEM studies of the 2212 BSCCO/Ag interface suggest that (001) faceting and half cell of 2201 phase were formed at the 2212 BSCCO/Ag interface on an atomic scale, and a very strong texturing of (001) planes of the 2212 BSCCO parallel to the Ag was detected [98]. The silver-sheath-induced texture formation may be related to the interaction at the interface with silver, which is known to lower the partial melting temperature of the BSCCO superconductor and may help initiate nucleation.

Based on observations of the microstructure during growth, an alternative texture mechanism has been suggested [30]; It is speculated that 2212 nucleates and grows at random orientations in the initial stages of growth. Grain growth is much faster in the a-, and b-directions than in the c-direction, so the growing grains assume a plate-like habit. With continued cooling, those grains that are aligned with their a-b planes nearly parallel to the plane of the tape are favorably oriented to grow to large size, as these grains are least hindered by the silver sheath as they grow.

The 2212 continues to align during the low-temperature anneal, which is below the equilibrium solidus temperature. Ray et al. [98] and Feng et al. [29] found that melt processed tapes that were fast cooled (240°C / h) to 840°C then fast quenched had much less alignment than tapes that were slow cooled (10°C/h) to 840°C then fast quenched.

After 100 h of annealing at 840°C, the alignment had increased in the fast-cooled sample, whereas it had not increased significantly in the slow-cooled sample.

The exact mechanism by which the alignment increases during the low-temperature anneal is not known, but a possible explanation is as follows: fast and slow-cooled tapes have many favorably oriented grains when cooled to 840°C. As 2212 grains grow during the long-term, low-temperature anneal, favorably aligned grains can continue to grow relatively easily as they are not impeded by the silver sheath and few misoriented grains exist to block their growth. In addition, as the favorably oriented grains become large, they consume some of the smaller, misaligned grains. In contrast, it is much more difficult for misoriented grains to grow, as they are impeded by the large number of favorably oriented grains.

The second phases and pores interrupt the local 2212 alignment, perhaps because they interfere with 2212 growth along the plane of the tape. In some micrographs, the 2212 grains appear to have flowed around the second phases, whereas in other cases, the 2212 alignment is totally disrupted in the vicinity of the second phases. It may be possible to modify the deleterious second phases by varying the processing conditions (e.g., time, temperature, heating and cooling rate, and oxygen partial pressure).

It is desirable to align the ab-planes parallel to the current flow, which is parallel to the plane of the two-dimensional tapes and films, and parallel to the wire axis in the one dimensional wires. Even if the sample were perfectly aligned, as shown schematically in Figure 12, it is not known whether supercurrent would be able to pass through the tilt boundaries that are perpendicular to the a-b planes, since supercurrent transport across individual grain boundaries in BSCCO conductors has not yet been measured.

The skepticism about transport across tilt boundaries comes from work on $YBa_2Cu_3O_7$, where it is clear that transport across high-angle grain boundaries is

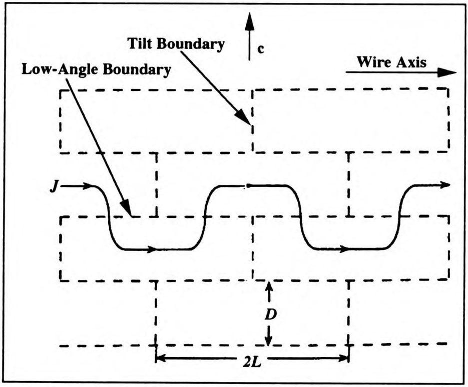

Figure 12. Brick-wall model. The length of each superconducting brick is 2L and the thickness is D (Ref. 99)

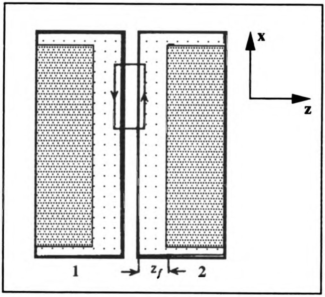

Figure 13. Junction between two bricks showing the integration path. Shading represents the vortex-filled region. The vortex-free region is of thickness z_f (Ref. 99)

difficult [11] because such grain boundaries tend to be weakly coupled. Instead, a "brick wall" model [99] is used to explain supercurrent transport between grains. In this model, the supercurrent avoids the tilt boundaries by moving in the c-direction, as shown in Figure 12 and 13. For high-current transport, this model requires a microstructure with 2212 grains that are thin in the c-direction and long in the a-, and b-directions.

2.5 Application of Crystal Plasticity Theory for Oxides

Crystal plasticity based on crystallographic slip, and in some cases twinning, is being widely used in finite elastic-plastic deformation of single crystals [100]. Based on the choice of an interaction law that relates the local (single crystal) fields to the fields applied to the surrounding matrix, different averaging schemes are used to predict the stress-strain behavior of the polycrystalline matrix as well as the texture evolution during elastic-plastic deformation (Parks and Ahzi, 1990; Molinari, Canova. and Ahzi, 1987; Asaro and Needleman, 1985; and Kocks, 1970) [101-104].

It is well known that five independent slip and/or twinning systems are necessary for accommodating a general plastic deformation. However, many low symmetry crystals (non-cubic) have fewer than five independent systems and thus, an arbitrary plastic deformation cannot be accommodated by these crystals. Recently, Parks and Ahzi [102] have reported the problem of local deficiencies due to insufficient number of independent slip systems in some hexagonal and orthorhombic crystals. In their study, Parks and Ahzi proposed a constrained hybrid (CH) model that they applied to predict the stress-strain behavior and texture evolution in polycrystals with 4 and 3 independent slip systems. Superconducting oxides do not possess five independent slip (or twinning) systems and thus, these crystals belong to the class of low symmetry crystals with local kinematic deficiency.

2.5.1 CH Model

Following the Taylor model [103], the deformation gradient is assumed uniform within the polycrystal and therefore, all crystals are subject to the average deformation. This model has been used successfully for FCC polycrystals where an abundant number of slip systems is available. However, this model does not allow any constraints within the single crystals (except non volume change condition). For crystals with local constraints such as 2223 BSCCO crystals, Parks and Ahzi [101] proposed a modification of Taylor model that accounts for local kinematic deficiency without any loss of global compatibility. Followings are description of their model. This proposed constrained hybrid (CH) model allows a minimal deviation of the local plastic deformation rate D^P from the global one, $\bar{D}^P$, that is expressed as:

$$\bar{D}^P D^P = P{:}\langle P\rangle^{-1}{:}\bar{D}^P \qquad (20)$$

where the fourth order tensor P is given by:

$$P = I - \frac{3}{2}C' \otimes C' - \frac{1}{2}B' \otimes B' \qquad (21)$$

with I representing the symmetric fourth order identity tensor. The symbol '$\otimes$' indicates a tensor (dyadic) products, i.e. two side-by-side tensors yielding a tensor with a rank equal to the sum of the ranks of the two; an example is $\mathbf{a}\otimes\mathbf{a}=a_i a_j$. It is shown from (20) that the global compatibility ($< D^P >= \bar{D}^P$) is verified. The operator P in (20) imposes vanishing plastic strain rate components in the constrained directions. If we neglect the shape effect, the local spin can be chosen as:

$$W = \bar{W} \qquad (22)$$

which also satisfies the global compatibility condition ($\langle W\rangle = \bar{W}$).

If the local kinematics are prescribed, the stress tensor σ^* can be computed. To complete full knowledge of σ^*, the components σ_1 and σ_2 must be determined from equilibrium consideration. Following the work of Parks and Ahzi [101], σ_1 and σ_2 are estimated by their corresponding macroscopic stress components:

$$\sigma_1 = \frac{3}{2}\sigma^{'}:C^{'} \cong \frac{3}{2}\bar{\sigma}^{'}:C^{'} \qquad (23\ (a))$$

$$\sigma_2 = \frac{3}{2}\sigma^{'}:B^{'} \cong \frac{3}{2}\bar{\sigma}^{'}:B^{'} \qquad (23\ (b))$$

Using the approximations (23 ab), the generalized global equilibrium condition is expressed as:

$$\bar{\sigma}^{'} = \langle P\rangle^{-1}\langle\sigma^{\bullet}\rangle \qquad (24)$$

Relation (24) is used to compute $\bar{\sigma}^{'}$ and can also be used to solve for the mixed boundary conditions.

2.5.2 The Viscoplastic Self-Consistent Model

Recently, Molinari et al. [102] proposed a viscoplastic self-consistent model for plasticity of polycrystal deforming by crystallographic slip. By neglecting elasticity and using the integral equations method, these authors derived a self-consistent interaction law for finite deformations and texture evolution in different crystal structures [105].

The formulation of the self-consistent model starts by expressing the single crystal behavior, in the tangent form. viz.

$$\sigma^{'} = A:D^{P} + \sigma^{o} \qquad (25)$$

where σ^{o} is a D^{P} dependent deviatoric stress, and A is a fourth order tensor representing the tangent moduli of the single crystal, which can be defined as:

$$A = \left.\frac{\partial\sigma^{'}}{\partial D^{P}}\right|_{\sigma^{'} = \sigma^{\bullet}} = \frac{1}{m}M^{-1} \qquad (26)$$

From (26), it is obvious that the compliance tensor M: is assumed invertible. This is not the case for 2223 BSCCO crystals since they possess only three independent slip systems. To use this self-consistent formulation for crystals lacking five independent slip systems, the "penalty" method has been adopted as a means of including the missing degree of freedom within these constrained crystals. Note that this numerical method was used by Hutchinson [106] to validate the use of his self-consistent model when elasticity is neglected and plasticity occurs by crystallographic slip.

The compliance tensor M becomes non-singular. This tensor can then be defined by:

$$M = \dot{\gamma}_o \left\{ \sum_{\alpha} \left| \frac{\tau^{\alpha}}{g^{\alpha}} \right|^{m-1} \frac{P^{\alpha} \otimes P^{\alpha}}{g^{\alpha}} + \frac{1}{K} \left(\frac{B' \otimes B'}{B' : B'} + \frac{C' \otimes C'}{C' : C'} \right) \right\} \qquad (27)$$

2.5.4 A Simple Theory for the Development of Rolling Textures

Plane strain compression is usually used to approximate the primary stress and strain state of rolling. However the actual strain states achieved in rolling are characterized by superimposed shear strains on the compressive strains. To account for these shear strains, Lee et al. [107] used simple boundary conditions. This simplificatian consists of accounting for the shear strains involved in rolling by adding a shear component to the prescribed deformation gradient of the plane strain conditions. This method has been recently used by Lee et al. [107] to simulate rolling textures in deformed FCC polycrystals. A brief description of their model is as follows.

It is customary when simulating rolling texture development using Taylor theory to assume plane strain conditions, i.e., $\varepsilon_{11} = -\varepsilon_{33}$, and that all other components are zero. Measurement shows that strip widening is negligible; hence, the path integral of strain is that defined as plane strain. However, detailed analysis of the geometry of the plastic zone in rolling shows a position dependence of both strain and strain rate. Figure 14 (a) shows a schematic diagram of strip rolling, together with a highly simplified geometrical model of the process (Figure 14 (b)). This Figure emphasizes geometrical effects and treats the roiling gap as a wedge-shaped channel through which the metal flows. The half channel shown in Figure 14 (b) shows that each element moving along the stream lines located away from the neutral plane undergoes a shear in the sense indicated. The value of the ratio of shear e_{13} to rolling deformation e_{11} is γ_g and changes sign as well as magnitude with instantaneous position through the channel. This is the shear arising from geometry γ_g, and the deformation gradient tensor is:

$$E_i = \begin{bmatrix} -\frac{1}{2} & 0 & -\gamma_g \\ 0 & 0 & 0 \\ 0 & 0 & \frac{1}{2} \end{bmatrix} e_{11} \qquad (28)$$

and

$$E_o = \begin{bmatrix} -\frac{1}{2} & 0 & \gamma_g \\ 0 & 0 & 0 \\ 0 & 0 & \frac{1}{2} \end{bmatrix} e_{11} \qquad (29)$$

where suffixes *i* and *o* represent in and out, respectively, as in Figure 13.

For the simplified model, the deformation gradients are

$$\begin{aligned} e_{11} &= -ln(1-r) \cong r \\ e_{13} &= \frac{rd}{2} \end{aligned} \qquad \text{at the surface} \qquad (30)$$

i.e.,

$$e_{13} = \frac{rd}{2\sqrt{rRd - \left(\frac{rd}{2}\right)^2}} \qquad (31)$$

where *r* = reduction = (initial - final thickness)/initial thickness;

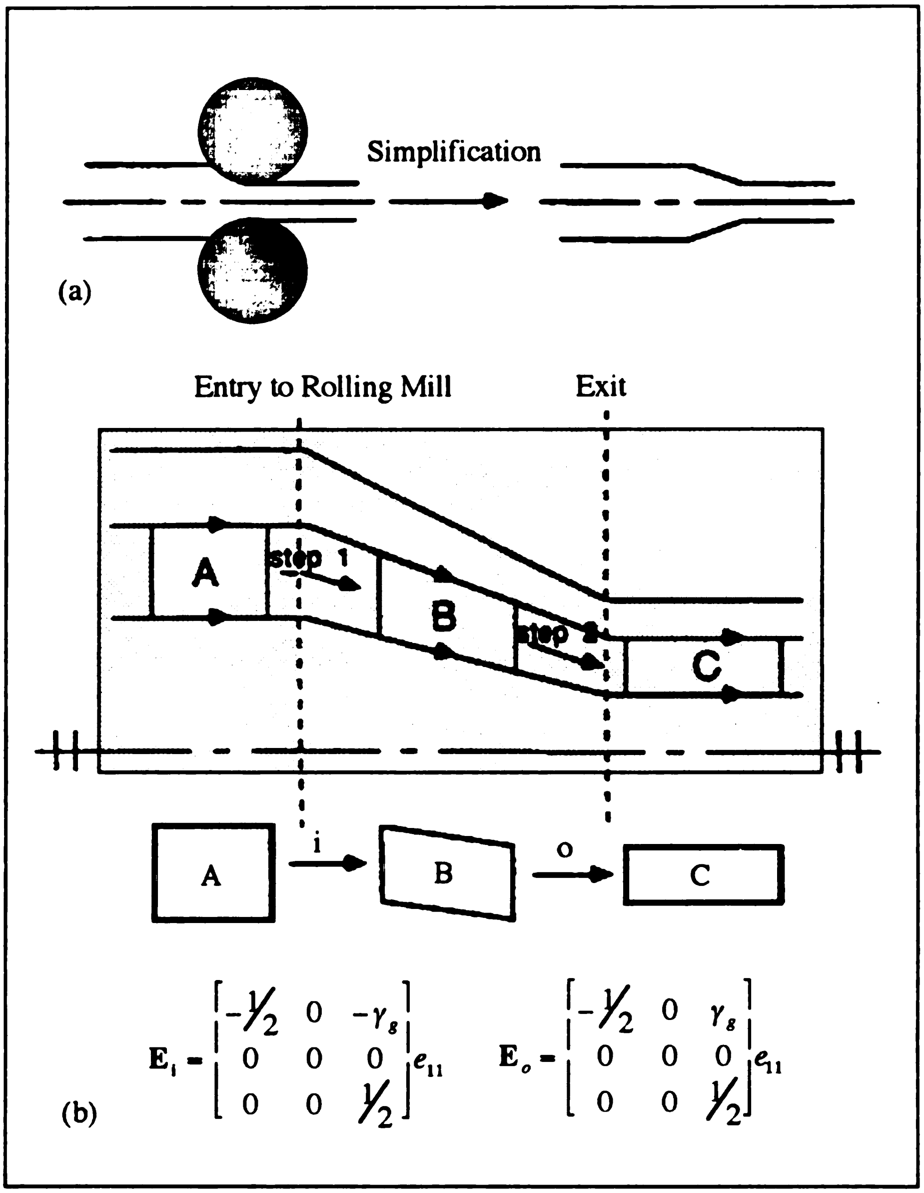

Figure 14. (a) Schematic diagram showing conventional rolling reduction and the convergent channel model. (b) Streamline through the convergent half-channel showing the geometrical changes an element experiences as it passes through. The deformation gradient tensors are modified by the geometrical factors as the material goes into (E_i) and comes out of (E_o) the channel (Ref. 107)

d = specimen thickness;

l = projected length of contact between roller and specimen; and

R = roll radius.

It is clear that γ_g at the surface is a function of Δ. The symbol 'Δ' is a characteristic parameter, which is defined as the mean thickness-to-length ratio of the plastic zone that fills it. Many researchers have demonstrated a correlation between Δ and the surface texture produced in cold drawing of mild steel strip [107]. It can be shown that for small values of reduction r,

$$\gamma_g = \frac{d}{2\sqrt{rRd}} = \frac{1}{2}\Delta = \frac{1}{2\left(\frac{l}{d}\right)} \qquad (32)$$

The effect of friction is modeled with the aid of schematic diagram shown in Figure 15. As the metal flows through the plastic zone, there is a velocity gradient which depends on the location of the element in the zone, this produces a shear component, as shown in Figure 15. Since there is a change in the sense that friction is considered to act on either side of the neutral plane as shown, the shear e_{31} is assumed to be equal and opposite on either side of the neutral plane. Defining γ_f as the ratio of shear due to friction e_{31} and rolling reduction e_{11} allowed, deformation gradient tensor to be written as

$$E_t = \begin{bmatrix} -\frac{1}{2} & 0 & 0 \\ 0 & 0 & 0 \\ \gamma_f & 0 & \frac{1}{2} \end{bmatrix} e_{11} \qquad (33)$$

and

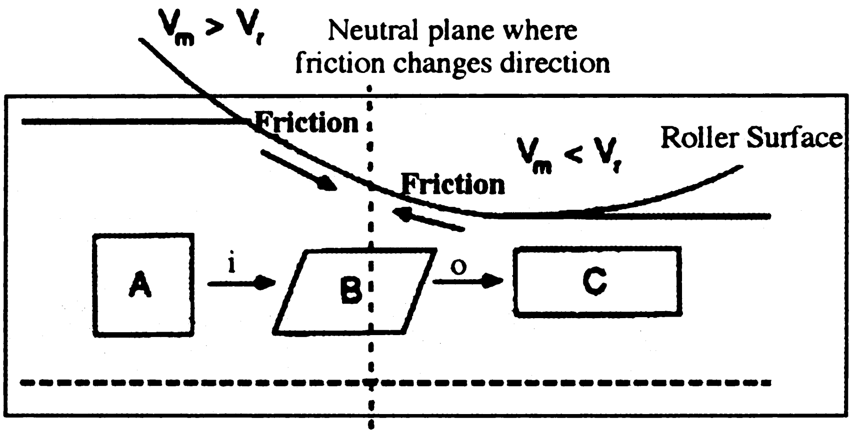

$$\mathbf{E}_i = \begin{bmatrix} -\tfrac{1}{2} & 0 & 0 \\ 0 & 0 & 0 \\ \gamma_f & 0 & \tfrac{1}{2} \end{bmatrix} e_{11} \qquad \mathbf{E}_o = \begin{bmatrix} -\tfrac{1}{2} & 0 & 0 \\ 0 & 0 & 0 \\ -\gamma_f & 0 & \tfrac{1}{2} \end{bmatrix} e_{11}$$

Figure 15. Schematic diagram showing the shear strain induced by friction, along with the "in" and "out" deformation gradient tensors (Ref 107)

$$E_o = \begin{bmatrix} -\frac{1}{2} & 0 & 0 \\ 0 & 0 & 0 \\ -\gamma_f & 0 & \frac{1}{2} \end{bmatrix} e_{11} \qquad (34)$$

Combining the effects of geometry and friction gives the deformation gradients as

$$E_i = \begin{bmatrix} -\frac{1}{2} & 0 & -\gamma_g \\ 0 & 0 & 0 \\ \gamma_f & 0 & \frac{1}{2} \end{bmatrix} e_{11} \qquad (35)$$

$$E_o = \begin{bmatrix} -\frac{1}{2} & 0 & \gamma_g \\ 0 & 0 & 0 \\ -\gamma_f & 0 & \frac{1}{2} \end{bmatrix} e_{11} \qquad (36)$$

Finally, these deformation gradient Equations (35) and (36) can be used to simulate the development of deformation (rolling) textures by employing simulation programs such as the Los Alamos Polycrystal Plasticity (LApp) code.

3. EXPERIMENTAL

3.1 Processing of High density 2223 BSCCO Superconductor

3.1.1 High T_c 2223 BSCCO Superconductor Preparation

High purity(>99.9%) oxides or carbonates of Bi, Pb, Sr, Ca, and Cu, with the cation ratio of 1.6:0.4:2.0:2.0:3.0, were carefully mixed, calcined, and reground. Initial grinding before calcination and intermediate grindings between multiple calcinations and final sintering were performed with a pestle and mortar. After initial crushing of large particles, methanol was added to form a slurry to increase the grinding efficiency. Methanol was chosen as the grinding medium to prevent possible degradation of the superconducting compound due to moisture pickup. The mixed compound was calcined at 820°C for 20 hours, ground, and sintered at 850°C for 50-100 hours. To enrich the high T_c phase in $Bi_{1.6}Pb_{0.4}Sr_2Ca_2Cu_3O_Z$ compound, intermediate pressing method [108,109] was used between calcination and sintering.

For normally-sintered sample comparison with HIP sample, the prepared superconductor powders were compacted in a closed stainless steel die with a hydraulic press to form round pellet. Following that, a solid state reaction/sintering was performed by heating the sample at 850°C for 3-200 hours in air and subsequent slow cooling to room temperature inside the furnace.

3.1.2 HIP Sample Preparation

The prepared high T_c BSCCO 2223 powder was first compacted into a cylindrical shape by uniaxial compression. The pressed samples were coated with 99.99 % purity boron nitride using BN spray (Union Carbide Co.) to inhibit reaction between sample and Pyrex by producing diffusion barrier. The samples were placed into a 12 mm (I.D) diameter and 2 mm thickness Pyrex tube, and individually encapsulated in an evacuated Pyrex tube. The Pyrex tube, with the sample, was evacuated for 20 minutes under a vacuum of 10^{-2} Pa and finally sealed by a gas torch, as shown in Figure 16.

3.1.3 HIP Processing

For hot isostatic pressing, an IPS (International Pressure Service, Inc.) Eagle-6 Hot Isostatic Press machine was used, as shown in Figure 17. The Eagle-6 uses a 6 inch internal diameter stamped monolithic pressure vessel with threaded closures. The endurable maximum pressure was rated around 200 MPa. This equipment is capable of reaching a temperature 2,000°C, using a graphite furnace, which is a modular plug-in unit with a hot zone measuring 3 inches in diameter and 4 inches in length, as shown in Figure 18. Argon gas was used as the pressure medium. A microprocessor-based controller was utilized to control and monitor the process temperature, pressure, time, valve position, compressors, volts, amps and electrical contacts.

Pressure and temperature was controlled by a programmed set point controller. A digital/analog strip chart recorder was used to record system pressure and temperatures as a function of time. Temperatures was monitored by using 5 different tungsten/rhenium thermocouples located at different levels within the furnace and the pressure vessel. The uncertainty in temperature measurement was estimated approximately within ~3°C of reported values.

The sealed capsule was placed into a specially designed graphite crucible and carefully inserted into the heating zone of the graphite furnace. In the HIP, in the first stage, the system was evacuated for 30 minutes and then purged 3 times by argon gas. The pressure was kept low to avoid glass cracking as the temperature was raised to 820°C, which is the Pyrex softening temperature. The applied heating rate was

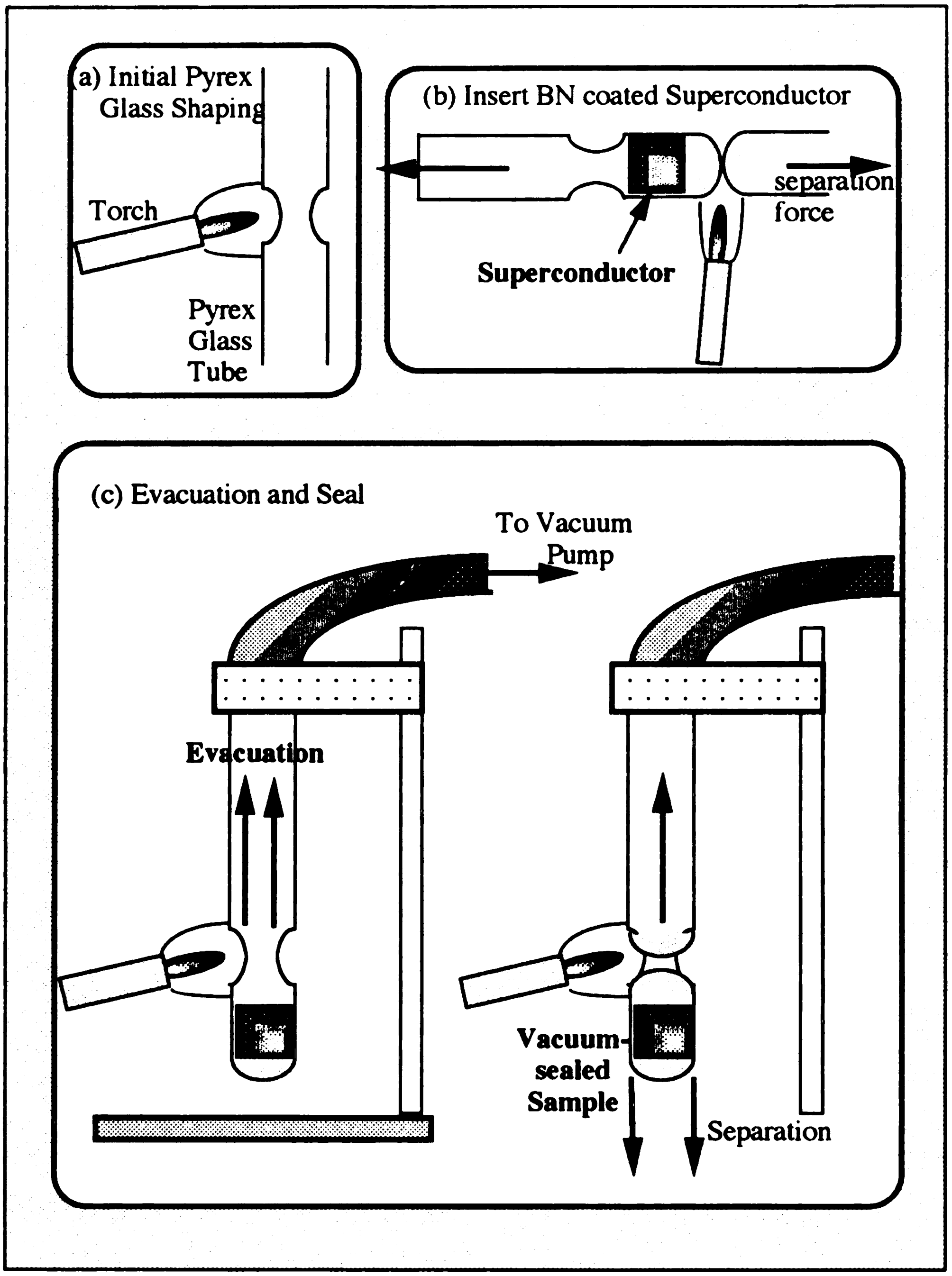

Figure 16. Schematic representation of the vacuum-sealed encapsulation procedure for HIP sample

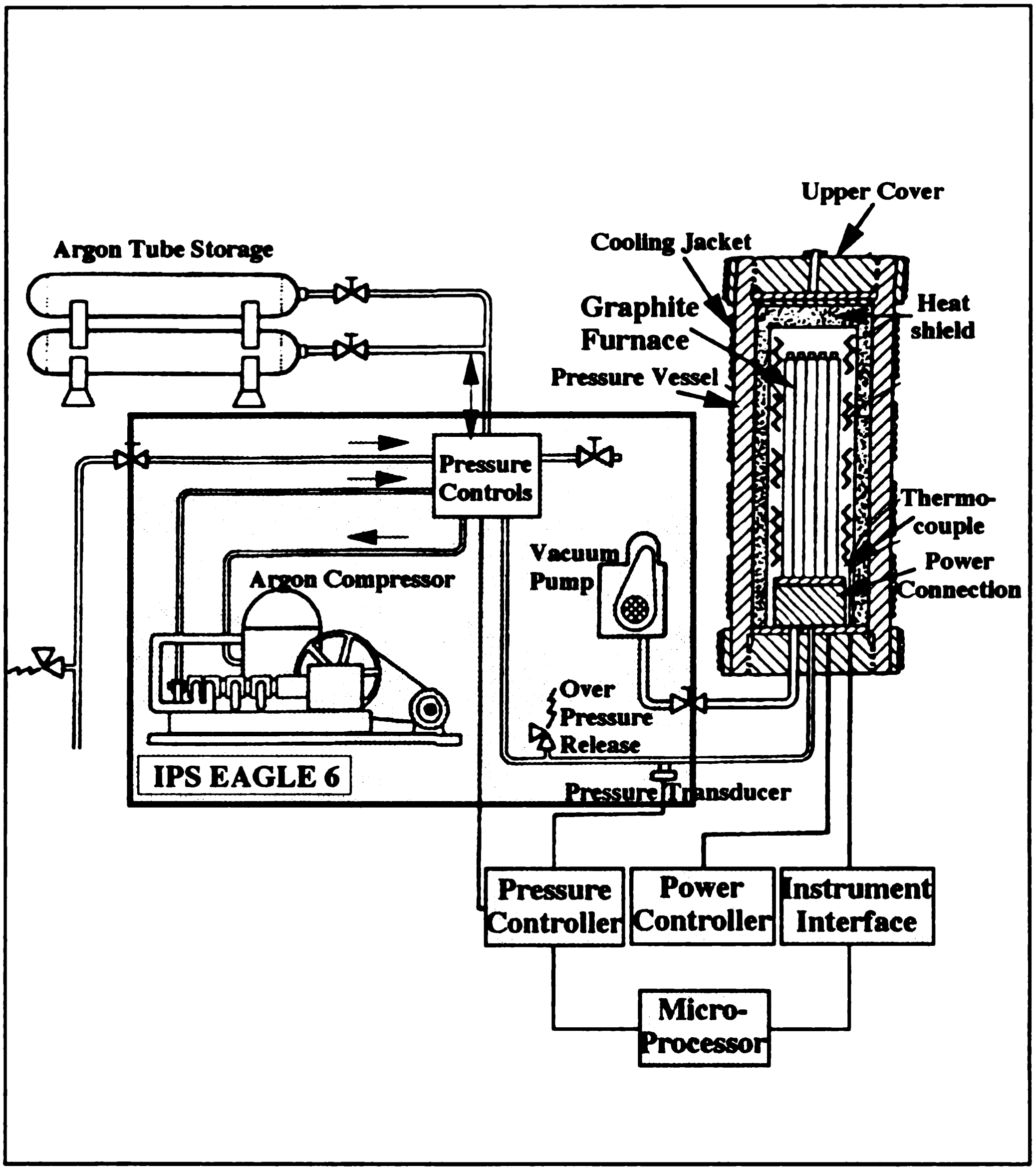

Figure 17. Schematic of micro-processor control of hot isostatic pressing system

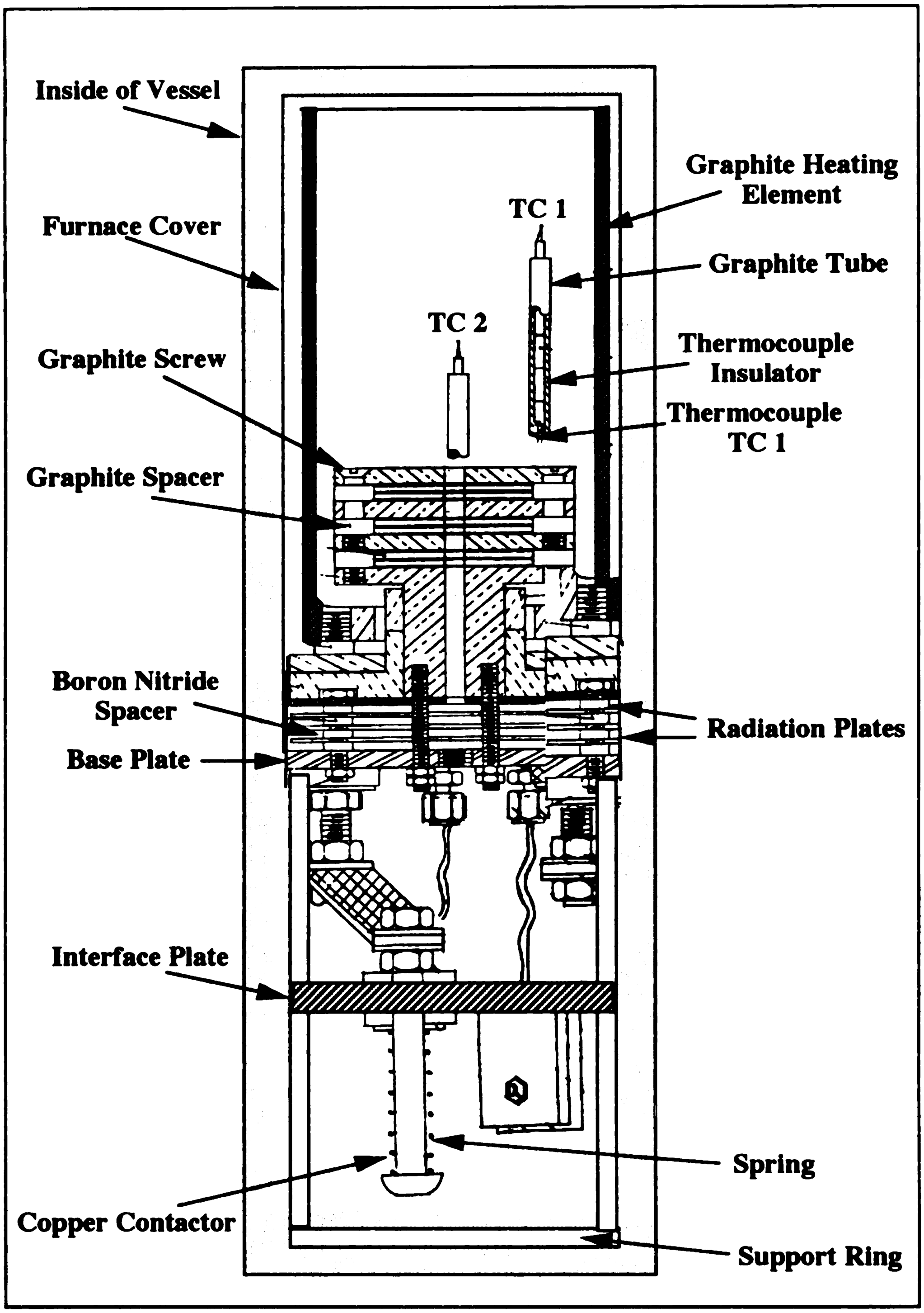

Figure 18. Schematic of the components of graphite furnace used in IPS Eagle 6 HIP

80°C/min. Temperature and pressure were then raised to 850~870°C and 138 MPa respectively and kept for a duration of 3 hours. At last, the temperature was slowly cooled to 500°C at a rate of 100°C/hour and further cooled down to room temperature. Pressure was then vented.

Figure 19 show the detailed HIP processing cycle in terms of pressure, temperature and time. Specimens were removed from the glass wall of the capsule. Some surface reaction between the Pyrex glass and BN coated surface(which was easily removed by grinding) was however observed.

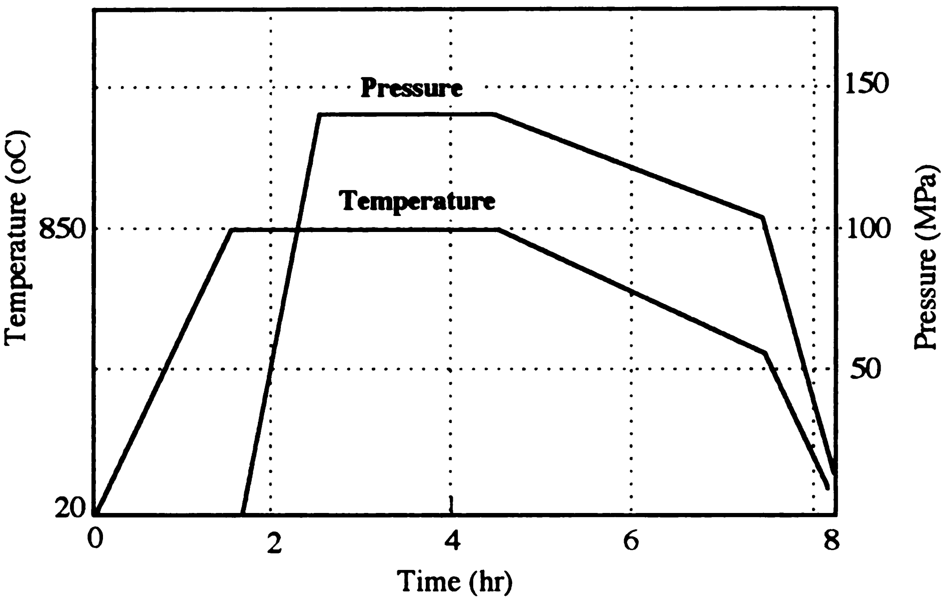

Figure 19. HIP processing cycle in terms of pressure, temperature, and time

3.2 Processing of 2223 BSCCO/Ag Tape by HIP Cladding Technique

3.2.1 Processing of the Multi-layer of 2223 BSCCO/Ag Composite by HIP Cladding

The 2223 BSCCO/Ag superconducting tape is fabricated by several processing steps. High purity(>99.9%) oxides or carbonates of Bi, Pb, Sr, Ca, and Cu with the cation ratio 1.6:0.4:2.0:2.0:3.0 were carefully mixed, heat treated, and reground. The prepared high T_c phase powder was first compacted into a cylindrical shape by compaction. Next step was HIP sample preparation. Multi-layer stacks consisted of alternate layers of 2223 (BSCCO) and silver are coated with BN spray and encapsulated in a Pyrex tube under vacuum.

As shown in the schematic diagram of Figure 20, the sealed samples were HIP processed in Ar atmosphere at a temperature of 850°C and a pressure of 138 MPa for a duration of 3 hours to obtain high density BSCCO layers and good BSCCO/Ag interface bonding strength prior to rolling. The Hipped samples were cooled slowly at a rate of ~100°C/h. Pre-forms for the cold rolling process were cut from these multi-layer stacks.

3.2.2 Thermomechanical Deformation

BSCCO/Ag composite tape was obtained by multiple passes cold rolling and intermediate annealing, as shown in Figure 20. During the successive rolling process two to three intermediate heat treatment were provided to prevent failure due to work hardening of silver. For the study of c-axis texture evolution during cold rolling process, several batches of samples were successively cold rolled at different degrees of thickness reduction(%) without annealing.

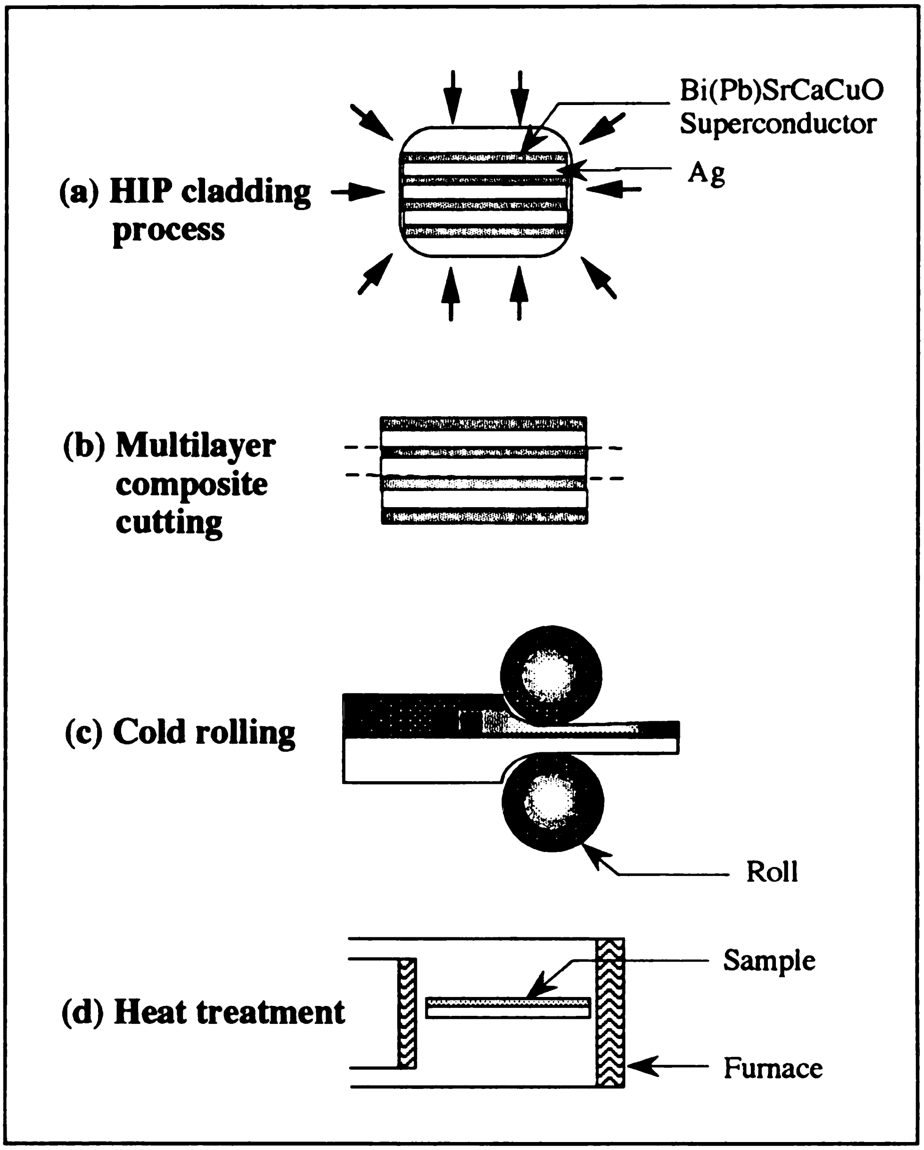

Figure 20. Schematic illustration of processing steps for 2223 BSCCO/Ag superconductor tape

3.3 Processing of Highly Textured 2212 BSCCO/Ag Tape by Melt Process

3.3.1 Low T_c 2212 BSCCO Superconductor Powder Preparation

For controlled melt process methods, appropriate amounts of Bi_2O_3, $SrCO_3$, $CaCO_3$, and CuO were mixed so that the cation ratios of the compound would be Bi:Sr:Ca:Cu = 2:2:1:2. The powder mixture was calcined at 850°C for 24 hours, uniaxially compressed by 10,000 psi for densification, and recalcined again at 850°C for 24 hours. The powder was then ground to a fine powder.

3.3.2 Controlled Melt Process

2212 BSCCO /Ag tapes were produced using the doctor-blade casting process which is shown in Figure 21. First, the 2212 BSCCO powder was mixed with glycerol and propanol into a slurry. The slurry was cast under a doctor blade onto silver foil sheets. The resulting green tape had dimensions of 13 mm width and 60 mm length. The thickness of the BSCCO superconductor layer and the silver thickness varied. One set was 125 μm total with a 50 μm BSCCO layer; the other set varied from 300~450 μm total thickness with a BSCCO layer of 125 μm. The BSCCO/Ag composite tape was placed in a furnace at 300°C for 2-3 hours to remove the organic solvents. The tapes were then cold rolled down to a final thickness of ~80 μm, ready for partial melt processing.

The following outline (Table 1) explains the melt processing conditions for the 2212 BSCCO/Ag tapes. Groups A (880°C), C (880°C), and D (920°C) were first partially melt processed for twenty minutes at the designated temperatures, then were cooled to the annealing temperature of 860°C at three different rates: 2°C/hr, 10°C/hr, and 120°C/hr. Once 860°C was reached, furnace was shut off for groups A and B and

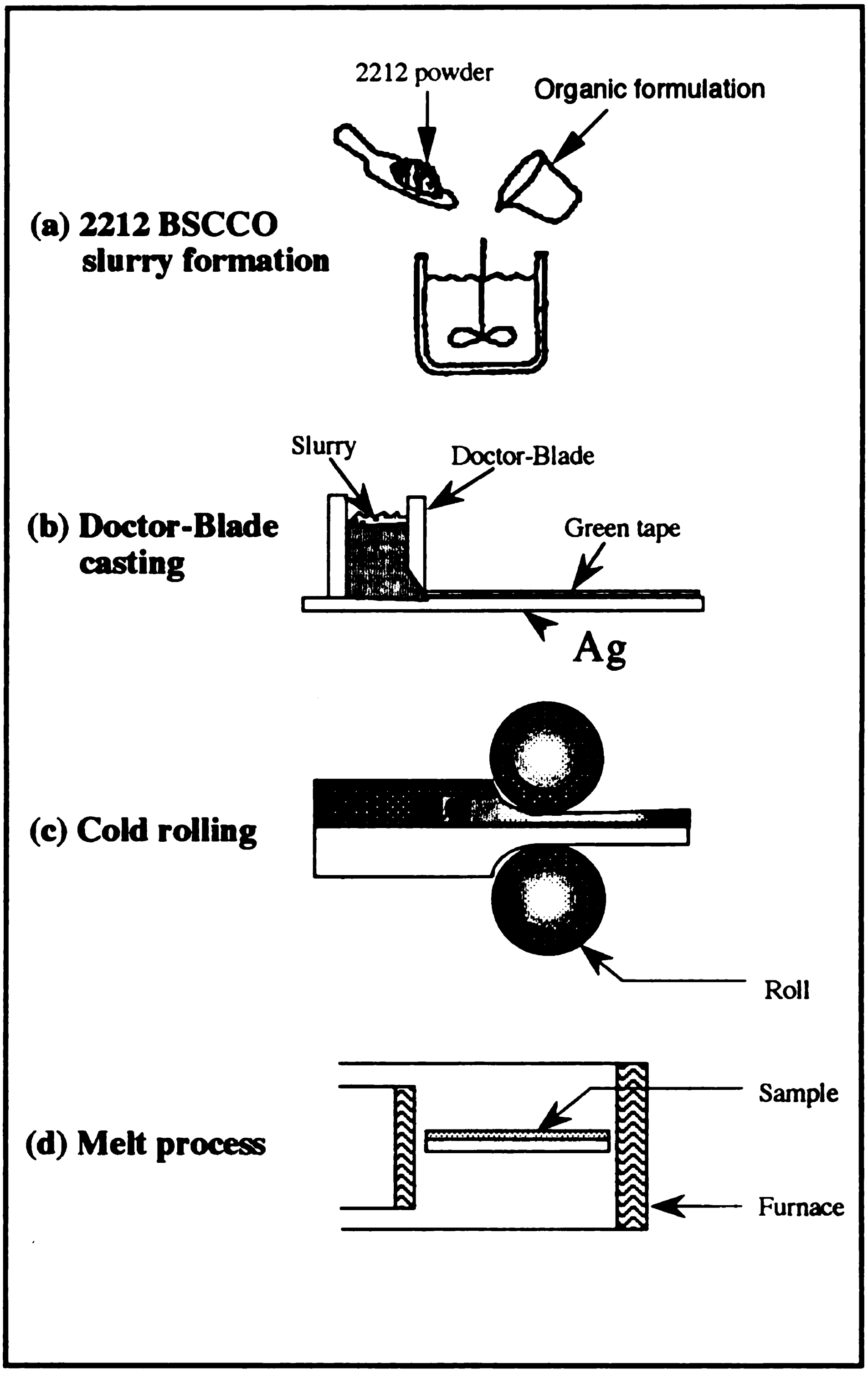

Figure 21. Schematic illustration of doctor-blade casting and melt processing for 2212 BSCCO/Ag superconductor tape

Table 1. Various melt processing conditions for the 2212 BSCCO/Ag tape

Sample name	Melt Process Temperature	Melt Process Time	Cooling rate	Anneal Time	Final Cooling
A1	880°C	20 min.	2°C/hr	- - - -	Furnace
A2	880°C	20 min.	10°C/hr	- - - -	Furnace
A3	880°C	20 min.	120°C/hr	- - - -	Furnace
C1	880°C	20 min.	2°C/hr	100 hrs.	Furnace
C2	880°C	20 min.	10°C/hr	100 hrs.	Furnace
D1	920°C	20 min.	10°C/hr	- - - -	Furnace
D2	920°C	20 min.	120°C/hr	- - - -	Furnace
S1	880°C	20 min.	- - - -	- - - -	Furnace
S2	880°C	20 min.	- - - -	- - - -	Quench
S3	880°C	120 min.	- - - -	- - - -	Quench
S4	900°C	120 min.	- - - -	- - - -	Quench
S5	920°C	120 min.	- - - -	- - - -	Quench

allowed to cool in the furnace (furnace cooling); group C tapes were annealed for 100 hours, then allowed to furnace cool. The main objective here was to observe the effect of holding time and cooling rate on the texture of the 2212 BSCCO superconductor.

Group S was used to determine the amount of secondary phase evolved during the partial melt process. The temperature for partial melt processing ranged from 880°C to 920°C; therefore, three tapes were processed at 880°C, 900°C, and 920°C respectively and air quenched to determine what phases are present in the material at these temperatures.

Once the tapes were melt processed, the crystal structure was identified using a Scintag XDS-2000 X-ray diffractometer. Pole figure measurements were made using a Scintag XDS-2000 X-ray pole figure goniometer. The samples were then characterized under a scanning electron microscope (SEM), equipped with energy dispersive analysis of X-ray (EDAX).

3.4 Sample Characterization Methods

3.4.1 Crystal Structure and Phase Identification

For the phase identification and crystal structure determination, X-ray diffraction (XRD) method were performed using a Scintag-XDS-2000 x-ray diffractometer, equipped with a computerized data collection system. Monochromatic CuKα radiation, obtained by using a Ni filter or a double-crystal monochrometer was used. A tube voltage of 40 kV and a tube current of 30 mA was used for all structural analysis.

3.4.2 Texture Measurement, Analysis and Representation

3.4.2.1 Pole figure Measurement

X-ray pole figures were obtained with the Schulz method [110]. Figure 22 is a scheme of the Schulz method geometry. The method requires a special specimen holder which tilts the sample with a horizontal axis BB', while rotating it in its own plane about an axis AA' normal to its surface. The horizontal axis lies on the specimen surface and is adjusted by a rotation about the diffractometer axis to make equal Bragg angles with the incident and diffracted beams.

The latitudinal and longitudinal rotations are provided by a vertical circle and a small horizontal azimuth circle, respectively. The latitudinal rotation, measured by an angle of ϕ , can be varied from 0° to 90°, practically limited up to 70° to 80° due to collision between sample holder and columnator fixture and low intensities detection, while the azimuthal scan versus an angle of δ, can be simultaneously taken from 0° to 360°.

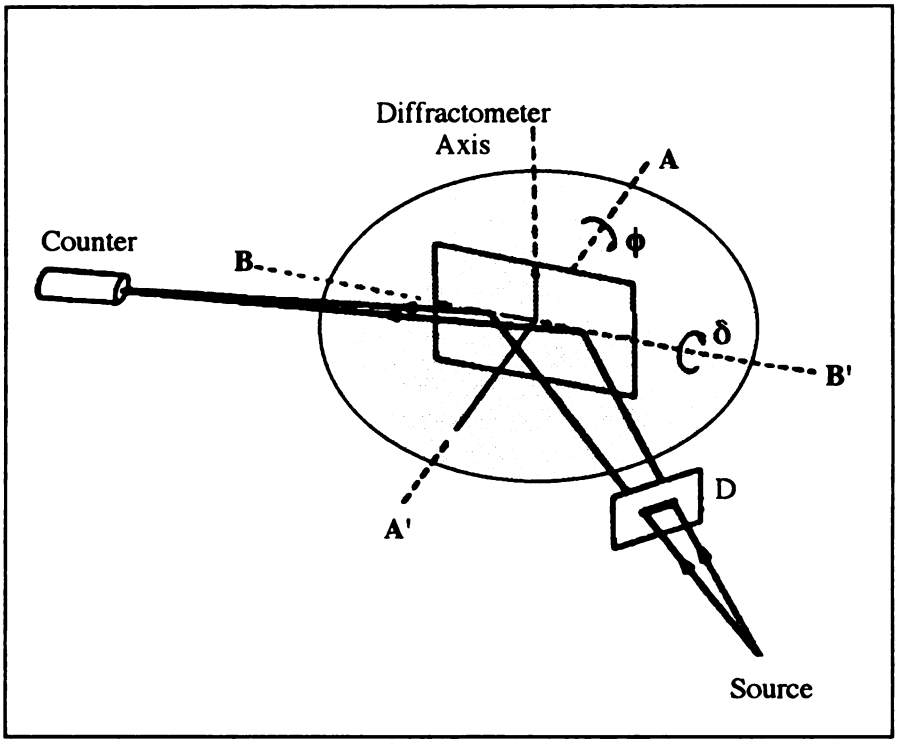

Figure 22. The geometry used in the x-ray pole figure analysis. The specimen can be simultaneously rotated latitudinally and azimuthally around the BB' and AA' axes, respectively (Ref. 110)

3.4.2.2 The Preferred Orientation Package-Los Alamos (popLA)

Anisotropic material properties have growing interest as the processing and use of materials are getting more sophisticated and more quantitative. The major reason of anisotropy in polycrystalline materials is due to preferred orientation, i.e. "texture". Texture analysis requires mathematically sophisticated techniques, and this has made it operationally difficult to the materials scientist. The Preferred Orientation Package-Los Alamos (popLA) [111] is a comprehensive coherent menu-driven set of utility programs that is independent of the texture measurement hardware and easy to use for non-experts in texture theory.

Experimental Pole figures

The starting point for texture analysis is diffraction intensity data (ASCII data files) taken on an X-ray pole figure goniometer, on a $5^\circ \times 5^\circ$ polar grid. Incomplete data (due to collision, as explained before) is taken from a single specimen, and a technique (using reflection from one face only, to a tilt of at least 70°). While the accuracy of the interpretation of orientation distribution (OD) always increases with increasing total number of independent measurements, the popLA program gives quite satisfactory results for a carefully chosen set of a very few incomplete pole figures [111].

The background should be measured on both sides of the Bragg peak; by finding appropriate locations in a 2θ scan. The background intensity is a function of the tilt but, since this dependence is not sensitive up to angles less than 80°, it is usually sufficient to measure the back ground at zero tilt only and to adjust it for defocusing with a curve which is similar for most materials; this is actually preferred because peaks often overlap at high tilts owing to broadening (due to elliptical shape of beam at high tilt). It is useful to perform a normalization on the existing data in each pole figure, even though the missing rim makes this preliminary.

Extending incomplete pole figures; normalization and WIMV analysis

A major advantage of undertaking "extending incomplete pole figures" is that it leads to a much better normalization of the pole figures with respect to each other, which makes them more self-consistent. First renormalizing the pole figures by the harmonic method and then doing a WIMV (Williams Imhoff Matties Vinnel) analysis [112] on the experimental data will gives us the best of both system.

The WIMV algorithm is one of various analysis schemes that establish "pointers" (or "vectors" or "matrices") which connect each cell in orientation space with all cells on the various pole figures into which they project. In other words, a set of pointers is used to relate each OD cell with its corresponding pole figure cell. The method thus essentially involves the inversion of a matrix that may be very large [111]. The pole figure data are stored on a $5^\circ \times 5^\circ$ polar grid as described above, and the OD (Orientation Distribution) space is to be calculated on a $5^\circ \times 5^\circ \times 5^\circ$ grid in the three Euler angles (Ψ, θ, and ϕ), as will be explained later.

The representation of texture

Orientations can be equally well described on pole figures or inverse pole figures; in other words, as the location of some crystal axes with respect to a sample reference frame (pole figure), or as the location of some sample axes with respect to a crystal reference frame (inverse pole figure) [113]. Figure 23(a) shows a series of pole figures in the various definitions. The coordinates X, Y, Z identify the sample coordinate system. Figure 23(b) shows a corresponding set of inverse pole figures, where x, y, z identify the crystal coordinate system (lower-case letters for the microscopic frame). All figures are plotted with the axes in the sequence of right-top-center, and the point to be

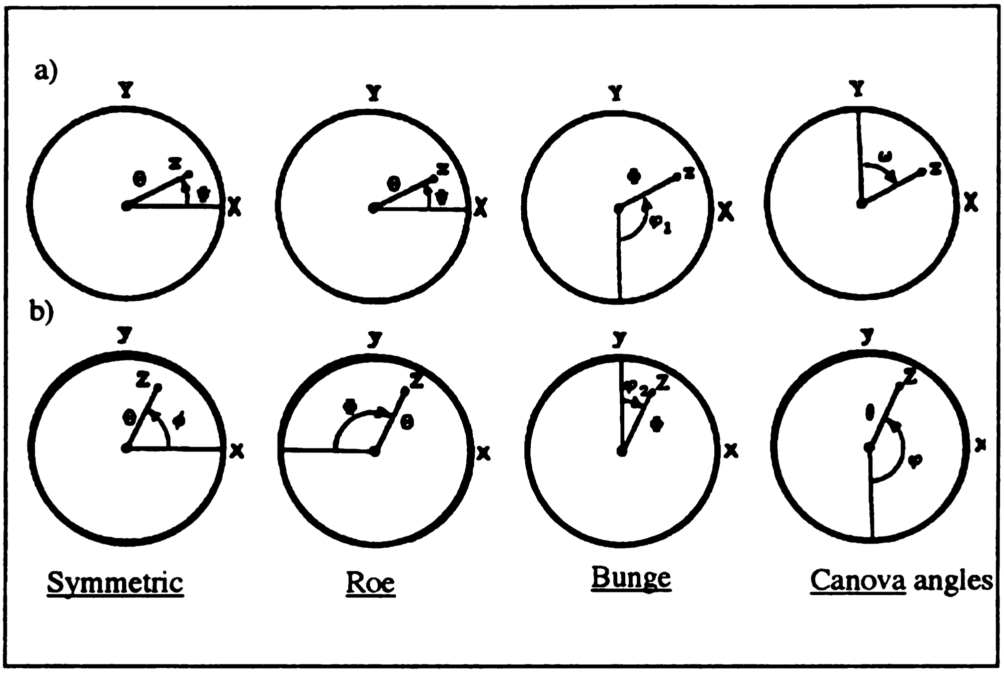

Figure 23. shows (a) a series of pole figures in the various definition. The coordinates X, Y, Z identify the sample coordinate system. (b) shows a corresponding set of inverse pole figures, where x, y, z identify the crystal coordinate system (Ref. 113)

described is chosen consistently to be in the first quadrant, with all coordinates being positive.

Figure 23 described only the projections of an orientation, each projection requiring only two angles. For a complete description of 3-D orientation space, one needs to combine the three angles (namely, three Euler angles). Following are the description of the definition of three Euler angles (Ψ, θ, and ϕ) reported by U. F. Kocks [113]. This definition will be used in the interpretation of sample orientation distribution (SOD) data, calculated by popLA program. Kocks described first the longitude and latitude of a direction on the surface of a sphere, then the azimuth around that point to construct the 3-D orientation space. Figure 24 is drawn with (a) the sample system as the reference frame (COD), (b) the crystal system as the reference frame (SOD); but they are drawn such that the relative situation of the boats is recognizably similar in the two cases.

The rule for defining the three euler angles then is as follows: Identify the location of each boat with the point of emergence of the axis Z (or z), and its heading as being towards its respective X-axis. Draw a connecting line (a great circle) between the two boats: its length is θ. Now define the angles Ψ and ϕ, respectively, as the counter-clockwise rotation needed to turn each boat's course toward the other boat (Ψ for the 'sample' boat, ϕ for the 'crystal' boat). The symmetry of describing one system in terms of the other, or the other in terms of the one, is evident.

3.4.3 Density Measurements

The densities of Hipped samples were measured according to ASTM B328-73 (buoyance method). About 3 grams of specimen was cleaned with acetone and then completely dried. After cleaning, samples were weighed in air atmosphere (W_A) and immersed in SAE 10 W-40 motor oil (viscosity of approximately 200 SUS at 100 °F) for

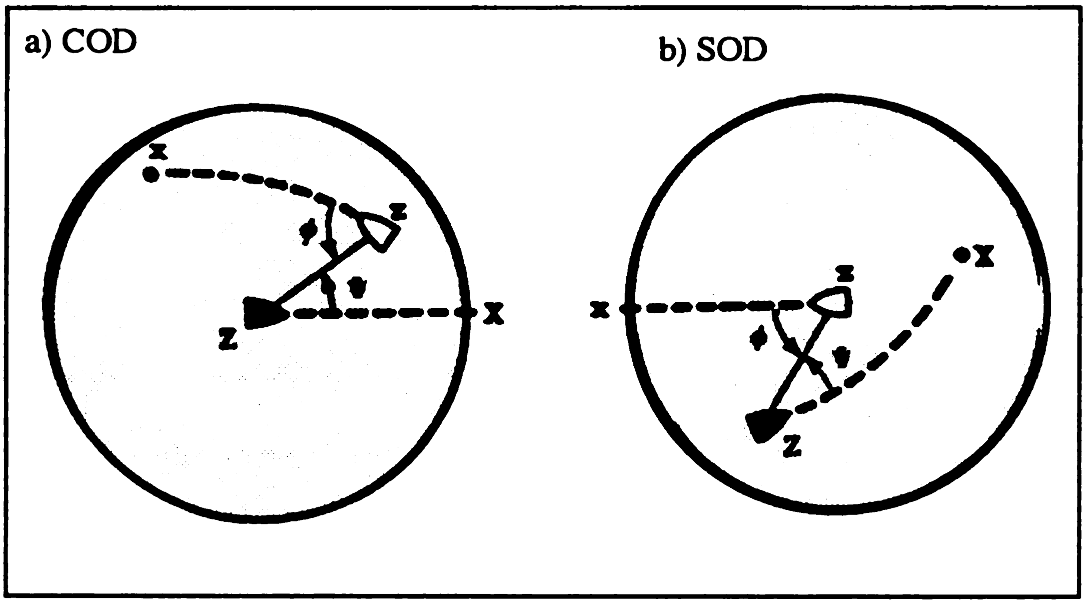

Figure 24. Symmetric definition of the Euler angles: (a) crystal axes xyz in sample system XYZ (b) sample axes XYZ in crystal system xyz (Ref. 113)

4 hours and held at 180°C. Then, the sample was immersed in oil at room temperature to lower to room temperature. The oil immersion introduces impregnation of the sample through interconnected pores (open pores).

Following this, the excess oil was wiped off with a damp cloth and the samples were weighed again (W_B). The samples impregnated with oil, were then tied with a 0.08mm diameter copper wire and suspended from the beam hook of a semimicro balance. Samples were completely immersed into a beaker filled with distilled water at 18°C, which was placed underneath the beam hook. The wired sample was weighed (W_C) and then the wire without the sample was immersed again into the distilled water for measurement (W_E). The density of sample can now be calculated from:

$$D = W_A/(W_B - W_C + W_E) \qquad (37)$$

where

D = density, g/cm^3

W_A = weight in air of oil-free specimen, g.

W_B = weight of oil-impregnated specimen, g,

W_C = weight of oil-impregnated specimen and wire in water, g, and

W_E = weight of wire in water, g.

3.4.4 Microstructure Examination and EDAX Analysis

For microstructural and compositional studies, thin-longitudinal cross-section samples (Figure 25) were metallographically mounted on a lucite block. Lucite mounted specimens were then polished with 0.3~0.5 μm diamond paste. Methanol was used to prevent any possible degradation of the microstructure due to moisture pick-up. Polished longitudinal cross-section samples were etched for 20-25 seconds with 1 part 65%

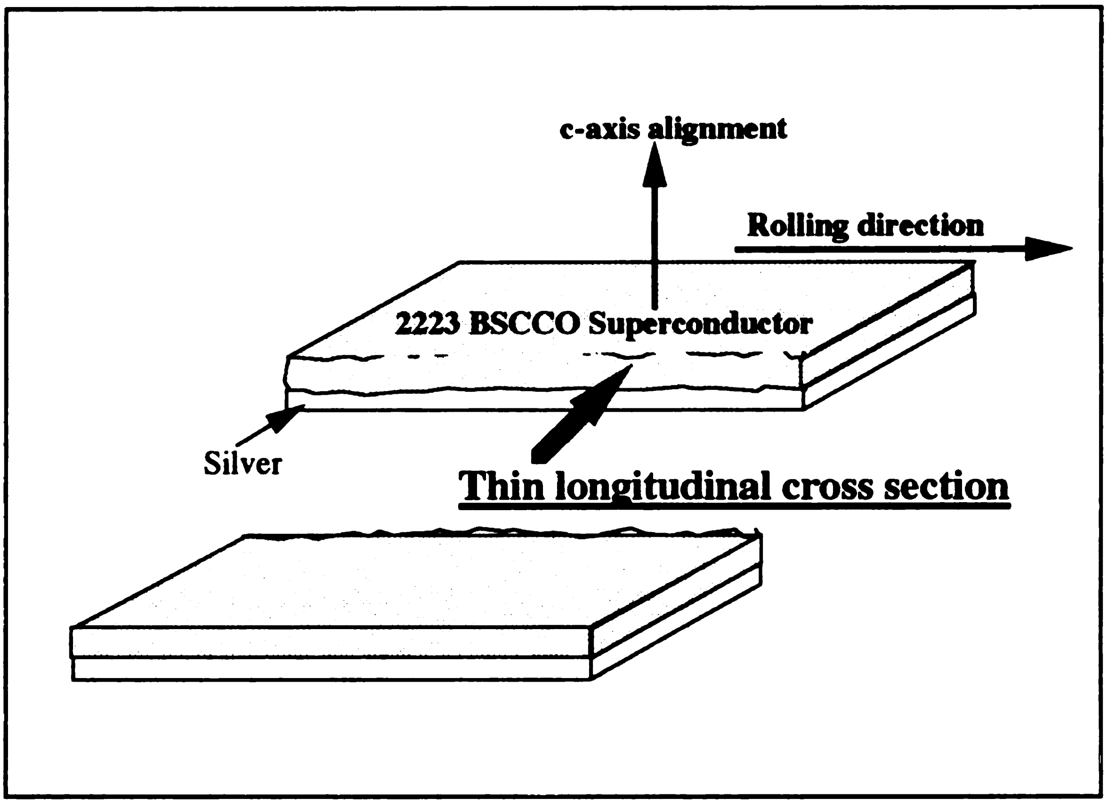

Figure 25. Schematic diagram showing the geometry of the samples for SEM. The viewing direction of thin longitudinal cross section are indicated by large arrows

perchloric acid mixed with 99 parts 2-butoxy-ethanol to expose the grain structure, with special emphasis on revealing interior alignment.

Fracture surfaces, produced by fracturing the tapes parallel to the rolling direction in the thin-longitudinal cross-section, as shown in Figure 25, were also studied. Fractured specimens were mounted on cylindrical aluminum stubs. Silver paint was used for electrical contact to ground and also to provide a better mechanical support. Both etched and fractured surfaces of longitudinal cross-section were examined by using a Hitachi S-2500C scanning electron microscope (SEM). A Link energy dispersive x-ray spectroscope (EDS) attached to the Hitachi S-2500C scanning electron microscope was used for chemical analysis.

3.4.5 Electrical Resistance and Critical Current Density Measurements

3.4.5.1 Critical Temperature Measurement

A continuous measurement of temperature dependence of resistance was carried out using an auto-balancing ac bridge with a lock-in amplifier (Linear Research LR-400) with a standard four-probe technique. Figure 26 shows a schematic of the 4-wire AC resistance measurement compound. Four gold plated wire pins were attached to the sample. The two outer ones were used for current supply and the inner two were used for voltage measurement.

Four standard gold plated wire wrapped socket pins, laid against one face of the sample, as shown in Figure 27, were used to make contact for measuring the AC resistance of the superconducting sample. A copper-constantan thermocouple was attached to the center of specimen. The rigid bakelite outer blocks were used to insure uniform clamping pressure on the four pins, and the deformable PVC inner blocks were

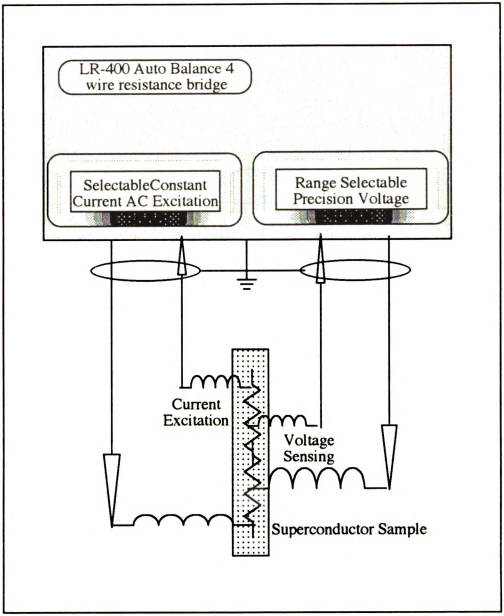

Figure 26. Schematic of the 4 probe resistance measurement

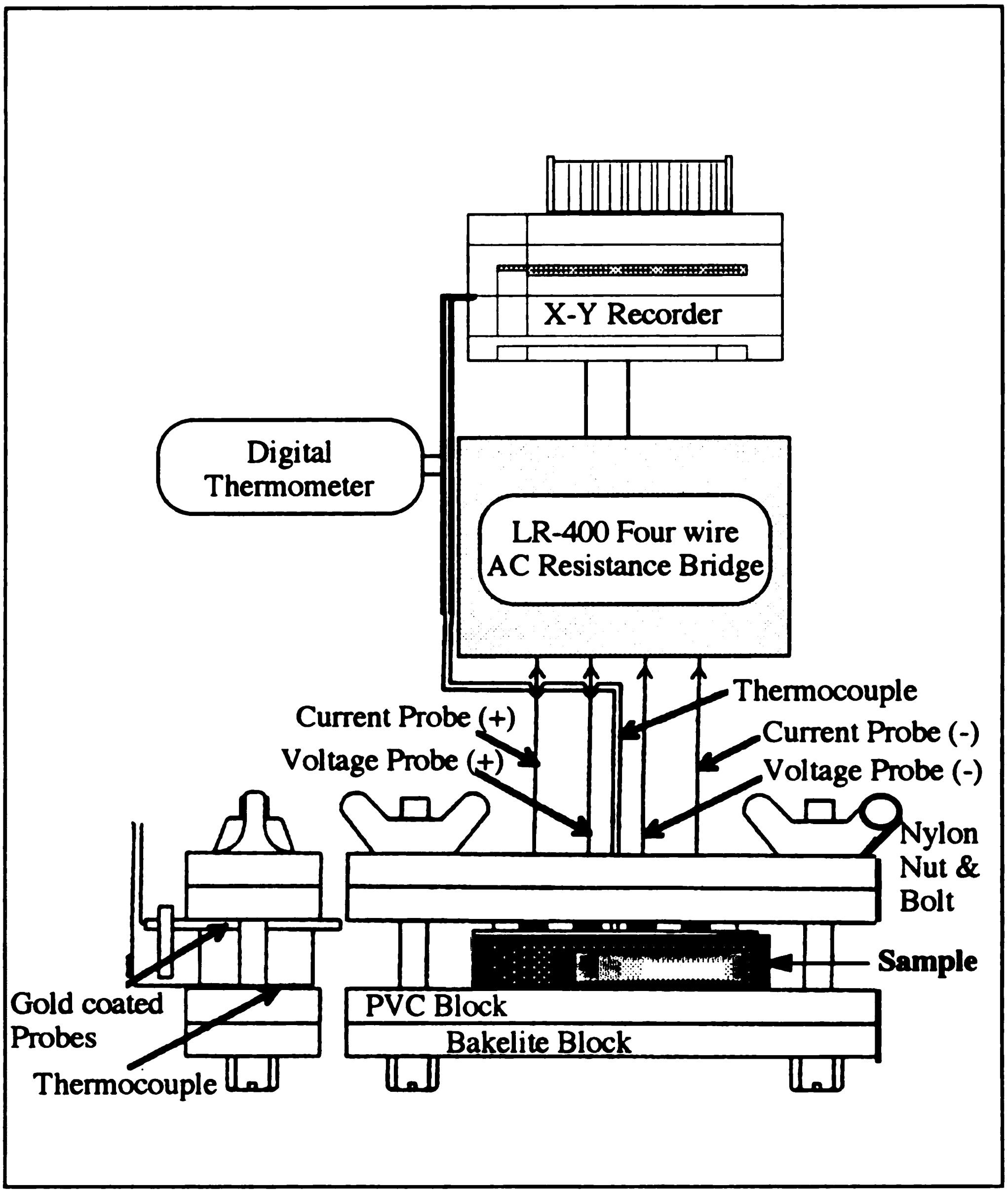

Figure 27. Resistance-temperature measurement set-up

used to accommodate the thermocouple and slight variation of the pins and sample thickness.

The entire assembly was immersed very slowly in the liquid nitrogen flask as shown in Figure 28. Temperature was monitored by a digital thermometer. The uncertainty in the temperature measurement was estimated to be approximately ± 0.5K. The electrical resistance was monitored by using the LR-400 AC resistance bridge (Linear Research Inc.). The monitored resistance was calculated by the voltage drop caused by passing a given constant current, while the temperature was changed from the liquid nitrogen boiling temperature, 77 K, to room temperature. The resolution of that machine is 1 micro ohm. The applied current used for this experiment was 3 mA. Temperature vs. resistance (voltage) was continuously recorded by using a Houston Instrument 200, X-Y recorder.

3.4.5.2 Critical Current Density Measurements

The critical current density values were measured at liquid nitrogen temperature (77K) by using a standard four-probe technique with zero magnetic field. The temperature was held constant at 77 K while the current through the sample was varied. The applied current range was from 0.2 to 9 Amp and the resistance was calculated from the voltage drop.

The value of J_c, was then deduced by dividing the critical current, at which the generated voltage was extrapolated to zero, over the effective cross section of specimen. In order to minimize the surface contact resistance, the contact surfaces of the cut samples were painted with silver. After drying for one hour, leads were attached to the silver contacts by using the silver paint; only the sample surfaces under contact were painted with Ag.

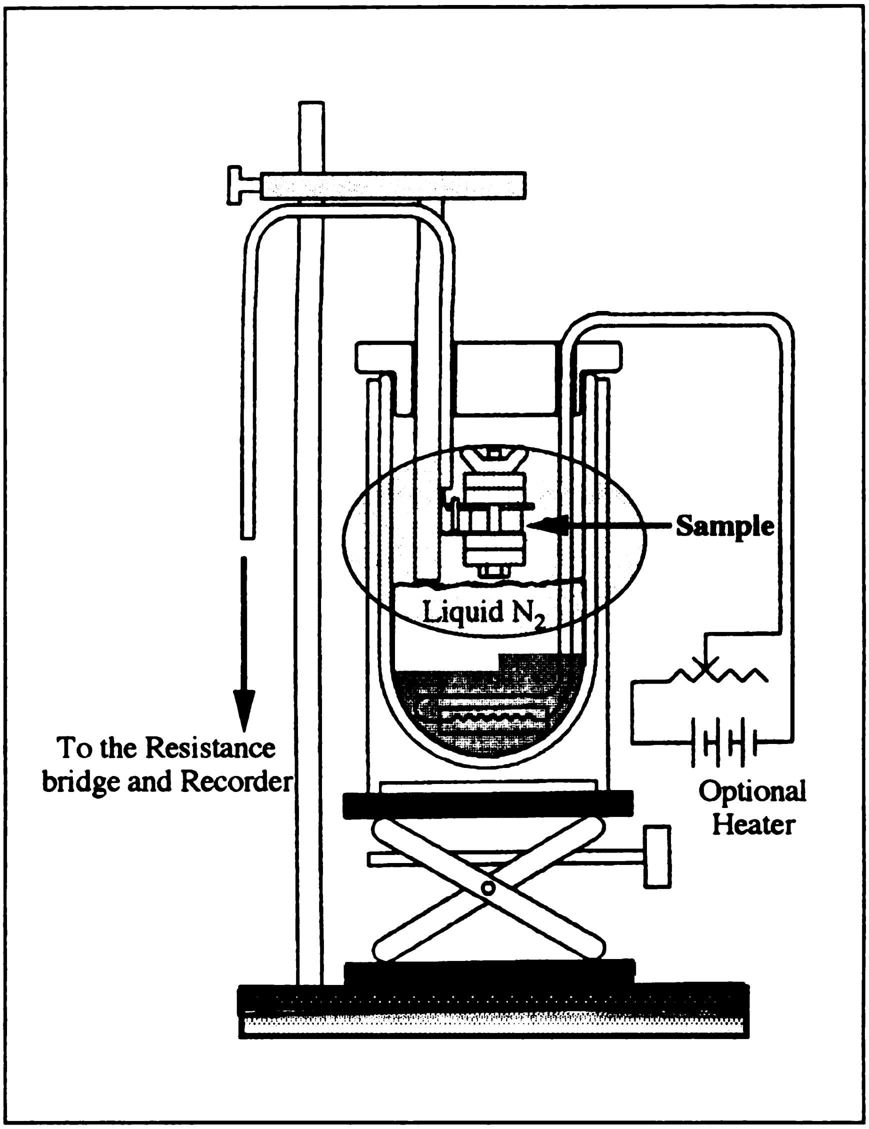

Figure 28. Cooling device for resistance-temperature measurement set-up

3.4.6 Magnetization and Magnetic Susceptibility Measurements

For the BSCCO/Ag tape, it requires much higher sensitivity for measuring electric and magnetic properties, typically a resolution in the order of μV for J_c and T_c. In these samples, magnetization and magnetic susceptibility were measured. For the magnetic moment measurement, a Quantum Design Magnetic Property Measurement System (MPMS, SQUID) was employed. The MPMS is a sophisticated analytical instrument specifically designed for the study of the magnetic properties of small experimental samples over a broad range of temperature and magnetic fields. The system hardware has two major components: (1) the MPMS dewar and probe assembly, and (2) the associated control system in the MPMS control console (Figure 29).

Automatic control and data collection were provided by a computer and two independent subsystem controllers. Most of the gas control and other ancillary functions in the system were also automated. The cryogenic probe integrates a 5.5 Tesla superconducting magnet with a SQUID detection system and a high-performance temperature control system to provide rapid precision measurements over a temperature range of 1.9 to 400 K. Liquid helium provides refrigeration for the SQUID detection system and magnet, as well as providing for operation down to 1.9 K.

The sample handling system (Figure 30) allows automatic sample measurements and position calibrations using a microstepping controller having a positioning resolution of 0.003 mm. The equipment is capable of resolving variations in magnetic moments as small as 10^{-8} emu. The measurement is made by inserting a pair of secondary coils into the sample area. Also, external to the secondary coil, is a long primary coil. The sample was inserted into the center of one of the two secondary coils. A low-frequency current was passed through the primary coils. Any change in the flux linking or Meissner effect in the sample will yield a voltage (mutual inductance) in the

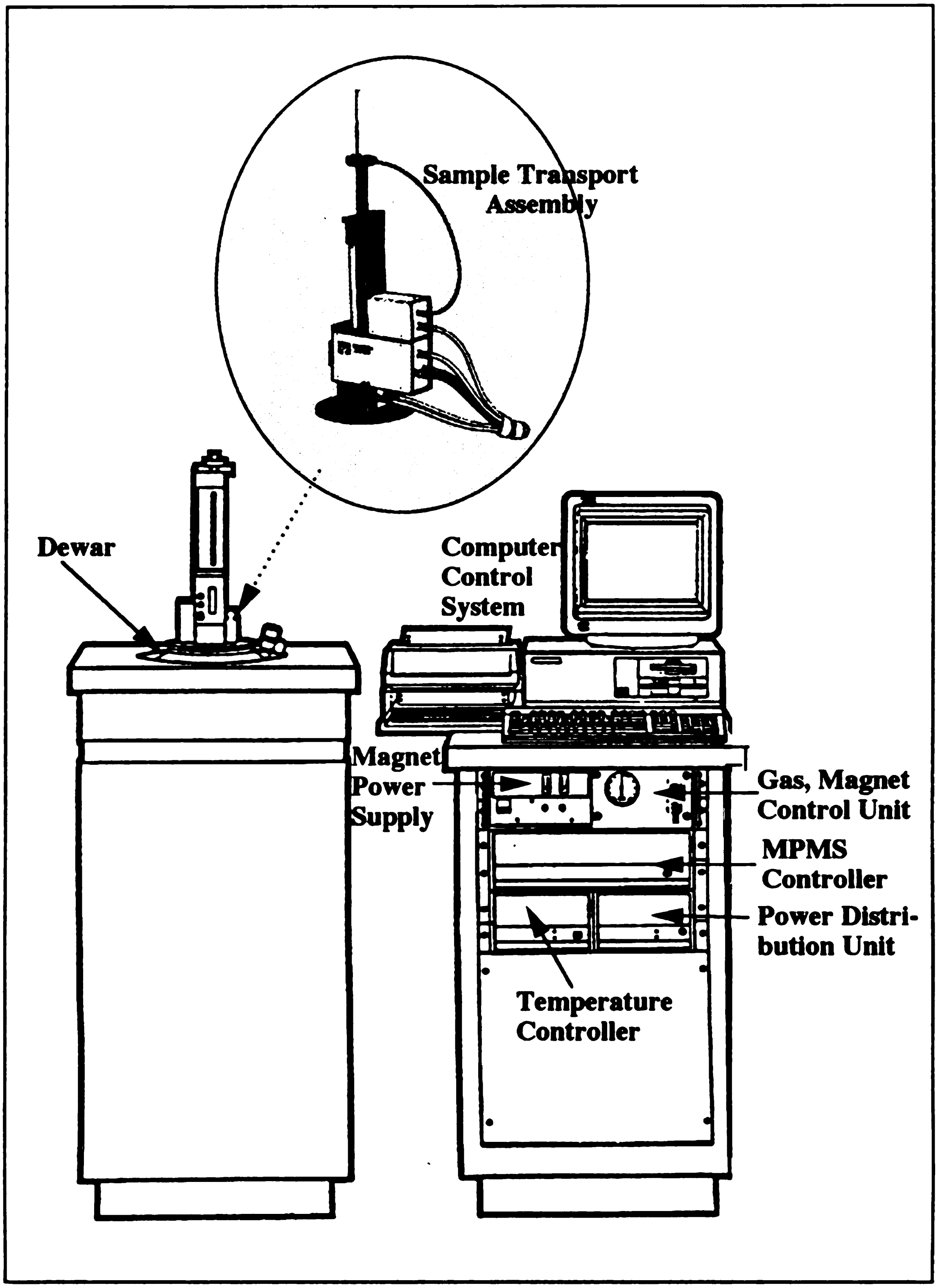

Figure 29. Schematic representation of Magnetic Property Measurement System

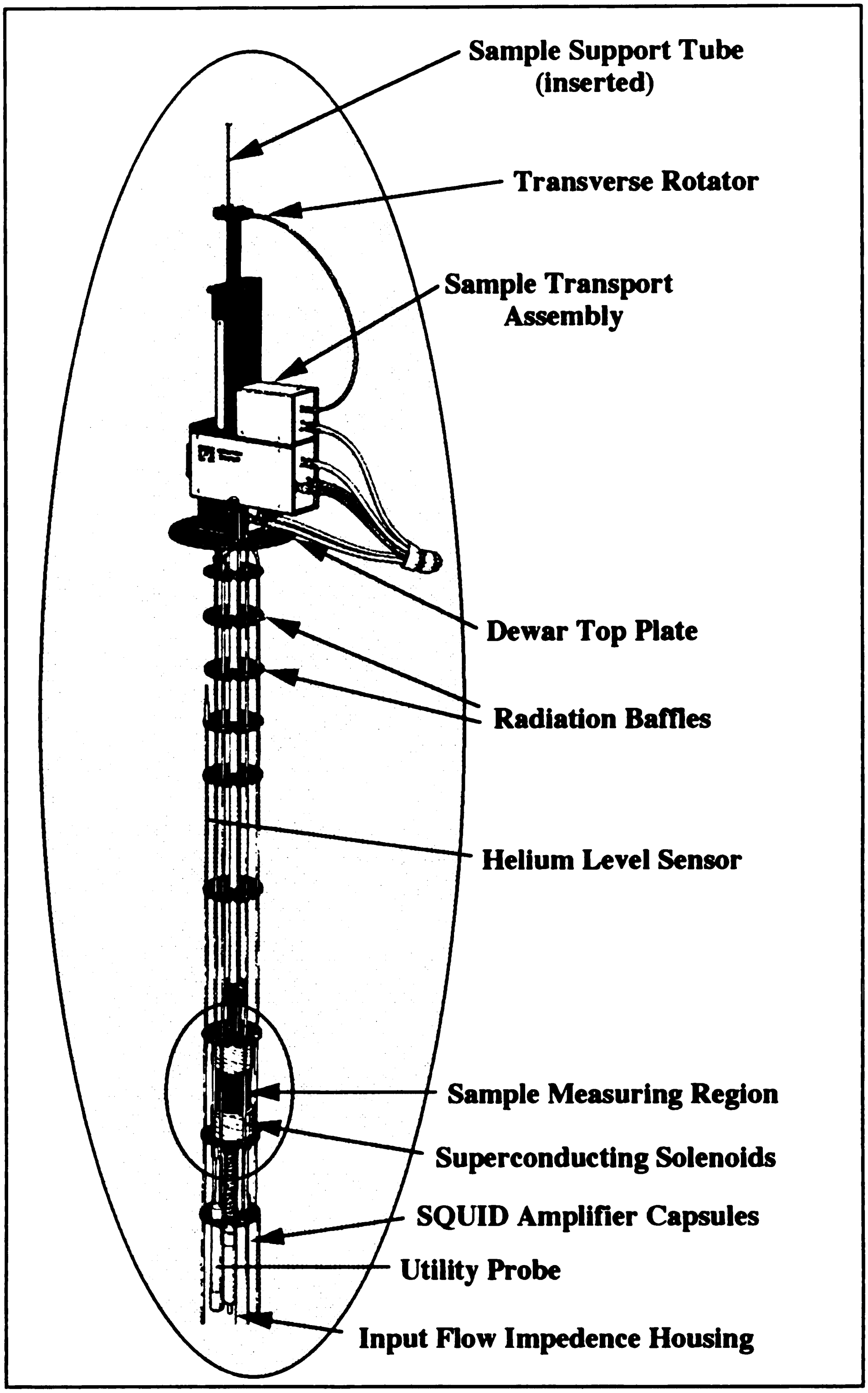

Figure 30. Sample transport assembly and SQUID probe components

secondary coils. A lock-in amplifier allows the magnetic susceptibility change to be detected.

For magnetization (EMU vs. Field) measurements, the samples were cooled down to liquid He temperature in a zero field and magnetization was measured from 5 K upon warming. The applied magnetic field used for this experiment ranged from 50,000 G to -50,000 G. The measurements were taken at various intervals, from 5 K to 100 K. For susceptibility (EMU vs. Temperature) measurements, the measurements were taken at 5K intervals, from 5 to 50 K, 3 K intervals between 50 and 80 K, and 2 K intervals from 80 to 120K. Standard deviation in this magnetic moment measurement was around 10^{-8} EMU.

4. RESULTS AND DISCUSSION

4.1 The High Density 2223 BSCCO Superconductor Prepared by Hot Isostatic Pressing

4.1.1 Observed Phases

X-ray diffraction results of Figure 31 (a)-(c) are for samples after the HIP process at various temperatures and Figure 31 (d) pertain to powder samples prepared by intermediate pressing before HIP process. The diffraction peaks corresponding to high-T_c and low-T_c phases were identified by utilizing the diffraction patterns published by Endo et.al [114]. The strong relative intensity of the (002) reflection for the (2223) phase, as shown in Figure 31 (d), results from the intermediate pressing process [109].

It is observed that peak intensities corresponding to high T_c phase are maintained and those of peaks corresponding to the low T_c phase are diminished substantially after HIP treatment at 850°C, as shown in Figure 31 (c). This suggests that HIP treated samples consist of nearly high-T_c phase. However, as HIP temperature increased to 870°C which is near the decomposition temperature of the high-T_c phase [115], the relative intensity of high-T_c peaks began to diminish and intensity of low-T_c peaks began to increase, as shown in Figure 31(a).

There is, however, no noticeable peak broadening which is often found for low temperature and high pressure synthesis [116]. This result, then suggests that crystalline imperfections are not introduced by hot isostatic pressing. A sample sintered for about 200 hours without intermediate pressing contains primarily the low-T_c(2212) phase, as shown in Figure 32(b). If such a sample is HIP processed, the resulting sample contains mostly the low-T_c phase with a small amount of (2223) phase, as shown in Figure 32(a).

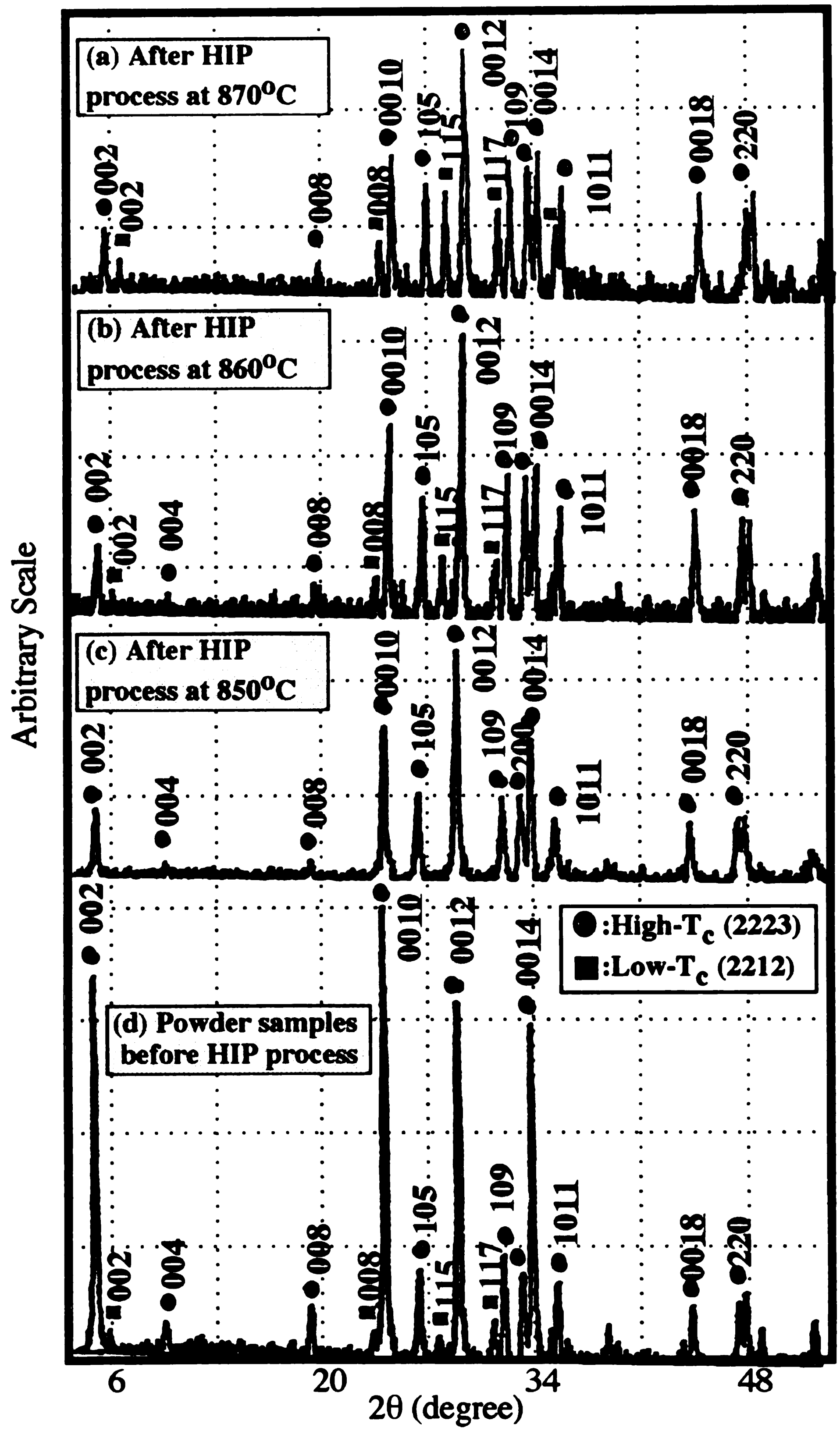

Figure 31. X-ray diffraction data for HIP process at (a) 870°C, (b) 860°C, (c) 850°C, and (d) for powder samples prepared by intermediate pressing before the HIP process

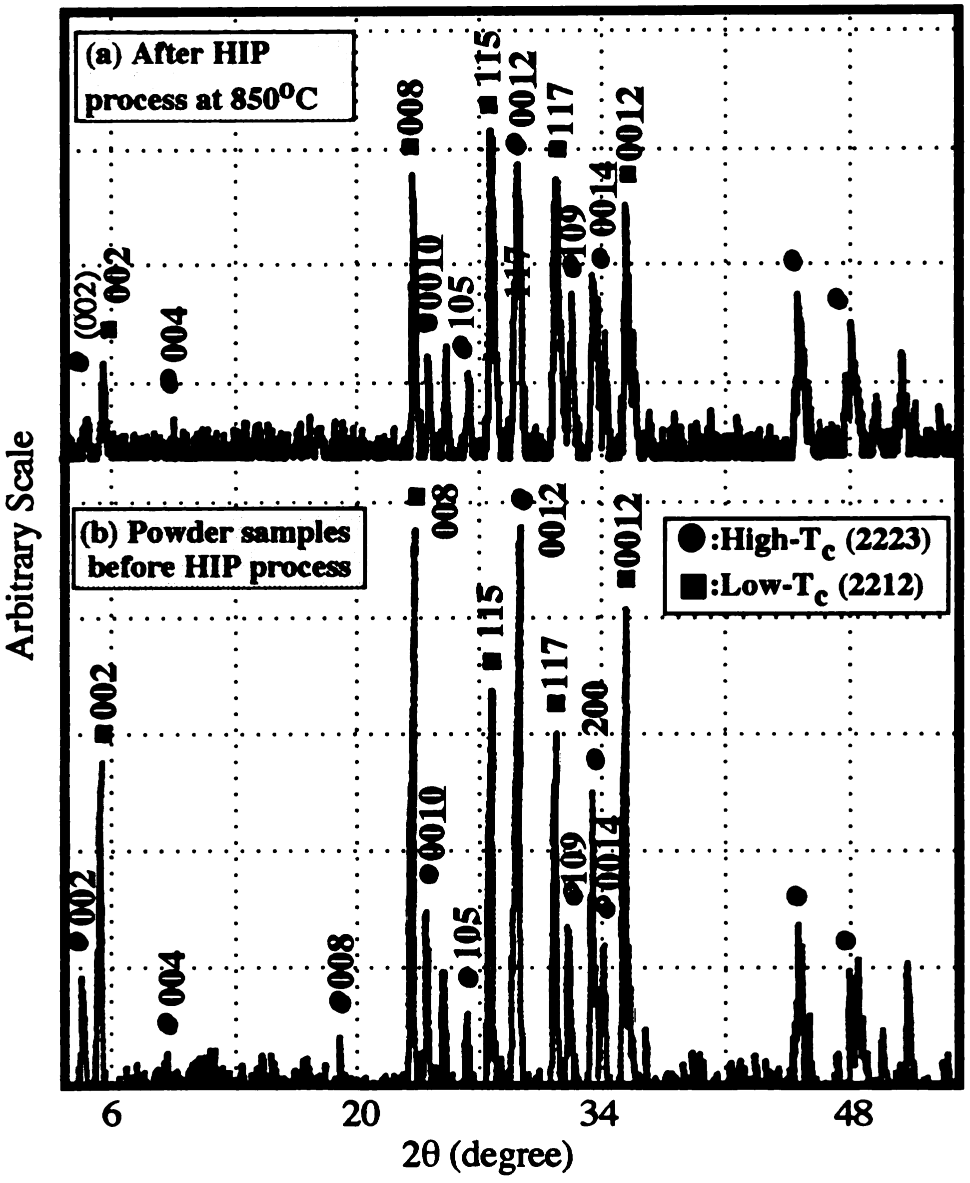

Figure 32. X-ray diffraction data (a) for HIP processing at (a) 850°C, and (b) for powder samples prepared by conventional sintering before the HIP process

4.1.2 Superconducting Properties and Density Measurement

Figure 33 shows the temperature dependence of resistivity for a sample HIP-treated at 850°C, (intermediate pressing+HIP) and the sample given conventional sintering+HIP. The resistivity for the first sample decreased monotonically with decreasing temperature and reached the zero resistivity state at 105K. Although the other sample, (Figure 33 (b)) containing a large volume percent of the low-T_c phase, exhibited a drop in the resistivity around 110K (similar to the first sample), its superconducting transition was broad and the $T_{c,zero}$ value was about 87K. From these results, it was tentatively concluded that the broad transition was related to the initial presence of a large percent of the low-T_c phase.

The densities of HIP-treated samples were measured by employing the Buoyance method(ASTM B328-73). The measured densities are 6.06 g/cm^3 for HIP at 850°C, 6.09 g/cm^3 for HIP at 860°C and 6.15 g/cm^3 for HIP at 870°C. These values are 94 %, 94.4 % and 95.3 % of the theoretical density, respectively. In contrast, specimens sintered conventionally in air had densities of 3 to 4 g/cm^3, ie., 46.5 % to 62 % of theoretical density. This significant improvement in densification is due to enhanced diffusion and/or void elimination under high pressure.

4.1.3 Microstructure of HIP-treated 2223 BSCCO Superconductor

Figure 34 (a) shows the microstructure on the fracture surface of the conventionally sintered specimen, sintered at 850°C for 3 hours. Figure 34 (b) shows the fracture surface of the sample HIP-treated at 850°C for 3 hours. The conventionally sintered specimen shows a rather porous structure which consists of plate like as well as some spherical grains. On the other hand, the fracture surface of the HIP-treated specimen shows that the grain size of the fully grown 2223 phase is much larger than

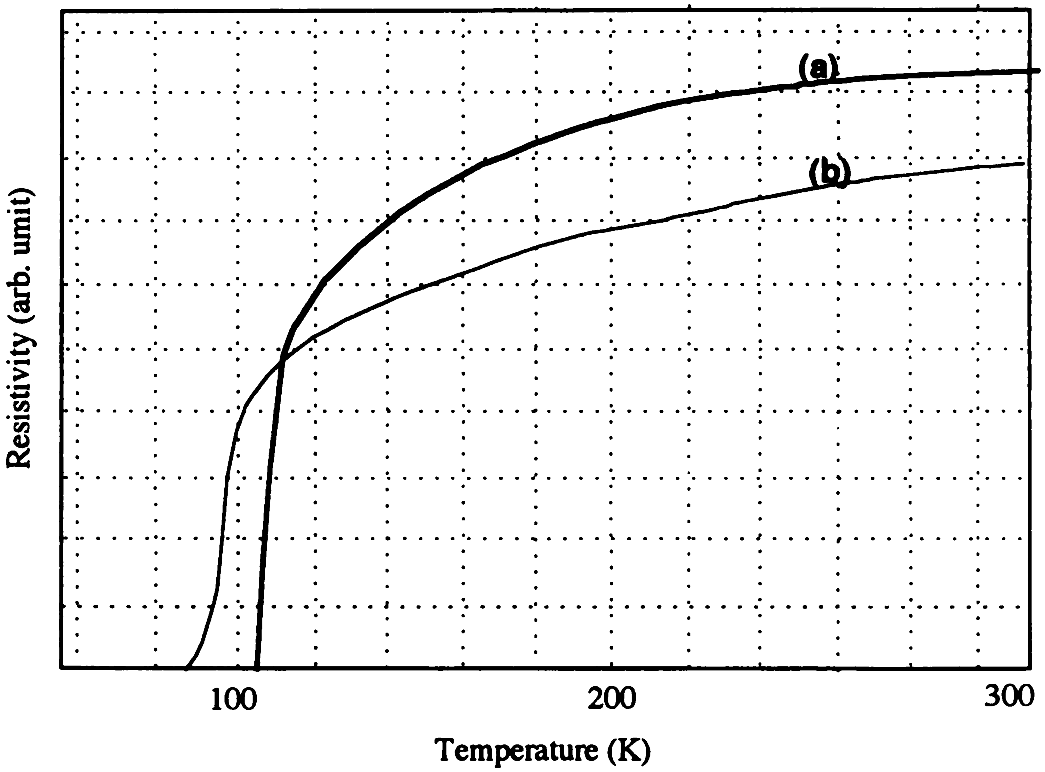

Figure 33. Temperature dependence of resistivity for Hipped sample of (a) intermediate pressing+HIP process and (b) conventional sintering+HIP process.

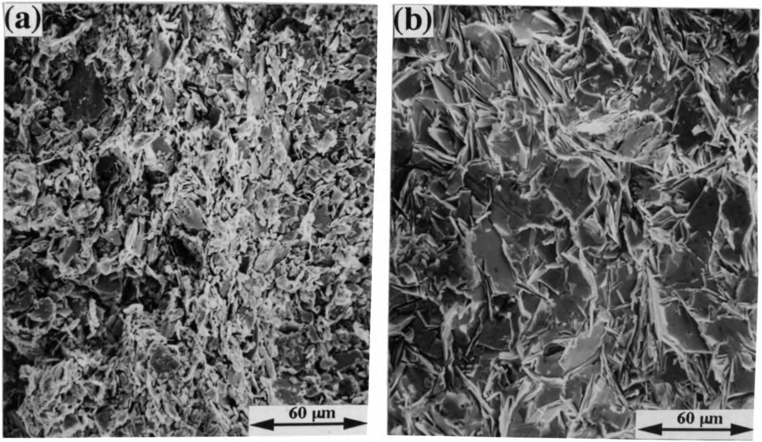

Figure 34. SEM micrograph of (a) normally sintered sample and (b) Hipped sample of 2223 BSCCO at 850°C for 3 hours.

those of the conventionally sintered samples. The microstructure also shows a dense packing of thin plate-like grains.

This remarkable growth of plate-like grains, during hot isostatic pressing is also responsible for pore elimination and densification. Improved densification related with grain growth can be explained by the enhanced diffusion due to stress gradients across boundaries which act as both sinks and sources of vacancies. Although a hydrostatic pressure is applied, shear deformation can undoubtedly occur due to the high elastic anisotropy of the crystal and due to the presence of dissimilar phases of varying elastic compliences.

Figure 35 shows the microstructure on the fracture surface of a specimen hot isostatically pressed at 870°C for 3h. It is observed that the grain size of the 2223 phase increases extensively. Some low-T_c phase particles were found in addition to particles of non superconducting phase or phases. It has been reported that the low-T_c phase starts to form as soon as the high-T_c phase begins to decompose at around 870°C [115]. The dark gray and darker phases as seen in Figure 35 (a) and (c) are identified as 2223 and (Ca,Sr) rich phases respectively. These conclusions are based on EDAX analysis. Figure 35 (a) and (b) show the compositions of the high-T_c and low-T_c phases, respectively. It is shown that the Ca and Cu contents of the low-T_c phase were lower than those in the high-T_c phase.

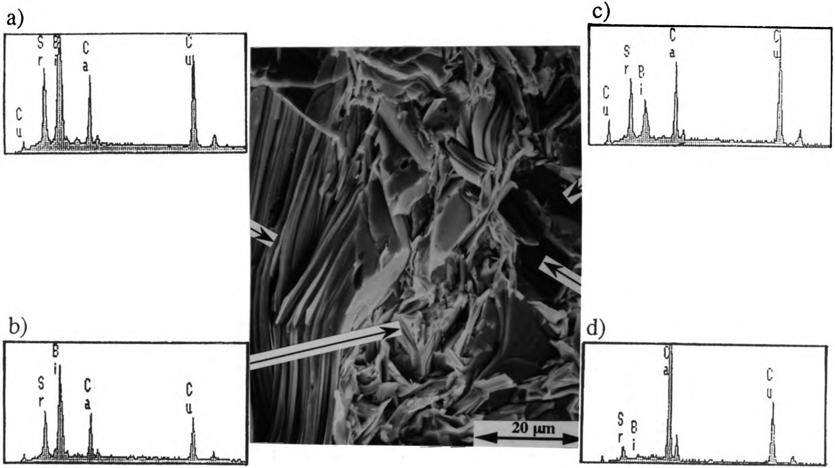

Figure 35. SEM & EDAX micrograph of 2223 BSCCO of sample HIPped at 870°C. The spectra (a) to (d) correspond to (2223) phase, (2212) phase, (Ca,Sr) rich phase, and Ca rich phase, respectively

4.2 High-T_c 2223 BSCCO/Ag Tape Fabricated by HIP-clad and Thermomechanical Deformation

4.2.1 Effect of Mechanical Deformation on the Evolution of c-axis Texture

X-ray diffraction studies of the BSCCO/Ag tape produced by OPIT (oxide powder in tube) technique [58,86] have been widely used to investigate the c-axis alignment. This technique gives a good overview of the alignment averaged over a length and breadth of a few mm and over an X-ray penetration depth of a few μm. However, one concern is that the X-ray penetration depth for Cu Kα radiation is only about few μm. This dimension is smaller than the 10~60 μm BSCCO core thickness. Thus there can be considerable ambiguity in the X-ray diffraction measurements, since the measured alignment will depend on the location of the exposed surface with respect to the Ag cladding.

Since the most common method of exposing the BSCCO layer produced by "powder in tube" method is to grind off one side of the Ag cladding, the exposed layer generally lies close to the Ag/BSCCO interface where the alignment is greatest [29]. These X-ray diffraction measurements will consequently tend to overestimate the overall c-axis grain alignment of all samples and will minimize the differences between samples.

In our experiments, however, without peeling off the silver, directly rolled surfaces were studied by X-ray diffractometry and pole figure goniometry. Even then the X-ray penetration depth problem can not be excluded. Figure 36 shows the measured X-ray diffraction data for a successively cold rolled sample as a function of cold rolling thickness reduction(%). A thickness reduction ratio R(%) was used to describe the deformation extent, as:

$$R = (t_1 - t_2)/t_1 \qquad (38)$$

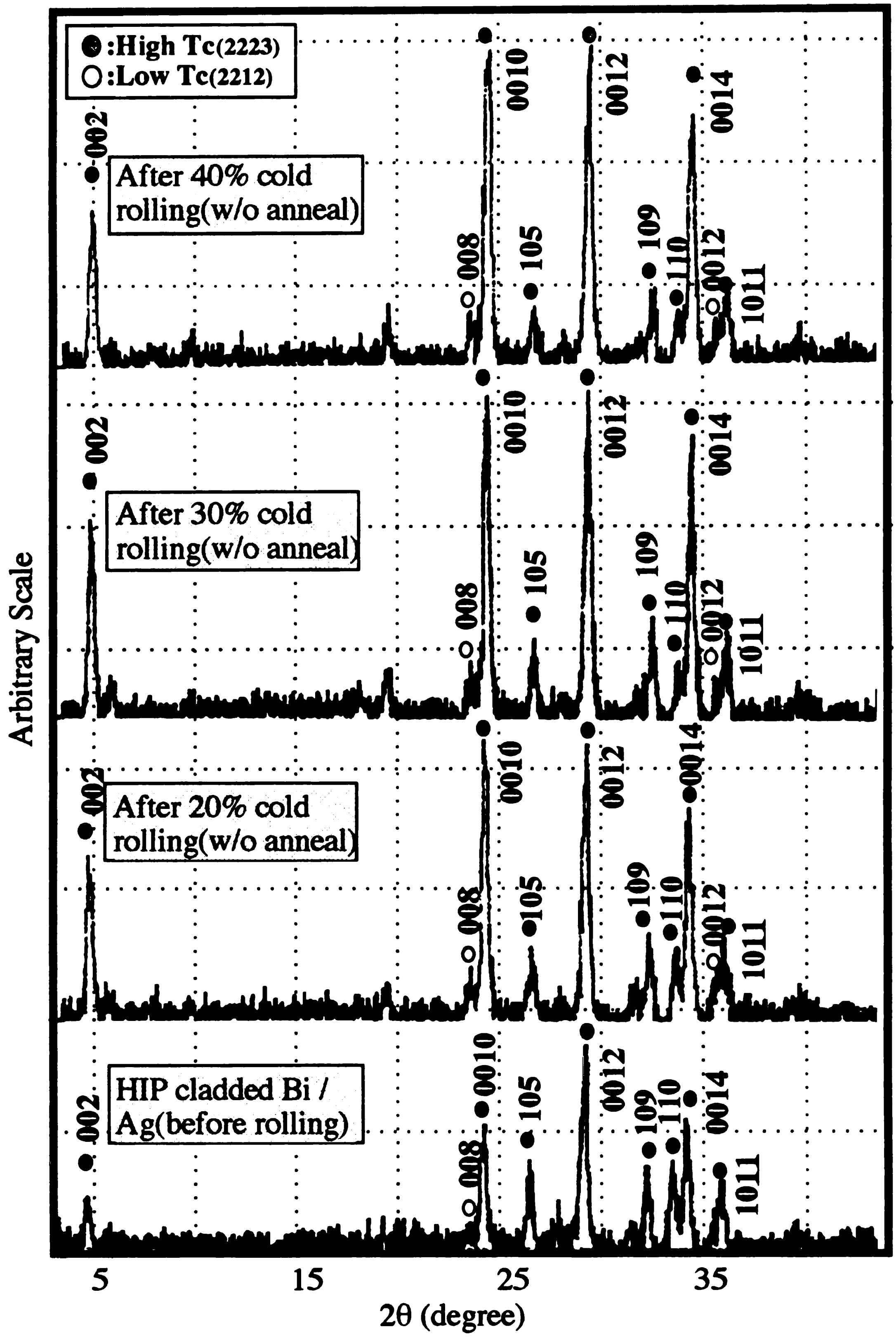

Figure 36. The measured X-ray diffraction data of a successively cold rolled sample with respect to cold rolling reduction %.

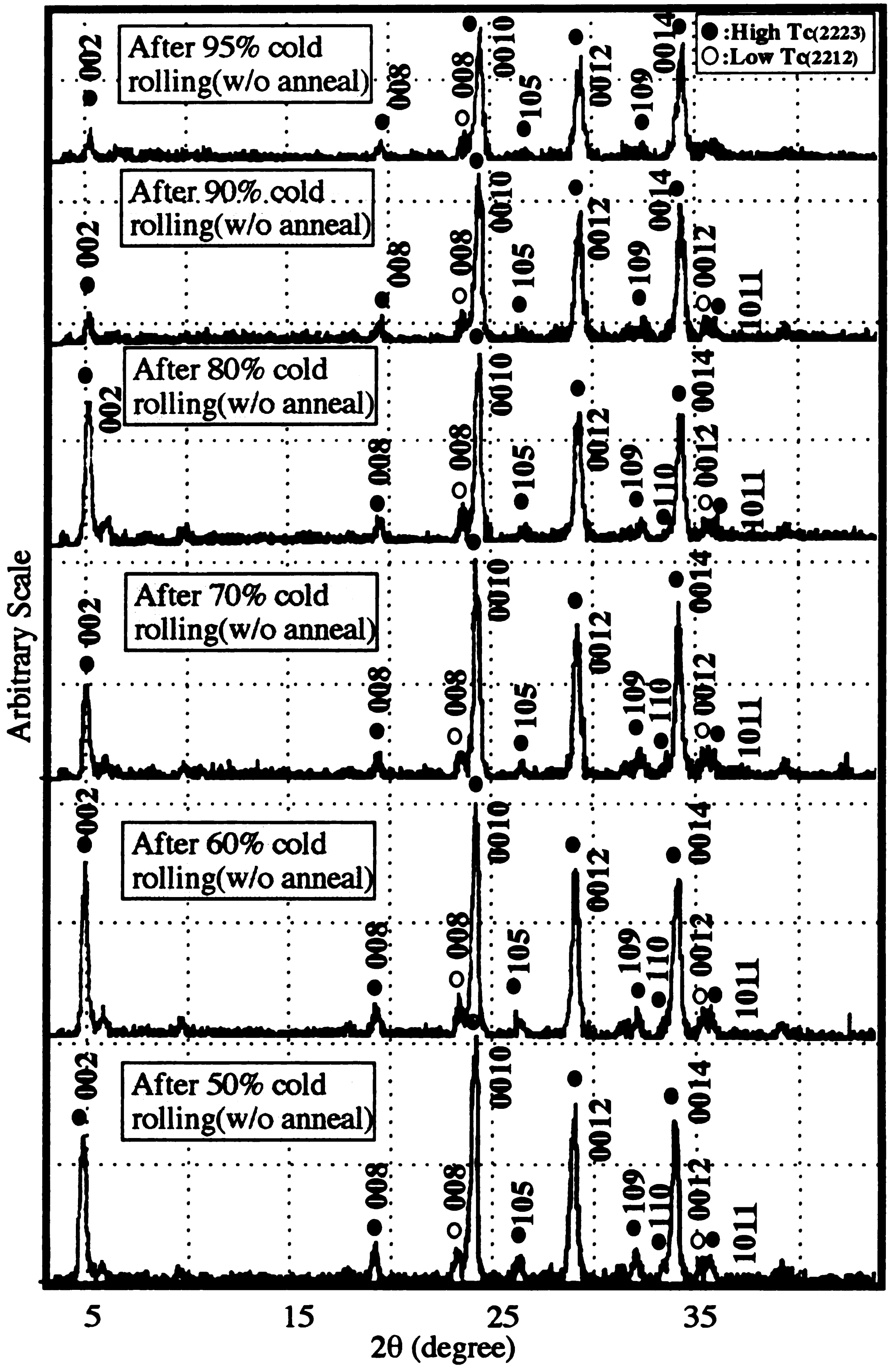

Figure 36. (continued)

where t_1 and t_2 are the thickness of the BSCCO/Ag before and after deformation. After the HIP cladding process, the surface X-ray diffraction contains numerous peaks such as (105), (109), (110), and $(10\underline{11})$ along with the $\{00l\}$ type peaks. The $(00\underline{10})$, $(00\underline{14})$ peak intensities increased while (105), (110), (109), and $(10\underline{11})$ peak intensities decreased after 20 % reduction. After 95 % reduction, the (105) peak intensity almost disappeared, and a very little trace of (109), $(10\underline{11})$ remained. There is, however, a slight peak broadening, which suggests that the particle size resulting from severe mechanical deformation is smaller, which is often found for low temperature and high pressure synthesis [116]. The comparison of X-ray data reveals that the $(00\underline{10})$ and $(00\underline{14})$ peak intensities increased with the amount of cold rolling reduction.

Lotgering introduced a simple method to quantify the degree of $\{00l\}$ texturing in polycrystalline ceramics [117]. The ratio of the intensities of the $\{00l\}$ to the (hkl) reflections increases with the increasing c-axis orientation, and this fact can be used to quantify the extent of texturing. A factor *F*, called the Lotgering factor, is defined as :

$$F = \frac{(P - P_o)}{(1 - P_o)} \quad \text{where } P = \frac{\sum_{l} I(00l)}{\sum_{hkl} I(hkl)} \qquad (39)$$

where I refers to the X-ray peak intensity. P is the ratio of the sum of integrated intensities for all $\{00l\}$ reflections to the sum of all intensities of (hkl) in the textured specimen. P_0 is an equivalent parameter for a random specimen.

In the present experiments our experimental results, from ground powders of the BSCCO 2223 phase, gave $P_0 = 0.29$. Figure 37 shows a plot of the Lotgering factor F versus deformation extent R. The four points in the plot, with rapidly increasing F, correspond to specimens after 20, 30, 40, and 50% R of cold rolling deformation. It is observed that the F factor reached 0.83 when a sample was 50 % cold rolled, increasing

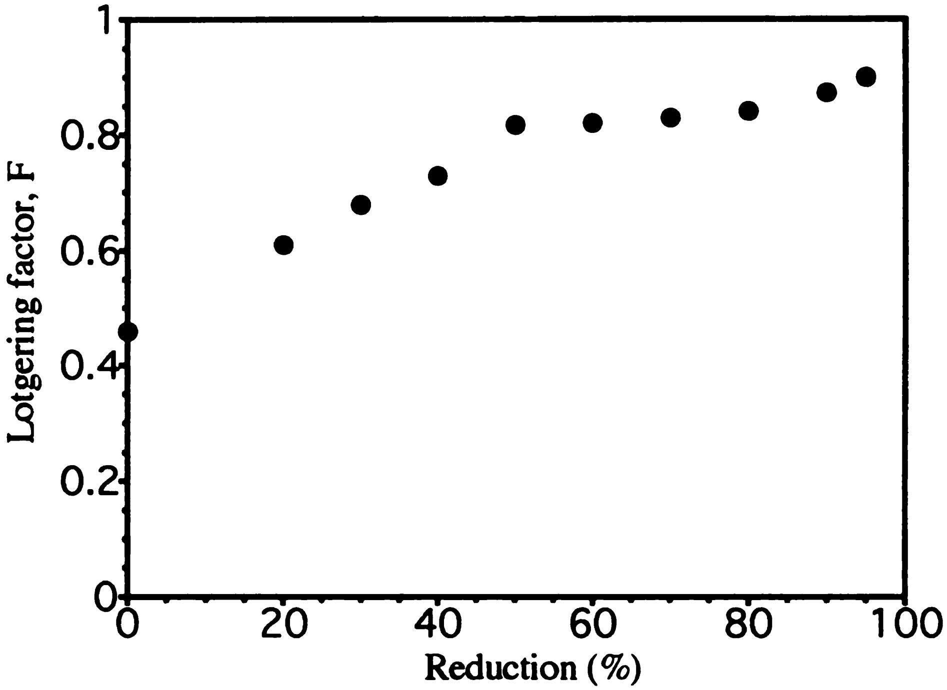

Figure 37. A plot of Lotgering factor vs. deformation extent R(%), calculated from Figure 36

from an initial F value of 0.465, and steadily increased with respect to further rolling. After 95 % reduction, the F factor was 0.901.

4.2.2 Effect of Heat Treatment on 2223 BSCCO/Ag Tape

During the superconducting tape processing, the annealing steps help to heal the fractured particles which result from cold rolling deformation. In order to study the effect of annealing temperature on the c-axis texture, cold rolled 2223 BSCCO/Ag tape was annealed at various temperatures as shown in Figure 38. It can be observed that the peak intensities corresponding to the high-T_c phase are maintained up to an annealing temperature of 850°C, and the strong {00*l*} reflections are dominant. As the annealing temperature increased to 860°C, the high-T_c 2223 phase abruptly decomposed into the low-T_c 2212 phase. Normally, the high-T_c 2223 phase is reported to decompose around 870°C [115]. This change is presumably due to the lowering of the superconductor melting point by silver [118].

In BSCCO superconductors, long term annealing or sintering enhances grain growth of the quasi-two-dimensional BSCCO grains. Grain growth is much faster in the ' a' and ' b' directions than in the ' c' direction, so the growing grains assume a plate like morphology. Actually it is beneficial to have annealing texture, if the preferentially oriented grains maintained the pre-alignment resulting from cold rolling deformation and grew larger by consuming some of the smaller misaligned grains. In contrast, it is much more difficult for misoriented grains to grow, since their growth is impeded by the more numerous preferentially oriented grains. However, long term annealing also promotes gradual decomposition of the high-T_c 2223 phase into low-T_c 2212 phase, and to non {00*l*} grain growth as shown in Figure 39.

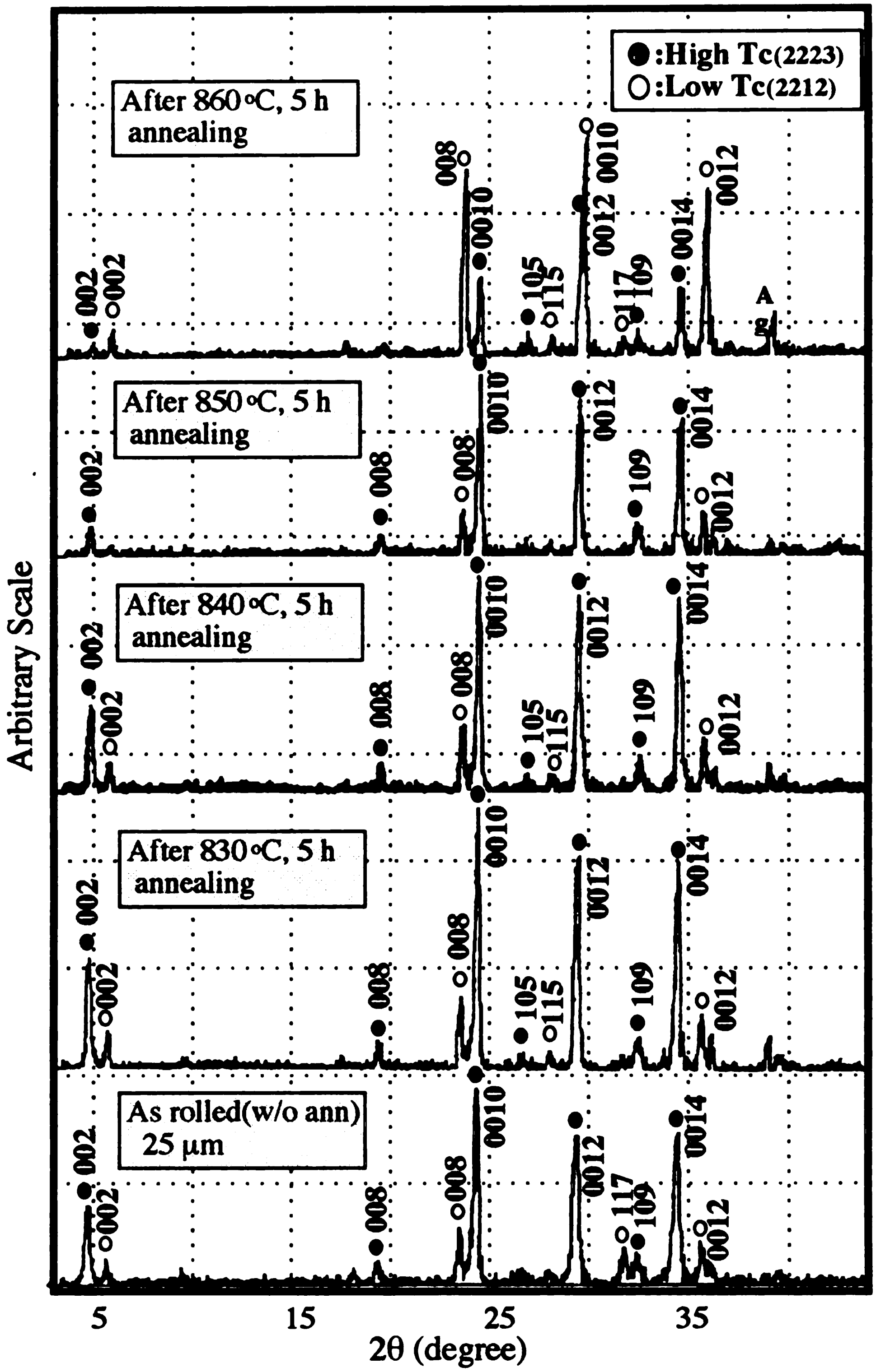

Figure 38. The comparative X-ray diffraction data for annealed BSCCO/Ag tape. The BSCCO/Ag tapes are annealed at 830°C, 840°C, 850°C, and 860 °C for 5 hours.

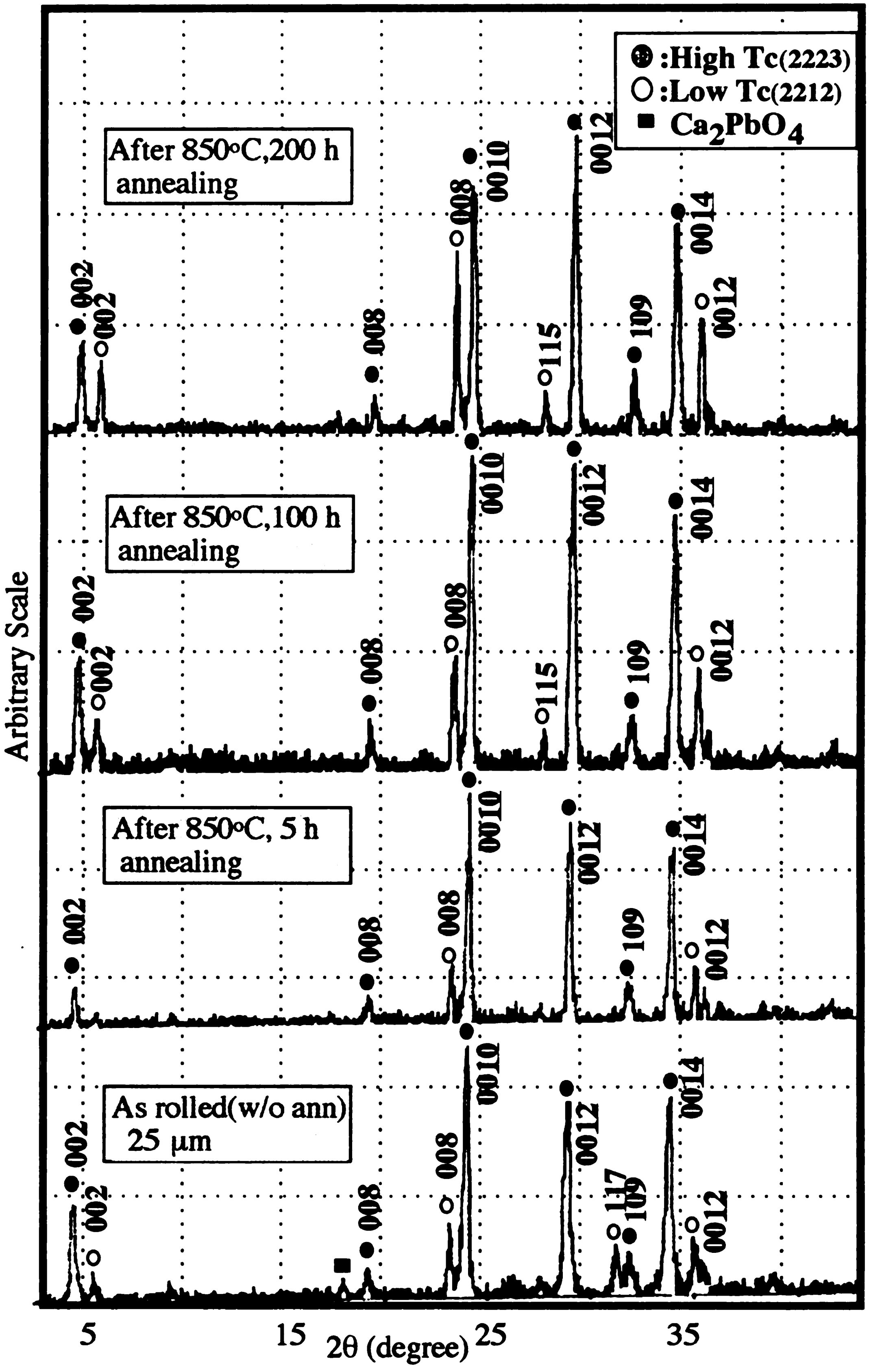

Figure 39. The comparative X-ray diffraction data for annealed BSCCO/Ag tape. The BSCCO/Ag tapes are annealed at 850°C for 5 , 100, and 200 hours.

4.2.3 Magnetic Susceptibility and Critical Current Density Measurements

For the BSCCO/Ag tape, it requires much higher sensitivity for measuring electric and magnetic properties due to the presence of Ag-clad. Since magnetization measurements usually use a much more severe voltage standard (10^{-10} V/cm) [17] than that for transport measurements, magnetization measurements are more sensitive to the flux motion. In these sample, magnetic susceptibility were measured to determine T_c.

The temperature dependence of the magnetic susceptibility for 2223 BSCCO/Ag tape with 850°C annealed condition is shown in Figure 40. As can be seen in this Figure 40, the magnetic moment is systematically changed with increasing temperature. The sample shows sharp transition and has the T_c value of 105 K.

Decomposition of high-T_c 2223 phase into low-T_c 2212 phase significantly affects the critical current density (J_c). The 2223 BSCCO/Ag tape which was annealed at 850°C had a J_c value of 4300 A/cm^2, while the 2223 BSCCO/Ag tape which was annealed at 860 °C had a J_c value of 2000 A/cm^2, as shown in Figure 41.

4.2.4 Microstructure of the Thermomechanically Processed 2223 BSCCO/Ag Tape

We investigated fracture surfaces that were produced by fracturing the tapes parallel to the rolling direction in the thin longitudinal cross section. Figure 42. compares SEM micrographs of a longitudinal section of a cold rolled sample and an annealed sample. Well aligned grains along the rolling direction are reasonably clear. The 2223 BSCCO grain is small and coarsened, which is in agreement with the results of the X-ray data after cold rolling. The fracture morphology of the annealed tape suggests a plate-like grain morphology.

As mentioned above, long term annealing can significantly enhance the annealing texture, as shown in rocking curve measurement (Figure 43). Long-term

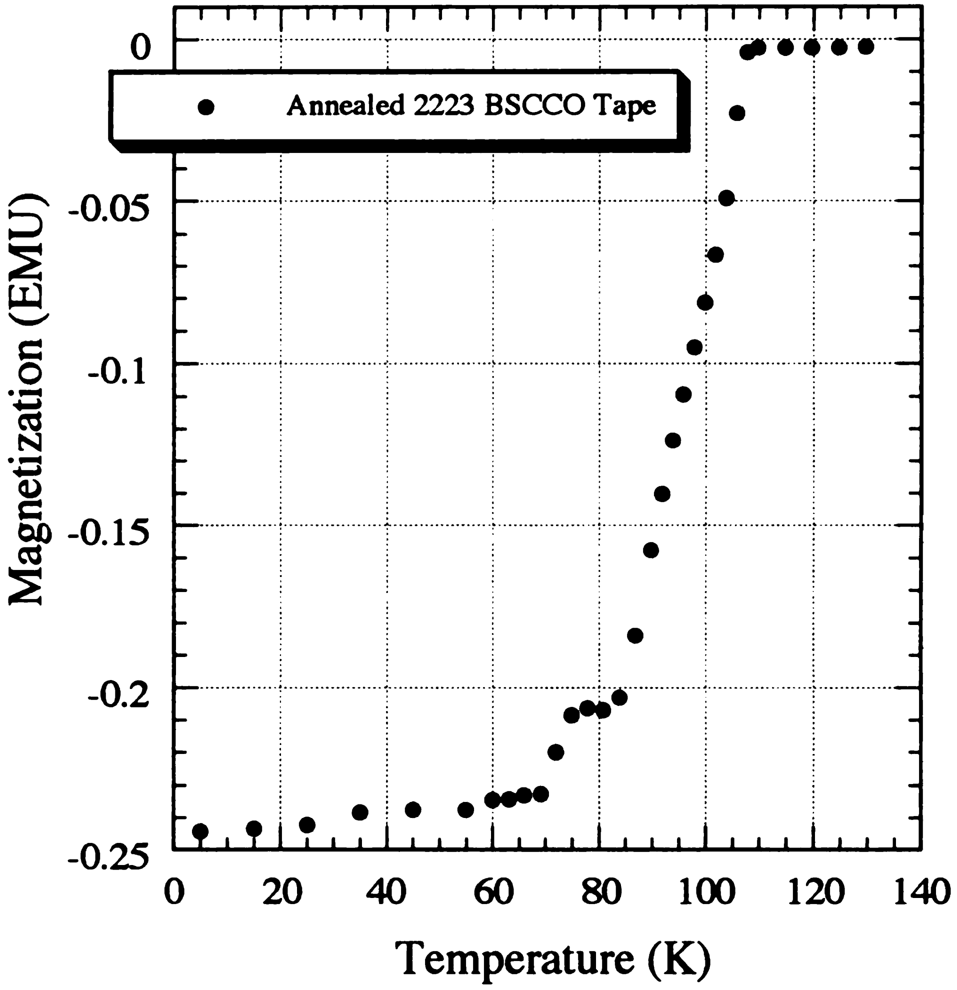

Figure 40. Susceptibility measurements (EMU vs Temp.)

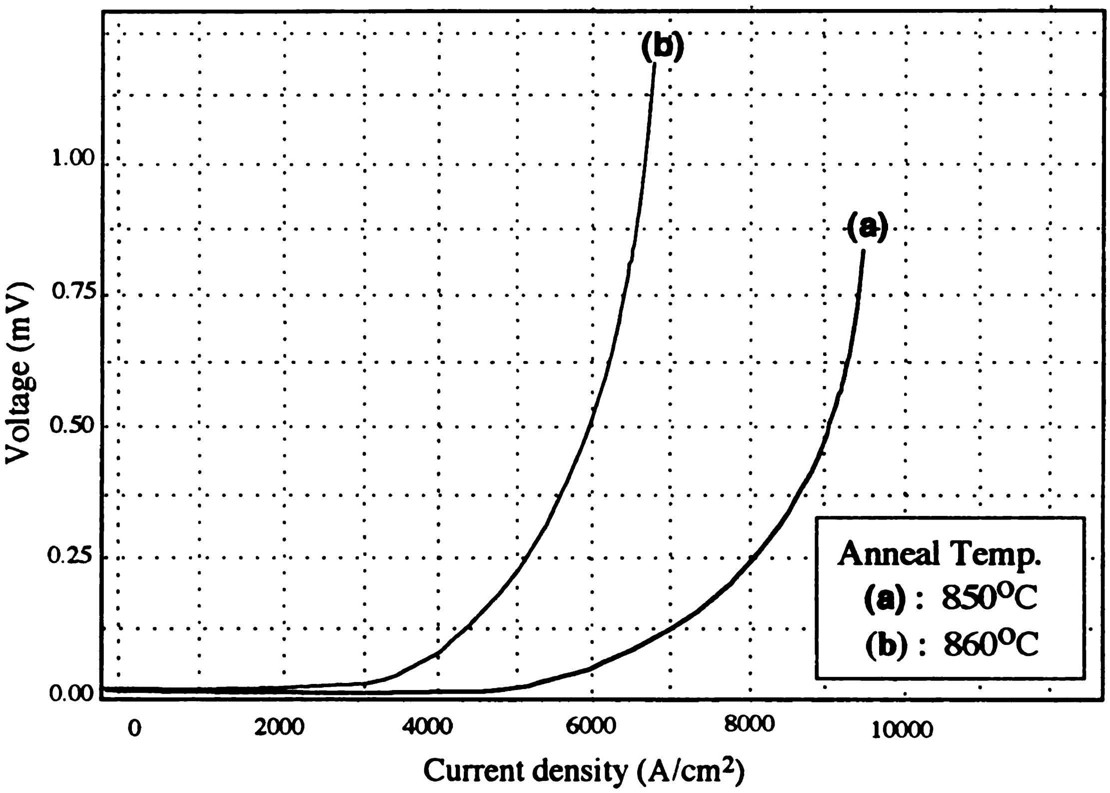

Figure 41. Critical current density measurement

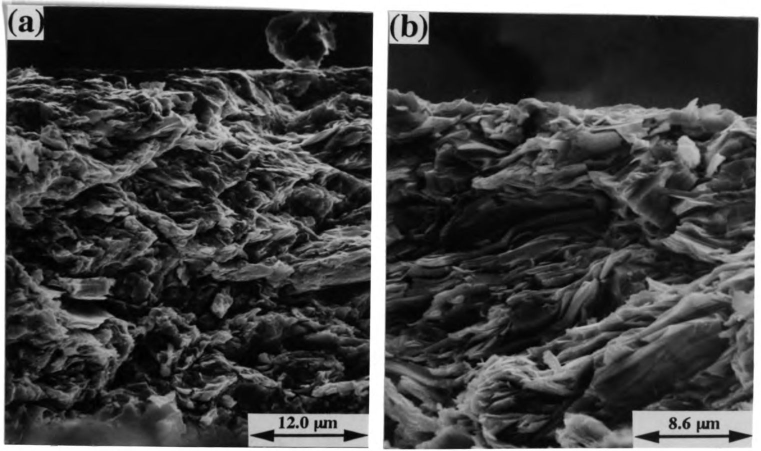

Figure 42. SEM micrographs of fractured longitudinal cross sections of 2223 BSCCO/Ag tape: a). as rolled(without annealing) and b). annealed at 850 °C for 5 hours.

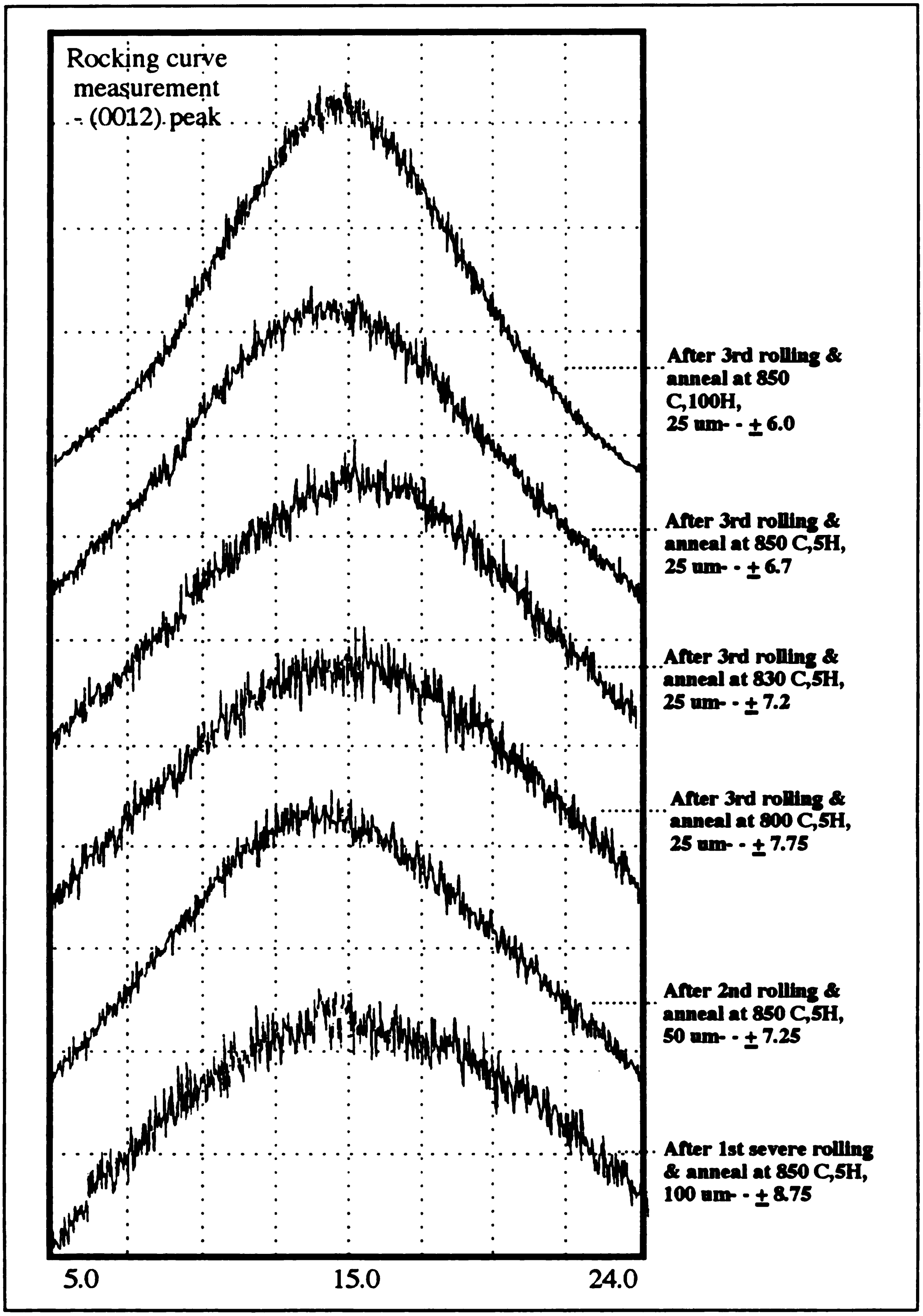

Figure 43. Comparative Rocking curve measurement for the various thermomechanical conditions of 2223 BSCCO/Ag tape

annealing also promotes low-T_c phase conversion, and a small amount of non-superconducting phase forms. SEM and EDAX data of the long-term annealed sample (Figure 44) suggest that the top surface contains nearly all 2223 phase and a very little Ag, while near the Ag interface, the (Ca, Cu) deficient phase (that is low-T_c 2212 phase) was found. Some of the darker and rounded grains are the (Ca, Cu) rich phase that was possibly produced from the decomposition of the 2223 phase. These conclusions are based on the EDAX analysis. Near the top surface, long well-aligned plate-like grains, parallel to the rolling direction, are apparent as shown in higher magnification micrographs (Figure 45).

Figure 46 compares longitudinal cross section of samples annealed for 5 hours and 100 hours at 850°C. The $\{00l\}$ grains are small and slightly tilted from ideal alignment in the 5 hour annealed sample. For the 100 hour annealed sample, in contrast, the superconductor material near the BSCCO/Ag interface appears to experience a more extensive melting. A layer-like growth (c-axis texture), which extends macroscopically from the Ag interface is observed.

The silver-sheath-induced texture formation may be related to the interaction at the interface with silver, which is known to lower the partial melting temperature of the BSCCO superconductor and may help initiate nucleation. Also recent high resolution TEM studies of the 2212 BSCCO/Ag interface suggest that (001) faceting and 2201 phase were formed at the BSCCO/Ag interface on an atomic scale, and a very strong texturing of $\{00l\}$ planes of the BSCCO parallel to the Ag was detected [98]. However, there is still the general question of why the $\{00l\}$ planes of the 2212 BSCCO phase tend to align macroscopically with the Ag interface. Additional research is required to elucidate the silver-sheath-induced annealing texture formation mechanism.

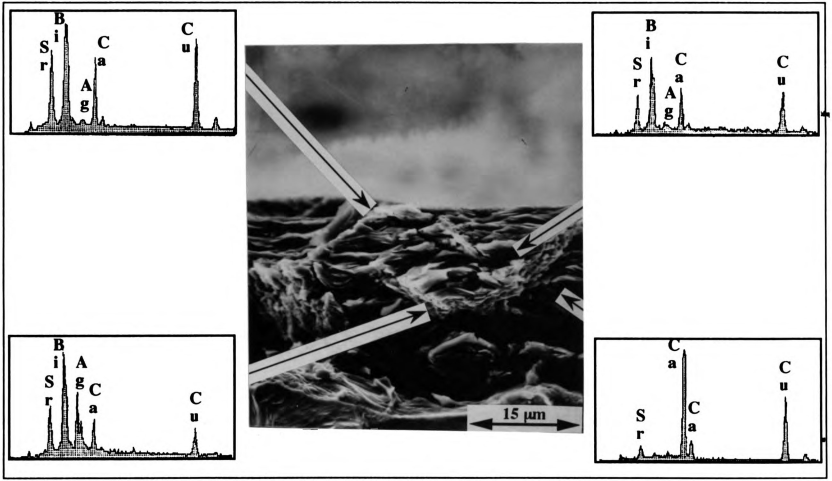

Figure 44. SEM & EDAX of fractured longitudinal cross section of BSCCO/Ag tape.
The tape was annealed at 850°C for 100 hours.

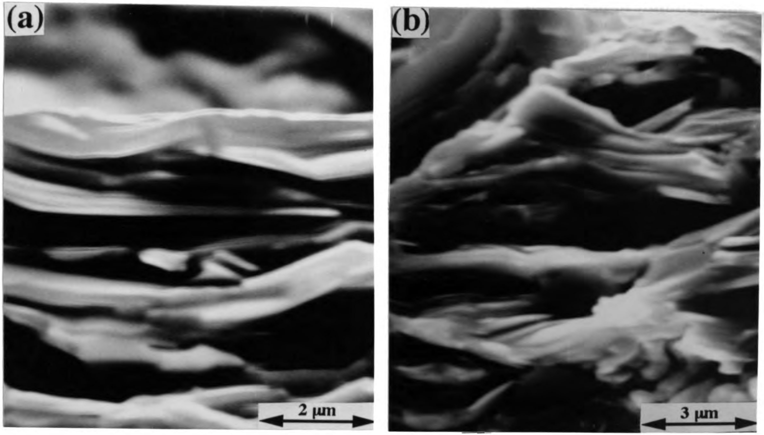

Figure 45. SEM micrographs of fractured longitudinal cross sections: a) top surface and b) ~middle layer of 2223 BSCCO/Ag tape. The tape was annealed at 850 °C for 100 hour of BSCCO/Ag tape.

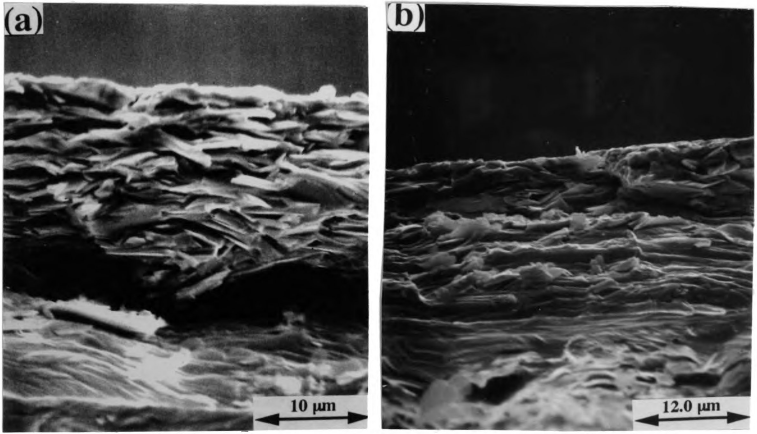

Figure 46. SEM micrographs of fractured longitudinal cross sections: a). annealed at 850 °C for 5 hour and b). annealed at 850 °C for 100 hour of BSCCO/Ag tape.

4.3 Texture Analysis of the Mechanically Deformed 2223 BSCCO/Ag Composite

4.3.1 Experimental Pole figure

X-ray $\theta - 2\theta$ diffraction studies, however, do not provide enough information about the preferential orientation, *i.e.* "texture" and the orientational perfection of the crystal with respect to a certain direction. Such properties are better determined by X-ray pole figure analysis, since the X-ray pole figure goniometers are designed to measure the diffracted intensity from a sample as it is tilted and rotated to different orientations with respect to the X-ray beam. In brief, a pole figure is a map of the statistical distribution of the crystallographic-plane-normals of a polycrystalline sample, and therefore, it provides a complete picture of the texture of the sample.

Experimental $(00\underline{14})$ pole figures were measured from the initial HIP cladded surface, and from surfaces of samples with different amounts of cold rolling as shown in Figure 47. As the amount of cold rolling reduction increased, a tighter clustering of the $(00\underline{14})$ poles indicated that randomly oriented c-axis of grains, from the initial HIP cladded surface, rotated nearly parallel to the compression direction of rolling as shown in Figure 47 (a)-(h). This evolution of c-axis texture during deformation is also confirmed by the distribution of (109) poles as shown in Figure 48 (a)-(h). At low deformation (~15-40% R), it appears that a weak fibre-like texture is beginning to appear during this stage of deformation as shown in Figure 48 (a)-(d).

The angle between the compression direction of rolling (normal direction) and the fiber is the angle between the c-axis and the (109) plane normals of the orthorhombic unit cell. The observed tilt angle of (109) fiber texture from normal direction is 45 to 50 degrees, which is in good agreement with the theoretical calculation of 47.16 degrees. From the group of (109) pole figure, it exhibited a basal texture of the $\{00l\}\langle hk0\rangle$ type that we could distinguish as orientations of the $(001)\langle 010\rangle$, $(001)\langle 110\rangle$, and

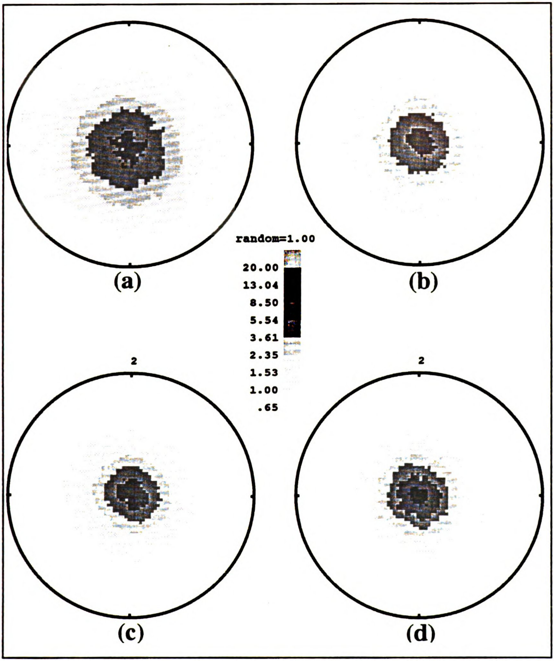

Figure 47. Measured (0014) pole figures from successively cold rolled sample. a). HIP cladded sample, b). 15%, c). 30%, d). 40%, e). 50%, f). 70%, g). 90%, and h). 98% cold rolled sample.

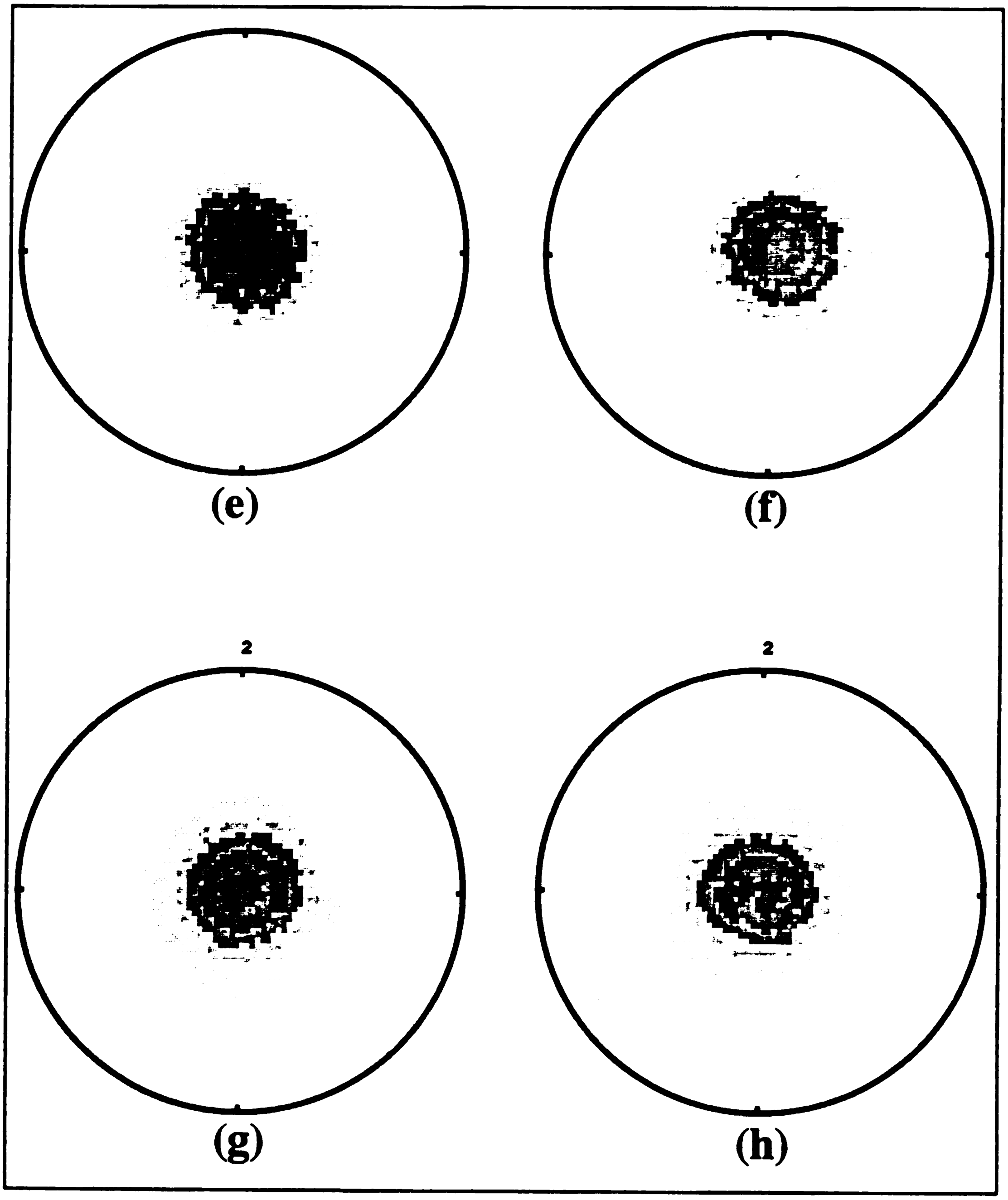

Figure 47. (continued)

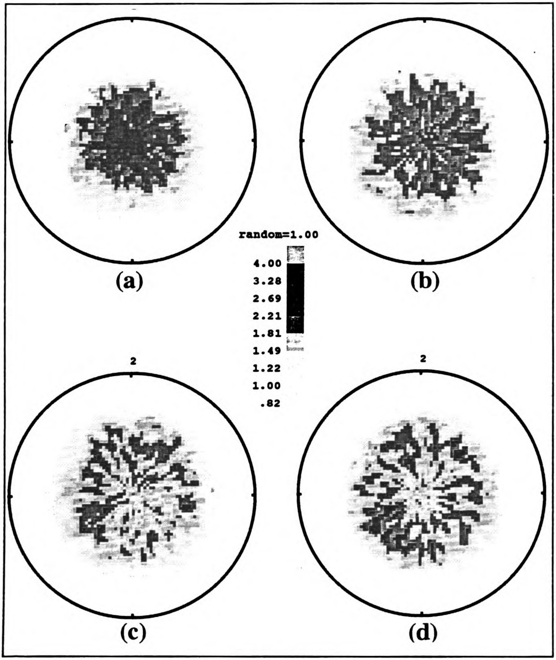

Figure 48. Measured (109) pole figures from successively cold rolled sample. a). HIP cladded sample, b). 15%, c). 30%, d). 40%, e). 50%, f). 70%, g). 90%, and h). 98% cold rolled sample.

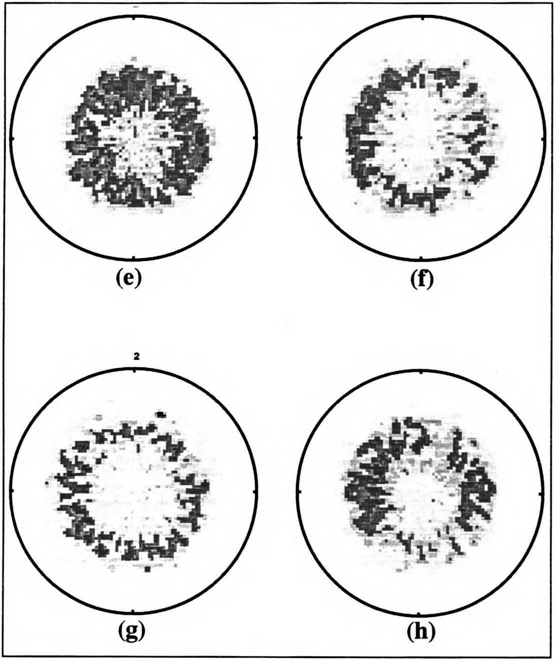

(e) (f)

(g) (h)

Figure 48. (continued)

(001)<210> types. The group of experimental (00<u>14</u>) and (109) pole figures show that under deformation, the c-plane normals rotate toward the compression direction of rolling and the (109) plane normals tend to form a fibre texture around the compression direction (normal direction), as shown in Figure 49.

After achieving a certain degree of texturing (at ~50% R), saturation of the evolution of deformation texture was observed with respect to further deformation. This can be explained by the fact that a number of non-{001} oriented crystals, responsible for accommodating deformation, rotate toward {001} orientations that do not support continued deformation. For a higher deformation (~98% R), some of the c-plane normals continue to rotate, but with a spread of these normals toward the constrained direction (transverse direction). The spread of the c-plane normals is also indicated in the distribution of the (109) pole (Figure 48 (h)). The strong fibre-like distribution of the (109) poles that was observed at ~70% R is degraded with increasing deformation (~98% R).

4.3.2 c-axis-oriented Grains: [001] Projection

From the experimental (105), (109), (00<u>14</u>) pole figures, using the popLA software package [111], which employs harmonic analysis and WIMV (Williams-Imhoff-Matties-Vinell) method, the sample orientation distribution (SOD) and the inverse pole figure were computed. The evolution of {00*l*} texture under low deformation ($\leq$ 50% R) is clearly shown in the series of SOD data (Figure 50-53). The sample orientation distribution (Figure 54) for short term (5 hours) annealed sample shows a strong c-axis texture, with the c-axes aligned within 20° tilt range, perpendicular to the plane of the tape and no preferred alignment of the ' a' and ' b' axes. This result shows a good agreement with the microstructure observations for identical sample conditions, previously shown in Figure 46 (a).

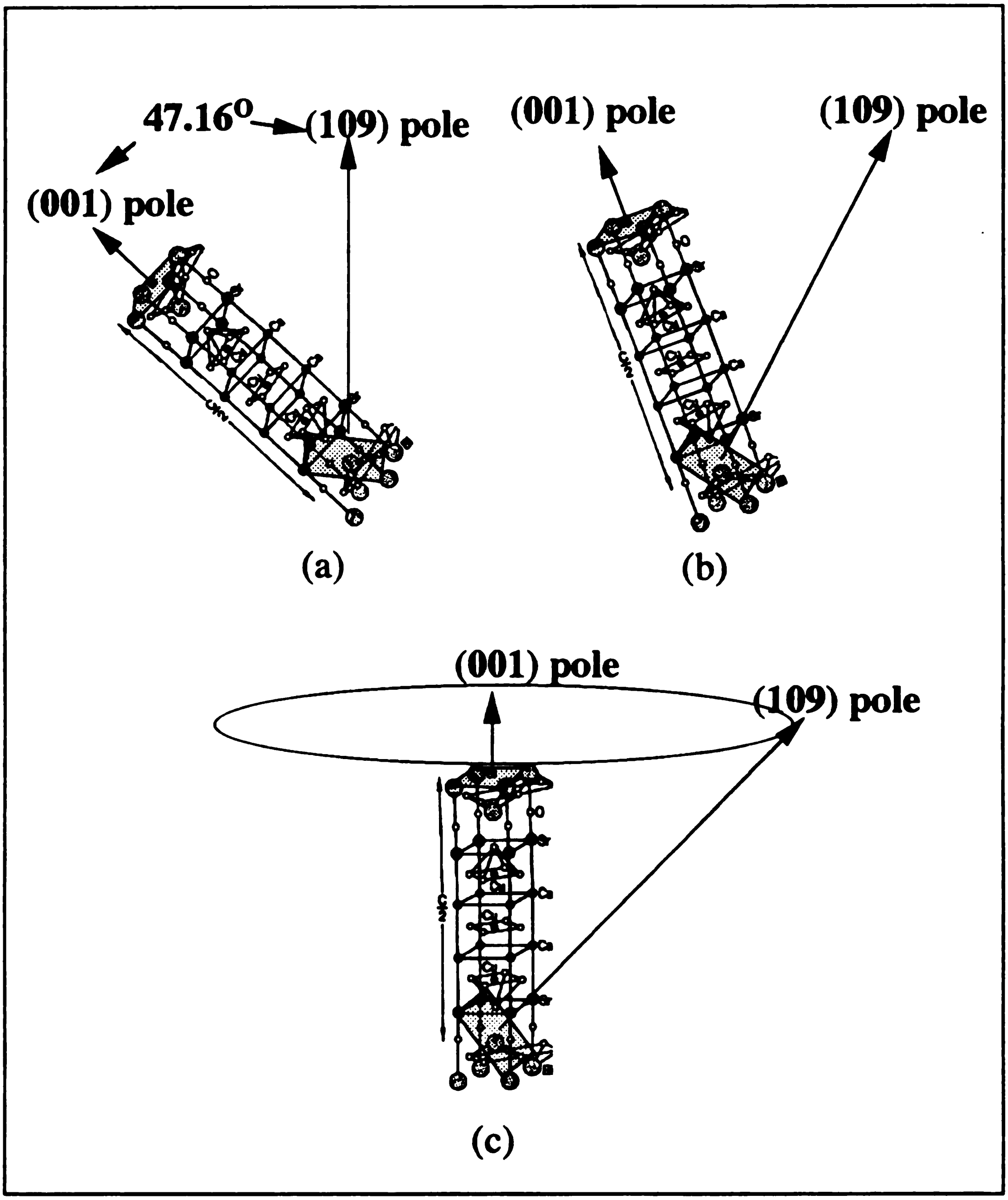

Figure 49. Schematic illustration of the rotation of (109) pole, finally forming fibre texture around the compression direction of rolling

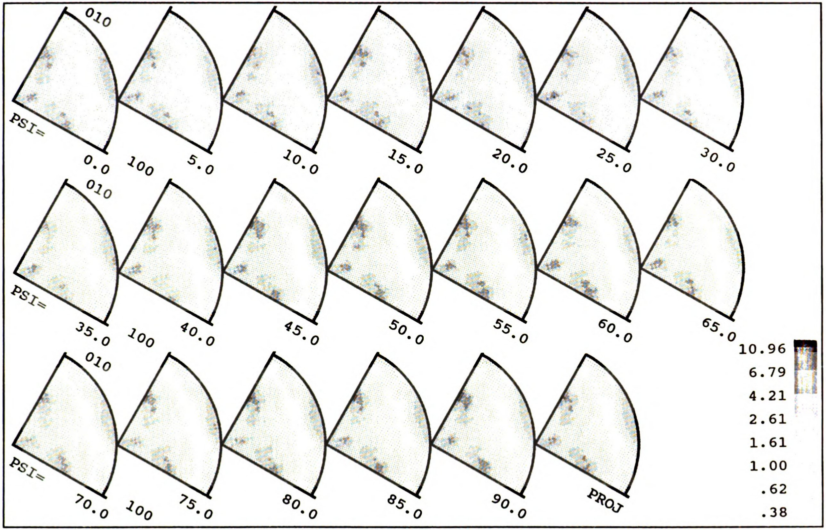

Figure 50. Orientation Distribution calculated from pole figures of a HIP cladded sample. The last quadrant (PROJ) is the mean of the sections and shows the inverse pole figure for the sample.

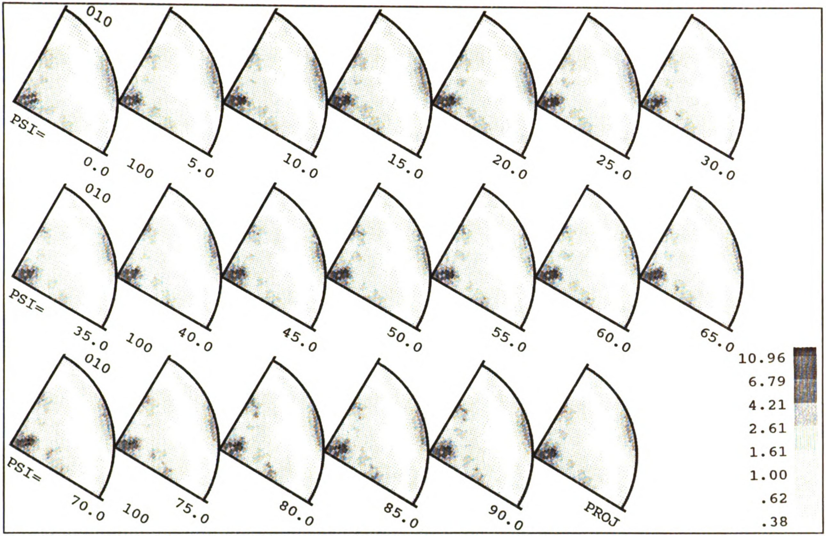

Figure 52. Orientation Distribution calculated from pole figures of a 30% cold rolled sample. The last quadrant (PROJ) is the mean of the sections and shows the inverse pole figure for the sample.

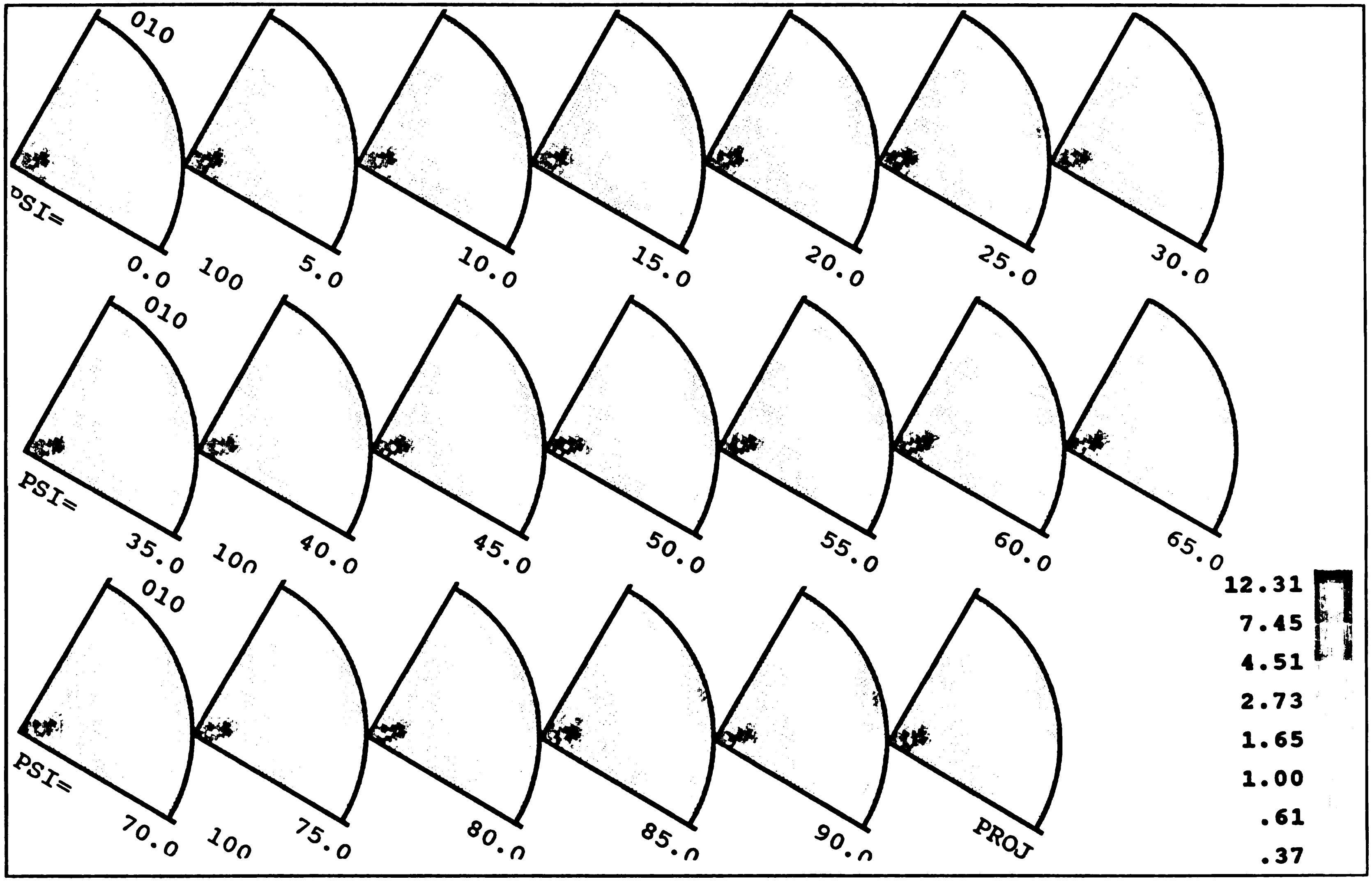

Figure 53. Orientation Distribution calculated from pole figures of a 50% cold rolled sample. The last quadrant (PROJ) is the mean of the sections and shows the inverse pole figure for the sample.

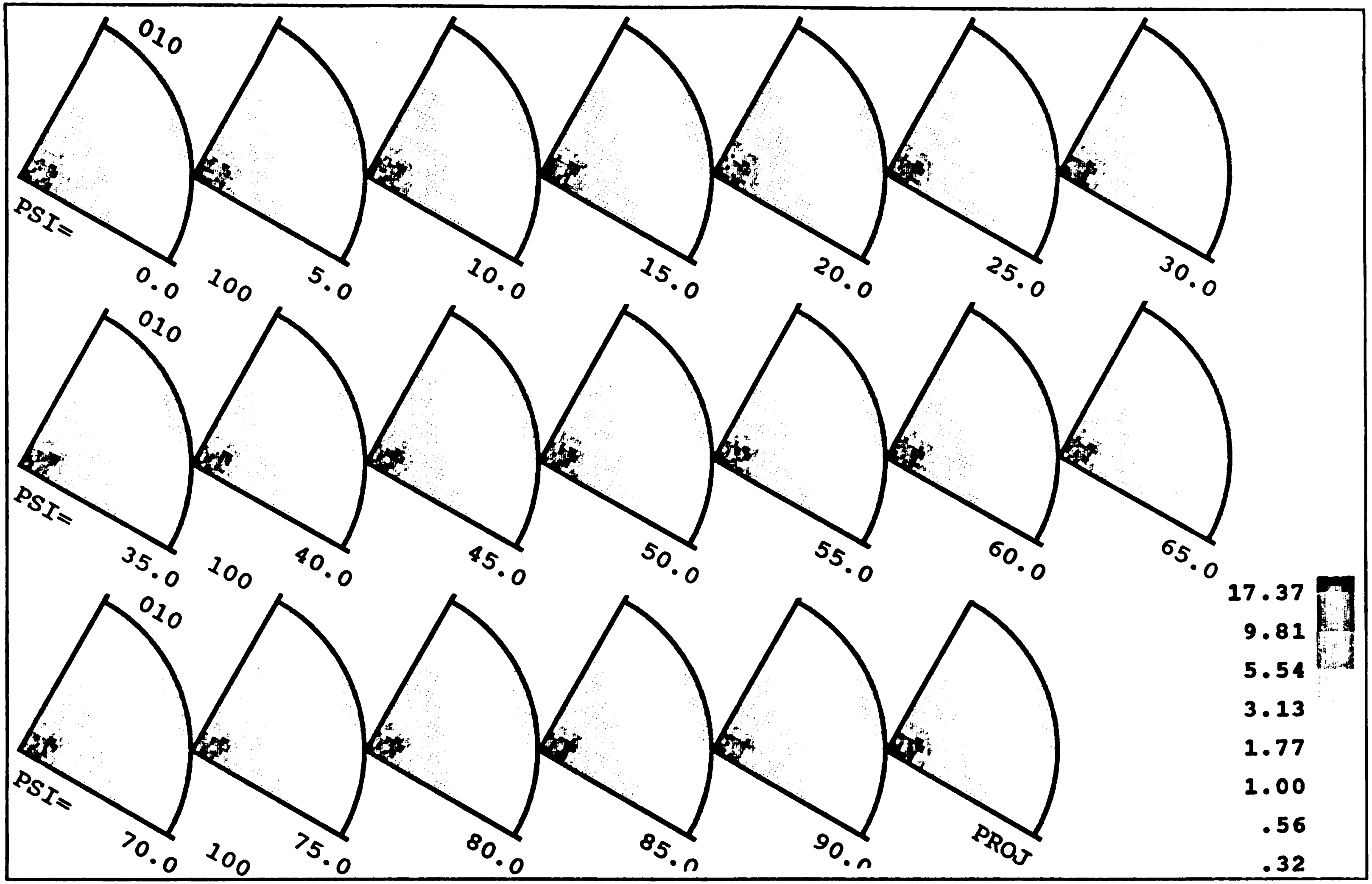

Figure 54. Orientation Distribution calculated from pole figures of a sample annealed at 850°C for 5 hour. The last quadrant (PROJ) is the mean of the sections and shows the inverse pole figure for the sample.

The standard (001) stereographic projection for 2223 BSCCO (Figure 55) was constructed with the information given in Table 2, which shows the theoretical calculation of stereographic projection angles for the 2223 BSCCO superconductor. Inverse pole figure data (Figure 56) reveals that: i) scattered {00*l*} plane normals are oriented nearly perpendicular to the plane of the tape, ii) (019), (109), (015), and (105) grains could rotate towards the compression direction of rolling (normal direction) that is parallel to the c-axis, iii) after achieving a certain degree of texturing (at ~50% R), the saturation of deformation texture was also observed with respect to further deformation.

Plots are shown in Figure 57 of the distribution of the {00*l*} plane normals with respect to the compression direction of rolling, calculated from the inverse pole figure. The angle between the {00*l*} plane normal and the compression direction decreases with increasing deformation extent R(%). The {00*l*} plane normals rotate towards the compression direction under increasing deformation extent R(%).

At ~50% R, most of the c-axes become nearly parallel to the compression direction with a negligible spread in other directions. However, as the amount of non-{00*l*} grains, such as (109), (105), (112), and (110) that are responsible for accommodating deformation, is decreased, an increase in orientation density of {00*l*} plane normal becomes restricted and saturated with respect to further deformation. This result is in good agreement with the result of F-factor calculations and the measurement of (00$\underline{14}$), and (109) experimental pole figures.

4.3.3 Textural Hardening

For the BSCCO superconductor, the possible slip system is of a basal plane type; allowing easy cleavage along the (001) plane due to the weak structural bonding between two adjacent Bi-O planes [7,35]. However, a deformation along lateral plane (a- and b-planes), which may be attributed to sliding following fracture, is also possible.

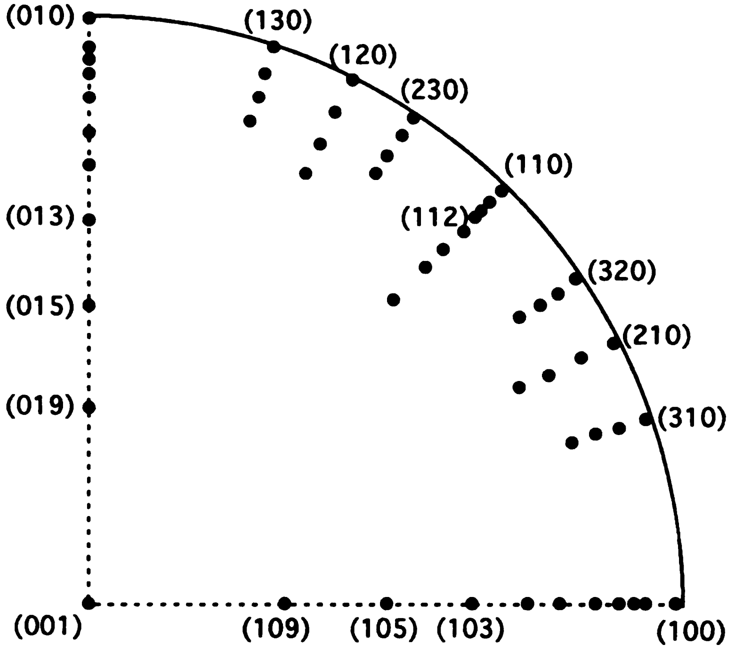

Figure 55. Calculated [001]stereographic projection of the 2223 BSCCO phase

Table 2. The calculated d-spacing value and stereographic projection angles of the Bi(Pb)SrCaCuO 2223 phase.(The latitudinal angles *Φ* [001], *Φ* [010], and *Φ* [100] are designated as those for the [001], [010], and [100] projections. a = 3.818, b = 3.825, c = 37.070 Å)

hkl	d-spacing	*Φ* [001]	*Φ* [010]	*Φ* [100]	*hkl*	d-spacing	*Φ* [001]	*Φ* [010]	*Φ* [100]
002	18.53		90	90	017	3.10	54.16	35.84	90
004	9.27		90	90	107	3.10	54.21	90	35.79
006	6.18		90	90	0012	3.09		90	90
008	4.63		90	90	019	2.80	47.09	42.89	90
0010	3.71		90	90	109	2.80	47.16	90	42.83
013	3.65	72.78	17.22	90	110	2.70	90	45.07	44.93
103	3.64	72.82	90	17.17	112	2.67	81.69	45.67	45.52
015	3.39	62.68	27.31	90	0014	2.65		90	90
105	3.39	62.74	90	27.25					

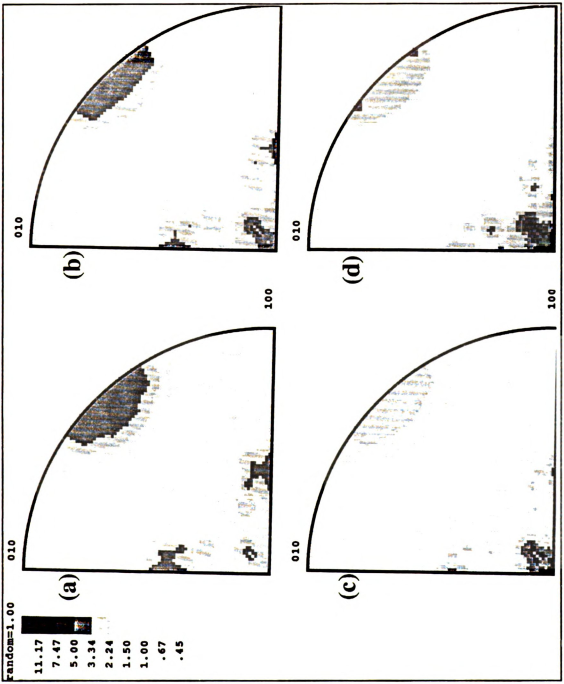

Figure 56. Inverse pole figures for the normal direction calculated from the SOD of the samples after a). HIP cladded sample, b). 15%, c). 30%, d). 40%, e). 50%, f). 70%, g). 90%, and h). 98% cold rolled sample.

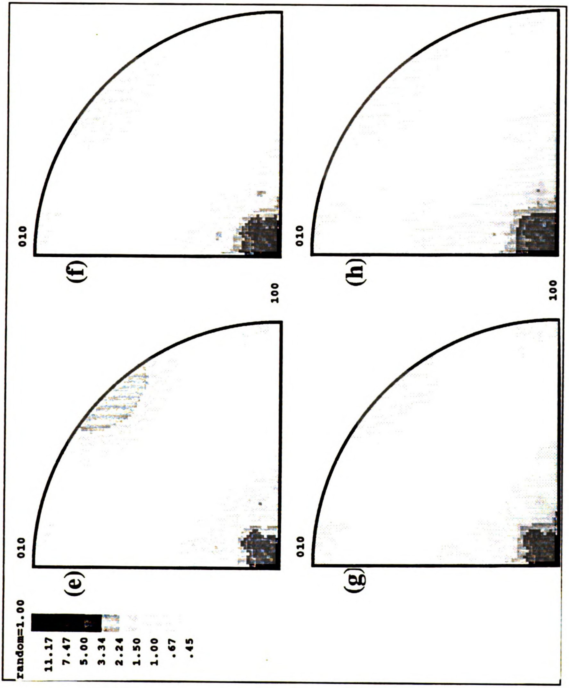

Figure 56. (continued)

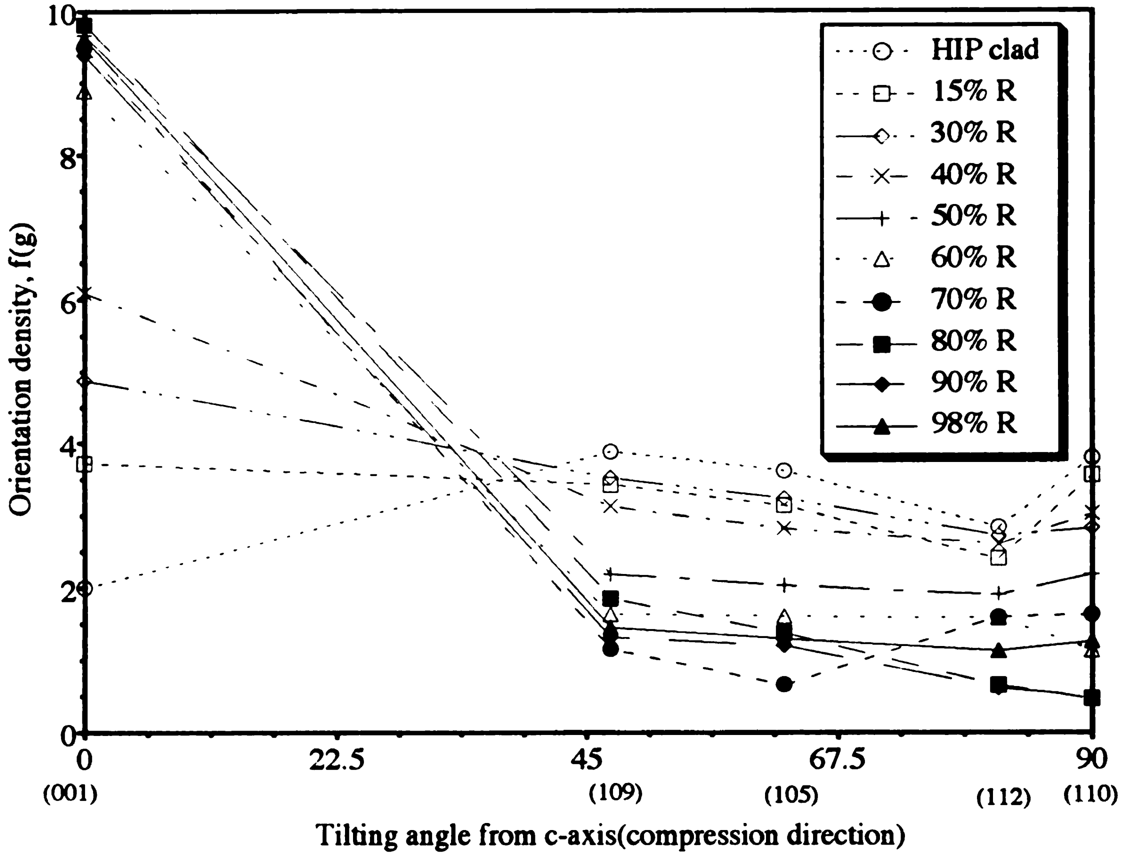

Figure 57. Plots for orientation density f(g) vs. tilting angle from compression direction, calculated from the inverse polefigure. Random = 1.0 in f(g)

Basal slip comprises two systems, (001) [100] and (001) [010], and lateral slip comprises four possible systems: (100) [010], (010) [100], (100) [001], and (010) [001]. According to our experimental texture analysis, the evolution of a c-axis texture during the cold rolling process strongly supports basal and lateral plane sliding.

Figure 58 (a) shows how these non-{001} grains play an important role in accommodating deformation, when we assume plane strain compression to approximate the primary stress and strain state of rolling. After achieving a strong {001} texture, with this approximation, the c-axis is parallel to the compression direction for the crystals, and therefore, the resolved shear stress on the basal, (c-planes), and lateral planes (a, b-planes) vanishes and no more deformation can be accommodated [119], as shown in Figure 58 (b).

The {001} texture aggregate leads to a stiff response with respect to further compression of rolling due to a lack of non-{001} grains to support continued deformation (the predominant slip systems are no longer oriented to support slip), so the textural hardening induces a locking of the textured material at high strains. This locking is observed in Figure 58 (b), by the rapid increase of the equivalent stress level [119]. This explains how plastic locking occurs as a result of strong texture development; and results in a rapid increase in stress level since further deformation along the imposed strain path occurs by an essentially elastic deformation. Fracture, as a result of the high stresses, is inevitable.

4.3.4 Microstructure Analysis

A more representative method for examining the {001} texture along the rolling direction is to prepare polished sections. Until recently such sections have not been very informative, because the BSCCO grain structure (unlike the twinned microstructure of $YBa_2Cu_3O_X$ superconductor) is not clearly evident on a polished surface. However, it

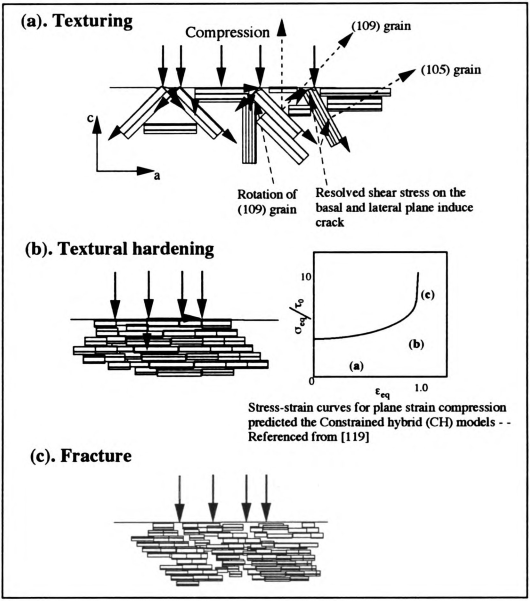

Stress-strain curves for plane strain compression predicted the Constrained hybrid (CH) models - - Referenced from [119]

Figure 58. Schematic illustration of the development of texture, textural hardening, and fracture.

can be effectively revealed by the perchloric acid etch, although excessive etching results in the destruction of 2223 BSCCO structure.

Figure 59 shows a group of SEM secondary electron images for HIP-cladded and 30%-R samples. These are longitudinal cross-section micrographs with the horizontal direction parallel to the long axis of the sample. At low deformation (~30% R), it appears that non-{00*l*} grains such as (109) and (105) begin to rotate toward c-axis at this stage of deformation. During this mechanical processing, texturing, cracking, and particle fracturing (resulting from rotation) are intimately related. The second phase appears to be an important parameter of interior alignment at this low deformation stage. It appears that the second phase induces damage in the form of fragmented particles during deformation and interrupts the local grain alignment, as shown in Figure 59 (d) and at a higher magnification in Figure 60. At higher deformations (~70% R), the second phase is broken up and dispersed as small size particles throughout the microstructure as shown in Figure 61 (a)

Figure 61 compares the longitudinal cross sections of 70% and 98% cold rolled samples . As the deformation extent increases to 98% R, propagation of cracks throughout the microstructure, and very small, fractured basal plane aligned particles are seen (Figure 61 (d)). As mentioned above, after developing a strong {00*l*} texture, an elastically stiff response, with respect to further rolling occurs due to the lack of non {001} grains to accommodate deformation. Further deformation along the imposed strain path will produce fracture, as a result of the high stresses. A strong crystallographic textures has the tendency to induce cracking, and large cracks have an obviously deleterious effect on conductivity, especially if the crack planes are perpendicular to the current path. This implies that the method of cold rolling process must be chosen to mitigate mechanical states that tend to promote fracture as well as produce strong crystallographic textures.

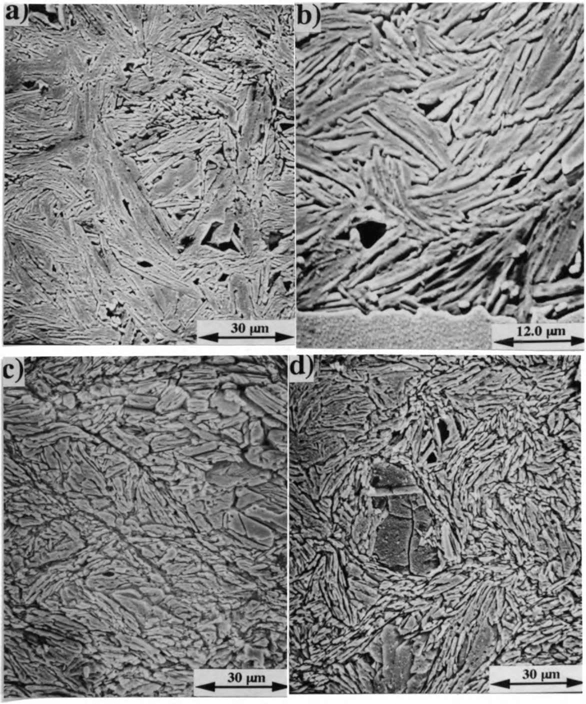

Figure 59. SEM secondary electron micrographs from polished and etched longitudinal cross-section samples: (a) HIP cladded sample (interior area), (b) HIP cladded sample (near Ag interface area), (c) 30% cold rolled sample, (d) 30% cold rolled sample with the presence of second phase particles

Figure 60. SEM secondary electron micrographs from polished and etched longitudinal cross-section of 30% cold rolled sample (with higher magnification of Figure 59. (d)) - - - The local grain alignment interrupted by second phase particles can be seen clearly

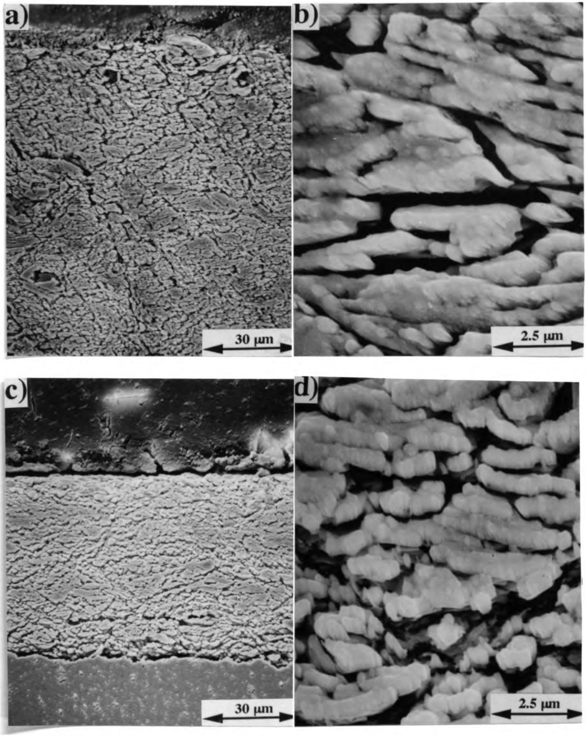

Figure 61. SEM secondary electron micrographs from polished and etched longitudinal cross-section samples: (a) 70% cold rolled sample, (b) 70% cold rolled sample with higher magnification, (c) 98% cold rolled sample, (b) 98% cold rolled sample with higher magnification

Plane strain compression is usually used to approximate the primary stress and strain state of rolling. However, based on the microstructure observation, the propagation of shear crack throughout the microstructure implies that the additional strain states achieved in rolling are characterized by superimposed shear strains on the compressive strains [107]. In practice, it is necessary to assume a superimposed shear strain (due to friction) on the compressive strains to explain the propagation of shear cracks and larger amounts of inelastic deformation before such strong textures are obtained.

4.4 Highly Textured 2212 BSCCO/Ag Tape Fabricated by Controlled Melt Process

4.4.1 The Effect of Cooling Rate

In order to investigate the effect of cooling rate on the microstructure development and to find out optimum cooling rate for the texture development and the minimum formation of second phase, various cooling rates were used. By investigating the x-ray diffraction peaks for each group, it is seen that there are changes in the number of second phase peaks. X-ray diffraction patterns (Figure 62) for the fully processed tapes show that the surfaces of both the tapes are predominately composed of 2212 phase with a strong c-axis alignment. Other than the major 2212 phase, some of the minor peaks are from 2201 and Cu free phases. The remaining peaks are most likely due to Bi-free phase. At the cooling rate of 120°C/hr (sample A3), there are considerable intensities of non-(00*l*) peaks such as (115), (117), and (200) planes while major peaks are from (008), ($00\underline{10}$), and ($00\underline{12}$) planes. It is thought that 120°C/hr is too fast to produce oriented 2212 phase grains.

At 2°C/hr (sample A1), there are strong 2212 peaks; however, a 2201 peak does appear with ~5% of the intensity of the highest 2212 peak. Furthermore, the diffraction spectra shows small amount of a second phase material peaks such as the Cu-free phase. Considering that Bi is the strongest x-ray scatterer, there will be a substantial amount of second phase that can cause problems with alignment. The final tape evaluated in this group was subjectected to the 10°C/hr cooling rate (sample A2). The x-ray spectra from this tape showed strongly c-axis oriented 2212 peaks; however, slight intensities of the 2201 and the second phase peaks were also detected. The sample A2 has a lower intensity of 2201 and the second phase peak than that of the sample A1, indicating the A2 has a lower content of the 2201 phase.

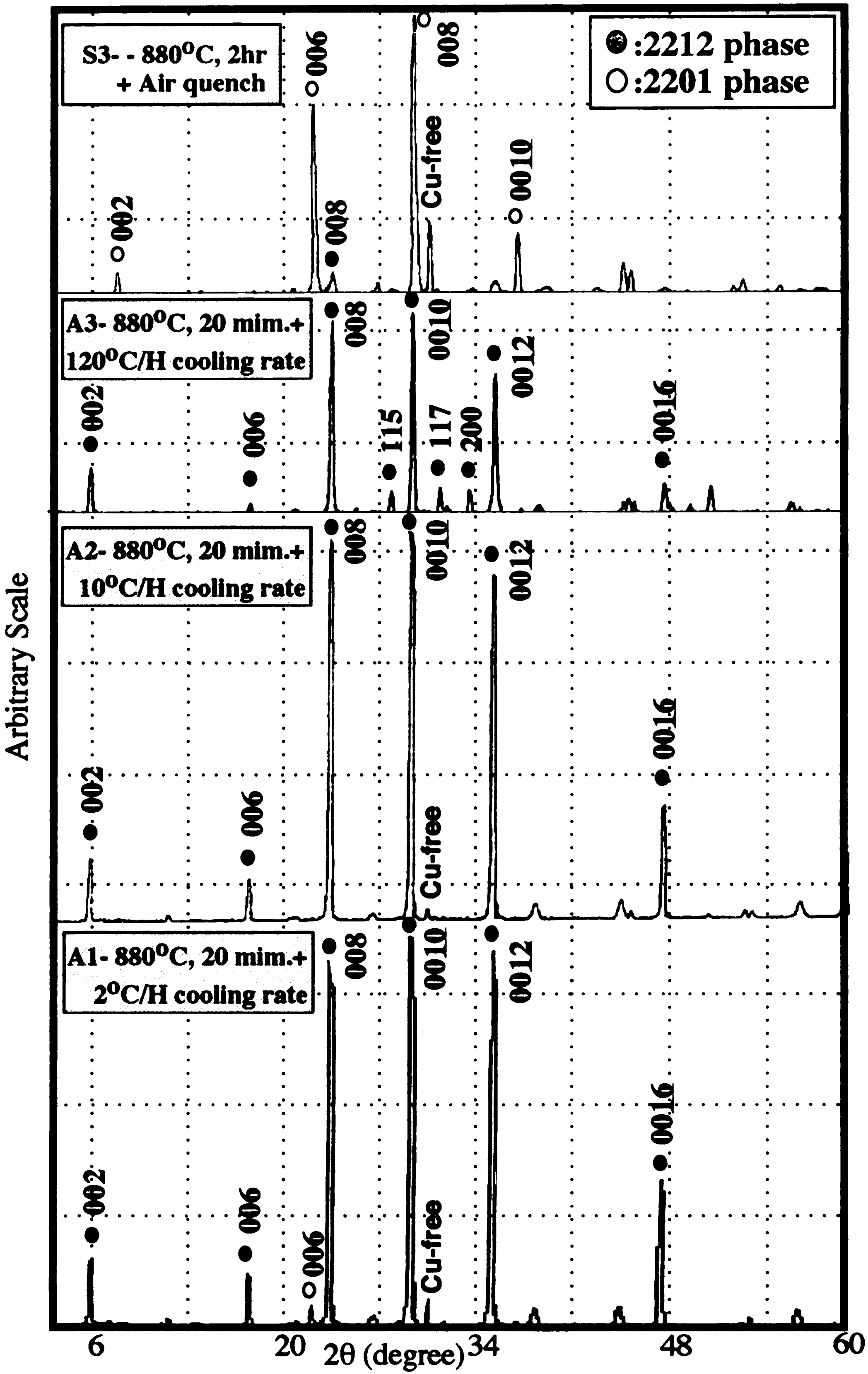

Figure 62. The effect of cooling rate on melt processed 2212 BSCCO/Ag superconducting tape (sample- - - S3, A3, A2, and A1)

The experimental pole figure for group A (Figure 63) also suggests that the 10°C/hr cooling rate yields the best texture, which has the maximum texture intensity of 350 (350 times stronger than the random case). For each sample, the pole figures for the $(00\underline{10})$, (115), and (200) planes were measured. For sample A3 (120°C/hr), the $(00\underline{10})$ pole figure shows much lower texture intensity and wider scattering range, compared to samples A1 and A2. The (115) pole figure of sample A3 also suggests a wider variation of fiber texture.

Tape A1 experiences a much better alignment in the $(00\underline{10})$ direction. The area covered by the contours is much smaller than that for A3. The high intensity region is more compact than that seen for A3. Despite the compactness of the pole figure, some scattering of $(00\underline{10})$ pole is observed in the surrounding area. There will be a slight amount of misoriented grains within the BSCCO layer.

The (115) pole figure (Figure 64) also suggests that there is some variation of the (115) fiber texture. The angle between the normal direction and the fiber is the angle between the c-axis and the (115) plane normal of the tetragonal unit cell, as shown in Figure 65 for the ideal case of alignment. The best $(00\underline{10})$ pole figure belongs to tape A2. The 10°C/hr cooling rate yielded a very concise and compact pole figure with very slight scattering range. The high intensity region is much smaller than the other two tapes. This 10°C/hr cooling rate produces a highly oriented 2212 structure with little, if any, scattering.

4.4.2 The Effect of Long-term Annealing

The effect that annealing time has on the texture, can be seen by comparing group A to group C. Group C samples were subsequently annealed at 860°C for 100 hrs. Specifically a comparison of A1 and C1 is very revealing. The sample C1 has lower intensity peaks for the secondary phase materials such as Cu-free phase, but the small

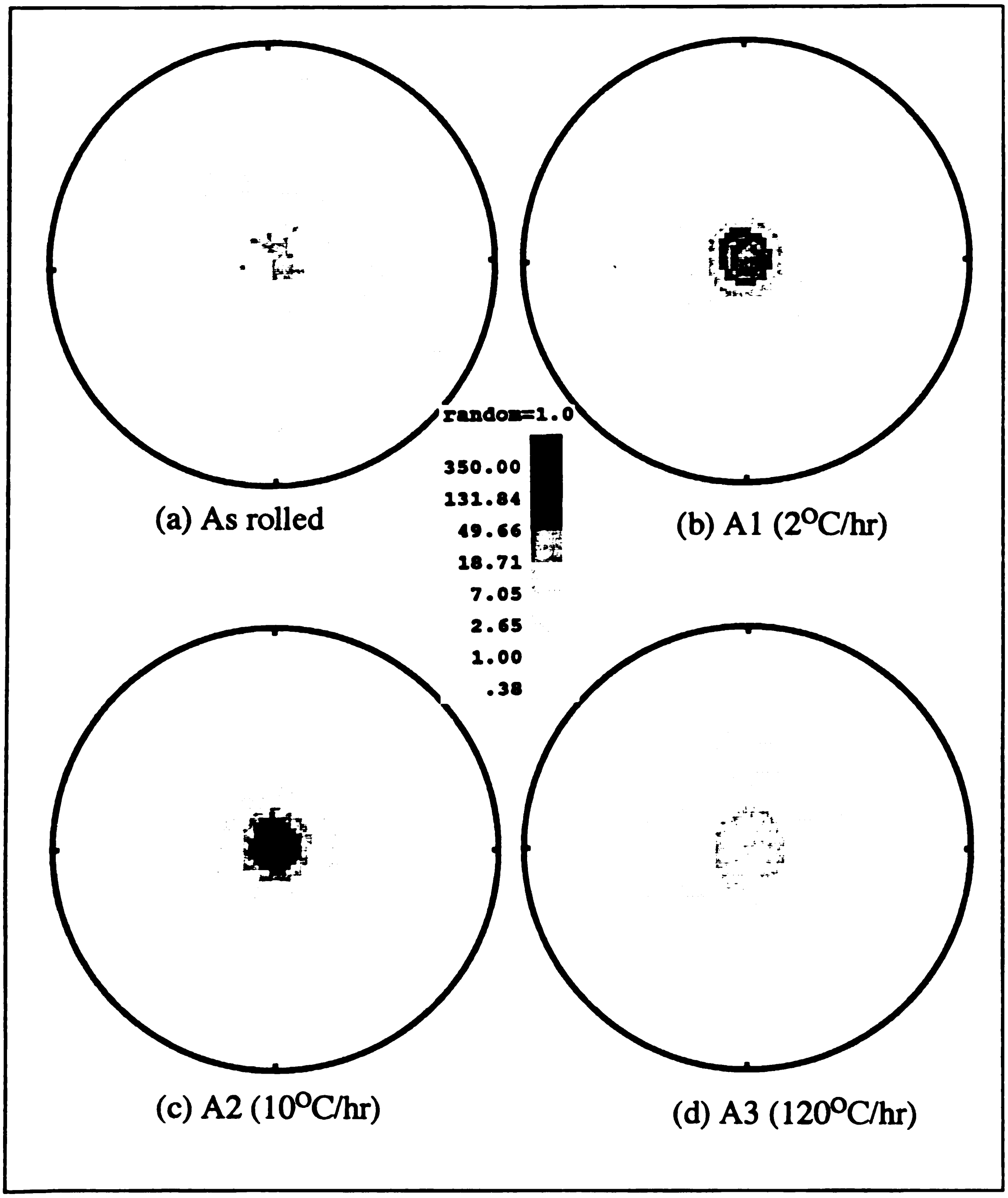

(a) As rolled

(b) A1 (2°C/hr)

(c) A2 (10°C/hr)

(d) A3 (120°C/hr)

Figure 63. Measured $(00\underline{10})$ pole figures from the sample having different cooling rates. a). As rolled, b). A1, c). A2, d). A3

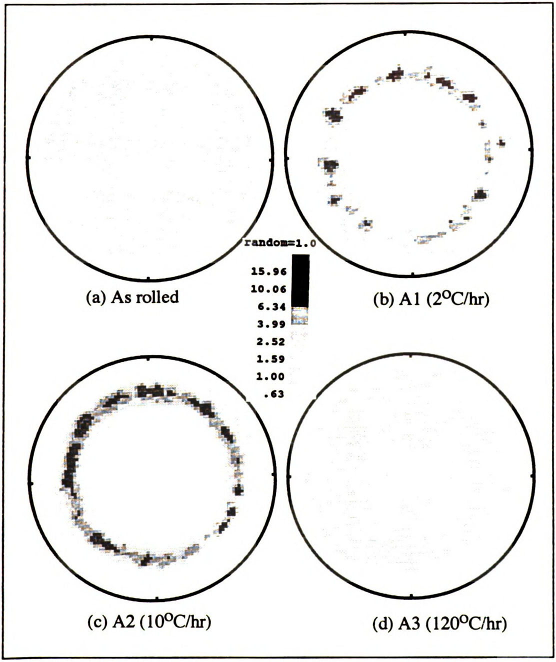

(a) As rolled

(b) A1 (2°C/hr)

(c) A2 (10°C/hr)

(d) A3 (120°C/hr)

Figure 64. Measured (115) pole figures from the sample having different cooling rates. a). As rolled, b). A1, c). A2, d). A3,

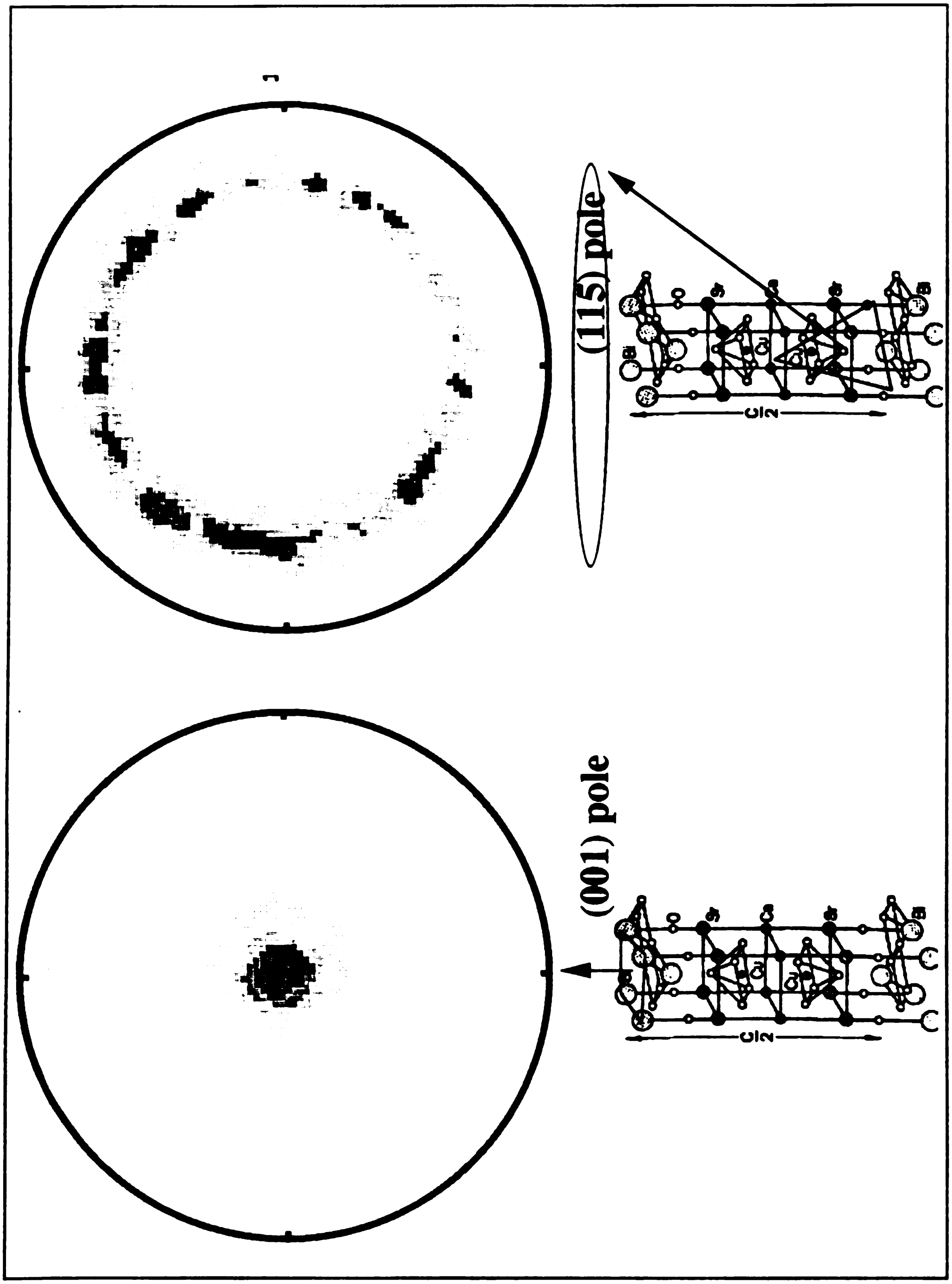

Figure 65. Measured experimental polefigure from melt processed 2212/Ag tape

amount of 2201 phase is still present, as shown in Figure 66. This suggests that the annealing process transforms more secondary phase material into 2212 grain.

The above results agree with what was expected. However, the pole figures of these two groups (Figure 67) indicate some phenomenon that was not expected. The $(00\underline{10})$ pole figure of group A1 is symmetrically circular in nature; but, the C1 $(00\underline{10})$ pole figure looks asymmetric. There is also a degree of scattering around central area. This indicates that the alignment of the grains was a little skewed during the annealing process.

The temperature dependence of the magnetic susceptibility for the melt processed 2212 tape with different condition is shown in Figure 68. All these samples show superconducting transition around 80 K. The T_c value of samples is 82 K, 80 K, and 77K for the C2, A2, and A1, respectively. From the comparison of magnetic susceptibility measurements, sample A2 shows sharp transition and stronger diamagnetic behavior, which implies large amount of superconducting phase, even though sample C2 has higher T_c.

4.4.3 Microstructure Analysis of Melt Processed 2212 BSCCO/Ag Tape

As mentioned in section 4.2.1, one concern that can be raised about X-ray results is that x-ray penetration depth is only about 3-4 μm [29]. This is much smaller than the 2212 layer thickness of ~50 μm that was used in this study. Moreover, all the above diffraction patterns and pole figures for texture analysis were obtained from the top surface of the tape where the alignment is expected to be greater than the inside core region. X-ray results will thus tend to overestimate the overall texture of all samples and give no information about the inside local grain alignment.

The local alignment is a very important factor since critical current density (J_c) depends predominantly on extrinsic microstructural features such as second phases,

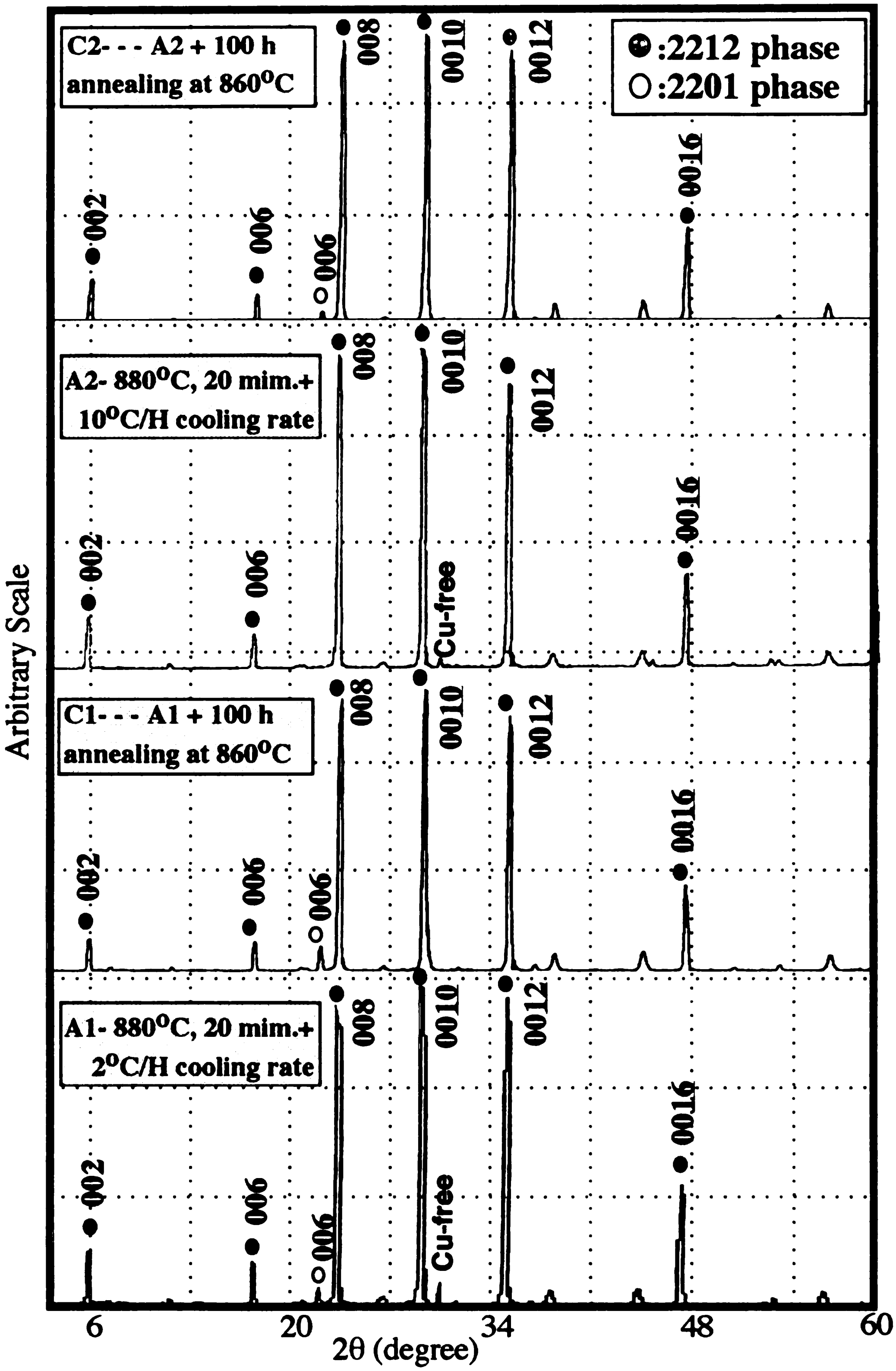

Figure 66. The effect of long-term annealing on melt processed 2212 BSCCO/Ag superconducting tape (sample- - - C2, A2, C1, and A1)

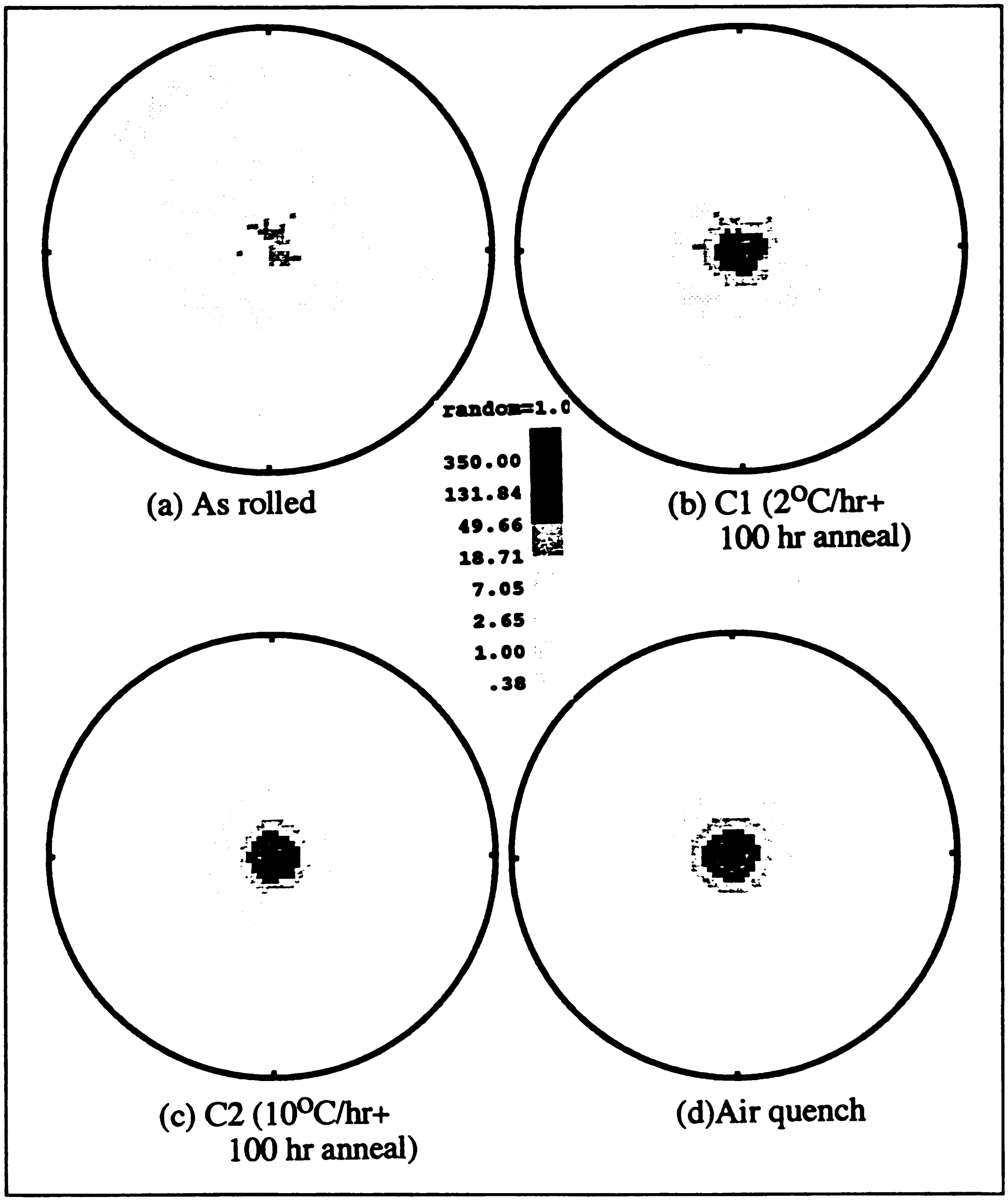

Figure 67. Measured (00$\underline{10}$) pole figures from the sample of a). As rolled, b). C1, c). C2, d). Air quench

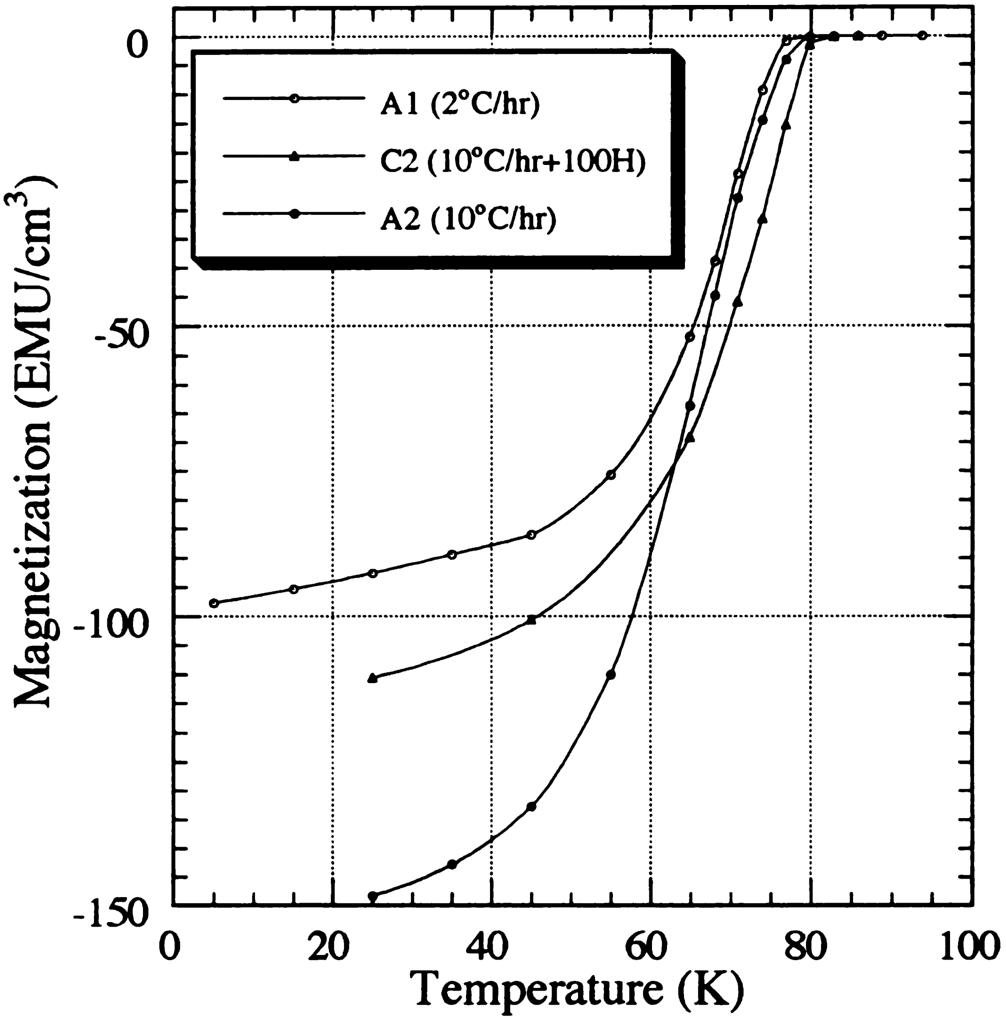

Figure 68. Susceptibility Measurements (EMU vs. Temp.) of the melt processed 2212 BSCCO/Ag tape

which will interrupt the local alignment and block the current path, as shown in Figure 69. Therefore, the examination of the overall quality of tape should be accompanied with the observation of microstructure inside the core region to determine what phases are present in the processed tapes. This local alignment can be examined by using SEM micrographs of polished and etched cross-sections.

Figure 69 shows SEM micrographs of polished and etched longitudinal section of the sample Dl and D2 obtained with a cooling rate of 10°C/hr and 120°C/hr, respectively, after melting and holding at 920°C for 20 minutes. These are longitudinal section micrographs with the horizontal direction parallel to the long axis of the sample. In these samples, near the 2212/Ag interface and top surface, plate-like 2212 grains are well aligned with their a-b planes parallel to the tape surface. However, the inside core region, especially near the second phases, shows poor alignment with a considerable amount of a blocky second phase, which was identified as (Sr, Ca) rich phase (dark blocky phase) by EDAX analysis. These second phases interrupt the local grain alignment and reduce the useful current carrying cross section. For most deleterious phase, $(Sr,Ca)CuO_2$, large grains are formed approaching the thickness of the oxide core, as shown in Figure 69 (b).

At this high temperature (920°C) used for melt processing (sample D group), vaporization of the components could be a factor giving rise to the big second phase particles. Sata et al. [95] calculated the apparent vapor pressure of copper and bismuth over 2212 by the transpiration method. In PIT processed wires and tapes, vaporization is a relatively minor problem, as the major loss occurs through the open ends of the wire or tape. Vaporization from the surface of thin films, on the other hand, can be a serious problem in tapes cast by doctor-blade. To reduce this problem, the total time at elevated temperature must be minimized, which will require careful optimization of temperature, time, and cooling rate to attain high J_c.

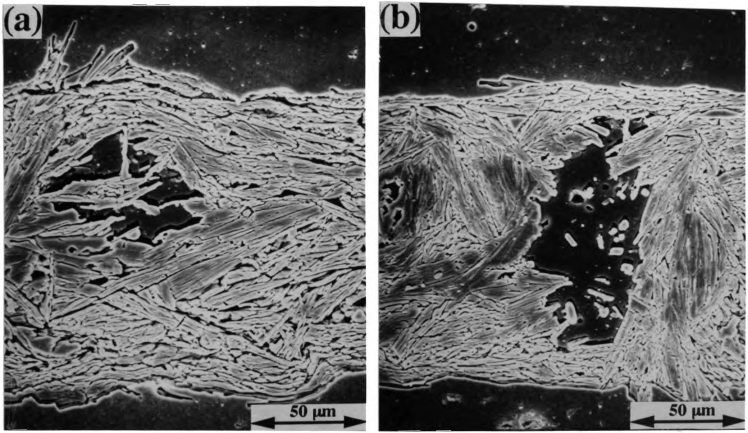

(a) D2 (b) D1

Figure 69. SEM micrographs of polished and etched longitudinal section of a). 2212 BSCCO/Ag tape, melted at 920°C for 20 min. with 120°C/hr cooling rate and b). 10°C/hr cooling rate

In contrast to the group D samples, the group A samples, which were processed at 880°C have lesser amounts of chunky second phase, as shown in Figure 70 and 71. Among the samples of group A, the microstructure of sample A2 (Figure 70) shows impressive alignment over the entire sample A1 and A3 (Figure 71 (a) and(b)). This morphological data is consistent with the x-ray diffraction pattern and pole figure analysis. For the sample A1, it shows a well-aligned microstructure, but still, it contains small size second phase particles in the interior region, as shown in Figure 71 (a).

At a faster cooling rate (sample A3), it is seen that most of the plate-like grains are moderately aligned parallel to the tape surface. However, the alignment of the core region is disrupted and grain size is small; less than 15 μm. From the experimental results for the sample A and sample D, it was tentatively concluded that processing at 880°C, followed by a faster cooling rate (120°C/hr) does not give enough time to produce partial melting. Processing at 920°C, followed by a faster cooling rate of 120°C/hr (sample D2) gives more favorable results than slow cooling rate (sample D1), which is consistent with x-ray diffraction results (Figure 72). With a slower cooling rate between 880°C and 860°C, second phases are rarely seen and alignment is further improved, while a very slow cooling rate (2°C/hr) is not beneficial for ideal microstructure development, since this cooling rate requires about 10 hours to reach the stable temperature range.

SEM photographs of the surfaces of samples in A and C groups are shown in Figure 73 and 74. The same tendency of microstructural development is shown in the figure for the sample A and C group, as discussed above. The surface of the samples subjected to faster cooling rate (A3) seems to reveal intermediate situation between solid state sintering and partial melt processing: small grain size and misalignment (Figure 73 (c) and (d)).

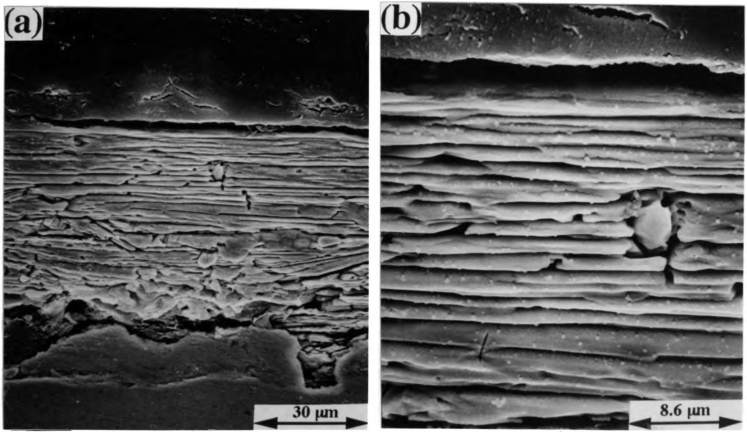

(a) A2

(b) A2

Figure 70. SEM micrographs of polished and etched longitudinal section of a). 2212 BSCCO/Ag tape, processed with 10°C/hr cooling rate and b). same sample of a) but higher magnification

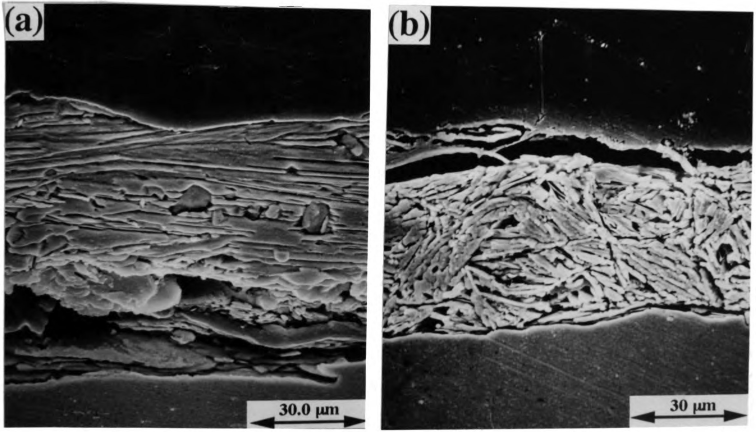

(a) A1

(b) A3

Figure 71. SEM micrographs of polished and etched longitudinal section of a). 2212 BSCCO/Ag tape, processed with 2°C/hr cooling rate and b). 120°C/hr cooling rate

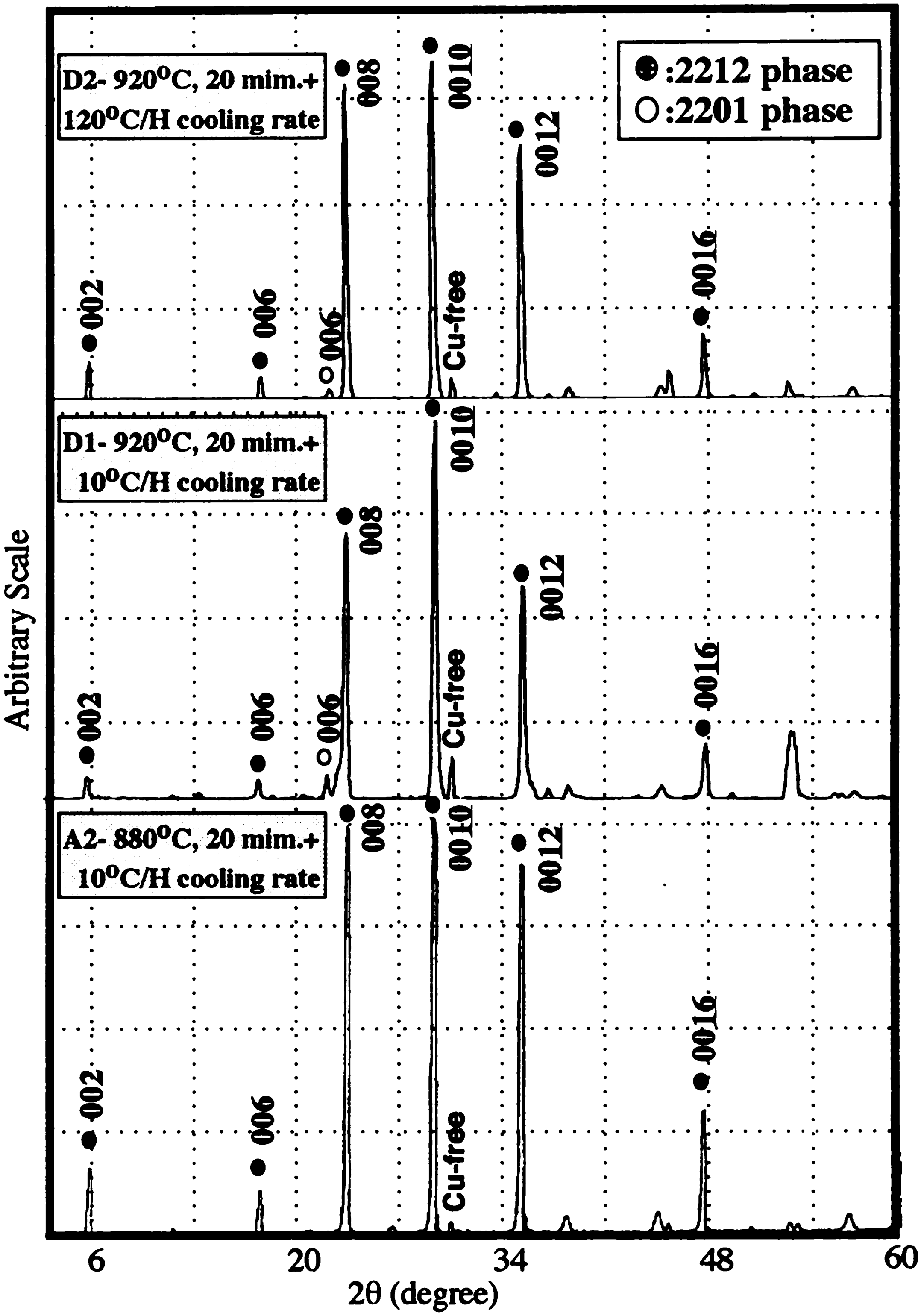

Figure 72. The comparisonal X-ray diffraction data of melt processed 2212 BSCCO/Ag superconducting tape (sample- - - D2, D1, and A2)

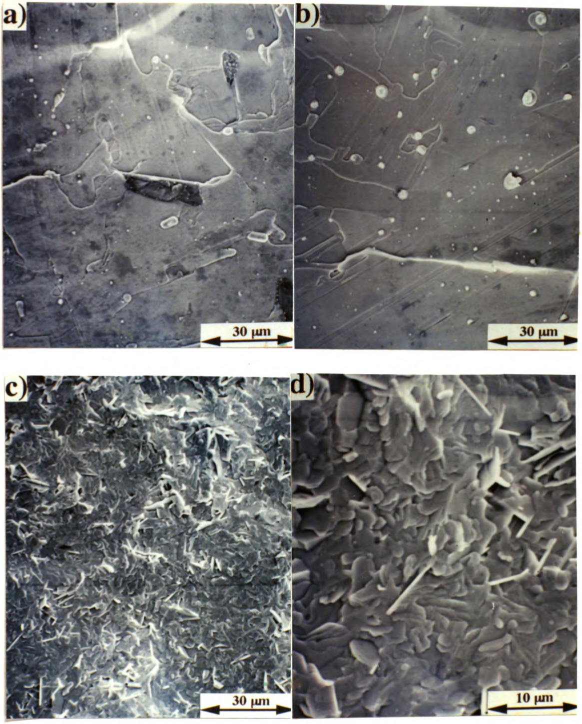

Figure 73. SEM micrographs of the group A samples surface of a). A1, b). A2, c). A3, and d). same of A3 condition but higher magnification.

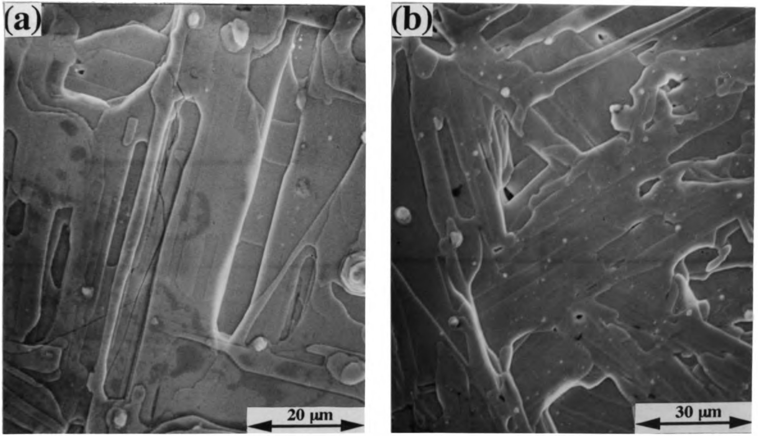

(a) C1

(b) C2

Figure 74. SEM micrographs of long-term annealed 2212 BSCCO/Ag tapes surface of a). C1 and b). C2 condition.

4.5 Magnetization, Critical Current Density, and Pinning Mechanism in BSCCO

4.5.1 HIP-treated 2223 BSCCO Superconductor

High-field hysteresis (Magnetization vs. Field) loops have been measured for HIP-treated samples, and the results are shown in Figure 75 and 76 as a function of magnetic field and temperature. The magnetic field was applied perpendicular to the pressed surface. The directional dependence of field such as perpendicular and parallel to the sample surface will be negligible, considering the orientation of grain. The most prominent feature of the hysteresis loop at 5K, in Figure 76, is that the decrease of the magnitude beyond the maximum value at a few hundred gauss is much slower, and the shape is not like the "bird wing" which will be seen in Figure 77 for a conventionally sintered powder sample. This slow gradual decrease of the magnetization at high field means that the high field property of the "magnetically determined" J_c will be improved by the HIP.

The "magnetic" J_c can be obtained from the hysteresis loop, through the following equation [63]:

$$\Delta M = \frac{J_{c1} t}{20}\left(1 - \frac{t}{3l}\frac{J_{c1}}{J_{c2}}\right) \qquad (11)$$

where $\Delta M=(M_+)-(M_-)$, and M_+ and M_- are positive and negative hysteritic magnetizations respectively. J_{c1}, J_{c2}, t, and l are defined earlier equation. Since the high-field hysteresis loop reflects the internal critical current within the grains [120], the field dependence of the magnetization indicates the following two facts. One is that the intragrain J_c (deduced from ΔM) will decreases almost linearly against the magnetic field at the high-field region. The second is that the intragrain J_c, for HIP sample is much

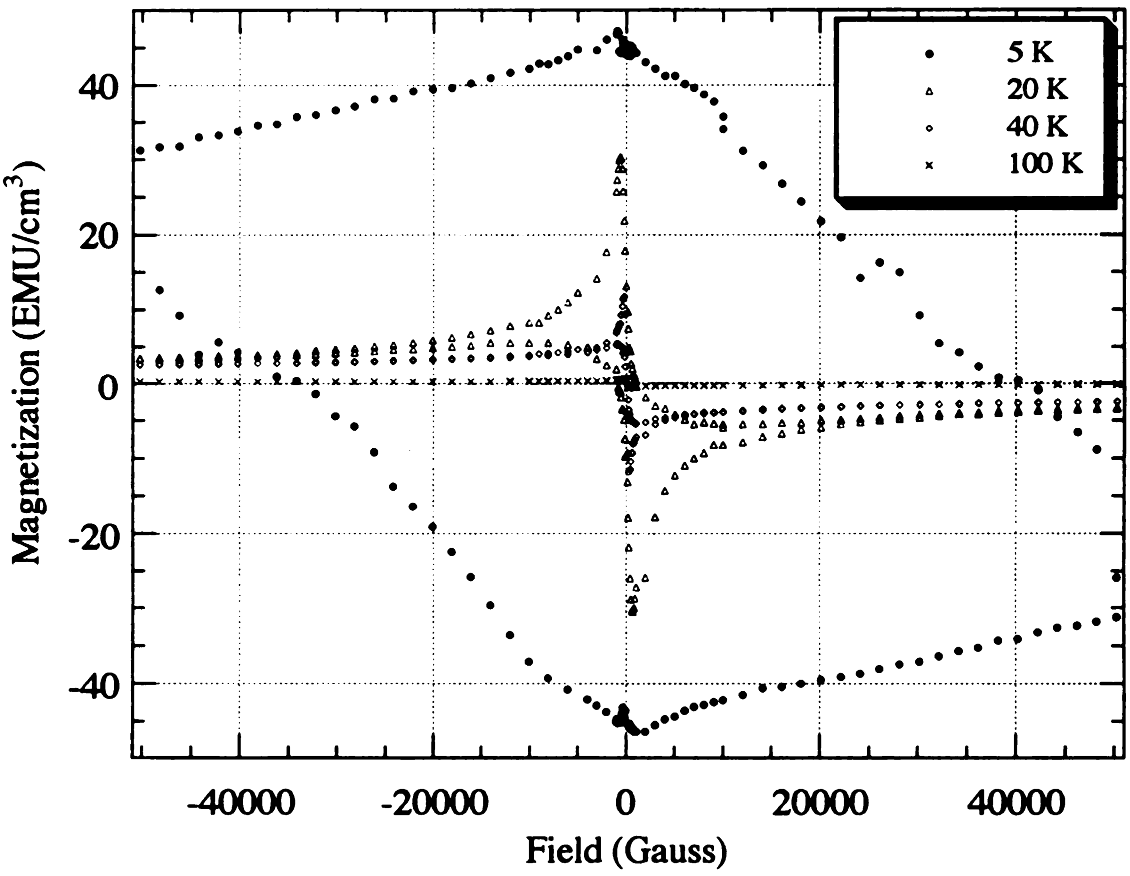

Figure 75. Temperature dependence of magnetization of the HIPped bulk 2223 BSCCO superconductor (HIP Temp: 850 °C)

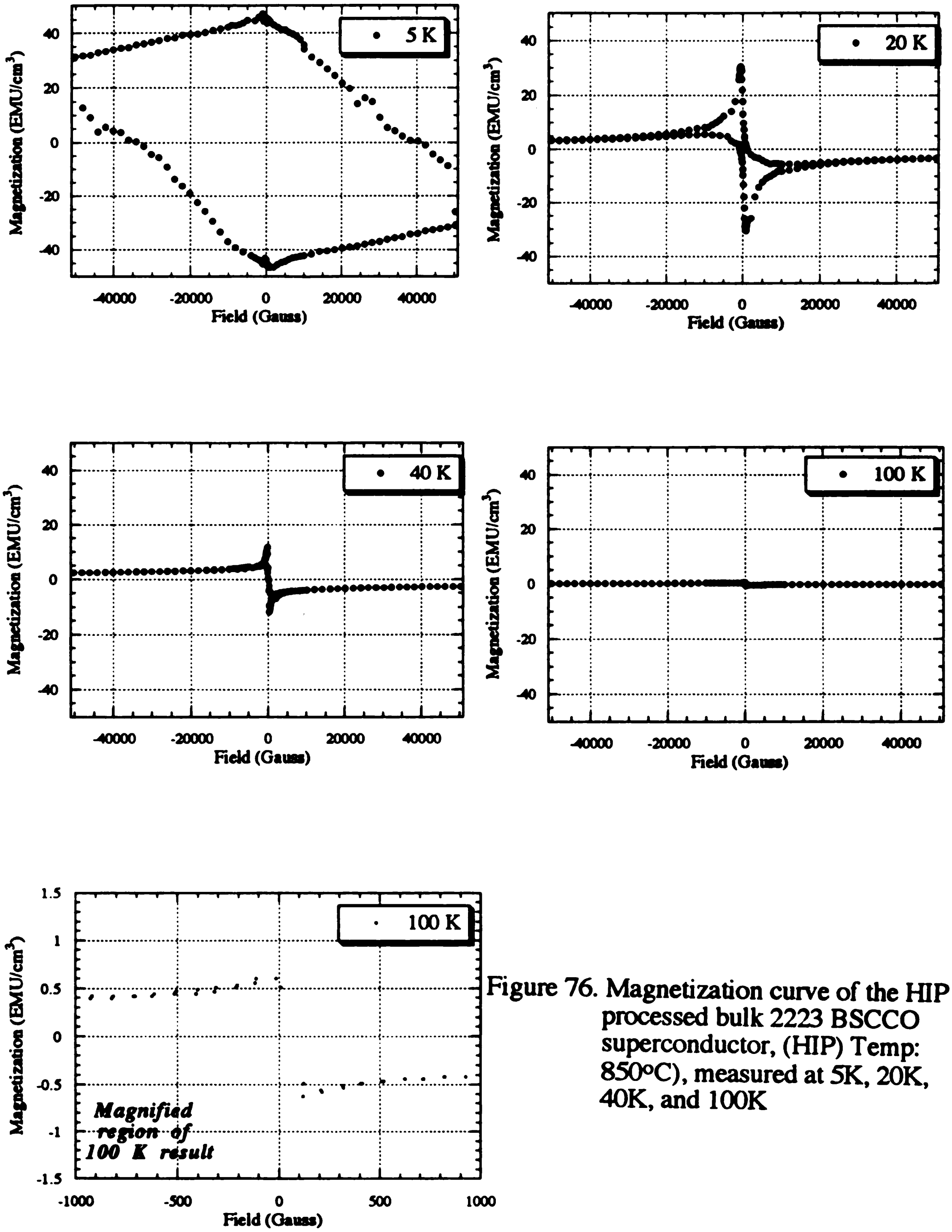

Figure 76. Magnetization curve of the HIP processed bulk 2223 BSCCO superconductor, (HIP) Temp: 850°C), measured at 5K, 20K, 40K, and 100K

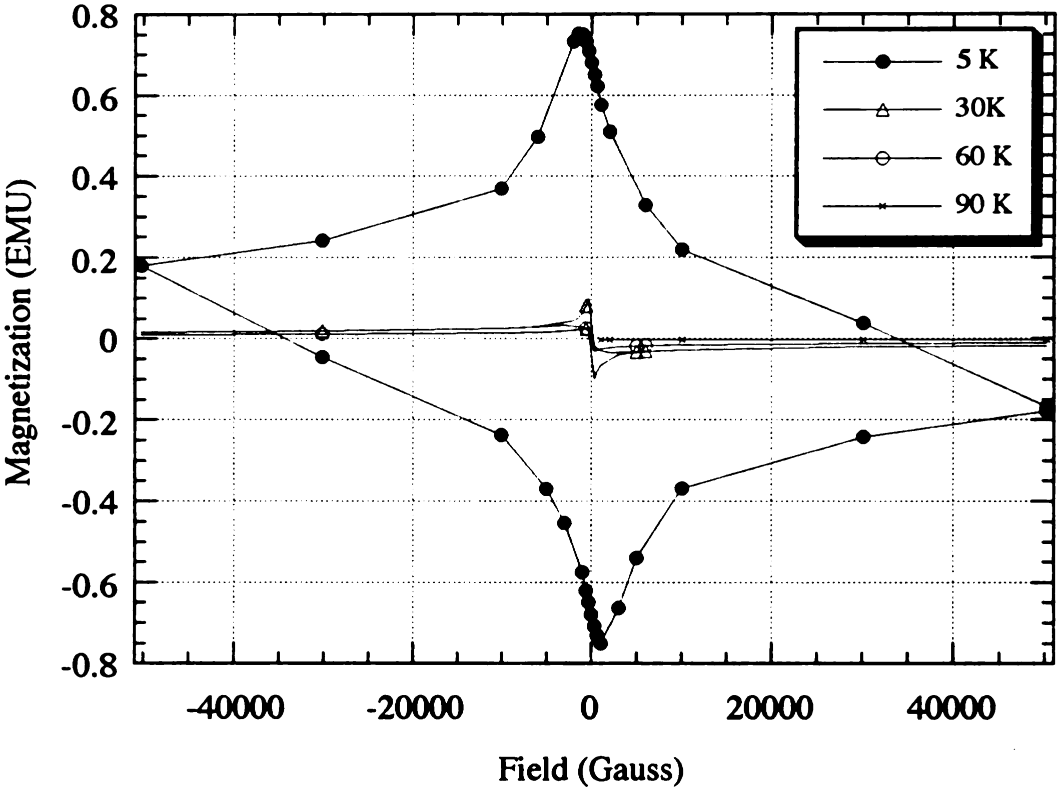

Figure 77. Temperature dependence of the magnetization of powder 2223 BSCCO superconductor

higher than that of 2223 powder sample (Figure 77) at 5K. The latter fact suggests that HIP does not weaken the pinning force within the grains at 5 K compared to those in the powder samples.

Contrary to the result at 5K, the difference of magnetic J_c (or $\sim\Delta M$ since J_c is proportional to ΔM) between HIP and powder sample at higher temperature is not so marked, and almost the same at high magnetic fields. At more than 40 K, the intragrain J_c ($\sim\Delta M$) will be close to each other for HIP and powder sample. Thus the pinning forces in HIP and powder samples must be comparable to each other at 40 K (high temperature). Referring to the difference of the magnetic J_c, at 5 K mentioned above, it is probable that HIP does not enhance the magnitude of the pinning potentials (U_o), but increases the number of pinning centers.

4.5.2 Melt Processed 2212 BSCCO/Ag Tape

For major bulk applications, high J_c in a magnetic field of at least several tesla (1Tesla=10000 Gauss) is desirable. The J_c behavior of the melt processed 2212 BSCCO/Ag tape indicates that the operating temperature for the high-field applications of the melt processed 2212 BSCCO tapes will have to be limited to below ~30 K [17]. Shown in Figure 78 and 79 are the M-H loops at various temperatures (5, 20, and 40 K) of the melt processed 2212 BSCCO/Ag tape (sample:A1), which is processed at a cooling rate of 2°C between 880°C and 860°C. The magnetization hysteresis loops were taken using a magnetic field up to 50000 Gauss.

The most prominent features of the hysteresis loop at 5K for the sample are that the magnitude of M at very low field up to 5000 gauss is very large and it has high ΔM value, which will be translated in to J_c value of $10^6 \sim 10^5$ A/cm^2. As magnetic field increased, however, the decrease of the magnitude beyond the maximum value is fast, and the hysteresis of magnetization (ΔM) was rapidly reduced. In addition as temperature

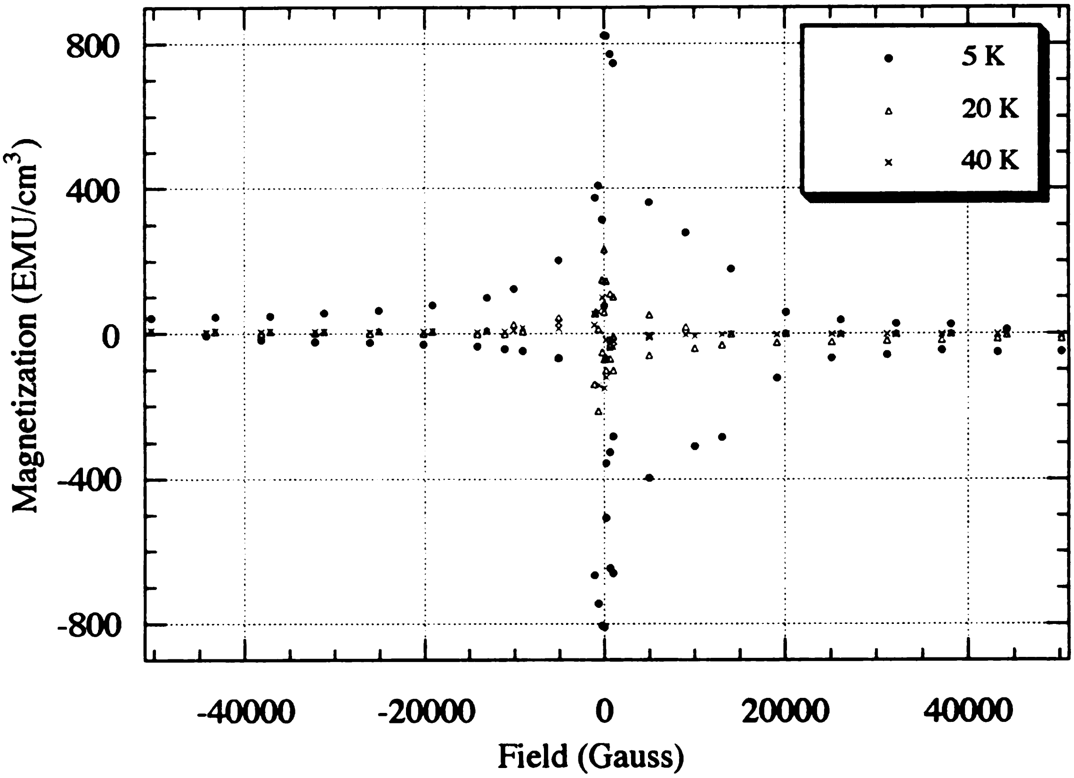

Figure 78. Temperature dependence of magnetization (M vs. H) curve of melt processed 2212 BSCCO/Ag tape (sample: A1- - 2°C/hr)

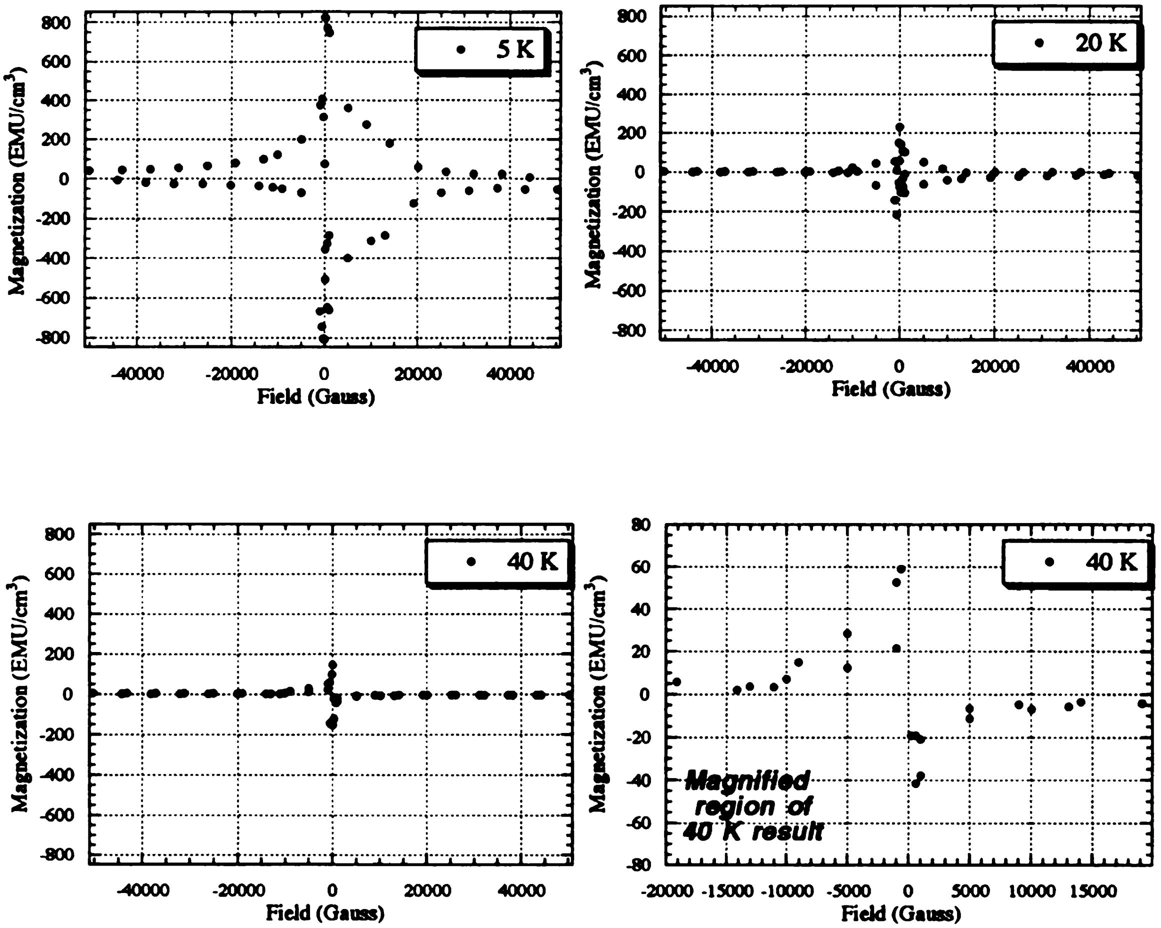

Figure 79.Magnetization curve of the melt processed 2212 BSCCO/Ag tape (sample A1- - 2°C/hr), measured at 5 K, 20K, and 40K

increased, the value of ΔM rapidly decreased. This phenomenon suggests that the pinning force in the melt processed 2212 BSCCO tape is significantly weak in comparison with that of thermomechanically processed 2223 BSCCO tape, as will be discussed later.

Figures 80 and 81 show the magnetization at various temperatures as a function of magnetic field for the same melt processed 2212 BSCCO/Ag tape (sample:A2), except the cooling rate is 10°C/hr. Even though it features the same behavior, the hysteresis of magnetization (ΔM) of sample A2 was less decline, in comparison with that of sample A1, at higher magnetic fields and temperatures. The ΔM value still holds 100 EMU/cm^3, which is much higher than that for sample A1. An estimate of the critical current density, magnetic J_c, can be made using the extended Bean model [63], as shown in Eq (11). For $l >> (J_{c1}\ t)/3J_{c2}$,

$$\Delta M = \frac{J_{c1} t}{20} \qquad (12),$$

the solution for a long slab of thickness t.

The dependence of J_c, deduced from magnetization measurement, on the external magnetic field as a function of temperature is shown in Figure 82 and 83 for the sample A1 and A2, respectively. At 5K, excellent J_c values of 4.8×10^5, 1.3×10^5, and 0.4×10^5A/cm^2 at H=0, 10,000, 50,000 gauss, respectively, have been obtained, as shown in Figure 83. These J_c data are comparable to the best J_c values in silver clad BSCCO wires [31,38] and doctor-blade/melt-processed tapes [87]. The high J_c values of ~10^5A/cm^2 are basically maintained up to a temperature of near 20 K and a field of 2,000 gauss as is evident in Figure 83. At 30 K, however, the high J_c (~10^4A/cm^2) is seen only at $H \le 5000$ gauss, and the J_c drops rapidly in higher fields, showing essentially no critical currents at $H \ge 35{,}000$ gauss. This behavior is attributed to the onset of thermally activated flux creep in BSCCO type superconductors above ~30 K [14,15,17], as mentioned in section 2.

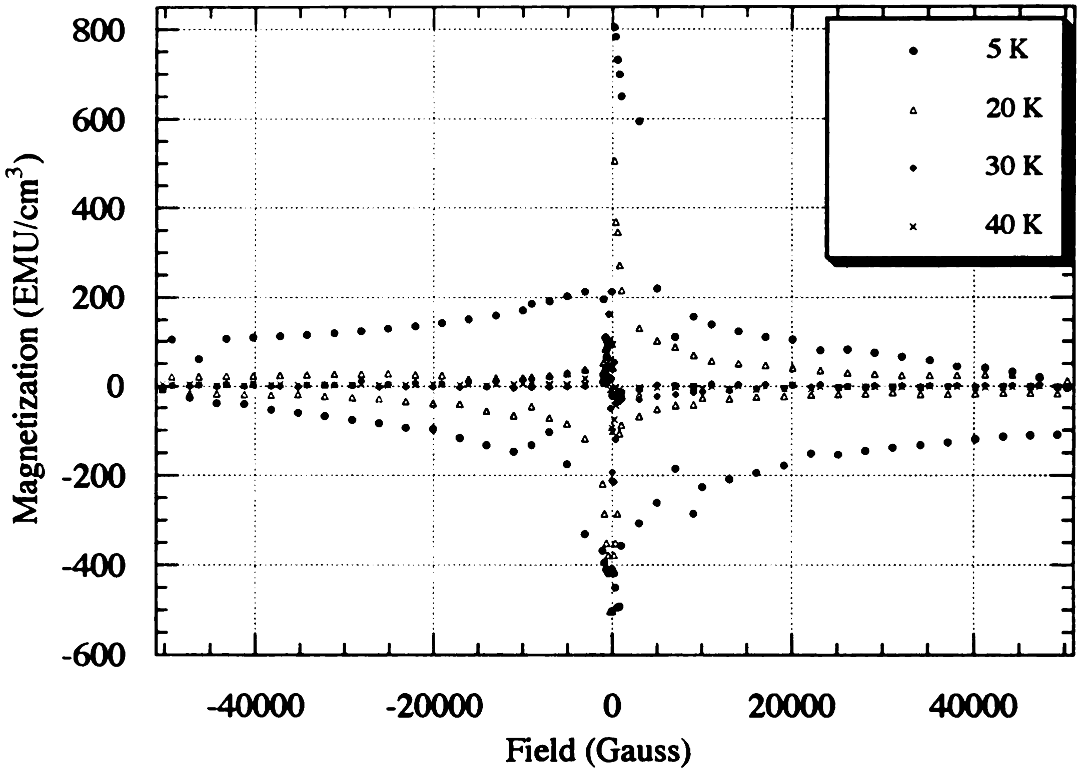

Figure 80. Temperature dependence of magnetization (M vs. H) curve of melt processed 2212 BSCCO/Ag tape (sample: A2- - 10°C/hr)

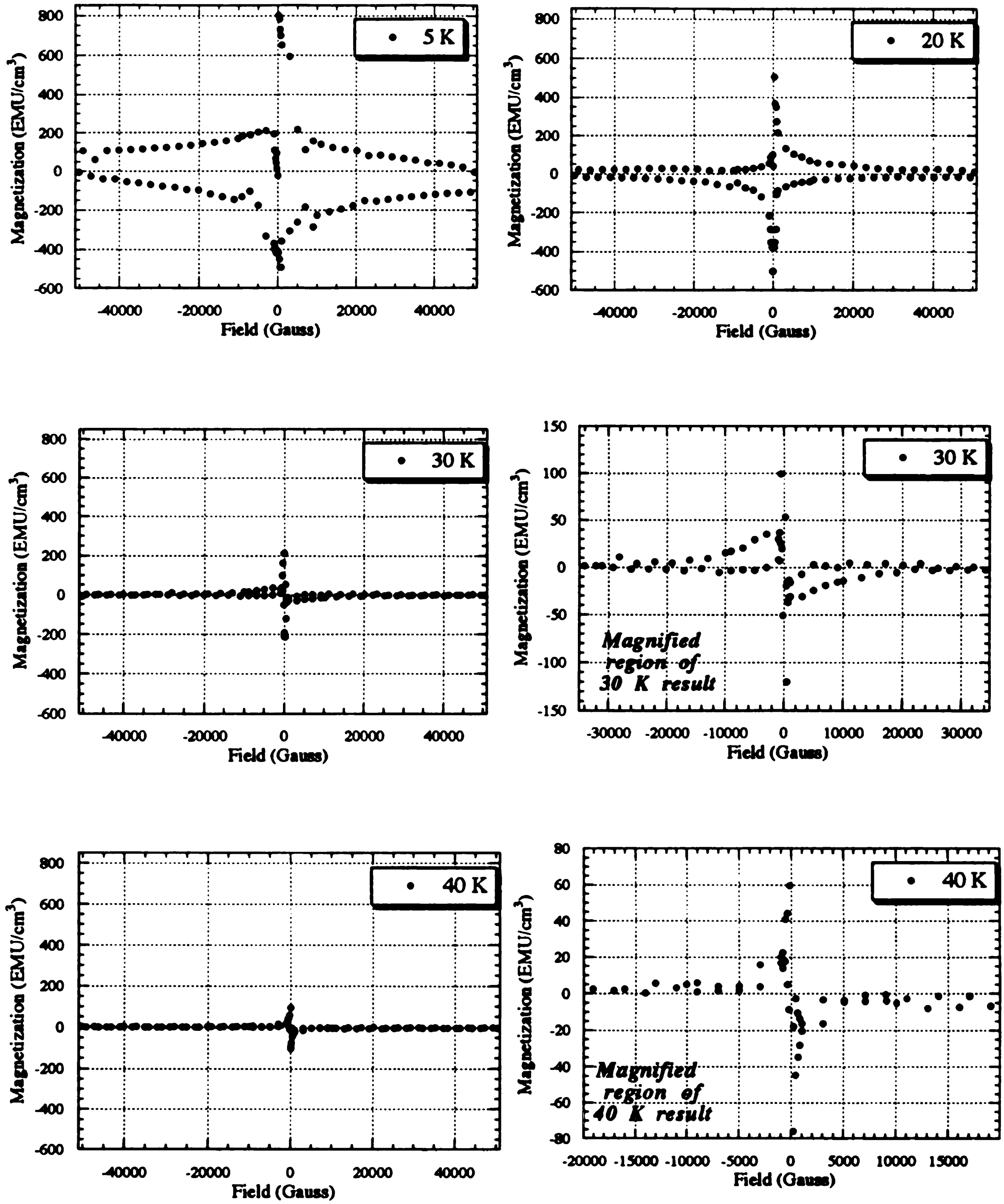

Figure 81. Magnetization curve of the melt processed 2212 BSCCO/Ag tape (sample A2- - 10°C/hr), measured at 5K, 20K, 30K, and 40K

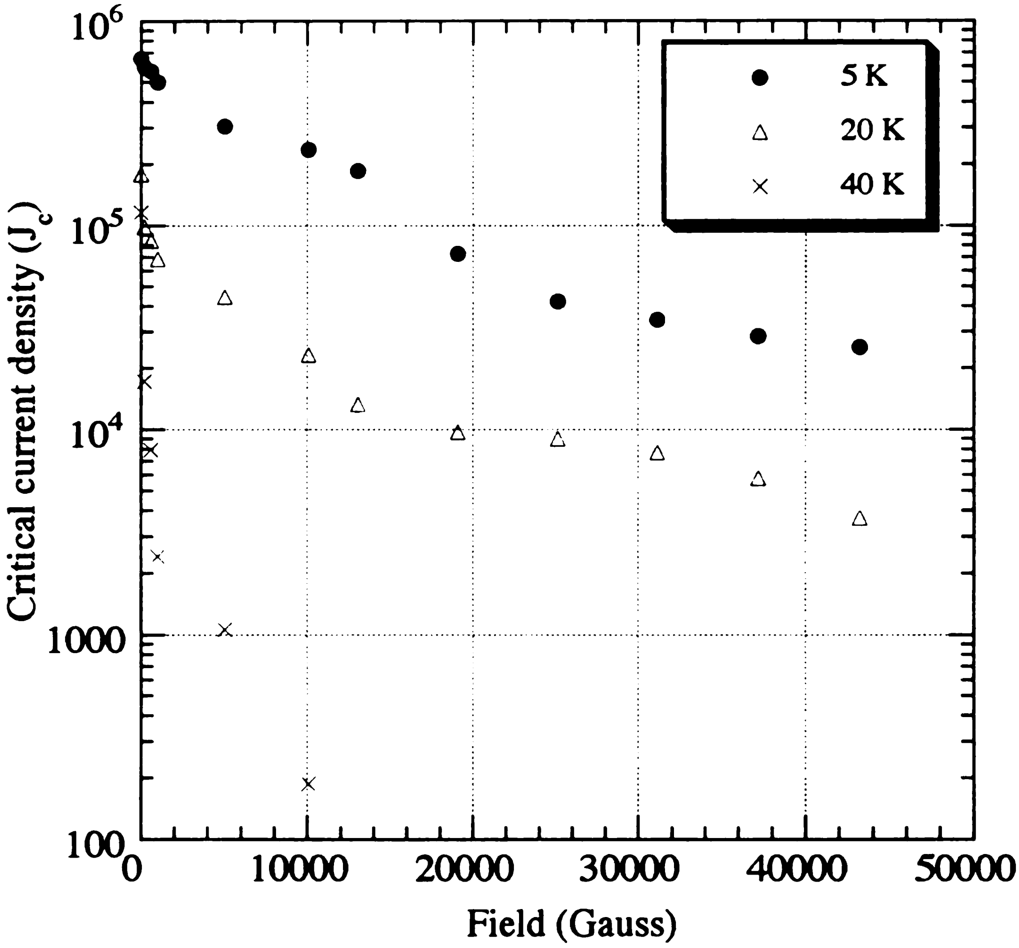

Figure 82. Temperature and magnetic field dependence of the critical current density of melt processed 2212 BSCCO/Ag tape (A1- - 2^0C/hr)

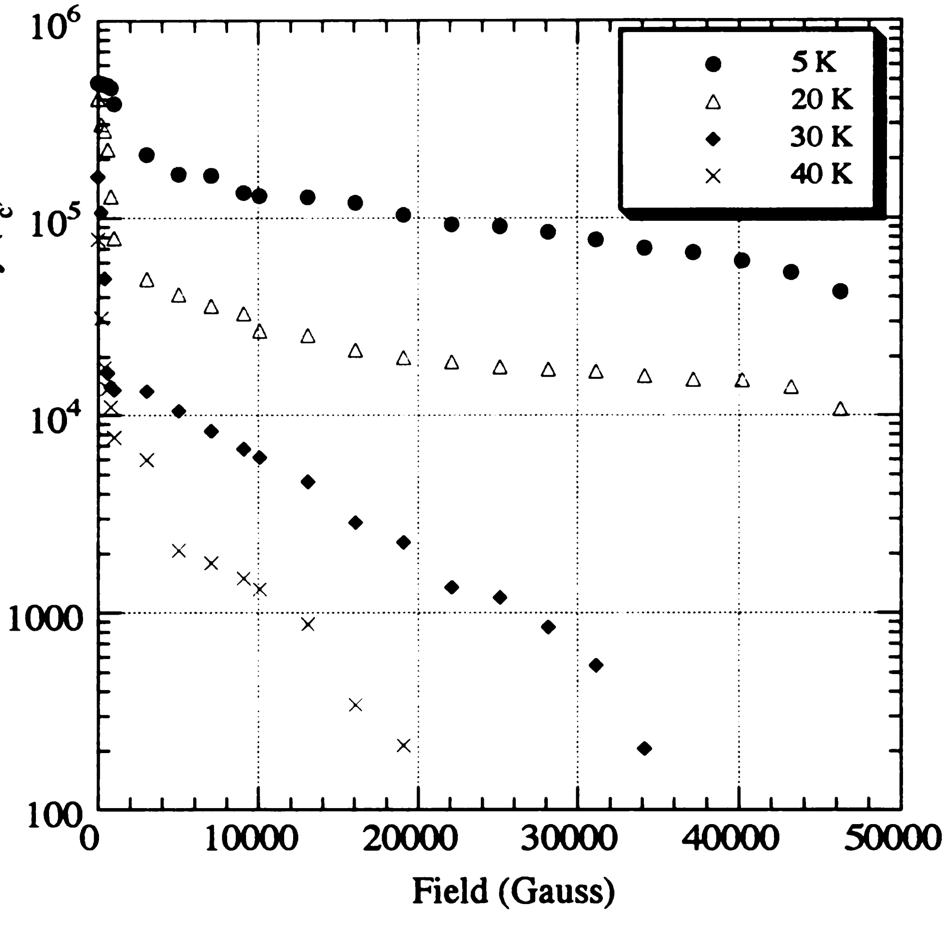

Figure 83. Temperature and magnetic field dependence of the critical current density of melt processed 2212 BSCCO/Ag tape (A2- - 10^0C/hr)

For the sample A1 (Figure 82), the problem is more severe at higher fields and temperatures. At 40 K, the J_c of sample A1 virtually disappears at $H \geq 10{,}000$ gauss. In contrast to the sample A2 which consisted of well-aligned and elongated grains, with no large secondary phase particles (even it still has a smaller amount of second phases), the sample A1 contains larger amount of second phase, and texture is expected to be not as good as that of sample A2, due to the interruption. The weak-link effect depends on the quality of the grain boundaries which, in turn, depends on the materials processing. The different quality of the microstructure is responsible for the difference in the magnetization and J_c behavior of the two types of tapes.

4.5.3 Pinning Mechanism in Thermomechanically Processed 2223 BSCCO/Ag Tape

It has been realized that the impressive transport properties of the 2223 BSCCO/Ag superconducting wires are attributable to a desirable combination of the plate-like morphology together with an excellent c-axis alignment and grain connectivity between a-b planes in these wires. The large contact area between the plate-like grains substantially reduces the resistance for current flow in the c-axis direction. Moreover a "brick wall" model has been proposed to illustrate the current transport mechanism in the c-axis aligned tapes [99].

At higher temperatures, however, the J_c for these tapes shows a drastic decline with increasing magnetic field and a pronounced anisotropy, due to the thermally activated flux creep. This seems to suggest that at higher temperatures the transport current density is not limited by the grain boundary weak links but by the intragrain currents. Thus, it is evident that the flux pinning becomes important for maintaining the high J_c of the Ag clad Bi-based superconducting wires in magnetic field at high temperatures.

Some pinning mechanisms, such as Y_2BaCuO_5 precipitate pinning [57] and twin plane pinning [15], have been demonstrated in 123 $YBa_2Cu_3O_7$ superconductors. The pinning mechanism in Ag-clad Bi-based superconducting wires, however, has not been well studied. It is not clear that defects such as dislocations, stacking faults and interfaces can act as flux pinning centres. In fact, it is even not certain whether defects such as dislocations are present in the samples after prolonged annealing. In this regard, extensive temperature and field dependence of magnetization measurements were performed for samples cold rolled 30% and 98%, and annealed 2223 BSCCO/Ag tape, in addition to conventionally sintered 2223 powder samples. All measurements were made with the field parallel to the surface plane except for the annealed tape, which were studied with field in both direction ($H \perp$ C-axis, $H \parallel$ C-axis). For the 2223 BSCCO powder sample (Figure 77), the hysteresis of magnetization (ΔM) rapidly decreased as temperature increased to 30 K, and disappeared at an applied field of 10,000 gauss. From the comparison of magnetization measurements in cold rolled samples, as shown in Figure 84, 85, 86, and 87, the magnitude of magnetization (M) and the value of ΔM considerably increased with the extent of deformation.

For the 98% cold rolled sample (Figure 86 and 87), decrease of the magnitude beyond the maximum value is much slower than that for the 30 % cold rolled sample, and other HIP-treated samples, even though mechanical deformation does not significantly improve the magnetization value. The shape of magnetization hysteresis is not like the "bird wing" which was often found for conventionally sintered powder samples. Moreover, up to 60 K, it holds the viable ΔM value till the field reaches 20,000 gauss.

This slow gradual decrease of the magnetization at high field means that the tape samples contain more defects to pin flux compared to the powder samples. It is also probable that mechanical deformation not only improves the magnitude of the pinning potentials (U_o) showing ΔM value at higher temperatures, it also increases the number of

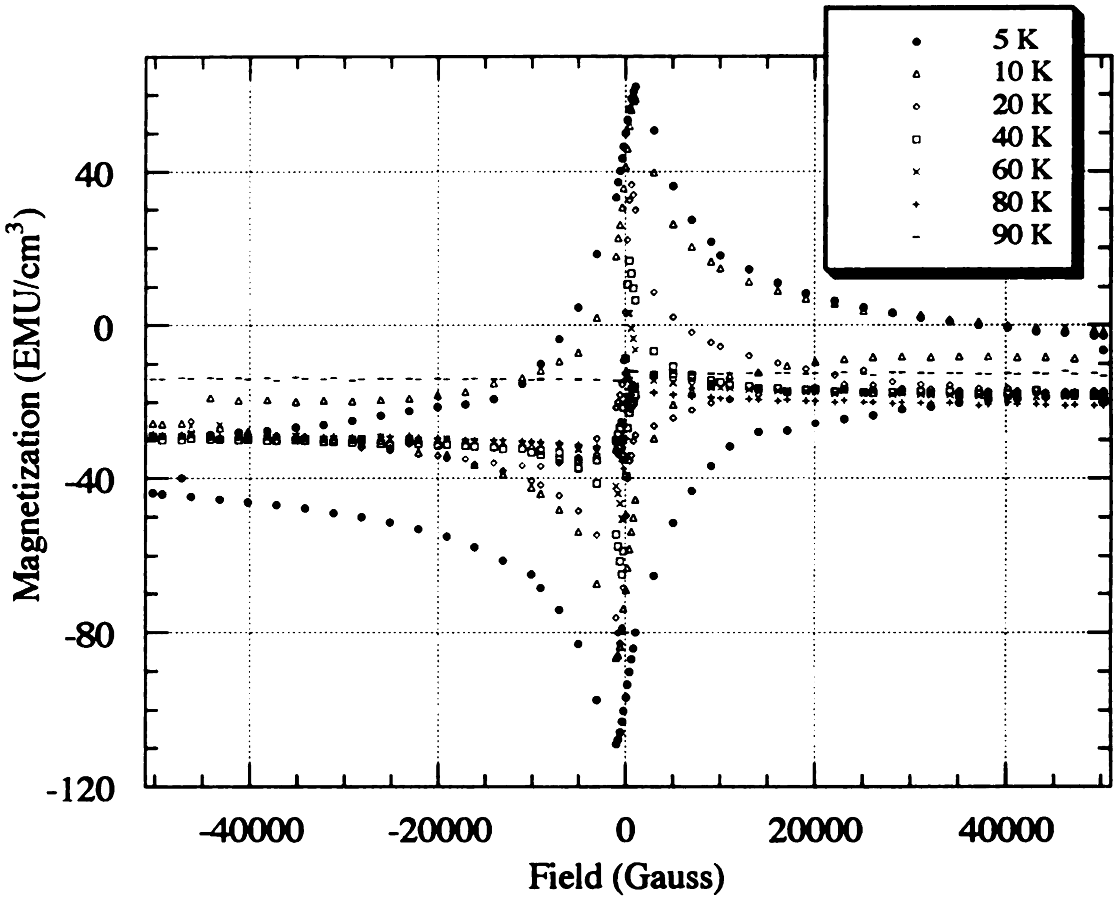

Figure 84. Temperature dependence of the magnetization of 30 % cold rolled 2223 BSCCO/Ag composite (30 %R)

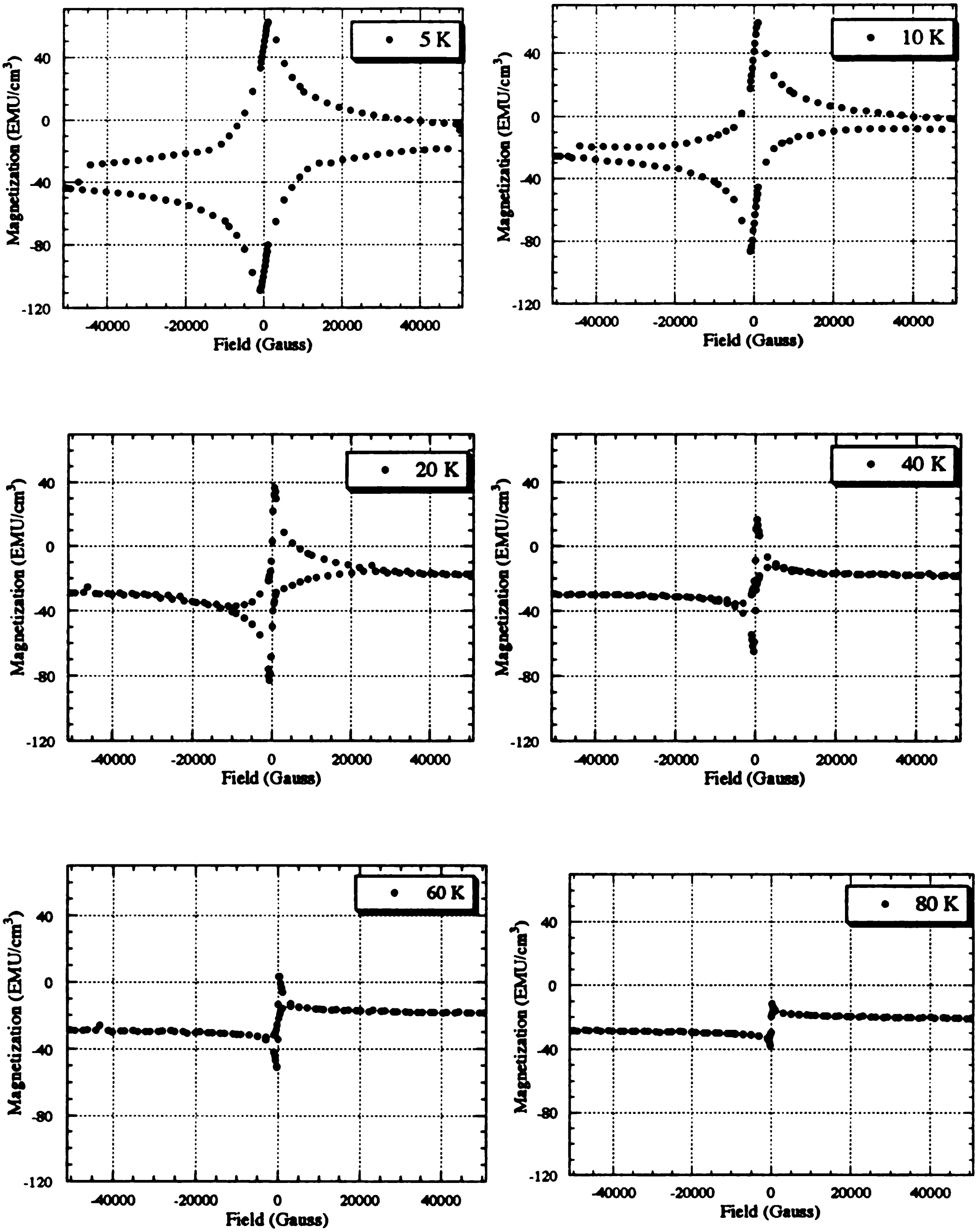

Figure 85. Magnetization curve of the 30% cold rolled 2223 BSCCO/Ag composite, measured at 5K, 10K, 20K, 40K, 60K, and 80K

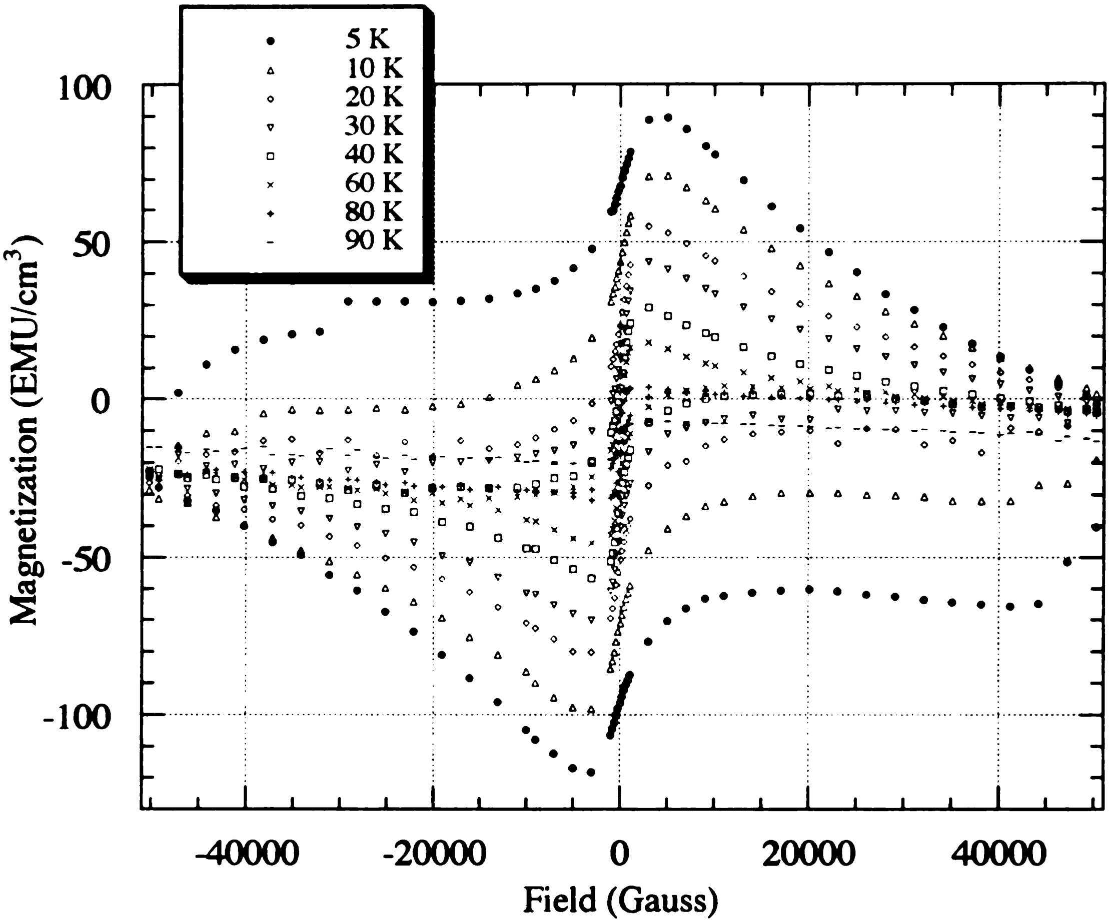

Figure 86. Temperature dependence of the magnetization of cold rolled 2223 BSCCO/Ag tape (98 %R)

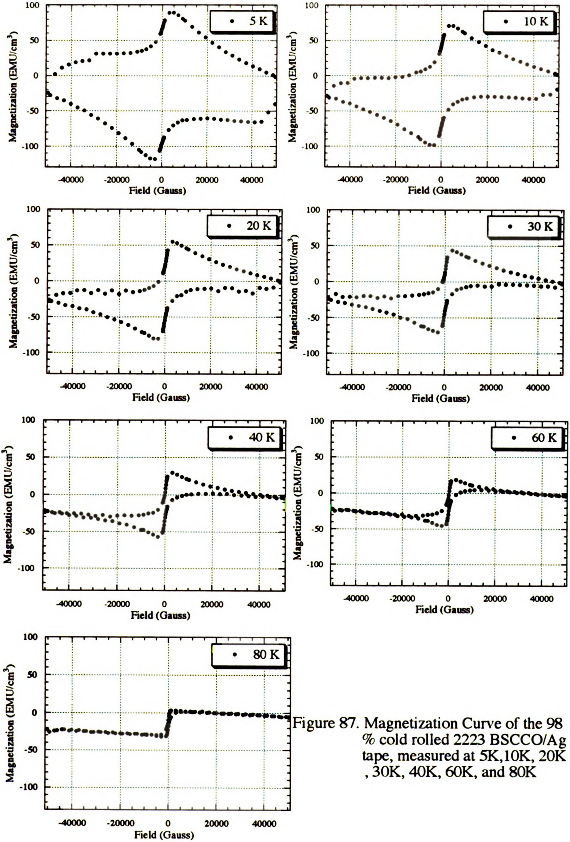

Figure 87. Magnetization Curve of the 98 % cold rolled 2223 BSCCO/Ag tape, measured at 5K,10K, 20K , 30K, 40K, 60K, and 80K

pinning centers. Comparatively in the HIP sample, only the number of pinning sites increased. This is an evidence that, at low temperatures, ΔM contains a large intragranular component arising from strong flux pinning within the grains.

For the annealed tape (Figure 88 and 89), there is a large improvement in the magnitude of M, which was expected due to an improvement in connectivity, but not the relative ΔM. The decrease of relative ΔM under magnetic fields shows same tendency in the cold rolled tape. The shape of magnetization curve at elevated temperatures is much better than that for the melt processed 2212 BSCCO/Ag tape samples. Therefore, thermomechanically processed 2223/Ag tape is a good candidate for the high temperature and high magnetic field applications. The grains in the tape samples contain more defects than those for the powder samples due to the harsh mechanical deformation used for processing the tapes.

If the magnetic field is applied parallel to the tape surface, $H \perp$ C-axis, instead of $H \parallel$C-axis, then the thermally activated dissipation becomes much smaller and high J_c can be obtained at temperatures higher than 30 K [17]. Our experimental data also agree with this trend. With the field parallel to the tape surface and perpendicular to the current flow direction, significant magnitude of $J_c(H) > 10^4$ A/cm^2 is measured at 30 K , as shown in Figure 90.

Figure 90 and 91 show the dependence of the J_c on magnetic field and temperatures, with magnetic field applied parallel and perpendicular to the tape surface ($H \perp$ C-axis and $H \parallel$C-axis) respectively. It is noticed that the J_c shows a strong anisotropy in relation to the direction of the applied magnetic field. The J_c with $H \parallel C$ is about 30% of the value for $H \perp C$ at 5 K. The problem is more severe at higher temperatures and magnetic field. For $H \perp C$, the tape holds 13 % of its zero-field J_c value at 10,000 gauss at 60 K (Figure 90), whereas the J_c for $H \parallel C$ loses more than 99% of its zero-field value at the same field and temperature (Figure 91), indicating that the pinning in the c-axis direction is extremely weak. It should be noted that different behavior of flux creep

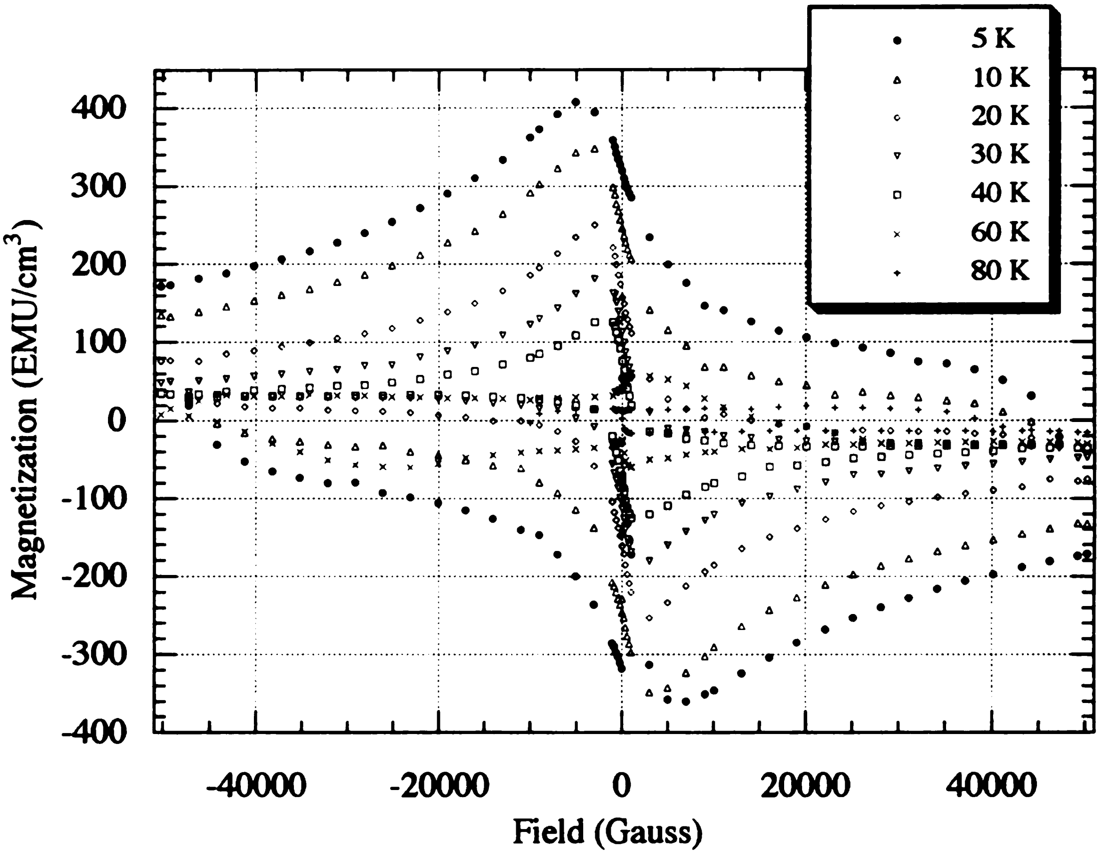

Figure 88. Temperature dependence of the magnetization of annealed 2223 BSCCO/Ag tape

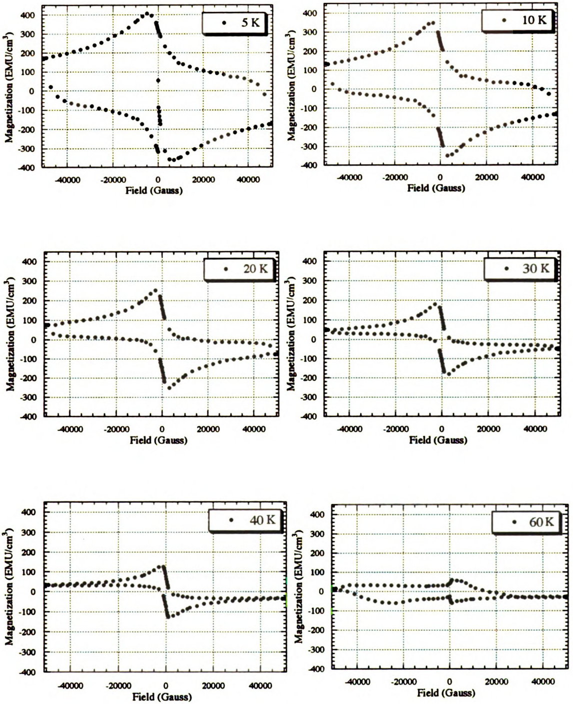

Figure 89. Magnetization Curve of the annealed 2223 BSCCO/Ag tape measured at 5K,10K, 20K,30K, 40K, and 60K

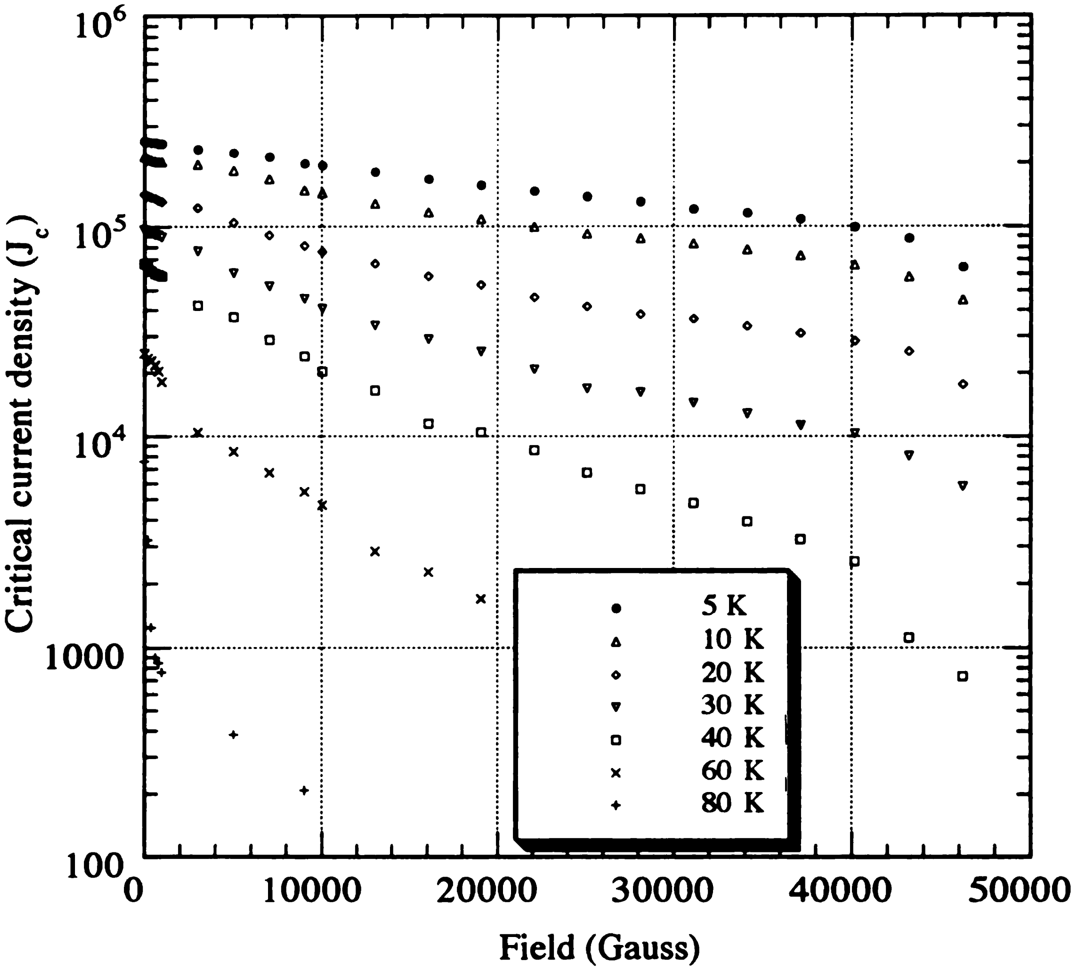

Figure 90. Temperature and magnetic field dependence of the critical current density of annealed 2223 BSCCO/Ag tape, with field applied parallel to the tape surface

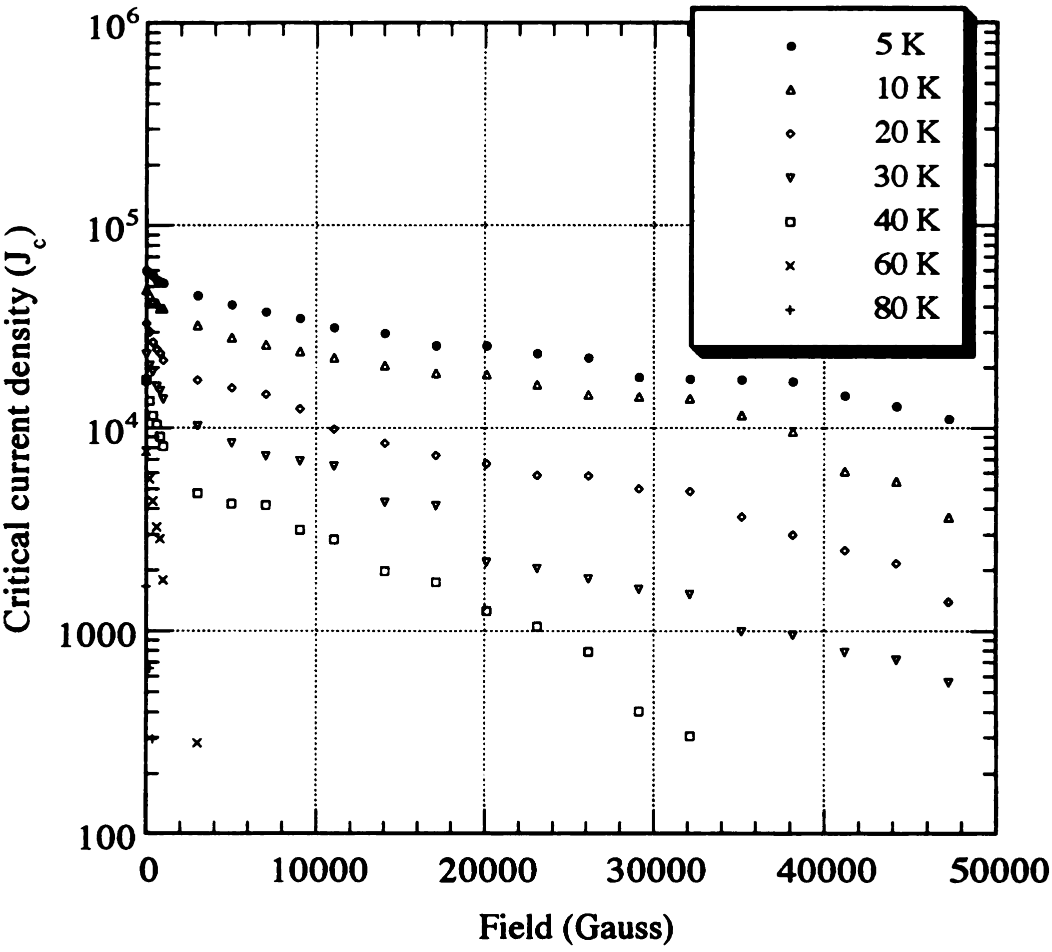

Figure 91. Temperature and magnetic field dependence of the critical current density of 2223 BSCCO/Ag Tape, with field applied perpendicular to the tape surface

is related to the different pinning energies resulting from the difference in anisotropy. Namely, it has been shown that the anisotropy in electronic properties is much larger in BSCCO than in YBaCuO [43,44]. A large electronic anisotropy directly results in a reduction of the correlation length along the flux lines L_c.

This can be explained by the fact that an important structural parameter is the distance between the Cu-O planes. Those compounds that have a single nonconducting oxide layer between Cu-O planes exhibit the least amount of anisotropic behavior and highest irreversibility temperature and field. In the bismuth and thallium 2223 and 2212 structures (Figure 8), two layers of Bi-O or Tl-O respectvely divide the unit cell into two isolated superconducting layers. For magnetic fields parallel to the c axis (perpendicular to the tape surface), these insulating layers are thought to cause flux lines to break up into short segments or "pancakes" that may decouple and move independently under the influence of the Lorentz force after having been thermally activated.

For flux pinning, two consequences of this decoupling are a reduction of the effective pinning volume by limiting the length of flux line pinned, and an increase in the required pin density, since each pancake along the length of a flux line must be pinned separately. As mentioned in section 2, $U_o = \mathbf{J}_c \times \mathbf{B} V_c r_p = \mathbf{J}_c \times \mathbf{B} R_c^2 L_c r_p$, and thus a short correlation length along the vortices L_c, results in a small activation energy, because of the small flux bundle volume [15]. Reduction of the pinning volume reduces the thermal activation barrier (U_O), and thus increases the rate of thermally activated flux motion.

To confirm the effect of the thermomechanical process on the flux pinning, the irreversibility lines (IL) for the c-axis aligned (98 % cold rolled and annealed) 2223 BSCCO/Ag tapes, 2223 BSCCO powder, and HIP-treated samples were determined from magnetization measurements as shown in Figure 92. The IL, the disappearance of pinning at a certain temperature and a certain field, can be determined from the magnetization curves by determining the disappearance of hysteresis (ΔM=0) in the magnetization curves at fixed temperatures [121]. The IL is defined as the disappearance

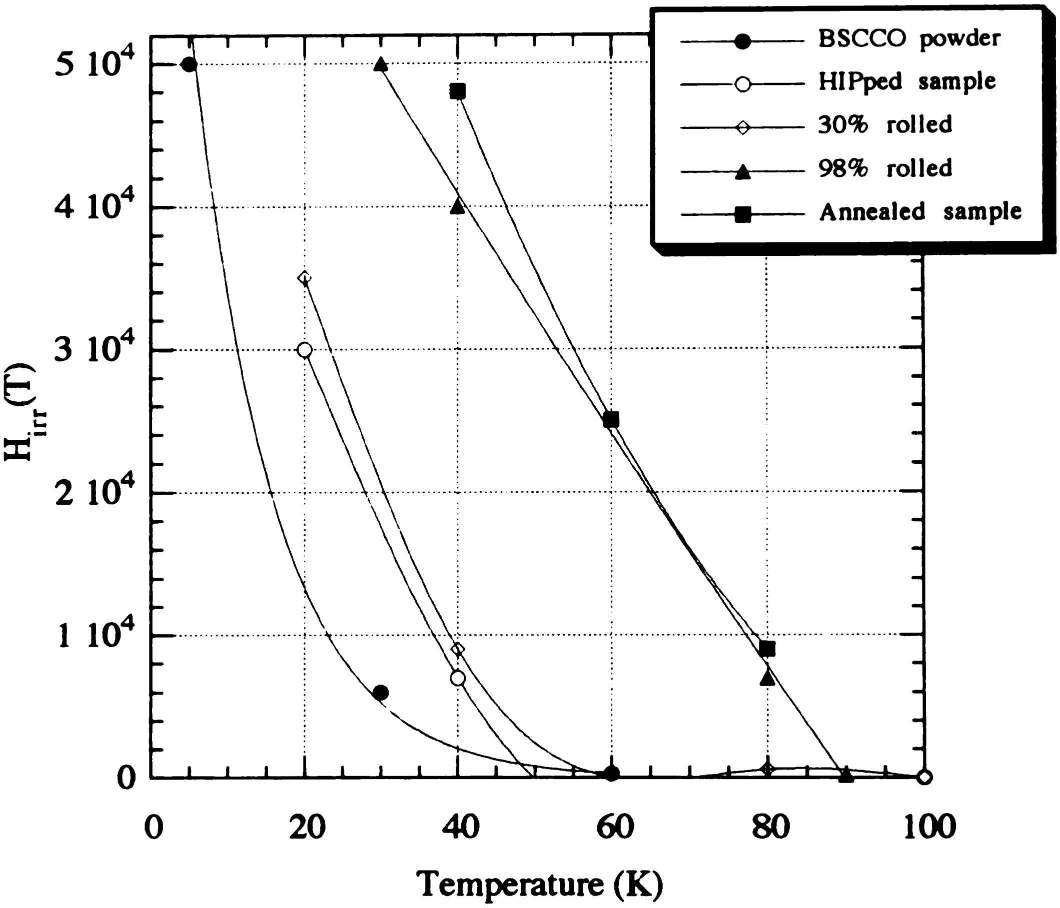

Figure 92. Irreversibility lines for 2223 BSCCO/Ag tape in comparison with other processed sample

of pinning at a certain temperature and a certain field, which holds the relation $J_c(H,T)=0$. In the present work, $H_{irr}(T)$ is defined as the field at which the magnetic hysteresis-width ΔM drops to the noise level of the measuring apparatus.

It is noted that the IL for the cold rolled 2223 BSCCO/Ag tape is shifted to higher temperatures and magnetic field compared to the IL for the 2223 BSCCO powder sample and HIP treated samples. On the other hand the IL for the annealed 2223 BSCCO tape does not shift to higher temperatures and field, compared to the IL for the cold rolled 2223 BSCCO/Ag tape. It is clear that the positions of the IL are not governed by grain connectivity and are close to intrinsic properties of the material. Since the IL gives the information on the core pinning, a considerable shift of the IL for the cold rolled tape is an indication of the enhancement of core pinning. The grains in the cold rolled and annealed 2223 BSCCO/Ag tape samples contain more defects than that for the other samples due to the extensive thermomechanical deformation. Thus the significant enhancement of the IL for the tape sample can be attributed to the defect pinning. From those experimental results, considering theoretical results of temperature dependence of pinning potential ($U_o(t)$)[15], we can write

$$U_o(t) = U_o(o)(1-t)^q, \text{ with } t=T/T_c. \qquad (40)$$

where $q=2-n/2$ (n=1 and 2) [15]. Thermomechanically processed 2223/BSCCO has a higher T_c and may have a higher initial pinning potential.

It is generally believed that the IL is a function of the coupling strength between the superconducting CuO_2 planes. The distance between the inter-CuO_2 planes is taken as a measure of the coupling strength, which means that the positions of the irreversibility line are intrinsic properties of the material, determined by its structure. Nevertheless, recent studies of flux pinning by radiation damage [46,50,51] indicate that the position of the irreversibility line depends, to a significant degree, on the specific characteristics of the pinning centers, and that it can be moved to a higher field and temperature by increasing the density of pinning centers.

In order to investigate the relationship between the processing variables and flux pinning behavior of BSCCO superconductors, the magnetization data for different processed samples are compared to each other at 5 K and 40 K, as shown in Figure 93 and 94 respectively. At 5 K, it is observed that magnetization hysteresis (ΔM) for most samples decreases slowly with field (Figure 93 and Table 3), compared to that for 40 K (Figure 94), which means that flux pinning is strong at low temperatures due to the intrinsic pinning. Therefore, the intragrain current is high, so the weak links become relatively important, as demonstrated in melt processed 2212 BSCCO/Ag sample at low magnetic field in Figure 93.

A processed sample with a stronger c-axis texture (which reduces weak link problem), shows a significant increase in magnetization hysteresis (ΔM) especially at low magnetic fields. This is because the low-field hysteresis reflects both intergrain and intragrain currents. A thermomechanically processed 2223 BSCCO/Ag sample has more magnetization hysteresis (ΔM) at magnetic fields greater than 16,000 gauss, as shown in Table 3, which means larger intragrain current due to enhanced defect pinning. The behavior of magnetization hysteresis (ΔM) is directly related to critical current density (J_c), as shown in Figure 95 at 5 K.

At 40 K, ΔM decreases rapidly with field except for the thermomechanically processed 2223 BSCCO tapes which show less decline of ΔM with field. For example, the melt processed 2212 BSCCO tapes hold very small value of ΔM at 19,000 gauss, as shown in Table 4. At high temperatures thermally activated flux motion become pronounced, flux pinning is weak and hence intragrain current controls the J_c. Thus, the melt processed 2212 BSCCO tape samples only have a J_c value of $\sim 10^4$ A/cm^2 at less than 2,000 gauss while thermomechanically processed 2223 BSCCO tape samples show a J_c value of $\sim 10^4$ A/cm^2 up to 20,000 gauss, as shown in Figure 95 at 40 K.

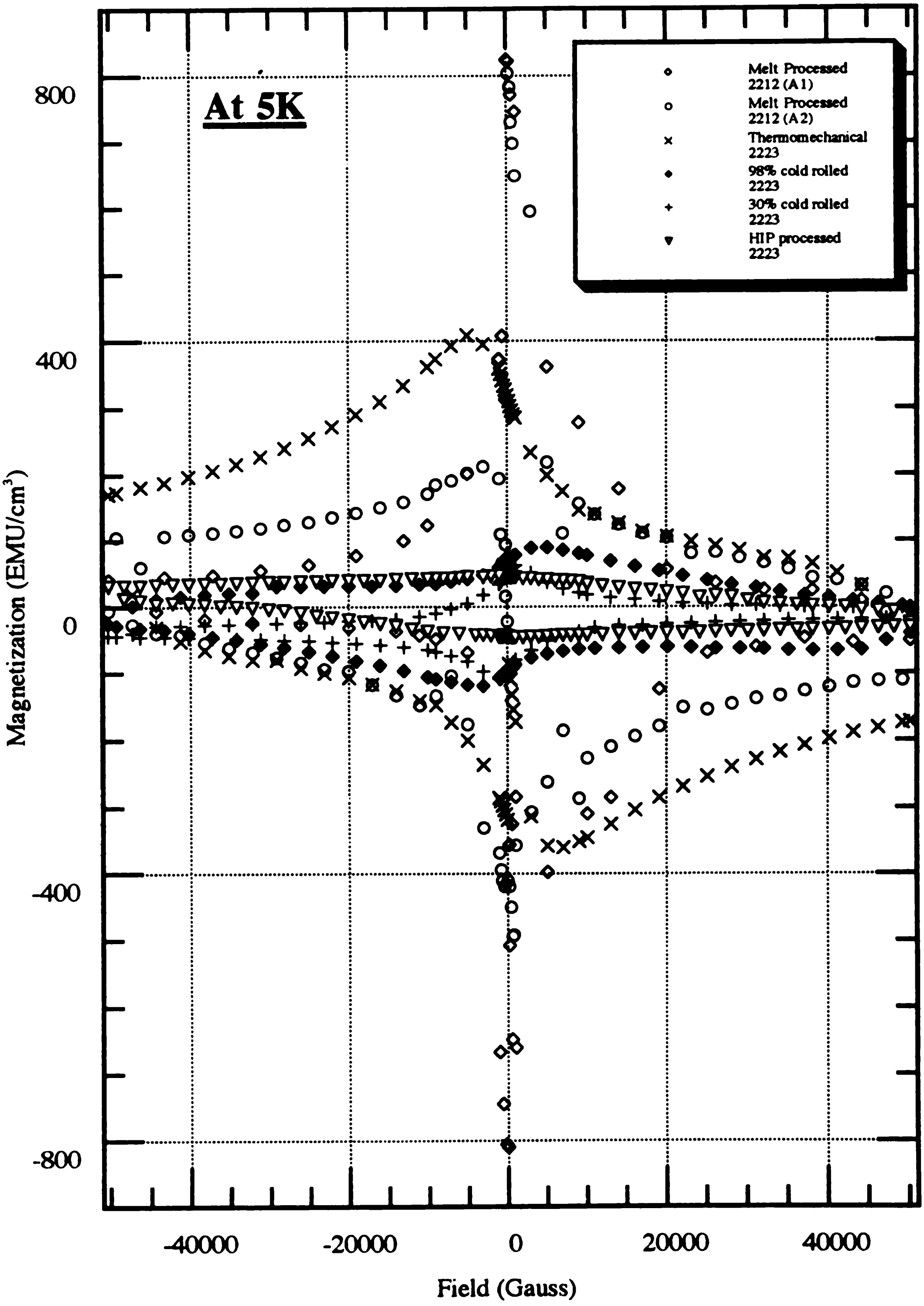

Figure 93. The comparison of magnetic field dependence of the magnetization data at 5K for different processed samples

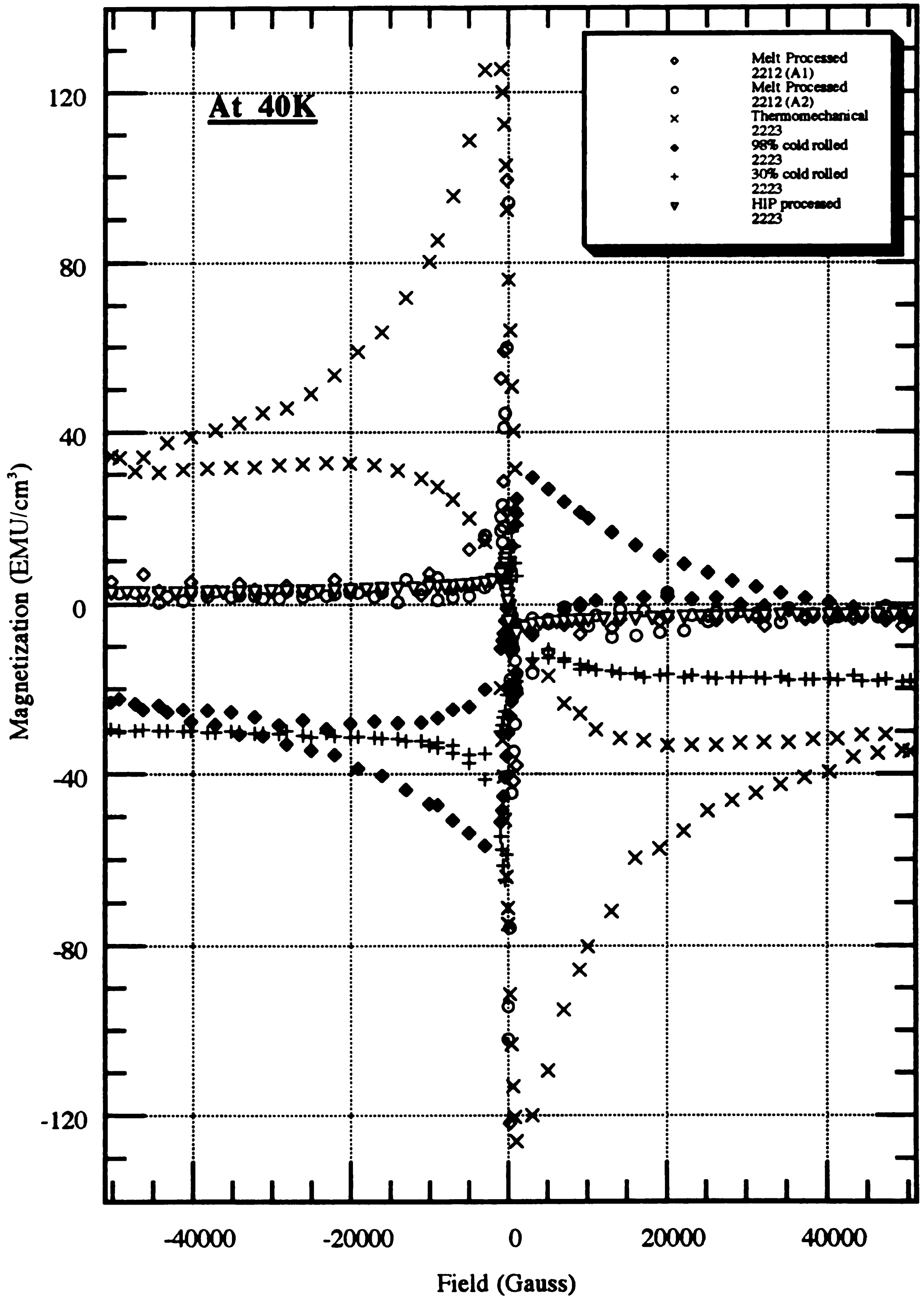

Figure 94. The comparison of magnetic field dependence of the magnetization data at 40K for different processed samples

Table 3. List of magnetization and hysteresis (ΔM) data at 5K under different processing condition

Melt processed 2212 BSCCO/Ag tape (sample: A1)				**Melt processed 2212 BSCCO/Ag tape (sample:A2)**			
Magnetic Field	Magnetization (M-)	Magnetization (M+)	Hysteresis (ΔM)	Magnetic Field	Magnetization (M-)	Magnetization (M+)	Hysteresis (ΔM)
Gauss	(EMU/cm^3)	(EMU/cm^3)	(EMU/cm^3)	(EMU/cm^3)	(EMU/cm^3)	(EMU/cm^3)	(EMU/cm^3)
0	-809.54	823.79	1633.3	0	-410.54	803.77	1214.3
208.79	-660.79	821.9	1482.7	215.39	-418.96	782.99	1201.9
				415.39	-449.8	730.8	1180.6
607.69	-648.27	771.24	1419.5	617.58	-493.7	698.36	1192.1
				818.68	-492.1	649.69	1141.8
1009.9	-507.48	746.25	1253.7	1018.7	-357.02	594.8	951.82
				3028.6	-306.61	219.19	525.8
5031.9	-397.52	361.74	759.26	5038.5	-261.6	156.64	418.24
				7048.4	-184.97	139.27	324.23
				9057.2	-286.07	124.37	410.44
10055	-309.38	278.19	587.56	10063	-226.09	111.47	337.56
13069	-284.64	178.21	462.85	13075	-208.74	111.4	320.14
				16090	-193.39	104.46	297.85
19098	-123.45	57.409	180.86	19104	-178.17	82.033	260.21
				22117	-150.76	80.873	231.63
25128	-69.479	36.294	105.77	25133	-153.31	74.489	227.8
				28148	-145.04	66.491	211.53
31154	-59.801	26.011	85.812	31162	-137.27	57.205	194.47
				34177	-133.05	43.714	176.76
37184	-46.72	24.755	71.475	37191	-126.28	40.776	167.06
				40206	-120.18	31.703	151.88
43214	-53.135	9.5542	62.69	43223	-113.44	19.897	133.34
				46237	-111.21	-4.8322	106.38

Table 3. (ccontinued)

Thermomechanically processed 2223 BSCCO/Ag tape				**98% cold rolled 2223 BSCCO/Ag tape**			
Magnetic Field	Magnetization (M-)	Magnetization (M+)	Hysteresis (ΔM)	Magnetic Field	Magnetization (M-)	Magnetization (M+)	Hysteresis (ΔM)
Gauss	(EMU/cm^3)	(EMU/cm^3)	(EMU/cm^3)	(EMU/cm^3)	(EMU/cm^3)	(EMU/cm^3)	(EMU/cm^3)
0	-318.39	318.71	637.1	17.58	-96.135	70.311	166.45
208.79	-320.28	309.72	629.99	215.39	-94.307	72.455	166.76
408.79	-324.68	303	627.68	413.19	-92.135	74.632	166.77
610.99	-328.89	296.15	625.04	627.47	-90.519	76.459	166.98
810.99	-330.41	290.13	620.54	824.18	-88.974	78.462	167.44
1013.2	-332.14	285.43	617.58	1023.1	-87.285	80.487	167.77
3023.1	-342.91	233.9	576.81	3027.5	-76.883	85.761	162.64
5031.9	-357.75	199.14	556.89	5048.4	-70.423	88.821	159.24
7041.8	-360.21	175.21	535.42	7055	-66.433	89.433	155.87
9050.6	-351.11	146.68	497.79	9059.4	-65.811	77.742	143.55
10056	-345.73	140.43	486.16	11065	-65.191	69.468	134.66
13069	-324.51	126.58	451.09	14089	-64.873	61.216	126.09
16084	-303.6	114.59	418.18	17098	-64.557	54.153	118.71
19098	-285.14	106.1	391.24	20107	-60.775	46.612	107.39
22109	-268.21	98.334	366.54	23131	-60.963	40.351	101.31
25126	-253.13	92.475	345.61	26140	-61.336	33.4	94.736
28141	-239.63	85.807	325.44	29164	-61.98	28.422	90.402
31154	-227.72	74.653	302.37	32173	-62.389	23.011	85.4
34169	-216.43	72.868	289.3	35180	-62.629	17.72	80.349
37185	-206.41	64.661	271.07	38206	-63.197	13.456	76.653
40197	-197.19	51.454	248.64	41214	-63.71	9.36	73.07
43213	-187.83	31.691	219.52	44223	-60.278	4.7718	65.05
46230	-180.86	-20.321	160.54	47247	-51.486	-1.6542	49.832

Table 3. (continued)

30% cold rolled 2223 BSCCO/Ag composite				HIP processed 2223 BSCCO			
Magnetic Field	Magnetization (M-)	Magnetization (M+)	Hysteresis (ΔM)	Magnetic Field	Magnetization (M-)	Magnetization (M+)	Hysteresis (ΔM)
Gauss	(EMU/cm^3)	(EMU/cm^3)	(EMU/cm^3)	(EMU/cm^3)	(EMU/cm^3)	(EMU/cm^3)	(EMU/cm^3)
14.29	-96.829	50.021	146.85	8.79	-43.64	45.284	88.924
212.09	-93.436	53.446	146.88	206.59	-45.462	45.062	90.524
409.89	-90.172	56.32	146.49	403.3	-45.395	44.818	90.213
624.18	-86.849	59.093	145.94	620.88	-46.151	44.529	90.68
821.98	-84.053	60.949	145	818.68	-46.506	44.284	90.791
1019.8	-79.977	62.139	142.12	1016.5	-46.506	43.862	90.369
3025.3	-65.224	50.739	115.96	3023.1	-45.618	42.174	87.791
5045.1	-51.438	36.134	87.571	5045.1	-44.44	41.174	85.614
7052.8	-43.295	27.347	70.642	7052.8	-43.107	39.618	82.725
9057.2	-36.862	21.614	58.476	9056.1	-42.485	37.73	80.214
11063	-31.588	18.104	49.692	10060	-42.196	35.685	77.881
14087	-27.761	14.398	42.159	14085	-40.64	29.175	69.815
17095	-27.542	10.901	38.443	16089	-40.418	26.775	67.193
20103	-25.584	8.2746	33.859	20101	-39.552	21.709	61.261
23129	-24.512	6.3024	30.814	22120	-39.107	19.598	58.705
26136	-23.402	4.5829	27.985	26133	-38.063	14.91	52.972
29161	-21.879	3.1793	25.058	28140	-37.441	14.199	51.639
32170	-21.212	2.0545	23.266	32167	-36.374	5.4439	41.818
35178	-20.155	1.0261	21.181	34173	-35.685	4.2218	39.907
38203	-19.576	0.15912	19.735	38200	-34.263	0.73326	34.997
41212	-19.05	-0.68874	18.362	40204	-34.174	0.42218	34.597
44221	-18.647	-1.6634	16.983	44218	-32.641	-4.5329	28.108
47245	-18.321	-1.9847	16.336	46239	-32.33	-6.5549	25.775

Table 4. Selected magnetization hysteresis (ΔM) data at 5K and 40K under different processing condition (**MP** and **TMP** stands for 'melt processed' and 'thermo-mechanically processed', respectively), where A1 and A2 represents 2°C/hr and 10°C/hr cooling rate, respectively

	MP 2212 (A1)	**MP 2212 (A2)**	**TMP 2223**
Temp., Field	Hysteresis (ΔM)	Hysteresis (ΔM)	Hysteresis (ΔM)
(K, Gauss)	(EMU/cm^3)	(EMU/cm^3)	(EMU/cm^3)
5, ~19,000	180.86	260.21	391.24
40, ~19,000	0.83	3.99	24.31
	98% rolled 2223	**30% rolled 2223**	**HIPped 2223**
Temp., Field	Hysteresis (ΔM)	Hysteresis (ΔM)	Hysteresis (ΔM)
(K, Gauss)	(EMU/cm^3)	(EMU/cm^3)	(EMU/cm^3)
5, ~20,000	107.39	33.859	61.261
40, ~20,000	9.42	0	0

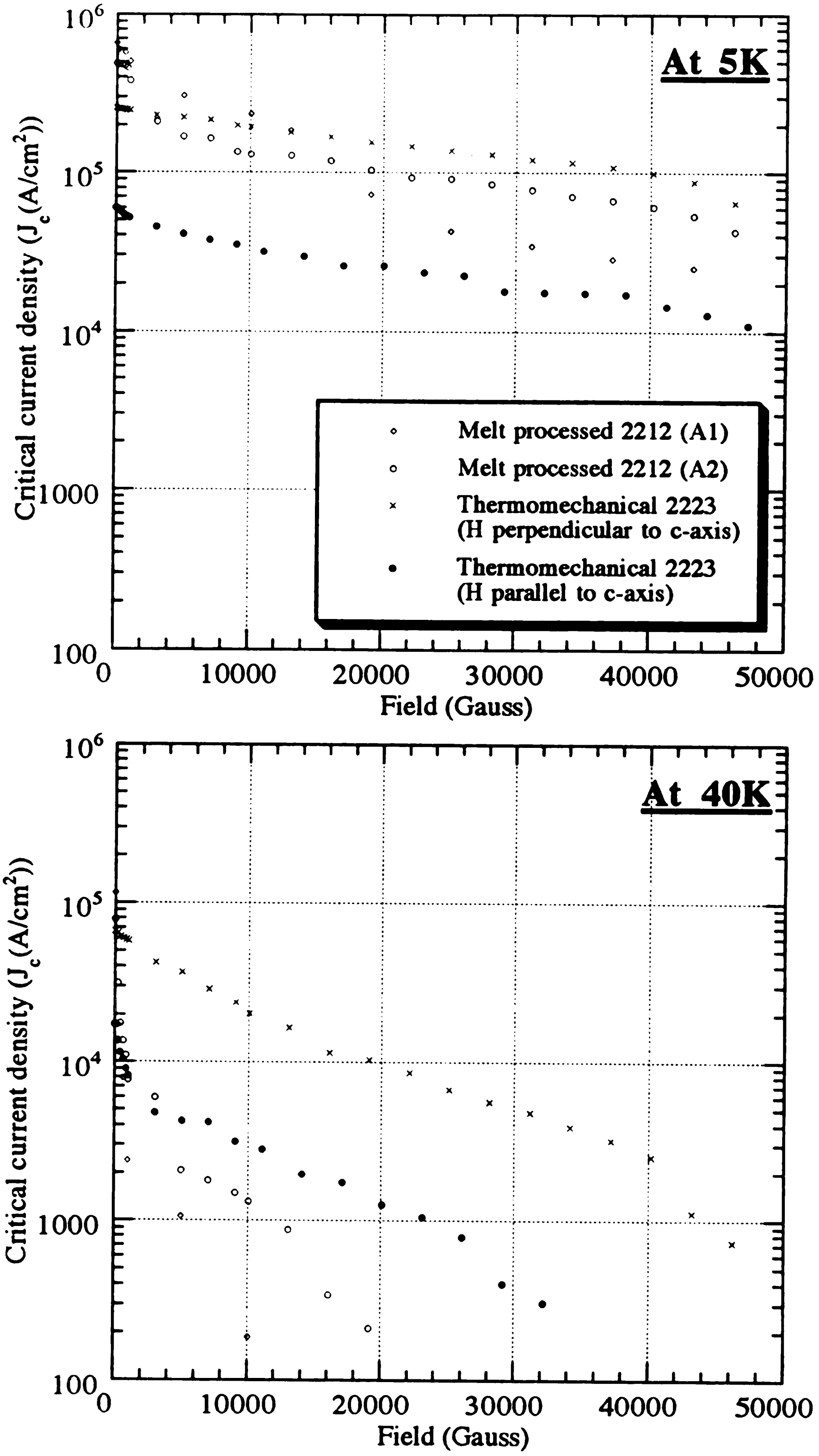

Figure 95. The comparison of magnetic field dependence of the critical current density (J_c) at 5K and 40K for melt processed 2212 and thermomechanically processed 2223 BSCCO/Ag tapes

5. CONCLUSIONS

The primary objective of this research was to mitigate two fundamental problems, weak-link and flux creep, in a high T_c superconductor, and to find the optimum processing conditions that will yield the correct chemical, mechanical, and electromagnetic properties. Following are the main conclusions of this research.

5.1 The High Density 2223 BSCCO Superconductor Prepared by Hot Isostatic Pressing

1. The problem associated with densification in sintering of high-T_c 2223 BSCCO system has been studied. A HIP process for 2223 BSCCO system was established with the consideration that the crystal structure of 2223 BSCCO superconducting compound is quite stable with respect to oxygen stoichiometry under increasing temperature up to 850°C and high pressure, compared to 123 YBaCuO superconductor.

2. The most significant result of the present study is that it demonstrates that HIP processing can be used to consolidate 2223 BSCCO superconducting compounds to obtain as high as 94 % of theoretical density while maintaining the high T_c phase.

5.2 High-T_c 2223 BSCCO/Ag Tape Fabricated by HIP-clad and Thermomechanical Deformation

1. With a mechanical deformation, $\{00l\}$ grain alignment (%) is increased, reaching a maximum value of ~90% alignment calculated from Lotgering factor.

2. It is observed that peak intensities corresponding to high-T_c phase are maintained up to an annealing temperature of 850°C and strong, sharp $\{00l\}$ reflection peaks are dominant. As the annealing temperature increased to 860°C, high-T_c 2223 phase

abruptly decomposed into low-T_c 2212 phase. This is presumably due to the lowering of the melting temperature of the compound by silver.

3. A sample annealed for 100 hours, shows that the superconductor material near the BSCCO/Ag interface experiences a more extensive melting and layer-like growth (c-axis texture), which extends macroscopically from the Ag interface.

5.3 Texture Analysis of the Mechanically Deformed 2223 BSCCO/Ag Composite

1. At low deformations (~15-40% R), it appears that a weak, fiber-like texture begins to appear at the distribution of (109) poles. The group of the experimental (00$\underline{14}$) and (109) pole figures show that under deformation, the {00*l*} plane normals rotate toward the compression direction of rolling and the (109) plane normals tend to form a fibre texture around the compression direction. During this mechanical processing, texturing, cracking, and fracturing (resulting from rotation) are intimately related.

2. The WIMV algorithm has been used to analyze the texture of 2223 BSCCO/Ag superconducting tape. The sample orientation distribution of short term (5H) annealed samples show a c-axis texture, with the c-axes aligned perpendicular to the plane of the tape and no preferred alignment of the ' a' and ' b' axes.

3. Inverse pole figure data reveals that: i) (019), (109), (015), and (105) grains could rotate towards the compression direction of rolling that is parallel to the c-axis, ii) after achieving a certain degree of texturing (at ~50% R), saturation of the evolution of deformation texture was also observed with respect to further deformation.

4. For a higher deformation (~98% R), the strong fibre-like distribution of the (109) poles, which is observed at ~70% R, is degraded with increasing deformation (~98% R).

5. The initial presence of predominantly non-{00l} grains, introduced by HIP, partly helps to accommodate deformation, and mitigate catastrophic fracture or failure of this material during severe mechanical deformation.

5.4 Highly Textured 2212 BSCCO/Ag Tape Fabricated by Controlled Melt Processing

1. With a slower cooling rate between 880°C and 860°C, second phases are rarely seen, and alignment is further improved. 10°C/hr cooling rate was found to be the best for producing a highly textured 2212 phase at 880°C. At faster cooling rates (120°C/hr), it clearly shows that most of the surface grains are moderately aligned parallel to the tape surface, but the alignment of the core region is disrupted and the grain size is smaller.

2. The long term (100 hours) annealed sample shows lower intensity peaks for the secondary phases such as the Cu-free phase, while a small amount of 2201 phase is still present. The examination of the overall quality of the tape should be accompanied by the observation of microstructure inside the core region, not just by X-ray diffraction.

3. It has been found that higher processing temperature (~920°C) significantly increases the amount of secondary phases. Selective vaporization of the components might be a reason for this problem. To reduce this problem, the total time at elevated temperature must be minimized, which will require a careful optimization of temperature, time, and cooling rate.

5.5 Magnetization, Critical Current Density, and Pinning Mechanism in BSCCO

1. For the melt processed 2212 BSCCO/Ag tape, even though weak link problem has been significantly decreased by producing a highly textured microstructure, there is still a problem of thermally activated flux creep, which limits the operating

temperature range to less than 30 K and a small magnetic field for practical applications. However, at 5K, excellent J_c values of 4.8×10^5, 1.3×10^5, and $0.4\times 10^5 A/cm^2$ at H=0, 10,000, 50,000 gauss respectively have been calculated from magnetization measurements.

2. The enhancement in the magnetization hysteresis (ΔM) for the thermomechanically processed 2223 BSCCO/Ag tape, especially at relatively high temperatures and high fields, could be attributed to the defect pinning, in particular to the intragrain defects due to extensive thermomechanical deformation.

3. The comparison of magnetization measurements (2212 and 2223 BSCCO/Ag tape) suggests that the critical current is controlled by flux pinning at high temperatures. Since at high temperatures thermally activated flux motion becomes pronounced, flux pinning is weak and hence intragrain current controls the J_c. On the other hand, at low temperatures the flux pinning is strong due to the intrinsic pinning, the intragrain current is high, so the weak links become relatively important and limit the J_c.

REFERENCES

REFERENCES

1. H. Maeda, Y. Tanaka, M. Fukutomi, and T. Asano, Jpn. J. Appl. Phys., **27** (1988) L209.

2. J. M. Tarascon et al., Phys. Rev., B**37** (1988) 9382.

3. K. Kugimiya, S. Kawashima, O. Inoue, and S. Adachi, Appl. Phys. Lett. **52** (22) (1988) 1895.

4. C. W. Chu, P. H. Hor, R. L. Meng, L. Cao, and Z. J. Huang, Science, **235** (1987) 567.

5. R. J. Cava, B. Batlogg, R. B. Van Dover, D. W. Murphy, S. Sunshine, T. Siegriest, J. P. Rameika, E. A. Reitman, S. Zahurak and G. P. Espionosa, Phys. Rev. Lett., **58** (1987) 1676.

6. K. Hiraga, D. Shindo, M. Hirabayashi, M. Kikuchi, N. Kobayashi, and Y. Syono, Jpn. J. Appl. Phys., **27** (1988) L1848.

7. E. E. Hellstrom, MRS Bulletin, **August** (1992) 45.

8. Y. Matsui and S. Horiuchi, Jpn. J. Appl. Phys., **27** (1988) L2306

9. R. Dupree, Z. P. Han, A. P. Howes, D. M. Paul, M. E. Smith, and S. Male, Physica C, **175** (1991) 269.

10. J. W. Ekin et al., J. Appl. Phys., **62** (1987) 4821.

11. D. Dimos, P. Chaudhari, and J. Mannhart, Phys. Rev., B**41** (1990) 4038.

12. S. E. Babcock, X. Y. Cai, D. L. Kaiser, and D. C. Larbalestier, Nature, **347** (1990) 167.

13. S. E. Babcock, MRS Bulletin, **August** (1992) 20.

14. T. T. M. Palstra, B. Batlogg, L. F. Schneemeyer, and J. V. Waszczak, Phys. Rev. Lett., **61** (1988) 1662.

15. T. T. M. Palstra, B. Batlogg, R. B. van Dover, L. F. Schneemeyer, and J. V. Waszczak, Phys. Rev., B**41** (1990) 6621.

16. D. Dew-Hughes, Cryogenics, **28** (1988) 674.

17. S. Jin, R. B. van Dover, T. H. Tiefel, and J. E. Graebner, Appl. Phys. Lett., **58** (1991) 868.

18. H. Kumakura, K. Togano, E. Yanagisawa, J. Kase, and H. Maeda, Jpn. J. Appl. Phys., **29** (1990) L1652.

19. E. Zeldov, Physica A **168** (1990) 260.

20. A. D. Caplin, S. S. Bungre, S. M. Cassidy, J. R. Laverty, and Z. X. Shen, Physica A **168** (1990) 268.

21. D. W. Johnson, and W. W. Rhodes, J. Am. Ceram. Soc., **72** (1989) 2346.

22. S. X. Dou, H. K. Liu, M. H. Apperley, K. H. Song, and C. C. Sorrell, Physica C **167** (1990) 525.

23. H. Seino, K. Ishizaki, and M. Takata, Jpn. J. Appl. Phys., **28** (1989) L78.

24. J. M. Yoo and K. Mukherjee, J. Mater. Sci. 28 (1993) 2361.

25. H. Seikine, J. Schwartz, T. Kuroda, K. Inoue, H. Maeda, K. Numata, and H. Yamamoto, J. Appl. Phys., **70** (1991) 1596.

26. J. Kase, N. Irisawa, and T. Morimoto, Appl. Phys. Lett., **56** (1990) 970.

27. P. Haldar, J. G. Hoehn, J. A. Rice, and M. S. Walker, Appl. Phys. Lett., **61** (1992) 604.

28. S. Jin, J. E. Graebner, T. H. Tiefel, R. B. van Dover, A. E. White, and G. W. Kammlott, Physica C **177** (1991) 189.

29. Y. Feng, K. E. Hautanen, Y. E. High, D. C. Larbalestier, R. Ray II, E. E. Hellstrom, and S. E. Babcock, Physica C **192** (1992) 293.

30. E. E. Hellstrom, JOM, **October** (1992) 48.

31. T. Hikata, K. Sato, and H. Hitotsuyanagi, Jpn. J. Appl. Phys., **28** (1989) L82.

32. E. Yanagisawa, and T. Morimoto, Appl. Phys. Lett., **54** (1989) 2602.

33. D. R. Dietderich, B. Ullmann, H. C. Freyhardt, J. Kase, H. Kumakura, K. Togano, and H. Maeda, Jpn. J. Appl. Phys., **29** (1990) L1100.

34. A. Oota, A. Yata, and K. Ohba, Supercond. Sci. Technol., **5** (1992) S359.

35. H. K. Liu, Y. C. Guo, and S. X. Dou, Supercond. Sci. Technol., **5** (1992) 591.

36. S. X. Dou, H. K. Liu, Y. C. Guo, and C. C. Sorrell, Supercond. Sci. Technol., **5** (1992) S359.

37. T. R. Dinger, T. K. Worthington, W. J. Gallagher, and R.L. Sandstrom, Phys. Rev. Lett., **58** (1987) 2687.

38. N. Enomoto, H. Kikuchi, N. Uno, H. Kumakura, K. Togano, and N. Watanabe, Jpn. J. Appl. Phys. **29** (1990) L447.

39. G. Jin, J. E. Graebner, T. H. Tiefel, R. B. Van Dover, A. E. White, and G. W.

Kammlott, Phisica C 177 (1991) 189.

40. V. A. Kozlov, and A. V. Samokhvalov, Physica C **213** (1993) 103.

41. P. W. Anderson, and Y. B. Kim, Rev. Mod. Phys., **36** (1964) 39.

42. M. R. Beasley, R. Labusch, and W. W. Webb, Phys. Rev., **181** (1969) 682.

43. S. Martin, A. T. Fiory, R. M. Fleming, L. F. Schneemeyer, and J. V. Waszczak, Phys. Rev. Lett., **60** (1988) 2194.

44. D. E. Farrell, S. Bonham, J. Foster, Y. C. Chang, P. Z. Jiang, K. G. Vandervoort, D. J. Lam, V. G. Kogan, Phys. Rev. Lett., **63** (1989) 782.

45. D. E. Prober, R. E. Scwall, and M. R. Beasley, Phys. Rev. B**21** (1980) 2717.

46. L. Civale, T. K. Worthington, A. D. Marwick, F. Holtzberg, J. R. Thompson, M. A. Kirk, and R. wheeler, JOM, **October** (1992) 60.

47. A. Zhukov, H. Kupfer, R. Kresse, R. Meiner-Hirmer, S. Karabashev, Supercond. Sci. Technol., **5** (1992) S153.

48. J. R. Clem, Phys. Rev. B**43** (1991) 7837.

49. D. H. Kim et al., Physica C **177** (1991) 431.

50. R. L. Fleischer, H. R. Hart, K. W. Lay, and F. E. Luborsky, Phys. Rev. B**40** (1989) 2163.

51. R. B. van Dover et al., Nature, **342** (1989) 55.

52. R. B. van Dover et al., Appl. Phys. Lett., **56** (1990) 2681.

53. L. Civale et al., Phys. Rev. Lett., **67** (1991) 648.

54. A. Barbu et al., Europhys. Lett., **15** (1991) 37.

55. S. Jin et al., Appl. Phys. Lett., **56** (1990) 1287.

56. R. Ramesh, S. Jin, S. Nakahara, and T. H. Tiefel, Appl. Phys. Lett., **57** (1990) 1458.

57. M. Murakami, M. Morita, K. Doi, and K. Miyamoto, Jpn. J. Appl. Phys., **28** (1989) 1189.

58. T. Hikata, K. Sato, and H. Hitotsuyanagi, Jpn. J. Appl. Phys., **28** (1989) L82.

59. R. K. Singh, J. Narayan, A. K. Singh, and J. Krishawamy, Appl. Phys. Lett., **54** (1989) 2271.

60. K. Salama, V. Selvamanickam, L. Gao, and K. Sun, Appl. Phys. Lett., **54** (1989) 2253.

61. G. W. Crabtree et al., Phys. Rev. B**36** (1987) 4021.

62. C. P. Bean, Rev. Mod. Phys., **36** (1964) 31.

63. E. M. Gyorgy, R. B. van Dover, K. A. Jackson, L. F. Schneemeyer, and J. V. Waszczak, Appl. Phys. Lett., **55** (1989) 283.

64. Y. Yamada and S. Murase, Jpn. J. Appl. Phys., **27** (1988) L996.

65. M. Takano, J. Takada, K. Oda, H. Kidakuchi, Y. Miura, Y. Ikeda, Y. Tomii, and H. Mazaki, Jpn. J. Appl. Phys., **27** (1988) L 1041.

66. D. Shi et al., Appl. Phys. Lett., **55** (1989) 699.

67. M. Lagues et al., Science, **262** (1993) 1850.

68. Z. Z. Sheng and A. M. Hermann, Nature, **332** (1988) 55.

69. A. Schilling, M. Cantoni, J. D. Guo, and H. R. Ott, Nature, **363** (1993) 56.

70. I. Amato, Science, **262** (October) (1993) 31.

71. R. L. Coble, J. Appl. Phys., **32** (1961) 787.

72. K. Sadananda, A. K. Singh, M. A. Iman, M. Osofsky, V. Letourneau, and L. E. Richards, ADV. Ceram. Mater. **3** (1988) 524.

73. J. Niska, B. Loberg, and K. Eastering, J. Am. Ceram. Soc. **72** [8] (1989) 1508.

74. M. Aslan, H. Jaeger, K. Schulze, A. Frisch, and G. Petzow, J. Am. Ceram. Soc., **73** (1990) 450.

75. Y. Yamada, M. Yata, Y. Kaieda, H. Irie, and T. Matsumoto, Jpn. J. Appl. Phys., **28** (1989) L797.

76. B. C. Hendrix, T. Abe, J. C. Borofka, and J. K. Tien, Appl. Phys. Lett., **55** (1989) 313.

77. K. Donnelly, J. F. Lawler, J. M. D. Coey, and B. Raveau, Supercond. Sci. Technol., **4** (1991) 27.

78. K. Ishizaki, M. Takata, and H. Seino, J. Mater. Sci. Lett., **9** (1990) 16.

79. S. X. Dou, H. K. Liu, M. H. Apperley, K. H. Song, C. C. Sorell, K. E. Easterling, J. Niska, and S. J. Guo, Physica C **167** (1990) 525.

80. H. Seino, K. Ishizaki, and M. takata, Jpn. J. Appl. Phys., **28** (1988) L78.

81. M. C. Mercay, Industrial Heating, **June** (1988) 15.

82. H. Okada and K. Homma, CIMTEC, Proc. **6th** (1986) 1023.

83. W. A. Kaysser, M. Aslan, E. Arzt, M. Mitkov, and G. Petzow, Powder Metallurgy, **31** (1988) 63.

84. E. Arzt, M. F. Ashby, and K. E. Easterling, Metall. Trans., **14A** (1983) 211.

85. R. L. Coble, J. Appl. Phys., **41** (1970) 4798.

86. M. Ueyama, T. Hikata, T. Kato, and K. Sato, Jpn. J. Appl. Phys., **30** (1991) L1384.

87. J. Kase, K. Togano, H. Kumakura, D. R. Dietderich, N. Irisawa, T. Morimoto, and H. Maeda, Jpn. J. Appl. Phys., **29** (1990) L1096.

88. P. Hardar, L. Motowidlo, JOM, **October** (1992) 54.

89. K. H. Sandhage, G. N. Riley, and W. L. Carter, JOM, **43** (1991) 25.

90. J. Kase, T. Morimoto, K. Togano, H. Kumakura, D. R. Dietderich, and H. Maeda, IEEE Transactions on Magnetics, **27** (1991) 1254.

91. R. D. Ray II and E. E. Hellstrom, Physica C **175** (1991) 255.

92. J. Simoyama et al., Physica C **185** (1991) 931.

93. B. Hong and T. O. Mason, J. Am. Cer. Soc., **74** (1991) 1045.

94. Y. Oka et al., Jpn. J. Appl. Phys., **28** (1989) L801.

95. T. Sata, K. Sakai, and S. Tashiro, J. Am. Cer. Soc., **75** (1992) 805.

96. A. Umezawa et al., Physica C **198** (1992) 261.

97. R. D. Ray II and E. E. Hellstrom, Appl. Phys. Lett., **57** (1990) 2948.

98. Y. Feng, D. C. Larbalestier, S. E. Babcock, and J. B. Vandersande, Appl. Phys. Lett. **61** (1992) 1234.

99. L. N. Bulaevskii, J. R. Clem, L. I. Glazman, and A. P. Malozemoff, Phys. Rev. B**45** (1992) 2545.

100. R. J. Asaro, J. Appl. Mech., **50** (1983) 921.

101. D. M. Parks and S. Ahzi, J. Mech. Phys. Solids., **38** (1990) 701.

102. A. Morinari, G. Canova, and S. Ahzi, Acta Metall., **35** (1987) 2983.

103. R. J. Asaro and A. Needleman, Acta Metall., **33** (1985) 923.

104. U. F. Kocks, Metall. Trans., **1** (1970) 1121.

105. C. Tome, G. Canova, S. Ahzi, and A. Morinari, Proceedings of ICOTOM-**8** (1987) 395.

106. J. W. Hutchinson, Metall. Trans., **8A** (1977) 1465.

107. C. S. Lee and B. J. Dugan, Metall. Trans., **22A** (1991) 2637.

108. A. Ito, M. Matsuda, Y. Iwai, M. Ishi, M. Takata, T. Yamashita, and H. Koinuma, Jpn. J. Appl. Phys., **28** (1989) L380.

109. A. Oota, K. Ohba, A. Ishida, H. Noji, A. Kirihigashi, K. Iwasaki, and H. kuwajima, Jpn. J. Appl. Phys., **29** (1990) L262.

110. L. G. Schulz, J. Appl. Phys., **20** (1949) 1030.

111. J. S. Kallend, U. F. Kocks, A. D. Rollet, and H. R. Wenk, Mater. Sci. and Eng., **A132** (1991) 1.

112. S. Matthies and G. W. Vinel, Phys. Status. Solidi B, **112** (1982) K111.

113. U. F. Kocks, Proceedings of ICOTOM-**8** (1987) 31.

114. U. Endo, S. Koyama, and T. Kawai, Jpn. J. Appl. Phys., **27** (1988) L1476.

115. Y. Suzuki, T. Inove, S. Hayashi, and H. Komatsu, Jpn. J. Appl. Phys., **28** (1989) L1382.

116. H. Enami, N. Kawahara, T. shinohara, S. Kawabata, H. Hoshizaki, A. Matsumuro, and T. Imura, Jpn. J. Appl. Phys., **28** (1989) L377.

117. F. K. Lotgering, J. Inorg. Nucl. Chem. **9** (1959) 113.

118. G. Kozlowsky, I. Maartense, R. Spyker, R. Leese, and C. E. Oberly, Phisica C **173** (1991) 195.

119. S. Ahzi, R. J. Asaro, and D. M. Parks, Report of research in mechanics of materials Report No. **2** (1992).

120. R. Yoshizaki, H. Ikeda, K. Yoshikawa, and N. Tomita, Jpn. J. Appl. Phys., **29** (1990) L753.

121. W. Kritscha, F. M. Sauerzopf, H. W. Webber, G. W. Crabtree, Y. C. Chang, and P. Z. Jiang, Supercond. Sci. Technol., **5** (1992) S232.